UNIVERSITY OF CALIFORNIA

Santa Barbara

Toward Long Wavelength Absorption: Dinuclear Photo-activated CO Releasing Moieties

A dissertation submitted in partial satisfaction of the

requirements for the degree Doctor of Philosophy

in Chemistry

by

Zhi Li

Committee in charge:

Professor Peter C. Ford, Chair

Professor Martin Moskovits

Professor Steven K. Burrato

Professor Gabriel Ménard

January 2018

The dissertation of Zhi Li is approved.

Gabriel Ménard

Steven K. Burrato

Martin Moskovits

Peter C. Ford, Committee Chair

January 2018

Toward Long Wavelength Absorption: Dinuclear Photo-activated CO Releasing Moieties

by

Zhi Li

ACKNOWLEDGEMENTS

First, I would like to thank our generous funding source US National Science Foundation.

I want thank Dr. Ford. None of the work in the thesis would be possible without his mentoring, support and trust. I joined Ford group without any inorganic chemistry background. Dr. Ford taught me inorganic chemistry, photochemistry and kinetic in his class and chalk talk group meeting. I am very grateful for all the knowledge he taught me and the freedom he gave to me in my project to help me become an independent scientist. Most importantly, from Dr. Ford, I have learned critical thinking and great learning methods which will continuously direct me in my future research career.

I would also like to thank all Ford group members for working together in the lab. I want to especially thank Agustin, Poju, Jacob and John for their teaching, help and collaborations.

I must thank my family who always support me in my grad school time. My parents support and understand my pursuing for science and they never have complained that I have not been back to China to visit them for four years during my PhD study. Lastly, I want to thank my wife, Mengyuan. Even though we live so far away from each other, she always encourages and supports me.

VITA OF ZHI LI
January 2018

EDUCATION

UC Santa Barbara California, U.S. 2012-2017
Ph.D. Candidate, Chemistry (in progress)
Nankai University Tianjin, China 2009-2012
M.S., Organic Chemistry
Tianjin University Tianjin, China 2005-2009
B.S., Material Science and Engineering

RESEARCH SKILLS

Synthesis: Organic Compounds, Inorganic Compounds, Conjugated Oligomers, Polymers, Upconversion Nanoparticles.
Computation: Gaussian, Spartan and MATLAB
Device Fabrications: Solar Cell Device, Single Carrier Diode
Equipment: Schlenk line, Glove box, Clean Room, Uv-vis, Fluorimeter, NMR, EPR, GC, Mass Spectroscopy, Laser, Time-Resolved Spectroscopy, AFM, Photo-Conductive AFM, TGA, DSC, XRD/XRR, Kelvin Probe Force Microscope, Ellipsometer, Profilometer, sputtering.
Advanced understanding in: organic & inorganic chemistry, spectroscopy, photochemistry, photophysics, reaction kinetics, organic semiconductor, device physics.
Familiar with: polymer chemistry & physics.

PROFESSIONAL EXPERIENCE & CONTRIBUTIONS

Department of Chemistry & Biochemistry, UCSB
Graduate Student Researcher
2012-Current

- **Inorganic photochemistry**
  - Designed and synthesized a thermal-stable and high quantum yield IR light activate carbon monoxide releasing molecule.
  - Photochemistry study on inorganic complexes.
  - Self-learned DFT calculations for inorganic complex using Gaussian and Spartan.

- **Organic semiconductors**
  - Optimized the structure of ZnO layer in inverted organic solar cell and increased the power conversion efficiency by twice, to 6%.
  - Diagnosed one type of non-fullerene organic solar cell and concluded inefficient exciton harvesting to be efficiency limiting factor.
  - Measured exciton diffusion length of various organic semiconductors and probed into exciton trapping mechanisms.

- **Other achievements**
  - Reviewed and judged 15 research manuscripts for international journals: *Tetrahedron*, *Tetrahedron Letters*, *Dalton Transactions* and *Chemical Communications.*
  - 4 presentations in American Chemical Society Meetings and Southern California Inorganic Photochemistry Meetings.
  - Mentored 5 junior researchers in the lab.

Graduate Teaching Assistant
2014-2017

- Taught for 11 quarters. Lectured and supervised ~24 undergraduate students per session in chemistry labs and ensured safety.
- Constructively reviewed and graded lab assignments and reports.
- Elaborated difficult concepts understanding for upper-level undergraduate and graduate students in *Advanced Inorganic Chemistry* class review sessions.

Molecular Foundry, Lawrence Berkeley National Lab & UCSB
Visiting Researcher
March-April, 2016

- Synthesized core-shell structured upconverting nanoparticles (UCNPs) for therapeutic small molecule delivery.
- Worked on state-of-the-art robot for nanomaterial development.

Department of Chemistry, Nankai University
Graduate Student Researcher
2009-2012

- Core contributor to the leadership of the research group in small molecular organic solar cell area.
- Achieved worldwide efficiency record of 6.1% on solution processed small molecular organic solar cell.
- Pioneered the use of dye electron-withdrawing group in the donor material of organic solar cell.
- Developed cross-coupling synthetic pathway for a drug precursor for an affiliate company.

Department of Material Science and Engineering, Tianjin University
Undergraduate Student Researcher
2008-2009

- Synthesized amphiphilic copolymer poly(MPC-g-PEG-b-PLA) for lipophilic anti-cancer drug delivery and monitored drug releasing from microcapsules.

PUBLICATIONS

Total citations 1654

- **Zhi Li,** Agustin E. Pierri, Po-Ju Huang, Guang Wu, Alexei V. Iretskii and Peter C. Ford*. "Dinuclear PhotoCORMs: Dioxygen-Assisted CO Uncaging from Long Wavelength Absorbing Metal-Metal Bonded Carbonyl Complexes", ***Inorg. Chem***. 2017*, 56,* 6094–6104. (**Selected as ACS editor choice and front cover of issue 11 in Inorganic Chemistry**)
- **Zhi Li**, Guangrui He, Xiangjian Wan, Yongsheng Liu, Jiaoyan Zhou, Guankui Long, Yi Zuo, Yongsheng Chen*. "Solution processable rhodanine-based small molecule organic photovoltaic cells with high power conversion efficiency", ***Adv. Energy Mater***. 2012, *2*, 74-77. (**Citations: 240, rank: top 5%**)
- **Zhi Li,** Jason D.A. Lin, Hung Phan, Alexander Sharenko, Christopher M. Proctor, Peter Zalar, Zhihua Chen, Antonio Facchetti and Thuc-Quyen Nguyen*. "Competitive Absorption and Inefficient Exciton Harvesting: Lessons Learned from BHJ OPVs Utilizing the Polymer Acceptor P(NDI2OD-T2)", ***Adv. Funct. Mater***. 2014, *24*, 6989–6998.
- Jianyu Yuan*, Michael J. Ford, Yannan Zhang, Huilong Dong, **Zhi Li**, Youyong Li, Thuc-Quyen Nguyen, Guillermo C. Bazan*, and Wanli Ma*. "Toward Thermal Stable and High Photovoltaic Efficiency Ternary Conjugated Copolymers: Influence of Backbone Fluorination and Regioselectivity", ***Chem. Mater.*** 2017, *29*, 1758–1768
- Guangrui He, Xiangjian Wan, **Zhi Li**, Qian Zhang, Guankui Long, Yongsheng Liu, Yanhui Hou, Mingtao Zhang and Yongsheng Chen*. "Impact of fluorinated end groups on the properties of acceptor-donor-acceptor type oligothiophenes for solution-processed photovoltaic cells" ***J. Mater. Chem***. 2014. *2*. 1337-1345.
- Guankui Long , Xiangjian Wan*, Bin Kan , Yongsheng Liu , Guangrui He , **Zhi Li** ,Yawei Zhang , Yi Zhang , Qian Zhang , Mingtao Zhang , and Yongsheng Chen*. "Investigation of Quinquethiophene Derivatives with Different End Groups for High Open Circuit Voltage Solar Cells" ***Adv. Energy Mater***. 2013, 3, 639-636.
- Jiaoyan Zhou, Yi Zuo, Xiangjian Wan, Guankui Long, Qian Zhang, Wang Ni, Yongsheng Liu, **Zhi Li**, Guangrui He, Chenxi Li, Bin Kan, Miaomiao Li, and Yongsheng Chen*. "Solution-Processed and High-Performance Organic Solar Cells Using Small Molecules with a Benzodithiophene Unit" ***J. Am. Chem. Soc***. 2013, *135*, 8484−8487.
- Guangrui He, **Zhi Li**, Xiangjian Wan, Jiaoyan Zhou, Guankui Long, Shuzhong Zhang, Mingtao Zhang, Yongsheng Chen*. "Efficient small molecule bulk heterojunction solar cells with high fill factors via introduction of π -stacking moieties as end group", ***J. Mater. Chem. A***. 2013, *1*, 1801-1809.
- Guankui Long, Xiangjian Wan*, Jiaoyan Zhou, Yongsheng Liu , **Zhi Li** , Guangrui He , Mingtao Zhang , Yanhui Hou , Yongsheng Chen*. Isothianaphthene-Based Conjugated Polymers for Organic Photovoltaic Cells" ***Macromol. Chem. Phys***. 2012, *213*, 1596−1603.
- Guangrui He，**Zhi Li**, Xiangjian Wan, Yongsheng Liu, Jiaoyan Zhou, Guankui Long, Mingtao Zhang and Yongsheng Chen*. "Impact of dye end groups on acceptor–donor–acceptor type molecules for solution-processed photovoltaic cells", ***J. Mater. Chem***. 2012, *22*, 9173-9180.

- Jiaoyan Zhou, Xiangjian Wan, Yongsheng Liu, Yi Zuo, **Zhi Li**, Guangrui He, Guankui Long, Wang Ni, Chenxi Li, Xuncheng Su, and Yongsheng Chen*. "Small Molecules Based on Benzo[1,2-b:4,5-b]dithiophene Unit for High-Performance Solution-Processed Organic Solar Cells" ***J. Am. Chem. Soc***. 2012, *134*, 16345−16351.
- Chaoyong Liu, Lixia Long, **Zhi Li**, Bin He, Liuheng Wang, Jiapeng Wang, Xubo Yuan, Jing Sheng. "Hollow poly(MPC-g-PEG-b-PLA) graft copolymer microcapsule as a potential drug carrier" *Journal of Microencapsulation.* 2012, *29*, 242-249.
- Jiaoyan Zhou, Xiangjian Wan, Yongsheng Liu, Guankui Long, Fei Wang, **Zhi Li**, Yi Zuo, Chenxi Li, Yongsheng Chen. "A planar small molecule with dithienosilole core for high efficiency" ***Chem. Mater***. 2011, *23*, 4666.
- Yanhui Hou*, Huikai Wang, **Zhi Li**, Yongsheng Liu, Xiangjian Wan, Xiaosong Xue, Yongsheng Chen*, Ao Yu*. "Organic radicals based on phenalenyl and verdazyl units", ***Tetrahedron Letters***. 2011, *52*, 3670–3673.

PATENT

- Yongsheng Chen, Xiangjian Wan, Yongsheng Liu, **Zhi Li**, Jiaoyan Zhou, Fei Wang, Guangrui He, Guankui Long WO Patent **2012**,119,551. Photoelectric Material Preparation

CONFERENCES

253th ACS National Meeting, San Francisco, CA
Apr. 2017

- Oral presentation, title: "Dinuclear photoCORMS: Visible/near-infrared light activating CO release".

251th ACS National Meeting, San Diego, CA
Mar. 2016

- Poster, title: "Rhenium-manganese dinuclear carbonyl complexes as long wavelength absorbing photoCORMs"

Southern California Inorganic Photochemistry Conference
Sep. 2015

- Oral presentation, title: "Rhenium-manganese dinuclear metal carbonyl complexes as interesting photoCORMs"

AWARDS

- 2013 **Phi Lambda Upsilon Award** (National Honorary Chemical Society), UC Santa Barbara
- 2009 **Outstanding Student Scholarship** (Grade 1), Nankai University
- 2006 **Outstanding Student Award**, Tianjin University (Top 5)

ABSTRACT

Toward Long Wavelength Absorption: Dinuclear Photo-activated CO Releasing Moieties

by

Zhi Li

Although carbon monoxide is well known as a poisonous gas causing several adverse effects including fatality, CO has also been found to play a significant role in anti-inflammation, anti-apoptosis, wound healing, and vasorelaxation in mammals through various mechanisms. However, gaseous CO has a very low solubility in water (~1.8 mM) and hemoglobin's high affinity for CO serves as a buffer against beneficial effects at the cellular level. Photochemical CO release from appropriate precursors (mostly metal carbonyls) can give spatial and temporal control. Those precursors, known as photoCORMs (photo-induced carbon monoxide releasing moieties), should have biocompatibility, aerobic and thermal stability in dark and decent solubility in biosystem for in *vivo* CO delivery. Some of photoCORMs meet the above requirements but require Uv light which has low penetration into biological system and causes detrimental effects on cells during irradiation. Although employment of UCNP (upconverting nanoparticles) is accessible, multiphoton upconversion efficiency is still a limiting factor. Developing long wavelength visible light or near infrared light activated photoCORMs remains a challenge in this area.

In this work, a new strategy has been proposed for the delivery of carbon monoxide to physiological targets: rhenium-manganese dinuclear metal carbonyl complexes were synthesized, of which metal-metal (M-M) bond is the most labile bond, and the homolytic cleavage of this bond occur through the photo-excitation of a σ_{MM}^{b} to σ_{MM}* transition. With conjugated diimine ligands (L), σ_{MM}^{b} to π_{L}* charge transfer appears at even lower energy. The homolytic cleavage of the M-M bond generates the mononuclear metal radicals. Although the radicals themselves are unlikely to be particularly reactive toward CO release, they have proved to be reactive with dioxygen to form metal oxides, at the same time to form species that are much more labile toward CO release. In this context, we are studying photochemistry of these dinuclear carbonyl complexes and explored using the hydrophobic versions of these dinuclear complexes with biocompatible polymer PLGA (poly(lactic-co-glycolic acid)) matrices as their drug delivery systems in the form of nano/micro carriers.

TABLE OF CONTENTS

Chapter 1. Introduction

I. Source of carbon monoxide

Carbon monoxide (CO) was first recorded by Aristotle more than two thousand years ago, and was used in an ancient execution method. In 1776, chemist de Lassone generated CO by heating ZnO with coke, however, he claimed the gas product was hydrogen since it burned with a blue flame. In 18th century, the structure and properties of CO were first described by the English chemists Joseph Priestly, John Dalton and William Henry.[1]

Carbon monoxide is normally generated by the partial oxidation (lack of enough oxygen) of carbon containing compounds. During 19th and 20th century, humans have exposure to more CO from lighting, cooking, internal combustion engines, metallurgy and coal gasification, but the largest source of CO is from nature. There is about 5×10^{12} kilograms of CO generated by photochemical reactions in the troposphere every year along with other natural sources such as volcanoes and wild fires.[2]

In mammalian cells, carbon monoxide is generated from the breakdown of hemoglobins by the action of heme oxygenase (HO) enzymes (Shown in Figure 1.1). Besides CO, this breakdown process also leads to production of Fe^{II}, biliverdin and bilirubin (subsequently produced by biliverdin reductase). HO1 (one isoform of HO) is essential for mammalian life and individuals deficient in HO1 have a much higher premature death rate. For example, HO1 knockout mouse has a embryonical death rate >95% with survivors having a shortened life span. Insufficient production of carbon monoxide caused by HO deficiency is suspected to be the direct or indirect cause of premature death.

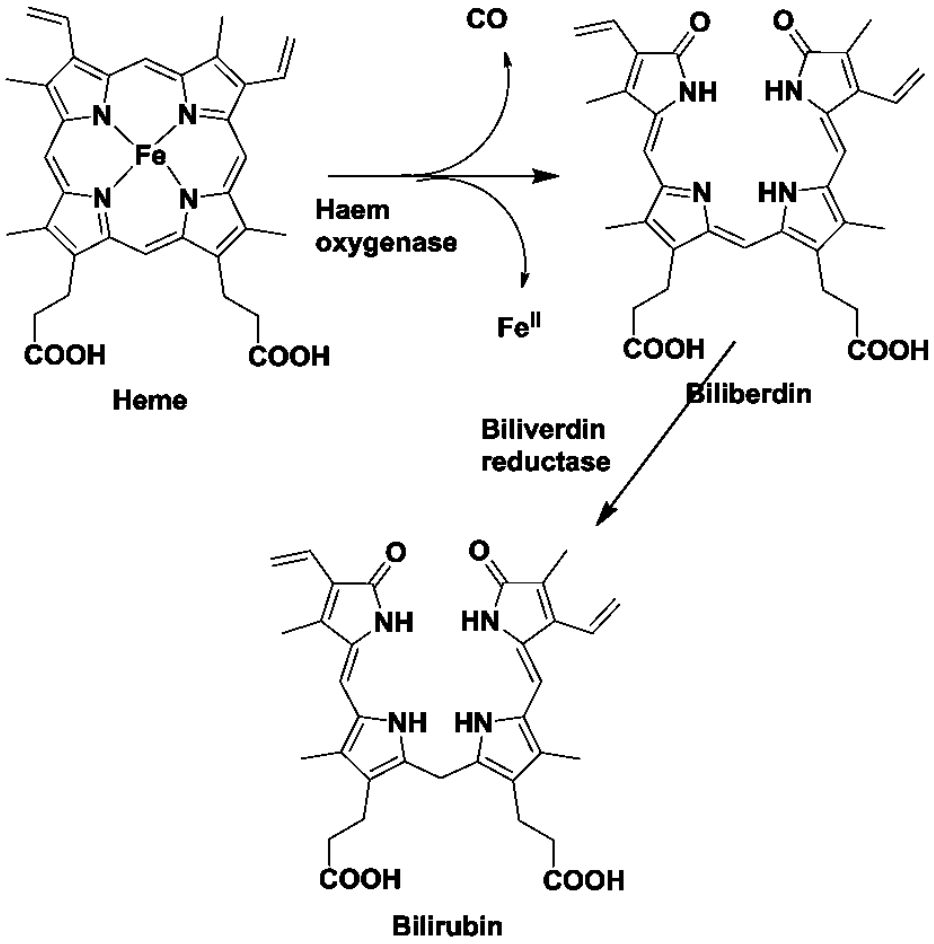

Figure 1. 1 Scheme depicting the breakdown of heme by heme oxygenase.

A. Toxicity of CO

For decades CO has been only considered as a 'silent killer' for its high affinity for haemoglobin (~230 times stronger than for oxygen). After binding with CO, carboxyhaemoglobin (COHb) is then no longer available for the oxygen transport. Although long-term consequences of a controlled amount of CO exposure remains to be evaluated, recent safety trials on healthy volunteers and preclinical toxicology tests suggested that there will be adverse effects in animal models when carboxyhaemoglobin (COHb) level reaches up to ~20%. With 50% of human hemoglobin taken by CO, one will have syndromes such as: headache, fatigue, dizziness, chest pain, seizures and coma. Sometimes this comes with fatal consequences. According to mortality public use data files from National Vital Statistics System, during 1999-2010, a total of 5,149 deaths from unintentional carbon monoxide poisoning happened in the United States with an average of 430 deaths per year.

In mammals, CO is not metabolized but reversibly binds to many cellular targets including active sites in mitochondria. Binding with mitochondria is considered as the main cause of CO toxicity by some researchers. CO as a neutral small molecule can diffuse into the cell and then binds heme-containing proteins cytochrome c oxidase, which is the terminal electron acceptor in the respiration chain of mitochondria. CO binding with cytochrome c oxidase will cause prohibition of ATP production and molecular oxygen may be partially reduced to reactive oxygen species (ROS) instead of water. ROS then causes damage to cell structures in a process is known as oxidative stress. However, CO's binding affinity to hemoglobin is much greater than its binding affinity to cytochrome c oxidase (by about 220 times).[3] Therefore hemoglobin can be somehow considered as a buffer against more toxic effects at the cellular level.

B. Beneficial effect of CO as signaling small molecule

After the 1990s when NO was discovered to be an important signaling small molecule in mammals[4,5], more investigations have been put into possible biological functions of other small molecules such as CO and H_2S. NO is now used in therapy on infants who suffer from pulmonary hypertension and H_2S is used as an intravenous pharmaceutical agent. Extensive physiological and pathophysiological studies have identified CO as a signaling molecule that plays roles in suppressing inflammation, vasorelaxation and wound healing. From a medical perspective, exogenous application of CO is linked to reduced organ graft rejection, to protection against ischemia/reperfusion injury and to anti-bacterial activity. Although CO is still in clinical trials, in the author's opinion, it has inherent advantages over NO and H_2S since it is more stable than other two molecules and reacts exclusively with transition metals with specific redox states. CO is proved to interact with a variety of targets such as: soluble guanylyl cyclase (sGC), heme-containing potassium channels, inducible NO synthase (iNOS), NADPH oxidase, and the heme-binding transcription factors (BACH1 and NPAS2). Through those targets, CO plays several therapeutic roles that are illustrated in Figure 1.2 and discussed below.

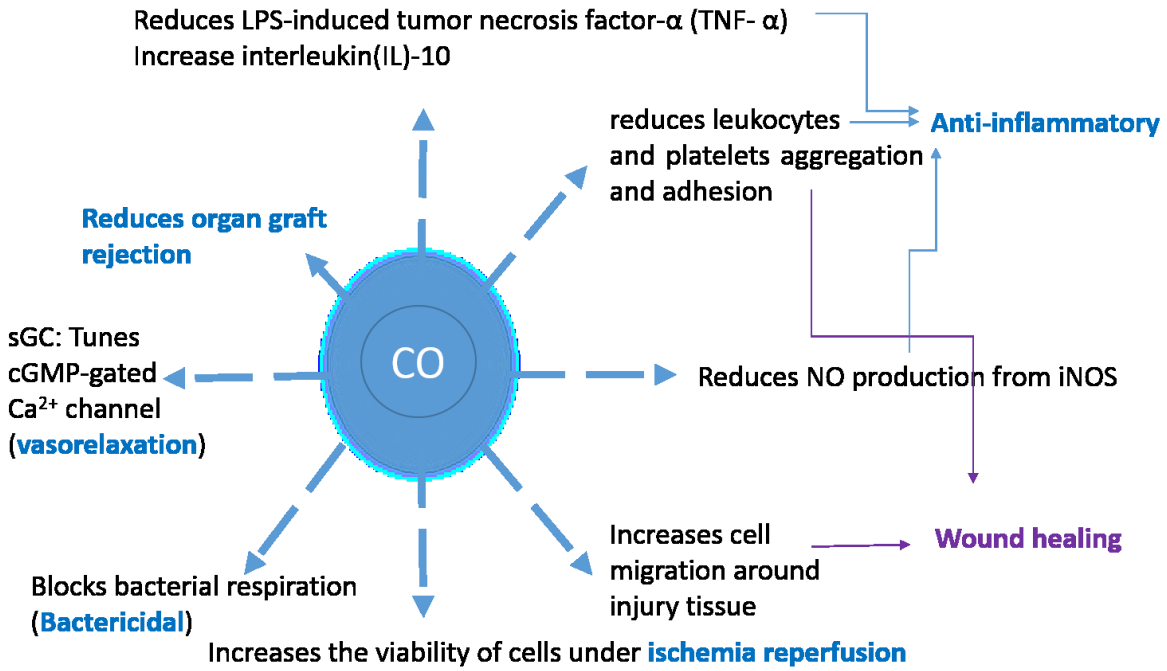

Figure 1. 2 Scheme depicting CO beneficial effects.

Based on current physiological studies, at low concentration CO has proved to have anti-inflammation activity. This property has been observed in several animal models. For example, this effect can be seen in a mouse model with cerebral malaria which causes inflammation in the brain and leads to morbidity and mortality (close to human parasite infection). Three days after infection, CO was administered and all individuals survived the disease while none of the blank models did[6]. CO exposure attenuates the endotoxic shock by selectively inhibiting the production of lipopolysaccharide (LPS) induced tumor necrosis factor-α (TNF- α) and increasing the production of interleukin (IL)-10 (an anti-inflammatory cytokine). This anti-inflammatory effect does not appear to involve the guanylate cyclase/cyclic GMP pathway but appears to involve the MKK3/p38 mitogen-activated protein (MAP) kinase signaling pathway (without direct evidence)[7]. For allergen-induced inflammation, CO was also found to block eosinophil influx and to decrease the production

of IL-5 (an allergen induced cytokine)[8]. CO also binds to soluble guanylyl cyclase (sGC) to activate the pathway, although it has a lower binding affinity with sGC compared to NO. In models with carrageenan-induced inflammation, the use of CO largely reduced leukocyte adhesion and neutrophil migration into the inflammatory site with a mechanism based on sGC activation[9]. CO also can bind with inducible NO synthase (iNOS) to reduce the production of NO to reduce inflammatory shock.

Antibiotic resistance is becoming a big threat to people worldwide. According to CDC reports, there are more than two million Americans suffering from antibiotic-resistant bacteria every year and at least 23,000 people die in US from those infections. Microbes gradually build up random genetic mutations which appear spontaneously. Drug resistant microbes are increasingly difficult to kill, requiring either new drugs or higher doses, both of which are more expensive or more toxic. However, bacteria do not seem to be able to mutate to go around metal containing proteins thus making CO a potential solution for antibiotic resistance. As a toxin, CO inhibits microbes' respiration process by binding cytochromes or cytochrome c oxidase in the membrane of bacteria and at the same time increasing the ROS. It is reported mice that have been administered with 250 ppm of CO after infection with gram-positive or gram negative bacterial, the survival rate is improved and organ failure rate is down[10–14]. Another bactericidal effect is that CO also affects the expression of genes encoding energy transducing pathway through binding with metal-containing transcription factors[15].

Besides anti-inflammation and anti-bacteria effects, CO also has following effects: 1) It tunes cGMP-gated Ca^{2+} channel and relaxes vascular smooth muscle cells to regulates blood pressure under stress conditions[16–22]; 2) Through MAP kinase system, CO is shown to protect against septic shock and lung injury[23,24]; 3) CO is shown to improve cell migration which is

key in wound healing[25,26]; 4) CO protects cells against ischemia/reperfusion injury[27,28]; 5) Organ graft rejection is suppressed by CO. Rats exposed to 400 ppm of CO gas for 2 days following transplant survived for 50 days compared to air-treated ones living up to 5 to 7 days[20,29,30].

There is no doubt that large amount of CO inhibits ATP production from mitochondrial, but some literatures show that low concentration of CO enhances overall mitochondrial biogenesis to increases ATP production and prevents stress-induced damage. However, the mechanisms remain unclear. Recently there is an interesting (but counter-intuitive) study from Leo E. Otterbein *et al*[31] claiming that macrophage-generated CO increases ATP production from bacteria respiration. The ATPs activate Nacht (nucleoside-triphosphatase), LRR (leucine-rich repeat), and PYD (pyrin) domains-containing protein 3 (NALP3) inflammasome which intensifies bacterial killing.

II. CO delivery for therapeutic applications

CO has very low solubility in water (~1.8 mM) and its partitioning to body fluids and tissues is also low. Additionally, Hb's high affinity for CO serves as a buffer against either more toxic or beneficial effects at the cellular level[3]. To reach appropriate level of CO in certain organs, high concentrations of CO were used. In the first randomized Phase I trial, CO was inhaled by healthy humans with a dose of 3.0 mg per kg per hour (single one dose or daily for ten days). The CO delivery device is a commercial product Covox DS. COHb levels in the blood reached to 12% without any adverse effects. However, there were several problems with the inhalation methods: 1) The percentage of CO applied to the desired target tissues or organs is unknown. 2) When CO is administered, it targets various molecules which complicates the process. 3) It is not applicable to carry out gaseous pharmaceutical delivery. Those issues have been addressed by using CO releasing moieties (CORMs) to deliver CO precisely to target organs or tissues.

A. CO releasing moieties (CORMs)

To address the problems of using gaseous CO as pharmaceutical, researchers have put growing efforts to develop solid forms of carbon monoxide storage, carbon monoxide releasing moieties, dubbed "CORMs"[3]. In those CORMs, CO are designed to be released to certain physiological targets by specific triggers including heat, light or enzyme[32–38]. Most of CORMs are metal carbonyl complexes which include a variety of transition metals such as Mo, W, V, Cr, Mn, Fe, Ru, Co, Ir, Re and different ligands as diimine, α,α-dialkylaldehydes, oxalates, boroncarboxylates, and silacarboxylates. Those early time CORMs reacted thermally to release CO under physiological conditions (compound **1**, **2** and **3**).

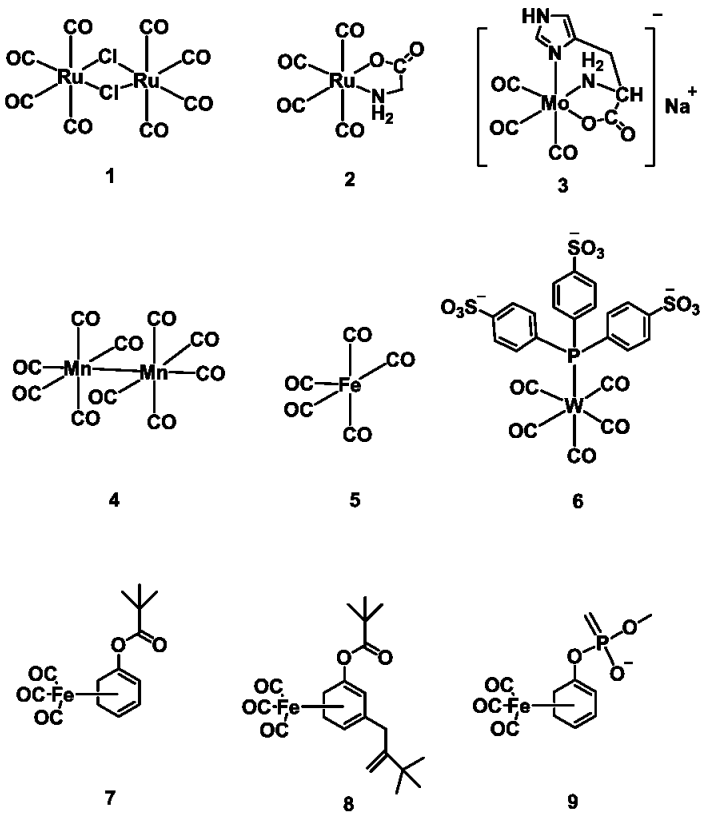

Figure 1. 3 Some early examples of CORMs.

For those thermal-activated CORMs, their kinetics of CO releasing process determine the potential for therapeutic applications. The half-life under physiological conditions should be long enough to allow them to reach biological sites. For example, compound **1** (CORM-2) and compound **2** (CORM-3) each have a half-life of ~1 min [19,39]. Compound **3** (ALF186) has a higher thermal activation energy and a half-life of ~24 mins under aerobic conditions and ~97 min under anaerobic conditions[40]. There is another group of CORMs which are stable in serum but can be triggered in the targeted tissue by a very specific stimulus, esterase (compound **7**, **8** and **9**)[37,41]. After reacted with esterase, iron slides from η^4 coordination to η^2 coordination to release free iron and three carbon monoxide. Lack of temporal and special control is a limiting factor with internal triggers like thermal activation and enzyme.

B. Photo-activated CO releasing moieties (PhotoCORMs)

The photo-activated carbon monoxide releasing moieties, dubbed photoCORMs (Fig. 1.3, compound **4**, **5**, **6**) [19,42], have the advantage of allowing one to define the location and timing of the CO release. What is more, since the extent of photochemical reaction is linearly depending on the amount of light been absorbed, it allows one also to control the dosage of CO release at the target.

1. Metal carbonyls and their photochemistry

PhotoCORMs are also mostly transition metal carbonyls and there are only few organic compounds as photoCORMs. As shown in figure 1.4, there is one example of organic based photoCORM[43]. The photoCORM, 6-hydroxy-3-oxo-3H-xanthene-9-carboxylic acid, releases CO in both water and methanol upon irradiation at with 500 nm light.

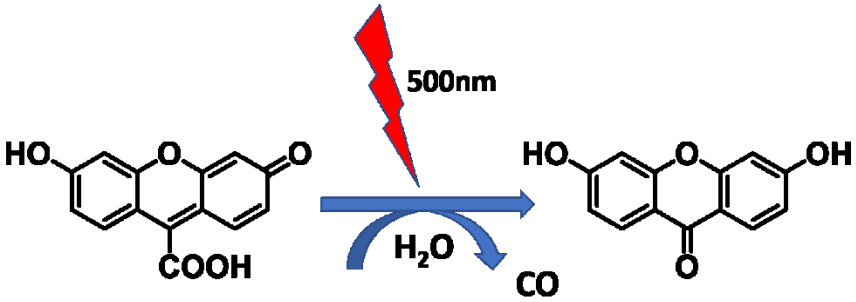

Figure 1. 4 A transition-metal-free visible light photoCORM.

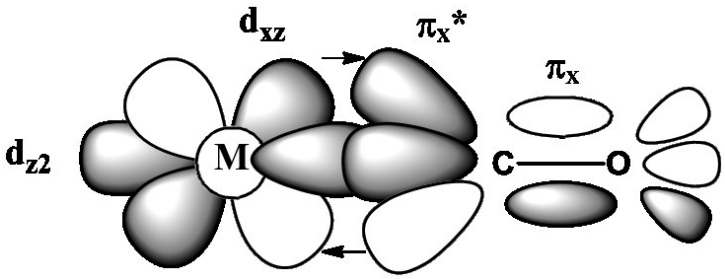

Figure 1.5. Bonding interactions of CO with transition metals

In metal carbonyl complexes, the transition metal to CO bond is usually linear. As shown in Fig. 1.5, if one takes z direction along the M-C-O bond, then the d_{z2}, d_{xz}, and d_{yz} orbitals have the proper symmetry to interact respectively with carbon sp-hybridized electron pair, the π_x^*, and π_y^*. Since carbon monoxide donates electron density from lone pair to the metal d_{z2} orbital in a σ fashion and accepts electron density from d_{xz} and d_{yz} orbitals to π* orbitals in a π fashion, CO is a strong field ligand.

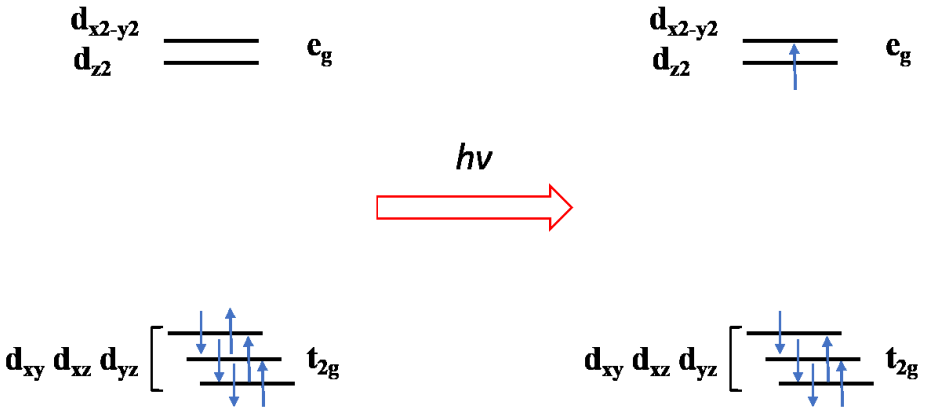

Figure 1.6. The representative electronic diagram of a d^6 low-spin metal carbonyl complex in the ground state and after LF excitation with light.

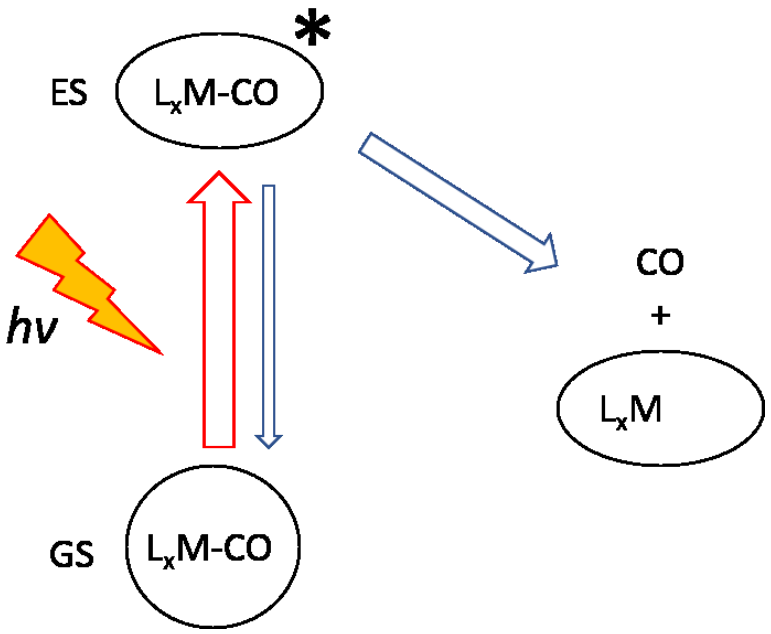

Figure 1.7. Scheme showing excitation of a photoCORM

Given the bonding fashion of M-CO, excitation of photoCORMs upon ligand field (LF) or so-called d orbital-d orbital transition will depopulate d_{yz}, d_{xz} or d_{xy} (t_{2g} orbitals in an octahedral compound) while populating d_{z2} or d_{x2-y2} (e_g orbitals in an octahedral compound) (see Figure 1.6). In metal carbonyls, depopulating the π bonding orbitals (t_{2g}) and populating σ antibonding (e_g) coherently lead to a bond weakening between the metal and CO. This excitation can either lead to relaxation back to the ground state or CO labilization and release (see Fig. 1.7).

Although photoreactivity of a compound has been defined in differently in the literatures, the most quantitative way is to calculate the quantum yields of the photochemical reactions. For photoCORMs, two quantum yields are mostly considered: complex depletion quantum yield ($\Phi_{complex}$) and CO releasing quantum yield (Φ_{CO}), which are defined as moles of complex reacted and moles of CO released versus Einsteins (one mole of photons) of photons absorbed respectively. For a photoCORM, its quantum yield can be dependent on factors including

excitation wavelength, temperature, pressure, solvent, concentration. In quantum yield measurements, one can use the power meter or actinometry to measure the light source power (P) incident on the solution at certain irradiation wavelength λ_{irr}. Photons absorbed (N_{abs}) were calculated from I_0 (incident photon flux in Einstein/s) and the solution absorbance (A) at λ_{irr} according to eqs. 1 and 2 (P = power in J s^{-1}, E = photon energy in J/Einstein at λ_{irr}, t = photolysis time in s).

$$I_0 = P/E \tag{1}$$

$$N_{abs} = (1 - 10^{-A})\, I_0 \times t \tag{2}$$

$$N_{reacted} = \frac{A_0 - A_t}{A_0 - A_{final}} \times C_0 \times V \tag{3}$$

$$\Phi_{complex} = N_{reacted} / N_{abs} \tag{4}$$

In eq. 3, the moles of molecules reacted ($N_{reacted}$) can be calculated from A_0 (initial absorbance at observed wavelength), A_t (absorbance at observed wavelength after irradiation time t), A_{final} (final absorbance at observed wavelength after exhaustive photolysis), C_0 (initial solution concentration in M) and V (solution volume in L). The quantum yield Φ can thus be determined from eq. 4. In practice, $\Phi_{complex}$ values were not determined from single data point but from the slopes of $N_{reacted}$ vs N_{abs} plots. All quantum yield measurements should be corrected for any dark reactions. For Φ_{CO}, the number of CO molecules need to be measured with various techniques which will be discussed later. From a therapeutic perspective, the *rate* of CO production would be more important than Φ_{CO}. For a unimolecular photoreaction under single photon excitation, the rate of CO production would be defined as the product of the photon flux of the excitation light absorbed (I_{abs}) times the quantum yield, that is, the *rate* =

$I_{abs} \times \Phi_{CO}$. The value of I_{abs} is a function of the extinction coefficient (ε) and of the incident photon flux of the light (I_0) at the point of its interaction with the photoCORM.

Based on the above, photoCORMs with high quantum yields and high extinction coefficient are certainly desirable since they should have a fast response to incident light. There are also some other properties that metal carbonyls might have to be good photoCORMs for therapeutic applications. One of the properties is solubility in aqueous solution or at least dimethylsulfoxide (DMSO)/ water solution (maximum 10% DMSO). In Figure 1.3, as early examples, compound **4** and **5** are insoluble in water or aqueous medium owing to their non-polar property. Compound **6**, an air-stable tungsten (0) carbonyl complex with trianionic tris(sulphonatophenyl)phosphine ligand synthesized by Ford lab is an example of water-soluble photoCORM[42].

The second desirable property is stability in aerated aqueous solution at physiological temperatures (~37°C) and other conditions typical to living organisms. Although spontaneous thermally activated decay at known rates is the expectation for CORMs, a photoCORM should release CO only when triggered by light[44].

Another key property would be photoreactivity at wavelengths where the transmission of light in tissue is optimal. According to the absorption spectra of major intracellular absorbers, penetration depth of light into tissue and blood is strongly wavelength dependent. Penetration is smallest for ultraviolet light, improved for visible light and reaching its maximum value in the near infrared (NIR) region (wavelength range ~700-1100 nm)[45]. Since CO is a strong field ligand, the d-d transitions that labilize CO normally need high energy, short wavelength excitation. To date most photoCORMs only release CO upon Uv light irradiation (Fig. 1.8): Cationic compound **10**, synthesized by Ford's lab, shows very good water-solubility, decent

luminescence quantum yield and photochemical quantum yield but is only labilized by 365 nm light[46]. Another example is compound **11** which was synthesized and characterized by Schatzschneider and co-workers. This compound is also cationic and shows good water-solubility and anticancer activity[47]. Mascharak group synthesized a Uv light activated photoCORM, compound **12,** a very similar derivative to compound **10**[48]. Researchers have been looking for an alternate way to weaken the metal-carbonyl bond, thereby to promote CO release. ligands with low lying molecular orbitals are introduced to metals, and it is possible that CO uncaging now comes from metal-to-ligand charge transfer (MLCT) where electrons are transferred from metal *d*-orbitals to ligand centered π anti-bonding orbitals. In 2011, Westerhausen and co-workers reported a dicarbonylbis(cysteamine)iron (II) complex (**13**, Figure 1.8) which can be activated by visible light (470 nm irradiation)[49]. Mascharak group reported another visible light activated Mn(I) cationic carbonyl with tripodal ligand (2-pyridylmethyl)(2-quinolylmethyl)amine (compound **14**, Figure 1.8). Another Mn(I) neutral complex (compound **15**, Figure 1.8) was reported by Bengali and co-workers. Compound **15** was proposed to rapidly release CO under 582 nm and 560 nm light irradiation by a typical substitution with solvent molecules[51]. The key of having low energy MLCT is to design an electron-withdrawing bidentate/tridentate conjugated ligand with a low lying LUMO. Recently, Zobi and co-workers realized the CO releasing activated by red light and NIR light[52]. They reported a group of Mn(I) complexes with substituted 2,2'-azopyridine ligands. Interestingly, both electron-donating groups and electron-withdrawing groups have been introduced to azopyridine. Certainly, the most red-shifted MLCT bands are shown in the $-CF_3$ substituted one (compound **16**, Fig. 1.8) which was shown to release CO when triggered with red light (>625 nm). Unfortunately, it is unstable and is totally decomposed in 200 mins in

dark in dichloromethane solution. In 2016, Petr Klan *at el.* reported the synthesis and properties of a group of unique transition-metal-free photoCORMs based on BODIPY chromophores activatable by visible-to-NIR (up to 730 nm) light (compound **17**, Fig. 1.8)[53]. However, the photochemical quantum yield of compound **17** is only around 1.4×10^{-5}.

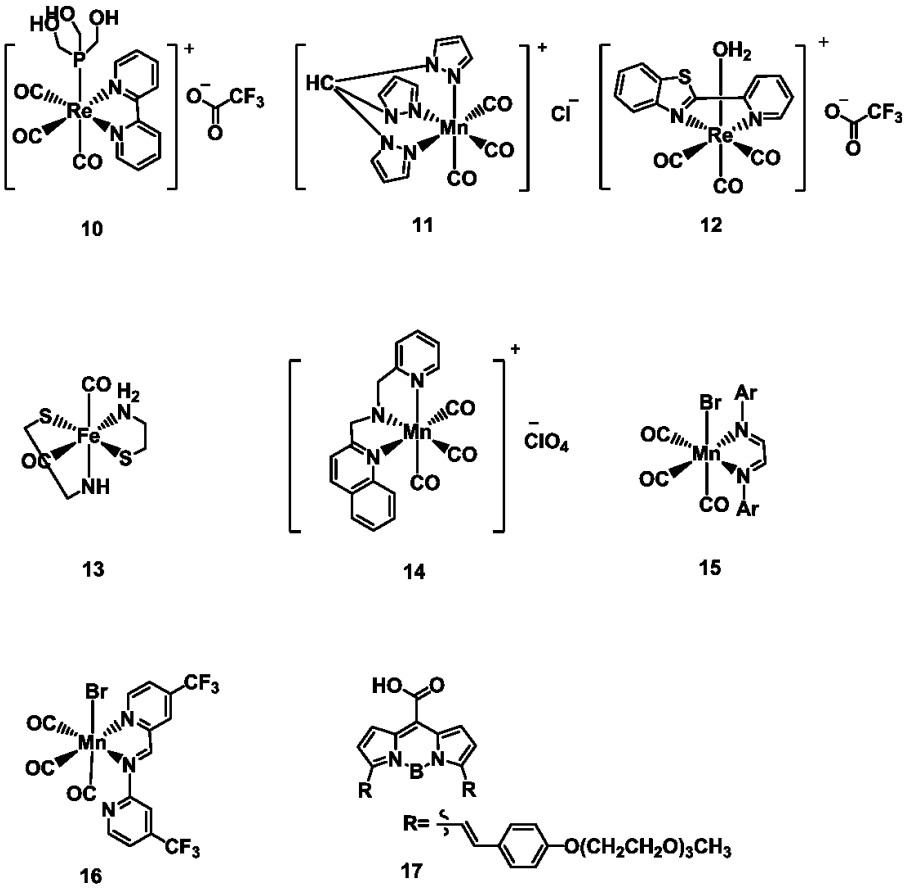

Figure 1. 8 PhotoCORMs examples.

Besides using MLCT or other molecular design approaches, there is another way to improve the responsivity of photoCORM to longer wavelengths. It is to attach a photoCORM to an antenna with a high NIR two photon excitation (TPE) cross-section. Excitation with a NIR laser could then generate states that can access high energy precursor states. Recently,

Ford's lab described carriers incorporating upconverting nanoparticles (UCNPs) that used multi-photon excitation with NIR light to trigger CO release from a Mn(I) carbonyl[54].

2. Therapeutic applications of PhotoCORMs

Water solubility and targeting must be considered in developing a photoCORM for therapeutic application. In photoCORM design, efforts have been put into introducing water soluble functional groups to metal carbonyls. It is also an option to synthesize metal complex that have ionic charges to improve aqueous solution solubility. One alternative strategy is to incorporate biocompatible materials in applications. Schiller and co-workers, embedded a tetranuclear Mn complex into a polylactide and polymethacrylate non-woven fabrics and used remote-controlled optical device to activate CO release from the photoCORM[55]. They put the water insoluble photoCORM $Mn_2(CO)_{10}$ (**4**, Figure 1.3) into a polylactide matrix and showed that the material has antimicrobial activity against *Staphylococcus aureus* using 405 nm irradiation[56]. Ford and co-workers incorporated a triflate salt of Mn(I) into an amphiphilic phospholipid-functionalized poly(enthylene glycol) together with UCNP and achieved both NIR light photochemical reactivity and water solubility[54]. In 2008, Schatzschneider *at el.* successfully conjugated Mn(I) to functionalized amino acids and model peptides using cross-coupling and click reaction for targeting and accumulating on specific site[57]. Mascharak and co-workers synthesized photoCORMs with adamantylamine ligand and some adamantylamine derivatives are already used in pharmaceutical market for the treatment of ovarian carcinoma or colon cancer[58]. In developing new photoCORMs for therapeutic application, short and long term toxicity of the complex and inactivated CORMs (iCORM) must be considered.

C. CO detection

Quantification of CO released is necessary when new photoCORMs are developed. An electrochemical gas analyzer has been used to monitor exhaled CO from asthmatic and diabetic patients. Recently a portable CO detector, Drager pac 7000 has been used in CO quantification by Schiller. But by far the most commonly used analytical method is doxymyoglobin (Mb) test. In this test, CO released is absorbed by Mb which absorption then changes at Soret band and Q-band. The Mb assay is relative accurate but has several drawbacks, one of which is a limitation to anaerobic conditions[59,60]. Another method uses FTIR spectrum (R and P branched centered at 2142 cm^{-1}) of CO to quantify the CO in the gas phase above the photolysis solution. The drawback of this method is that pressure must be constant since the intensity of the band is also dependent on gas pressure[61].

Another analytical method uses a programmable (temperature, pressure, flow) gas chromatograph equipped with either a carbon sieve packed column or a porous layer open tubular (PLOT) column and a thermal conductivity detector (TCD). A gas-tight syringe is used to remove a head space sample from a gas tight Schlenk cuvette containing the photolysis solution. Quantifications of CO and other gases (CO_2, N_2, CH_4, H_2) are achieved by comparing peak integration to calibration curves determined for each gas[42,46,54].

III. Summary

Recently discoveries of CO therapeutic effects in cell study and animal models has led CO into clinical trials, such as: gaseous CO treatment on pulmonary diseases. In order to better utilize CO in therapeutic applications, it is desirable to develop new CORMs and photoCORMs and to better understand CO's biological mechanisms. Such studies are important and should progress side by side and need close collaboration between chemists and biologists. In developing photoCORMs, there are two major strategies: 1) chemical modifications and tuning of ligands for water solubility, targeting, photo-reactivity; 2) using materials (nano/microparticle, non-woven fiber, etc.) to either improve water solubility, electronic absorption or encapsulation of potential toxic iCORMs.

CO-related physiology is still not fully understood and the available photoCORMs described in this chapter have not been optimized for clinical trials. More comprehensive studies regarding the mechanism of CORMs and photoCORMs in *vitro* and in *vivo* experiments are needed.

Reference

1. Molecules of Death http://www.worldscientific.com/worldscibooks/10.1142/p509 (accessed Jul 11, 2017).

2. Weinstock, B.; Niki, H. Carbon Monoxide Balance in Nature. Science **1972**, 176, 290–292.

3. Motterlini, R.; Otterbein, L. E. The Therapeutic Potential of Carbon Monoxide. *Nat Rev Drug Discov* **2010**, 9, 728–743.

4. Ignarro, L. J.; Cirino, G.; Casini, A.; Napoli, C. Nitric Oxide as a Signaling Molecule in the Vascular System: An Overview. *Journal of Cardiovascular Pharmacology* **1999**, 34, 879–886.

5. Moncada, S. Nitric Oxide: Discovery and Impact on Clinical Medicine. J R Soc Med 1999, 92, 164–169.

6. Pamplona, A.; Ferreira, A.; Balla, J.; Jeney, V.; Balla, G.; Epiphanio, S.; Chora, Â.; Rodrigues, C. D.; Gregoire, I. P.; Cunha-Rodrigues, M.; Portugal, S.; Soares, M. P.; Mota, M. M. Heme Oxygenase-1 and Carbon Monoxide Suppress the Pathogenesis of Experimental Cerebral Malaria. *Nat Med* **2007**, 13, 703–710.

7. Foey, A. D.; Parry, S. L.; Williams, L. M.; Feldmann, M.; Foxwell, B. M. J.; Brennan, F. M. Regulation of Monocyte IL-10 Synthesis by Endogenous IL-1 and TNF-α: Role of the p38 and p42/44 Mitogen-Activated Protein Kinases. *The Journal of Immunology* **1998**, 160, 920–928.

8. Chapman, J. T.; Otterbein, L. E.; Elias, J. A.; Choi, A. M. K. Carbon Monoxide Attenuates Aeroallergen-Induced Inflammation in Mice. *American Journal of Physiology - Lung Cellular and Molecular Physiology* **2001**, 281, L209–L216.

9. Freitas, A.; Alves-Filho, J. C.; Secco, D. D.; Neto, A. F.; Ferreira, S. H.; Barja-Fidalgo, C.; Cunha, F. Q. Heme Oxygenase/carbon Monoxide-Biliverdin Pathway down Regulates Neutrophil Rolling, Adhesion and Migration in Acute Inflammation. *British Journal of Pharmacology* **2006**, 149, 345–354.

10. Nobre, L. S.; Seixas, J. D.; Romão, C. C.; Saraiva, L. M. Antimicrobial Action of Carbon Monoxide-Releasing Compounds. *Antimicrob Agents Chemother* **2007**, 51, 4303–4307.

11. Tavares, A. F. N.; Teixeira, M.; Romão, C. C.; Seixas, J. D.; Nobre, L. S.; Saraiva, L. M. Reactive Oxygen Species Mediate Bactericidal Killing Elicited by Carbon Monoxide-Releasing Molecules. *J. Biol. Chem*. 2011, 286, 26708–26717.

12. Tinajero-Trejo, M.; Rana, N.; Nagel, C.; Jesse, H. E.; Smith, T. W.; Wareham, L. K.; Hippler, M.; Schatzschneider, U.; Poole, R. K. Antimicrobial Activity of the Manganese Photoactivated Carbon Monoxide-Releasing Molecule [Mn(CO)3(tpa-κ3N)]+ Against a Pathogenic Escherichia Coli That Causes Urinary Infections. *Antioxid Redox Signal* **2016**, 24, 765–780.

13. Klinger-Strobel, M.; Gläser, S.; Makarewicz, O.; Wyrwa, R.; Weisser, J.; Pletz, M. W.; Schiller, A. Bactericidal Effect of a Photoresponsive Carbon Monoxide Releasing Non-Woven against Staphylococcus Aureus Biofilms. *Antimicrob. Agents Chemother*. **2016**, AAC.00703-16.

14. Wegiel, B.; Gallo, D. J.; Raman, K. G.; Karlsson, J. M.; Ozanich, B.; Chin, B. Y.; Tzeng, E.; Ahmad, S.; Ahmed, A.; Baty, C. J.; Otterbein, L. E. Nitric Oxide–Dependent Bone Marrow Progenitor Mobilization by Carbon Monoxide Enhances Endothelial Repair After Vascular Injury. *Circulation* **2010**, 121, 537–548.

15. Wareham, L. K.; Begg, R.; Jesse, H. E.; van Beilen, J. W. A.; Ali, S.; Svistunenko, D.; McLean, S.; Hellingwerf, K. J.; Sanguinetti, G.; Poole, R. K. Carbon Monoxide Gas Is Not Inert, but Global, in Its Consequences for Bacterial Gene Expression, Iron Acquisition, and Antibiotic Resistance. *Antioxid Redox Signal* **2016**, 24, 1013–1028.

16. Foresti, R.; Hammad, J.; Clark, J. E.; Johnson, T. R.; Mann, B. E.; Friebe, A.; Green, C. J.; Motterlini, R. Vasoactive Properties of CORM-3, a Novel Water-Soluble Carbon Monoxide-Releasing Molecule. *British Journal of Pharmacology* **2004**, 142, 453–460.

17. Hou, S.; Xu, R.; Heinemann, S. H.; Hoshi, T. The RCK1 High-Affinity Ca2+ Sensor Confers Carbon Monoxide Sensitivity to Slo1 BK Channels. *PNAS* **2008**, 105, 4039–4043.

18. Marazioti, A.; Bucci, M.; Coletta, C.; Vellecco, V.; Baskaran, P.; Szabó, C.; Cirino, G.; Marques, A. R.; Guerreiro, B.; Gonçalves, A. M. L.; Seixas, J. D.; Beuve, A.; Romão, C. C.; Papapetropoulos, A. Inhibition of Nitric Oxide–Stimulated Vasorelaxation by Carbon Monoxide-Releasing Molecules. *Arterioscler Thromb Vasc Biol* **2011**, 31, 2570–2576.

19. Motterlini, R.; Clark, J. E.; Foresti, R.; Sarathchandra, P.; Mann, B. E.; Green, C. J. Carbon Monoxide-Releasing Molecules Characterization of Biochemical and Vascular Activities. *Circulation Research* **2002**, 90, e17–e24.

20. Otterbein, L. E.; Zuckerbraun, B. S.; Haga, M.; Liu, F.; Song, R.; Usheva, A.; Stachulak, C.; Bodyak, N.; Smith, R. N.; Csizmadia, E.; Tyagi, S.; Akamatsu, Y.; Flavell, R. J.; Billiar, T. R.; Tzeng, E.; Bach, F. H.; Choi, A. M. K.; Soares, M. P. Carbon Monoxide Suppresses Arteriosclerotic Lesions Associated with Chronic Graft Rejection and with Balloon Injury. *Nat Med* **2003**, 9, 183–190.

21. Stec, D. E.; Drummond, H. A.; Vera, T. Role of Carbon Monoxide in Blood Pressure Regulation. Hypertension **2008**, 51, 597–604.

22. Wilkinson, W. J.; Kemp, P. J. Carbon Monoxide: An Emerging Regulator of Ion Channels. *The Journal of Physiology* **2011**, 589, 3055–3062.

23. Clerch, L. B.; Massaro, D. Tolerance of Rats to Hyperoxia. Lung Antioxidant Enzyme Gene Expression. *J Clin Invest* **1993**, 91, 499–508.

24. Otterbein, L. E.; Kolls, J. K.; Mantell, L. L.; Cook, J. L.; Alam, J.; Choi, A. M. K. Exogenous Administration of Heme Oxygenase-1 by Gene Transfer Provides Protection against Hyperoxia-Induced Lung Injury. *J Clin Invest* **1999**, 103, 1047–1054.

25. Ahanger, A. A.; Prawez, S.; Kumar, D.; Prasad, R.; Amarpal; Tandan, S. K.; Kumar, D. Wound Healing Activity of Carbon Monoxide Liberated from CO-Releasing Molecule (CO-RM). *Naunyn-Schmiedeberg's Arch Pharmacol* **2011**, 384, 93–102.

26. Halilovic, A.; Patil, K. A.; Bellner, L.; Marrazzo, G.; Castellano, K.; Cullaro, G.; Dunn, M. W.; Schwartzman, M. L. Knockdown of Heme Oxygenase-2 Impairs Corneal Epithelial Cell Wound Healing. *J Cell Physiol* **2011**, 226, 1732–1740.

27. Zobi, F.; Blacque, O.; Jacobs, R. A.; Schaub, M. C.; Bogdanova, A. Y. 17 E−rhenium Dicarbonyl CO-Releasing Molecules on a Cobalamin Scaffold for Biological Application. *Dalton Trans*. **2011**, 41, 370–378.

28. Ryter, S. W.; Morse, D.; Choi, A. M. K. Carbon Monoxide and Bilirubin. *Am J Respir Cell Mol Biol* **2007**, 36, 175–182.

29. Sato, K.; Balla, J.; Otterbein, L.; Smith, R. N.; Brouard, S.; Lin, Y.; Csizmadia, E.; Sevigny, J.; Robson, S. C.; Vercellotti, G.; Choi, A. M.; Bach, F. H.; Soares, M. P. Carbon Monoxide Generated by Heme Oxygenase-1 Suppresses the Rejection of Mouse-to-Rat Cardiac Transplants. *The Journal of Immunology* **2001**, 166, 4185–4194.

30. Soares, M. P.; Lin, Y.; Anrather, J.; Csizmadia, E.; Takigami, K.; Sato, K.; Grey, S. T.; Colvin, R. B.; Choi, A. M.; Poss, K. D.; Bach, F. H. Expression of Heme Oxygenase-1 Can Determine Cardiac Xenograft Survival. *Nat Med* **1998**, 4, 1073–1077.

31. Wegiel, B.; Larsen, R.; Gallo, D.; Chin, B. Y.; Harris, C.; Mannam, P.; Kaczmarek, E.; Lee, P. J.; Zuckerbraun, B. S.; Flavell, R.; Soares, M. P.; Otterbein, L. E. Macrophages Sense and Kill Bacteria through Carbon Monoxide–dependent Inflammasome Activation. *J Clin Invest* **2014**, 124, 4926–4940.

32. Mann, B. E. CO-Releasing Molecules: A Personal View. *Organometallics* **2012**, 31 16, 5728–5735.

33. Schatzschneider, U. PhotoCORMs: Light-Triggered Release of Carbon Monoxide from the Coordination Sphere of Transition Metal Complexes for Biological Applications. *Inorganica Chimica Acta* **2011**, 374, 19–23.

34. Heinemann, S. H.; Hoshi, T.; Westerhausen, M.; Schiller, A. Carbon Monoxide – Physiology, Detection and Controlled Release. *Chem. Commun*. **2014**, 50, 3644–3660.

35. Romão, C. C.; Blättler, W. A.; Seixas, J. D.; Bernardes, G. J. L. Developing Drug Molecules for Therapy with Carbon Monoxide. *Chem. Soc. Rev*. 2012, 41, 3571–3583.

36. Schatzschneider, U. Novel Lead Structures and Activation Mechanisms for CO-Releasing Molecules (CORMs). *Br J Pharmacol* **2015**, 172, 1638–1650.

37. Romanski, S.; Kraus, B.; Schatzschneider, U.; Neudörfl, J.-M.; Amslinger, S.; Schmalz, H.-G. Acyloxybutadiene Iron Tricarbonyl Complexes as Enzyme-Triggered CO-Releasing Molecules (ET-CORMs). *Angew. Chem. Int. Ed*. **2011**, 50, 2392–2396.

38. Fujita, K.; Tanaka, Y.; Sho, T.; Ozeki, S.; Abe, S.; Hikage, T.; Kuchimaru, T.; Kizaka-Kondoh, S.; Ueno, T. Intracellular CO Release from Composite of Ferritin and Ruthenium Carbonyl Complexes. *J. Am. Chem. Soc*. **2014**, 136, 16902–16908.

39. Clark, J. E.; Naughton, P.; Shurey, S.; Green, C. J.; Johnson, T. R.; Mann, B. E.; Foresti, R.; Motterlini, R. Cardioprotective Actions by a Water-Soluble Carbon Monoxide–Releasing Molecule. *Circulation Research* **2003**, 93, e2–e8.

40. Bannenberg, G. L.; Vieira, H. L. Therapeutic Applications of the Gaseous Mediators Carbon Monoxide and Hydrogen Sulfide. *Expert Opinion on Therapeutic Patents* **2009**, 19, 663–682.

41. Botov, S.; Stamellou, E.; Romanski, S.; Guttentag, M.; Alberto, R.; Neudörfl, J.-M.; Yard, B.; Schmalz, H.-G. Synthesis and Performance of Acyloxy-Diene-Fe(CO)3 Complexes with Variable Chain Lengths as Enzyme-Triggered Carbon Monoxide-Releasing Molecules. *Organometallics* **2013**, 32, 3587–3594.

42. Rimmer, R. D.; Richter, H.; Ford, P. C. A Photochemical Precursor for Carbon Monoxide Release in Aerated Aqueous Media. *Inorg. Chem*. **2009**, 49 (3), 1180–1185.

43. Antony, L. A. P.; Slanina, T.; Šebej, P.; Šolomek, T.; Klán, P. Fluorescein Analogue Xanthene-9-Carboxylic Acid: A Transition-Metal-Free CO Releasing Molecule Activated by Green Light. *Org. Lett*. **2013**, 15, 4552–4555.

44. Rimmer, R. D.; Pierri, A. E.; Ford, P. C. Photochemically Activated Carbon Monoxide Release for Biological Targets. Toward Developing Air-Stable photoCORMs Labilized by Visible Light. *Coordination Chemistry Reviews* **2012**, 256, 1509–1519.

45. König, K. Multiphoton Microscopy in Life Sciences. *Journal of Microscopy* **2000**, 200, 83–104.

46. Pierri, A. E.; Pallaoro, A.; Wu, G.; Ford, P. C. A Luminescent and Biocompatible PhotoCORM. *J. Am. Chem. Soc*. **2012**, 134, 18197−18200.

47. Rudolf, P.; Kanal, F.; Knorr, J.; Nagel, C.; Niesel, J.; Brixner, T.; Schatzschneider, U.; Nuernberger, P. Ultrafast Photochemistry of a Manganese-Tricarbonyl CO-Releasing Molecule (CORM) in Aqueous Solution. *J. Phys. Chem. Lett*. **2013**, 4, 596–602.

48. Carrington, S. J.; Chakraborty, I.; Bernard, J. M. L.; Mascharak, P. K. A Theranostic Two-Tone Luminescent PhotoCORM Derived from Re(I) and (2-Pyridyl)-Benzothiazole: Trackable CO Delivery to Malignant Cells. *Inorg. Chem*. **2016**.

49. Kretschmer, R.; Gessner, G.; Görls, H.; Heinemann, S. H.; Westerhausen, M. Dicarbonyl-bis(cysteamine)iron(II): A Light Induced Carbon Monoxide Releasing Molecule Based on Iron (CORM-S1). *Journal of Inorganic Biochemistry* **2011**, 105, 6–9.

50. Gonzalez, M. A.; Yim, M. A.; Cheng, S.; Moyes, A.; Hobbs, A. J.; Mascharak, P. K. Manganese Carbonyls Bearing Tripodal Polypyridine Ligands as Photoactive Carbon Monoxide-Releasing Molecules. *Inorg. Chem*. **2012**, 51, 601–608.

51. Yempally, V.; Kyran, S. J.; Raju, R. K.; Fan, W. Y.; Brothers, E. N.; Darensbourg, D. J.; Bengali, A. A. Thermal and Photochemical Reactivity of Manganese Tricarbonyl and Tetracarbonyl Complexes with a Bulky Diazabutadiene Ligand. *Inorg. Chem*. **2014**, 53, 4081–4088.

52. Kottelat, E.; Ruggi, A.; Zobi, F. Red-Light Activated photoCORMs of Mn(I) Species Bearing Electron Deficient 2,2′-Azopyridines. *Dalton Trans*. **2016**, 45 (16), 6920–6927.

53. Palao, E.; Slanina, T.; Muchová, L.; Šolomek, T.; Vítek, L.; Klán, P. Transition-Metal-Free CO-Releasing BODIPY Derivatives Activatable by Visible to NIR Light as Promising Bioactive Molecules. *J. Am. Chem. Soc*. **2016**, 138, 126–133.

54. Pierri, A. E.; Huang, P.-J.; Garcia, J. V.; Stanfill, J. G.; Chui, M.; Wu, G.; Zheng, N.; Ford, P. C. A photoCORM Nanocarrier for CO Release Using NIR Light. *Chem. Commun*. **2014**, 51, 2072.

55. Gläser, S.; Mede, R.; Görls, H.; Seupel, S.; Bohlender, C.; Wyrwa, R.; Schirmer, S.; Dochow, S.; Reddy, G. U.; Popp, J.; Westerhausen, M.; Schiller, A. Remote-Controlled Delivery of CO via Photoactive CO-Releasing Materials on a Fiber Optical Device. *Dalton Trans*. **2016**, 45, 13222–13233.

56. Bohlender, C.; Gläser, S.; Klein, M.; Weisser, J.; Thein, S.; Neugebauer, U.; Popp, J.; Wyrwa, R.; Schiller, A. Light-Triggered CO Release from Nanoporous Non-Wovens. *J. Mater. Chem. B* **2014**, 2, 1454–1463.

57. Pfeiffer, H.; Rojas, A.; Niesel, J.; Schatzschneider, U. Sonogashira and "Click" Reactions for the N-Terminal and Side-Chain Functionalization of Peptides with $[Mn(CO)_3(tpm)]$+-Based CO Releasing Molecules (Tpm = Tris(pyrazolyl)methane). *Dalton Trans*. **2009**, 22, 4292–4298.

58. Jimenez, J.; Chakraborty, I.; Carrington, S. J.; Mascharak, P. K. Light-Triggered CO Delivery by a Water-Soluble and Biocompatible Manganese photoCORM. *Dalton Trans*. **2016**, 45, 13204–13213.

59. Berends, H.-M.; Kurz, P. Investigation of Light-Triggered Carbon Monoxide Release from Two Manganese photoCORMs by IR, UV–Vis and EPR Spectroscopy. *Inorganica Chimica Acta* **2012**, 380, 141–147.

60. Crook, S. H.; Mann, B. E.; Meijer, A. J. H. M.; Adams, H.; Sawle, P.; Scapens, D.; Motterlini, R. $[Mn(CO)_4\{S_2CNMe(CH_2CO_2H)\}]$, a New Water-Soluble CO-Releasing Molecule. *Dalton Trans*. **2011**, 40, 4230–4235.

61. Klein, M.; Neugebauer, U.; Gheisari, A.; Malassa, A.; Jazzazi, T. M. A.; Froehlich, F.; Westerhausen, M.; Schmitt, M.; Popp, J. IR Spectroscopic Methods for the Investigation of the CO Release from CORMs. *J. Phys. Chem. A* **2014**, 118, 5381–5390.

Chapter 2. Experimental

I. Materials

A. Gases

Argon, nitrogen, helium, carbon monoxide and oxygen were purchased from Praxair. Carbon monoxide and oxygen were used as received without further purification. Carbon monoxide must be stored in aluminum cylinders instead of steel to prevent the formation of $Fe(CO)_5$ in the high-pressure cylinder. To remove the trace amounts of water and oxygen, inert gases (Ar, N_2 and He) were passed through a chromium silica gel column[1]. The preparation method for the chromium silica gel column is as follows: Around 5 grams of CrO_3 was dissolved in 100 mL of water when mixed with 125 grams of silica gel. The mixture was filtered and solid was dried in oven for 24 hours to remove water. The chromium silica gel was then put into a glass tube with a stopcock and some glass fiber at each end. With continuous flowing of oxygen, the column was heated directly with a Fischer burner (500 °C). The chromium silica gel turned yellow when it was completely oxidized. Then carbon monoxide was flowed through the yellow chromium silica gel which was flame heated. After reduction, the chromium silica gel should turn blue. If the column turns black or green after cooled down, both oxidation and reduction process must be repeated. After column turns blue, Ar or N_2 was passed through the column while heated to remove residual CO. If the column turns brown after use, it can be regenerated by repeating the activation with O_2 and then CO.

B. Solvents

Non-hydrous organic solvents were purified before use according to literature procedures[2]. Most solvents were purified by distillation over desiccants (CaH_2, Na, $CaCl_2$) under an argon

atmosphere. They were collected in oven-dried flasks and stored under inert atmosphere. Desiccants and storage conditions for different solvent are shown in table 2.1. Non-hydrous solvents were used as soon as received.

Table 2.1 Desiccants and storage conditions for non-hydrous solvents

Solvent	Desiccant and procedure	Storage condition
Methylene Chloride	$CaCl_2$ first and then distilled	Dark, Ar
Chloroform	$CaCl_2$ first and then distilled	Dark, Ar
Methanol	CaH_2 distilled	Ar, molecular sieves
Acetonitrile	CaH_2 distilled	Ar, molecular sieves
Tetrahydrofuran	Sodium/benzophenone	Dark, Ar
Diethylether	Sodium/benzophenone	Dark, Ar

Nanopure water was obtained a Millipore water purification system at 18 MΩ. Phosphate buffered solutions were prepared using nanopure water and their pH was adjusted using an Edge pH meter from Hanna Instruments. To make 0.01M phosphate buffer (pH 7.4, ionic strength = 0.154 M), 0.0019 mole of NaH_2PO_4, 0.008 mole of K_2HPO_4 and 7.482 g NaCl were dissolved in 1000 mL nanopure water. The pH was adjusted to 7.4 by using H_3PO_4 and NaOH.

C. Reagents

All reagents were purchased in the highest available purity. Most reagents were used as received unless otherwise noted. Manganese pentacarbonyl bromide (98%), dirhenium decacarbonyl (98%), and anhydrous 1,10-phenanthroline (phen) were purchased from Strem Chemicals and used without further purification. Since homolytic metal carbonyls have strong ligand field nature, they are mostly white solids. Any colors in the solids was caused

contamination or decomposition, impurities were removed by sublimation under heat and Schlenk line vacuum. Chromatographic sorbents: neutral alumina and silica gel were used directly. Reagent for UCNP: Sodium tetraphenylborate, sodium trifluoroacetate, sodium oleate, ammonium fluoride, lanthanide chlorides (99.9+%), oleic acid (OA) (90%) and 1-octadecene (ODE) (90%) were purchased from Sigma-Aldrich Chemicals. The ligands 2,2'-bipyridine (bpy, 99%) and 2,2'-biquinoline (biq, 98%) were also purchased from Sigma-Aldrich Chemicals. The amine terminated poly(ethylene glycol) PG1-AM-2k was purchased from NANOCS (average mol. wt = 3135 Da). Poly(vinyl) alcohol with various molecular weights was also purchased from Sigma-Aldrich.

Sodium amalgam was prepared using metallic mercury and sodium metal. Three percent of sodium in mercury (by mass) are ideal. If sodium is more than 3%, the amalgam will solidify. Amalgam containing less than 3% of sodium will still be liquid which makes it easier to work with (Stir bars can move inside the reaction flasks). To avoid any contamination, sodium metal under inert atmosphere (glove box) was used instead sodium stored in oil. Mercury was weighed in a capped vial to avoid evaporation or contamination. The amalgam was made as follows. In the glovebox, 407 mg of dry and cleaned sodium was cut into small pieces and transferred to a dry flask under Ar flow. In the flask, 13.15 g of mercury was poured onto sodium and a Teflon-coated magnetic stir bar was stirring at the same time. After mixing for several seconds, two metals reacted violently and exothermically. A series of sparks was generated with mercury sputtering and black smoke. Na(Hg) amalgam is usually stable for two weeks under argon. But in all the synthesis here, it is used fresh.

II. Equipment and instrumentations

A. Schlenk glassware

All Schlenk glassware used for oxygen-sensitive operation was either custom made at UCSB, or purchased from Ace Glass (Fig.2.1). Schlenk cuvettes made up of a four-sided quartz cuvette with 1 cm path length, fused to a glass bulb and septum-sealed sampling port. These cuvettes have grease-less Teflon stopcocks and grease-less O-ring unions for the Schlenk line (Fig. 2.2). A J-Young tube was custom made in the department for air-free NMR experiments by fusing a normal NMR Tube to an adapter with a female joint which can be stopped by a J-Young valve (Fig. 2.3).

Figure 2.1 Photograph of a Schlenk flask with a sampling port.

Figure 2.2 Photograph of a Schlenk tube with a sampling port.

Figure 2.3 Photograph of a custom J-Young tube.

B. Schlenk line

The Schlenk line was custom made with grease-less Teflon stopcocks and the fittings on the line are grease-less O-ring unions. An Edwards oil pump was connected to the Schlenk line and used for all air-sensitive experiments. The Schlenk line was also equipped with a mercury manometer which can measure pressures between 850 and 50 mm Hg. The chromium silica gel column was placed between the Schlenk line and the Ar supply to remove trace amounts of water and oxygen from the gas tank.

C. Glovebox

For storage of air-sensitive reagents, dry solvents and air-free experiment not suitable on Schlenk line, a Nexus inert atmosphere glovebox from VAC Atmospheric was used. Although oxygen and water detectors are not equipped, diethylzinc was used periodically to check the presence of oxygen. When oxygen level is too high, glovebox catalyst was regenerated. Regeneration was performed using 10% hydrogen in argon.

D. Uv-vis absorbance spectroscopy

Electronic absorption spectra were recorded in 1.0 cm pathlength quartz cells using Shimadzu dual beam UV-2401 PC and StellarNet SL5-DH spectrophotometers. Extinction coefficients were determined by electronic absorption spectra of solution with various concentrations of a compound.

E. Infrared spectroscopy

Infrared spectra of solutions were measured in cells with CaF_2 windows using a Mattson Research Series FTIR spectrometer. Solid state IR spectra were obtained using a Perkin Elmer Spectrum Two UATR FT-IR Spectrometer. The diamond ATR requires only a minimal amount of sample in solid or liquid state and therefore KBr pellets were not used.

F. Fluorimeter

Emission spectra were obtained using a Photon Technology International fluorimeter with an 814 PMT detection system at 1 nm resolution. This system is equipped a Uv-vis-NIR tunable excitation source and NIR emission can also be detected.

G. Nuclear magnetic resonance

Solution NMR spectra were recorded using a Varian Unity Inova 500 MHz and Bruker 400 MHz spectrometers. Deuterated solvents were stored in dark with molecular sieves. NMR peaks were referenced to the solvent peaks or additives in their respective solutions.

H. Mass spectrometry

Exact molecular masses were measured using a Waters (Milford, Mass.) GCT Premier Time-of-flight mass spectrometer with field desorption (FD) ion sources. Samples were diluted to nano- to micro-molar rang in HPLC grade acetonitrile or dichloromethane.

I. Gas chromatography

Gases (CO and CO_2) were quantified using an Agilent 6890 gas chromatograph with a thermal conductivity detector (GC-TCD). The chromatographic separation was performed on a Carboxen-1006 PLOT Capillary GC Column (30 m × 0.32 mm, average thickness 15 μm) purchased from Sigma-Aldrich. Method parameters are shown below:

Inlet mode	Splitless
Inlet temperature	225 °C
Column mode	Constant pressure
Column helium flow	1 mL/min
Column pressure	0.05 bar
Oven temperature ramp	Oven ramp / Next temp / Hold time Initial / 35 °C / 20 mins 40 °C/min / 200 °C / 10 mins 10 °C/min / 250 °C / 35 mins
Detector type	Thermal conductivity
Detector temperature	230 °C
Detector reference Flow	12 mL/min
Detector make up flow	7 mL/min

Injection volumes of 50 μL using a gas-tight syringe. A sample chromatogram is shown in the retention times of air (13.5 min), carbon monoxide (15.0 min) and carbon dioxide (28.1 min) can be seen in Fig. 2.4.

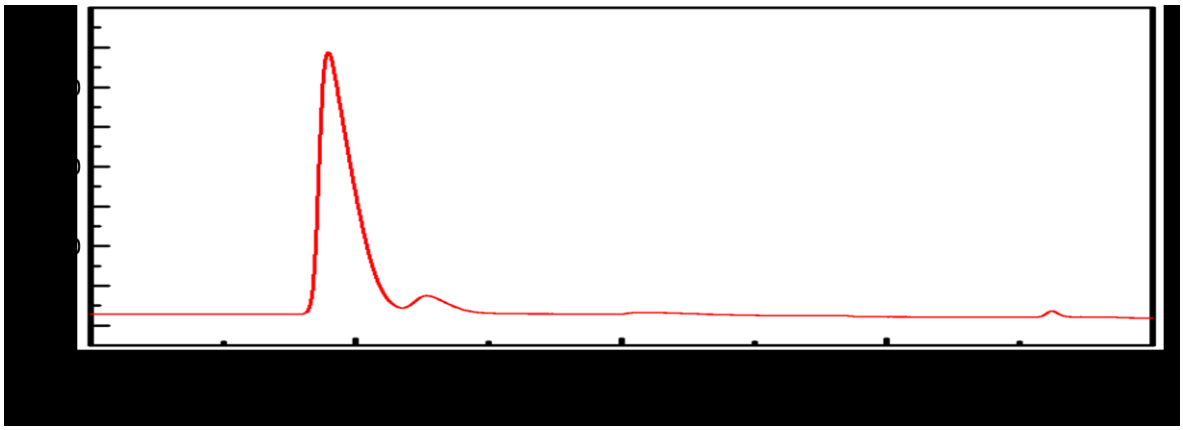

Figure 2.4 Sample chromatogram of a 50 μL injection of a sample containing air, carbon monoxide and carbon dioxide. The retention times of the components are air (13.5 min), carbon monoxide (15.0 min) and carbon dioxide (28.1 min)

J. Continuous photolysis

Continuous photolysis experiments were done by using optical trains to maintain repeatability. For photolysis in the UV range, the light source was Oriel 200 W mercury arc lamp in an Oriel lamp housing (model 66033) with Oriel light intensity controller (model 68910). The beam was aligned in the center of the optics and first passed through a long cell water filter to block infrared light. After the water filter, the beam passed through a glass neutral density filter to reduce its intensity before going through an interference filter with wavelength selections as 365 or 436 nm (mercury emission lines). The light beam then was

collected through a series of parabolic lenses, to focus to a spot with appropriate diameter (about 5 mm), and then it passed through a Uniblitz shutter which controlled the irradiation time. The sample solutions were present in a 1 cm pathlength quartz cuvette at the focused spot.

For visible light irradiation, a series of custom made LED light sources were used. They were made from mounting Luxeon Rebel diodes onto heat sinks. Like the mercury lamp train, LED light sources were mounted on an optical train (different from the mercury lamp) and the LED emission was collected and focused by a set of parabolic mirrors. The sample solutions were placed in a quartz with 1 cm pathlength at the focused spot. The emission spectra of LED light sources were characterized using StellarNet SL5-DH spectrophotometers. Their spectra are shown in Figure 2.5 and Table 2.2 lists their maximum emission wavelength and full width at half maximum (FWHM).

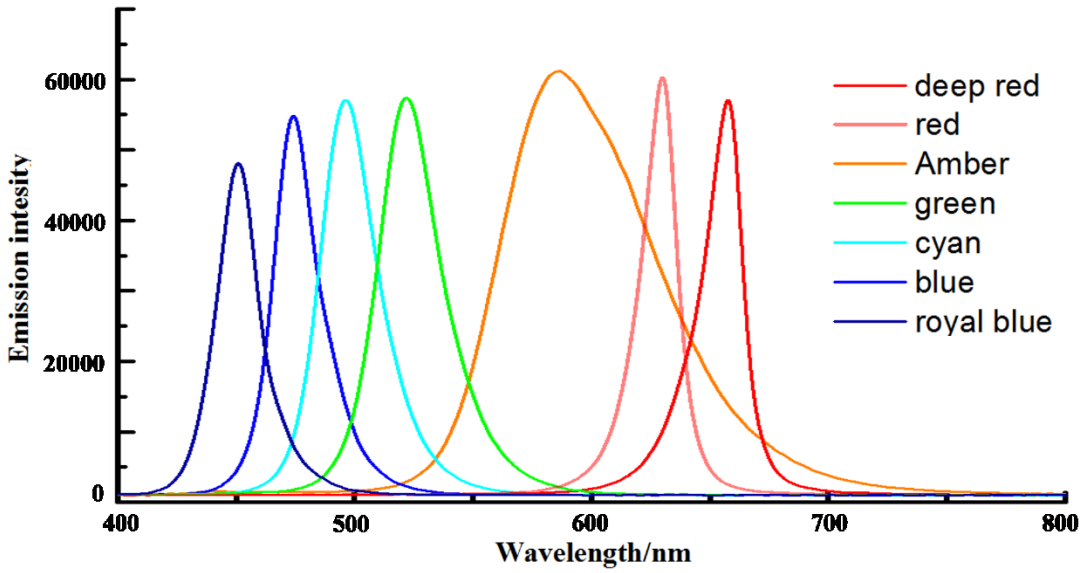

Figure 2.5 Emission spectra of LEDs in continuous photolysis.

Table 2.2 Emission wavelength and full width at half maximum (FWHM) of LEDs

	λ_{max}	FWHM
Royal blue	453 nm	20 nm
Blue	475 nm	25 nm
Cyan	498 nm	30 nm
Green	523 nm	40 nm
Amber	599 nm	77 nm
Red	631 nm	18 nm
Deep-red	659 nm	22 nm

For near infrared (NIR) light photolysis, a 798 nm SheauPac fiber coupled laser module was used. Emission wavelength was found to be 794 nm when operated at room temperature. There are some other basic parameters about the diode laser.

Model	SP-798-5-3
Center wavelength	794 nm
Spectral width	10 nm
Threshold current	<700 mA
Operating current	<4 A
Forward voltage	<2.2 V
Max output power	3 watts
Operating temperature	15-55 °C

The power of all the light sources mentioned above was measured by FieldMaxII-TO power meter from Coherent with a thermopile photodetector PM10V1. The power meter was calibrated within a year by the factory.

K. Time resolved spectroscopy

Emission lifetimes were measured using a lab assembled time resolved optical spectroscopy instrument (Fig. 2.6). A Nd:YAG Q-switched laser from Spectra Physics Quanta-Ray operated at the second harmonic (532 nm) or third harmonic (355 nm) was used as the excitation source. Laser light was steered towards the sample holder using corresponding dichroic mirrors. The sample holder is a specially built aluminum block mounted directly in front of the monochromator with openings on all four sides of the sample holder. The excitation beam hits the sample cuvette perpendicular to the opening of the monochromator2. The emission from the sample cuvette enters the monochromator2 and is detected using a side-on photomultiplier tube (Hamamatsu model 1P28). Time-resolved data is recorded and averaged on a LeCroy Waverunner LT 342 500MHZ oscilloscope. (note: Xenon lamp and monochromator1 were not used unless in transient absorption experiment)

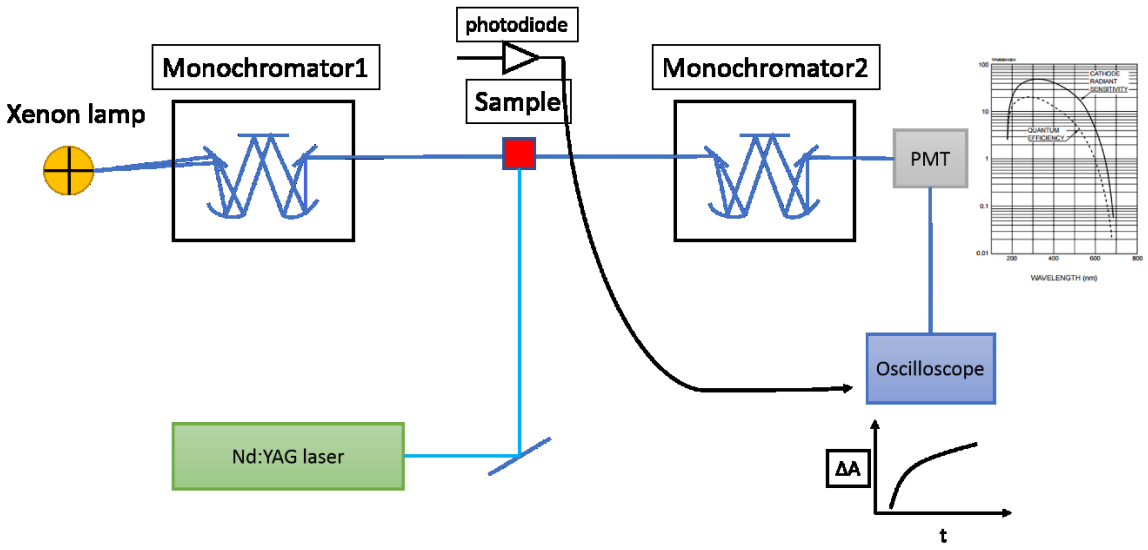

Figure 2.6 Schematic depicting the components of the time resolved optical spectroscopy instrument.

III. Techniques

A. Photon flux calculation

As discussed in Chapter 1, photochemistry quantum yields were calculated by absorption change versus absorbed photons. Photon flux was determined by the power meter and number incident of absorbed photons was calculated with equation below:

$$N_0 = I_0 \times t = \frac{P \times \lambda \times t}{h \times c \times N_A}$$

N_0 = incident photons (Einsteins)

I_0 = photon flux (Einsteins/second)

t = irradiation time

P = power (W)

λ = wavelength of photons (nm)

h = Planck's constant (6.626×10^{-34} J.s)

c = light speed (3.0×10^{8} m/s)

N_A = Avogadro's constant (6.022×10^{23} /mol)

Knowing the absorbance at irradiation wavelength, absorbed photon N_{abs} can be calculated from N_0. Then photochemical reaction quantum yields were determined by plotting moles of compound reacted versus N_{abs} over initial 10% of the reaction.

B. CO quantification with GC/TCD

To quantify the released CO from photolysis solutions, two types of gas-tight cuvettes were used: One is 1.0 cm pathlength septum cuvette of 5 mL volume and another one is custom-made Schlenk cuvette consisting of a 1.0 cm pathlength cuvette fused to glass tubing and stopcocks designed for attachment to a vacuum line (Fig. 2.2). After photolysis, the gas phase (head space) was sampled by drawing an aliquot with a gas-tight syringe and injecting the aliquot into GC-TCD. The total amount of gas (CO and CO_2) released during photolysis was then calculated based on most recent calibration curves by taking into account the cell volume, the solution volume, injection aliquot and the gas solubility in the solvent from which was determined the partitioning between the gas and liquid.

The calibration curves for CO (Fig. 2.7) and CO_2 (Fig. 2.8) were measured by sampling the gas from a Schlenk flask (Fig. 2.1) with known pressure (measured by monometer). When

the volume and pressure were known, moles of the gas in the Schlenk flask was calculated and so was the aliquot injected into GC-TCD. The moles of aliquot gas were plotted against integration of the peak of the gas as the gas calibration curves. It is worth noting that calibrations were done only in the relevant moles range.

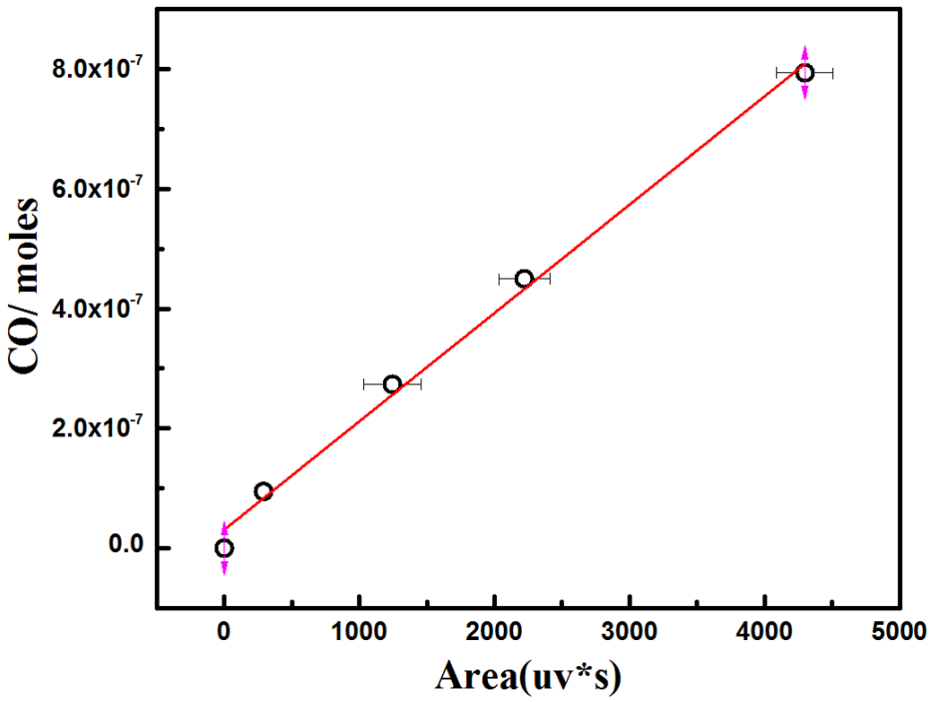

Figure 2.7 Calibration curve of CO from the GC-TCD.

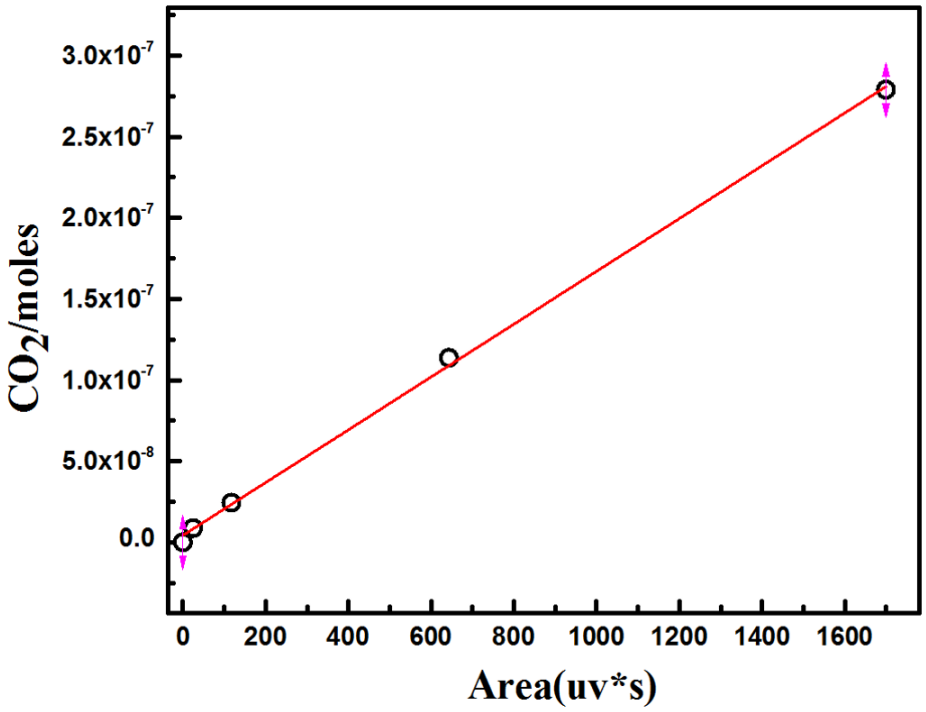

Figure 2.8 Calibration curve of CO_2 from the GC-TCD.

Reference

1. Wink, D. A Flash Photolysis Investigation of Catalytically Active Rhodium, Iridium and Ruthenium Complexes. Ph.D Dissertation, UCSB., Santa Barbara, CA **1985**.

2. Armarego, W. L. F.; Chai, C. L. L. Chapter 1 - Common Physical Techniques Used in Purification. In Purification of Laboratory Chemicals (Sixth Edition); Butterworth-Heinemann: Oxford, **2009**; pp 1–60.

Chapter 3. Dinuclear PhotoCORMs: Dioxygen-Assisted CO Uncaging from Long Wavelength Absorbing Metal-Metal Bonded Carbonyl Complexes

Reproduced in part with permission from *Inorg. Chem. 2017, 56, 6094–6104*. Zhi Li, Agustin E. Pierri, Po-Ju Huang, Guang Wu, Alexei V. Iretskii and Peter C. Ford*.

I. Introduction

For photoCORMs, the use of light offers exquisite spatial control of the timing and dosage of CO release. However, a major issue that needs to be addressed is concerned with the wavelength of light utilized in most such systems to facilitate CO uncaging. The short wavelength, high energy light needed to activate most metal carbonyl complexes toward CO uncaging has shallow penetration depths into mammalian tissue and can damage living cells[1]. Organic photoCORMs also have the similar problem, although several recent works that have extended the photosensitivity to much longer wavelengths.[2,3] Therefore, there is considerable interest in developing photochemical delivery systems that can be activated with more deeply penetrating, longer wavelength visible / near-infrared (NIR) light for the delivery of CO[4,5] and of other small molecule bioregulators in aerobic media.[6,7] There are several approaches to making photoCORM systems more responsive to longer wavelengths. Previously, this laboratory described carriers incorporating upconverting nanoparticles (UCNPs) that used multi-photon excitation with NIR light to trigger CO release from a Mn(I) carbonyl.[4] A different strategy is described here, where we utilize direct excitation of the long wavelength

absorbing metal-metal bond to ligand ($\sigma_{MM} \rightarrow \pi_L^*$) charge transfer (MMLCT)[8,9] transition of dinuclear complexes to generate reactive intermediates (proCORMs)[10] that, upon subsequent reaction(s), release CO. Specifically, MMLCT excitation of the dinuclear rhenium-manganese carbonyl complexes $(CO)_5ReMn(CO)_3(L)$ [L = 1,10-phenanthroline (phen, **1**), 2,2'-bipyridine (bpy, **2**), 2,2'-biquinoline (biq, **3**) and 1,10-phenanthroline-4-carboxaldehyde (phen-CHO, **4**)) leads to homolytic cleavage of the Re-Mn bond to give mononuclear metal radicals. In aerobic solution, these radicals react with O_2[11] to form new species that are much more labile toward CO release (uncaging). To our knowledge, this is the first photochemical study of such dinuclear photoCORMs in aerated media to demonstrate release of caged CO with long wavelength excitation.

II. Synthesis

A. Synthesis of precursors

1. $Na[Re(CO)_5]$

It was prepared by a modified published procedure.[12] Hg(Na) (3%) (13.56 g) was added to a dry round bottom flask containing ~50 mL dry THF under an argon atmosphere. Under flowing argon, solid $Re_2(CO)_{10}$ (0.414 g, 0.625 mmol) was added to this solution, which was allowed to stir at 22 °C for 5 h. The initially colorless $Re_2(CO)_{10}$ solution underwent a change to the orange/red of $Na[Re(CO)_5]$. This $Na[Re(CO)_5]$ was not isolated; instead the THF solution was kept under an argon atmosphere until using in the same day. The THF solution containing $Na[Re(CO)_5]$ was used in its entirety in each synthetic procedure.

2. 1,10-phenanthroline-4-carboxaldehyde (phenCHO)

This was prepared by a modification of a published procedure.[13] A solution prepared by dissolving SeO_2 (2.86 g 25.8 mmol) in 50 mL of *p*-dioxane/water (96:4) was heated to reflux in a 3-neck flash. To this was added dropwise a solution of 4-methyl-1,10-phenanthroline (2 g, 10.3 mmol) in 60 mL of *p*-dioxane:water (96:4) over a 1 h period. The solution was then refluxed for 3 h after which the resulting suspension was filtered through celite while still warm. The solution was concentrated under vacuum. Alumina (neutral) column purification was performed with CH_2Cl_2:MeOH = 19:1 (v/v) to afford beige powder (0.56 g, 27%).

3. $Mn(CO)_3(phen)Br$

This was prepared by a modified published procedure.[14] Bromidopentacarbonylmanganese(I) $Mn(CO)_5Br$ (0.743 g, 2.7 mmol) was stirred with 1,10-phenanthroline (0.535 g, 2.97 mmol) in dichloromethane (DCM, 20 mL) under ambient temperature for overnight under an argon atmosphere. Then the reaction solution was cooled to -40 °C (acetonitrile/dry ice bath) resulting in an orange precipitate with a yield of 0.71 g (66%).

4. $Mn(CO)_3(bpy)Br$

This was prepared by a modification of a published procedure.[15,16] $Mn(CO)_5Br$ (0.8 g, 2.9 mmol) was refluxed with 2,2' bipyridine (0.5 g, 3.2 mmol) in dry diethyl ether (100 mL) for 4 h under an argon atmosphere. Then the reaction solution was cooled to -40 °C (acetonitrile/dry ice bath) resulting in a yellow precipitate with yield of 1.02 g (93%). This

yellow solid was collected by filtering through two layers of filter papers and washed with -40 °C diethyl ether. $Mn(CO)_3(bpy)Br$ was found to be air-stable and could be stored under atmospheric conditions in the dark. The yellow compound was used without further purification.

5. $Mn(CO)_3(biq)Br$

The synthesis was analogous to that for **$Mn(CO)_3(phen)Br$** to give red powder with a 92 % yield**.**

6. $Mn(CO)_3(phenCHO)Br$

This was prepared by a procedure analogous to that for $Mn(CO)_3(phen)Br$. $Mn(CO)_5Br$ (1.054 g, 3.84 mmol) was stirred with phenCHO (0.877 g, 4.22 mmol) in dry dichloromethane (5 mL) overnight under an argon atmosphere. Then the reaction solution was cooled to -40°C resulting in a magenta precipitate. This magenta solid was collected by filtering over two layers of filter papers and washed with -40°C diethyl ether resulting a yield of 1.52 g (89.2%). The compound was used without further purification.

B. Synthesis of dinuclear metal carbonyls

Fig. 3.1 outlines the pathways used to prepare the dinuclear complexes $(CO)_5ReMn(CO)_3L$ (L = bpy, phen, biq or phen-CHO) from the reaction of $Mn(CO)_3(L)Br$ with $Na[Re(CO)_5]$ in anhydrous THF. During the reaction, the solution colors change from

pale orange to an intense violet, blue or green indicating the formation of the dinuclear complexes. After column chromatography, product yields generally exceeded 50%. The mechanism of M-M' bond formation in such reactions has been the subject of some debate.[17–21] Based on earlier work,[17] Morse and Wrighton[18] proposed electron transfer leading to two metal radicals, one a 17 e^- complex, the other a 19 e^- complex. The M-M' bond is formed by radical coupling after halide loss from the latter intermediate. Consistent with this pathway was the isolation of $M_2(CO)_{10}$ and $M'_2(CO)_6L_2$ co-products in addition to the desired heteronuclear complex $M(CO)_5M'(CO)_3L$. The observation that heteronuclear product yields are often quite high was explained by Tyler and coworkers[20,21] in terms of the solvent structure inhibiting escape of the heteronuclear radical pair generated by electron transfer thereby favoring formation of the M-M' bond. In the present case, chromatography of the crude product indicated minor byproducts that may be the result of some homonuclear coupling.

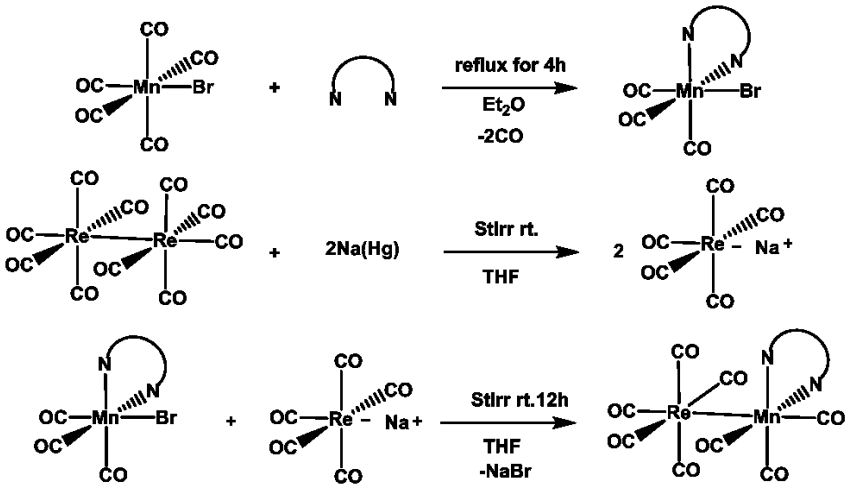

Figure 3.1 Steps leading to the syntheses of complexes **1-4**, the bidentate ligands are phen, bpy, biq and phenCHO, respectively.

1. $(CO)_5ReMn(CO)_3(phen)$ (compound 1)

Compound **1** was prepared by a modification of published procedures.[22,23] The THF solution containing the rhenium salt $Na[Re(CO)_5]$ (1.33 mmol) was transferred via cannula to a round bottom flask containing $Mn(CO)_3(bpy)Br$ (0.5 g, 1.33 mmol) dissolved in 25 mL dry THF. The color changed immediately from yellow to very dark purple. The mixed solution was then allowed to stir under argon in the dark. After 12 h, the solvent was removed under vacuum, and the resulting purple solid was purified by flash chromatography over activated alumina. The column was washed with one column volume of pure hexanes, then the product mixture was eluted with a gradient of DCM / hexanes (0%-50% DCM). The purple band was collected and was further purified by recrystallization from DCM by slow vacuum evaporation of solvent. Total yield was determined to be 63%. Elemental Analysis: Found: C 37.20%, H 1.23%, N 4.34%.; Calculated: C 37.21%, H 1.23%, N 4.34%.

2. $(CO)_5ReMn(CO)_3(bpy)$ (compound 2)

Compound **2**'s synthesis and purification procedures were analogous to those for **1**. Total yield was determined to be 62 %. Elemental Analysis: Found: C 34.56%, H 1.26%, N 4.49%; Calculated: C 34.79%, H 1.30%, N 4.51%.

3. $(CO)_5ReMn(CO)_3(biq)$ (compound 3)

The synthesis and purification procedures were analogous to those for **1**. Total yield was determined to be 33.0%. Elemental Analysis: Found: C 43.43%, H 1.63%, N 4.02%; Calculated: C 43.28%, H 1.68%, N 3.88%.

4. $(CO)_5ReMn(CO)_3$(phen-CHO) (compound 4)

The synthesis and purification procedures were analogous to those for **1**. THF solution (60 mL) containing the rhenium anion $Na[Re(CO)_5]$ (2.21 mmol) was transferred via cannula to another round bottom flask containing $Mn(CO)_3$(phenCHO)Br (0.8 g, 1.87 mmol) dissolved in 30 mL dry THF. The mixed solution was then allowed to stir overnight under argon, with exclusion of light. The color change from a magenta color to a dark blue was seen after addition. After overnight reaction, the solvent was removed under vacuum, and the resulting blue solid was purified by flash chromatography over activated alumina. The column was washed with one column volume of pure hexanes, then the product mixture was eluted with a gradient of DCM/hexanes (0%-50% DCM). The blue band was collected and was further purified by recrystallization from DCM by slow vacuum evaporation of solvent. Total yield was determined to be 0.22 g (23 %). Elemental Analysis: Found: C 37.66%, H 1.36%, N 3.79%; Calculated: C 37.45%, H 1.20%, N 4.16%.

5. Imine PEG conjugate of 4 (compound 5)

In glovebox, 88 mg (0.13 mmol) of $(CO)_5ReMn(CO)_3$(phen-CHO) and 234 mg of PG1-AM-2k (amino PEG) were added to anhydrous ethanol. Activated 3 Å molecular sieves (4 g) were added to the resulting solution which was then stirred at ambient temperature under Ar atmosphere with exclusion of light. The course of the reaction was monitored by TLC and stopped after ~12 h. The molecular sieves and their residue were removed by filtration and solvent was removed from the filtrate under vacuum. The resulting blue powder was purified

by flash chromatography through neutral alumina with methanol: DCM (1:1 v:v) and the blue band was collected according to TLC. Total yield was determined to be 60 mg (19 %).

III. Characterizations of compound 1-5 and precursors

The dinuclear complexes were characterized by recording their NMR, IR, mass spectra and UV-visible (Fig. 3.2-3.23). As shown in Fig. 3.20-3.23, the visible spectrum of each in acetonitrile (MeCN) solution displays a strong, longer wavelength absorption band that is sensitive to the nature of L (ligand). This band is attributed to a MMLCT ($\sigma_{MM} \rightarrow \pi_L^*$) transition in analogy to earlier studies with related complexes.[9,25] Fig. 3.24 is a qualitative MO diagram indicating the orbital origin for such transitions. The shorter wavelength bands in the electronic spectra include contributions from $\sigma_{MM}^b \rightarrow \sigma_{MM}^*$ (localized on the M-M bond), $d_\pi \rightarrow \pi_L^*$ (metal to ligand charge transfer) and $\pi_L \rightarrow \pi_L^*$ (intra-ligand) transitions. For the analogous $(CO)_5ReMn(CO)_3L$ complexes, the MMLCT band displays λ_{max} values of 550 nm, 550 nm and 719 nm for L = phen (**1**), bpy (**2**), and biq (**3**), respectively while **4** ($(CO)_5ReMn(CO)_3$(phenCHO)) has two MMLCT bands at 543 nm and 652 nm (Table 3.2).

A. ^{1}H NMR spectra

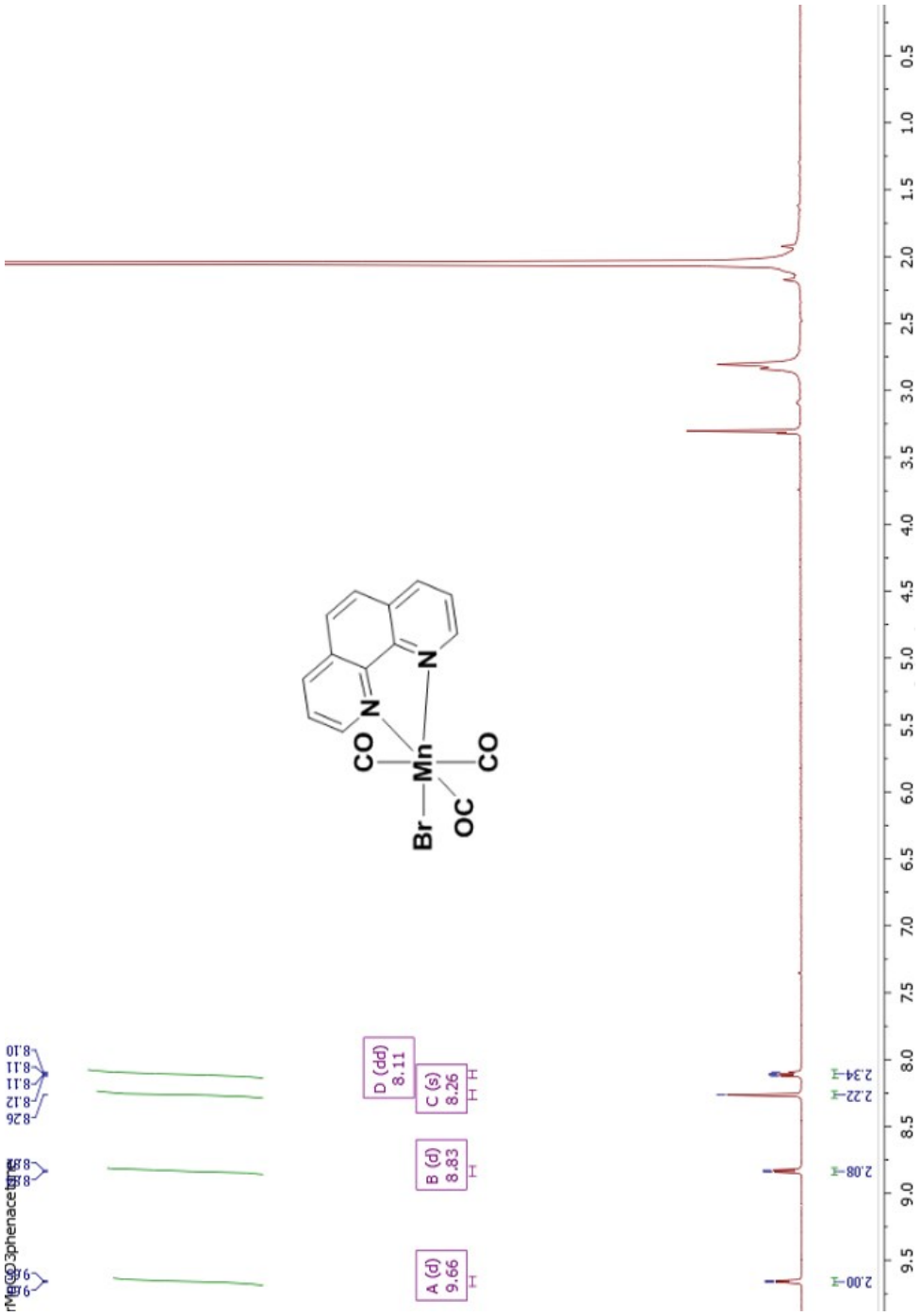

Figure 3.2 $Mn(CO)_3(phen)Br$ ^{1}H NMR spectrum agreed with reported values[14]: (500 MHz, acetone-d_6, ppm) δ = 9.66 (d, J(H,H) = 4.4 Hz, 2H), 8.83 (d, J(H,H) = 7.6 Hz, 2H), 8.26 (s, 2H), 8.11 (dd, J(H,H) = 8.1, 5.1 Hz, 2H).

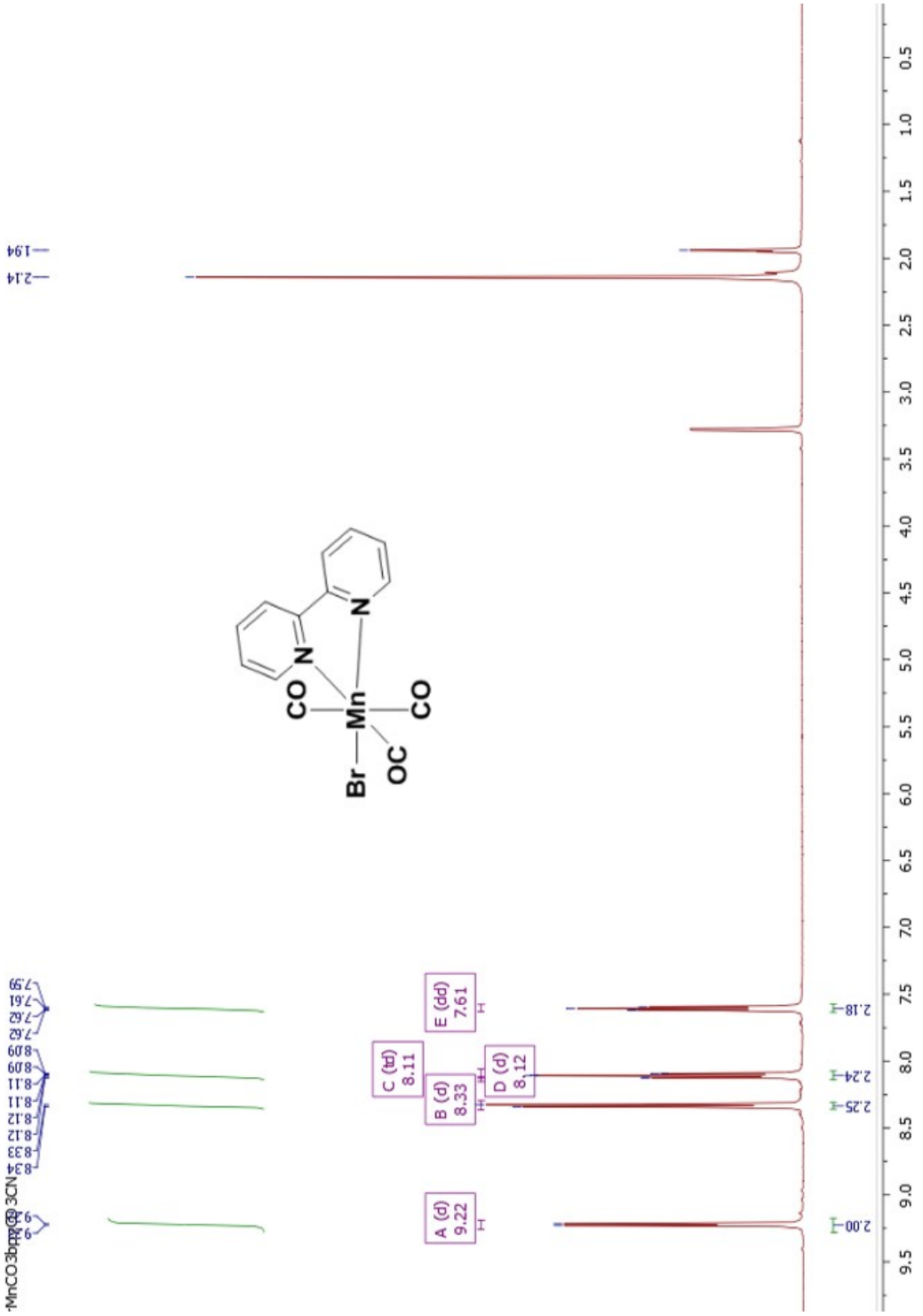

Figure 3.3 $Mn(CO)_3(bpy)Br$ ^1H NMR (500MHz, $CDCl_3$, ppm) δ = 10.63 (s, 1H), 9.90 (d, J(H,H) = 4.9 Hz, 1H), 9.62 (d, J(H,H) = 5.1 Hz, 1H), 9.18 (d, J(H,H) = 9.1, 1H), 8.54 (d, J(H,H) = 8.2, Hz, 1H), 8.20 (d, J(H,H) = 5.1 Hz, 1H), 8.17 (d, J(H,H) = 9.2 Hz, 1H), 7.93 (dd, J(H,H) = 8.2, 5.1 Hz, 1H).

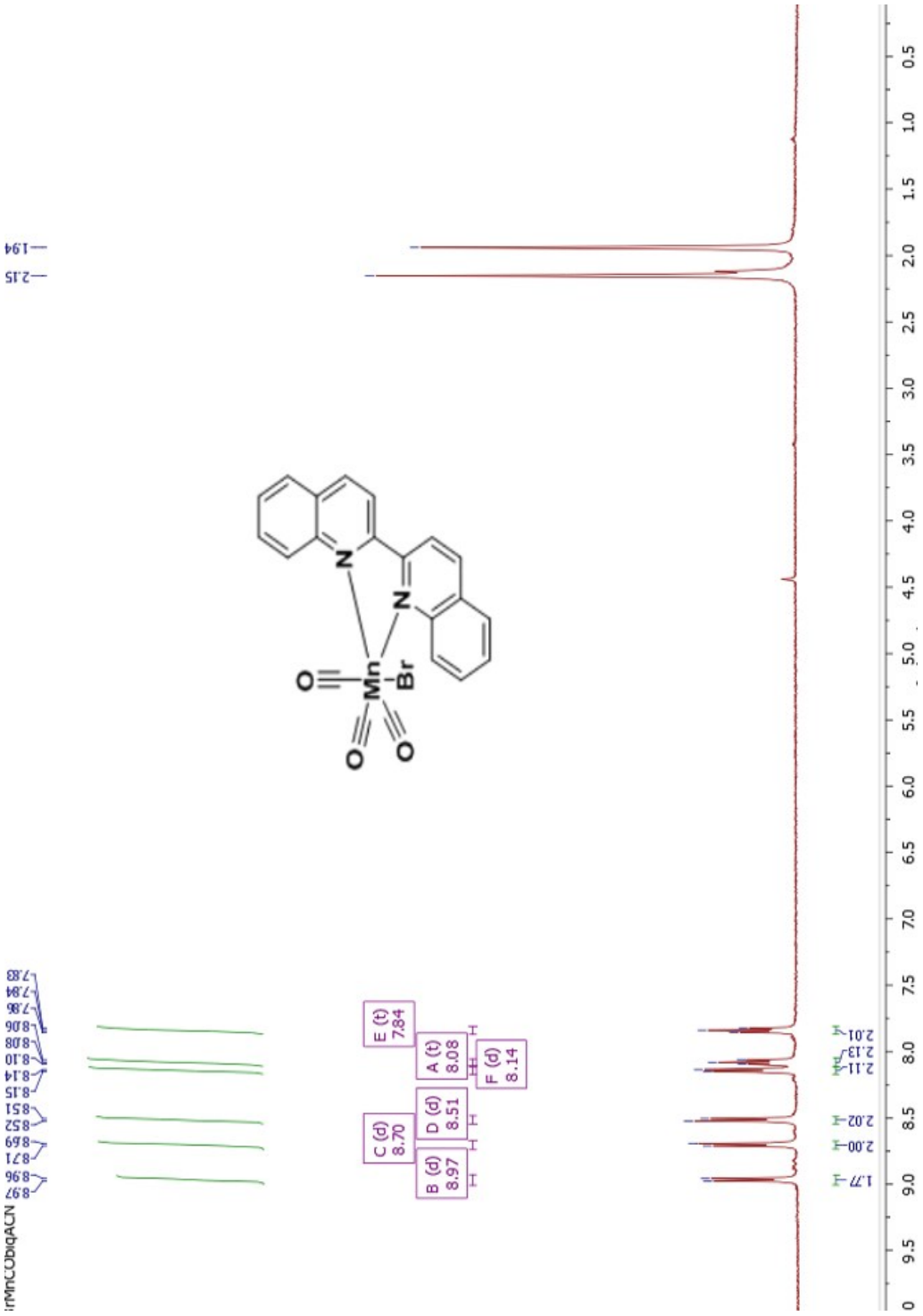

Figure 3.4 $Mn(CO)_3(biq)Br$ ^1H NMR (500 MHz, CD_3CN, ppm) δ = 8.97 (d, J(H,H) = 8.9 Hz, 2H), 8.70 (d, J(H,H) = 8.7 Hz, 2H), 8.51 (d, J(H,H) = 8.6 Hz, 2H), 8.14 (d, J(H,H) = 7.9 Hz, 2H), 8.08 (t, J(H,H) = 8.0 Hz, 2H), 7.84 (t, J(H,H) = 7.5 Hz, 2H).

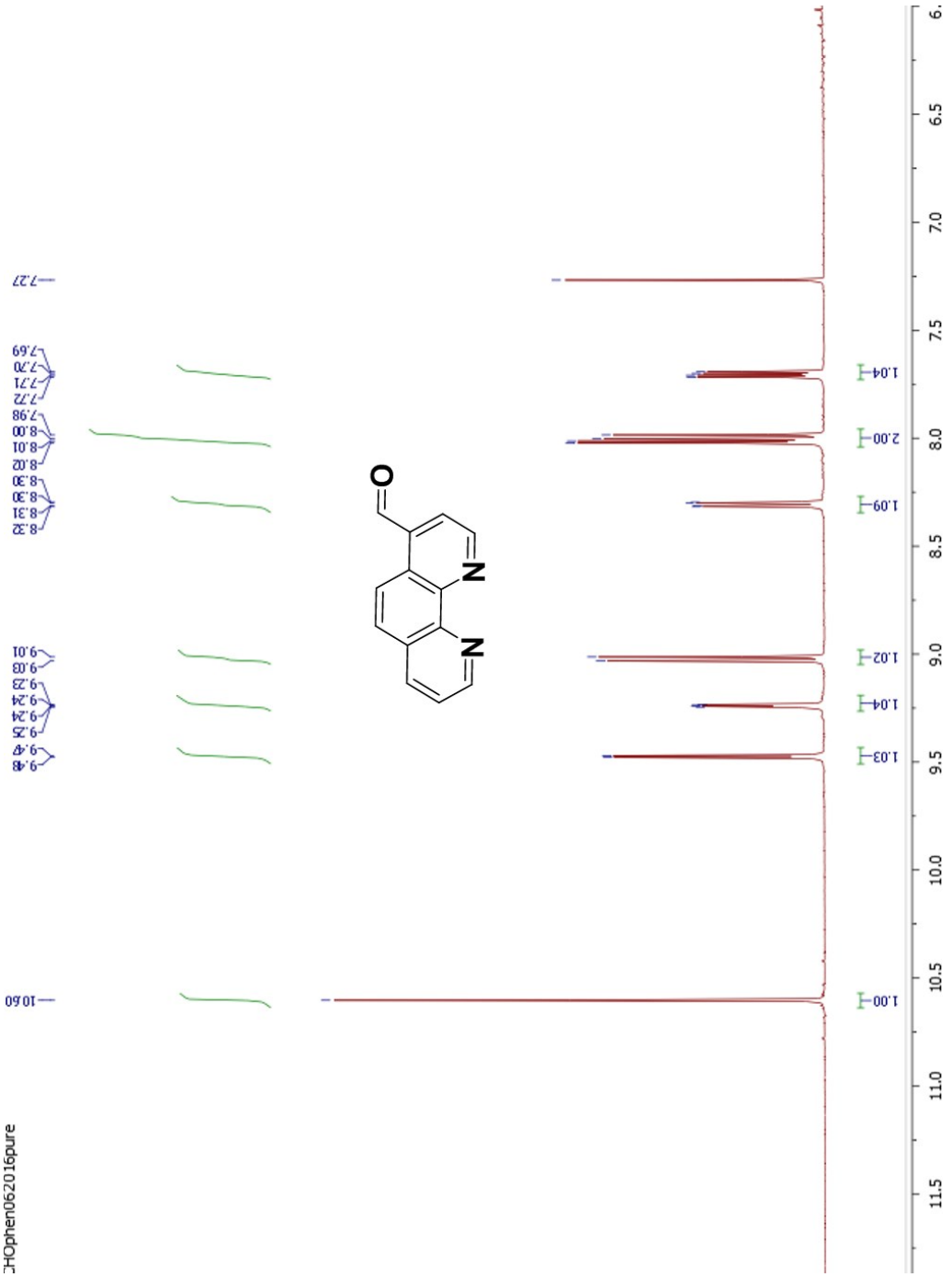

Figure 3.5 phenCHO ^{1}H NMR (500 MHz, $CDCl_3$, ppm) δ = 10.61 (s, 1H), 9.48 (d, J(H,H) = 4.3 Hz, 1H), 9.25 (dd, J(H,H) = 4.3, 1.7 Hz, 1H), 9.03 (d, J(H,H) = 9.2, 1H), 8.31 (dd, J(H,H) = 8.1, 1.7 Hz, 1H), 8.02 (d, J(H,H) = 4.3 Hz, 1H), 8.00 (d, J(H,H) = 9.2 Hz, 1H), 7.71 (dd, J(H,H) = 8.1, 4.3 Hz, 1H).

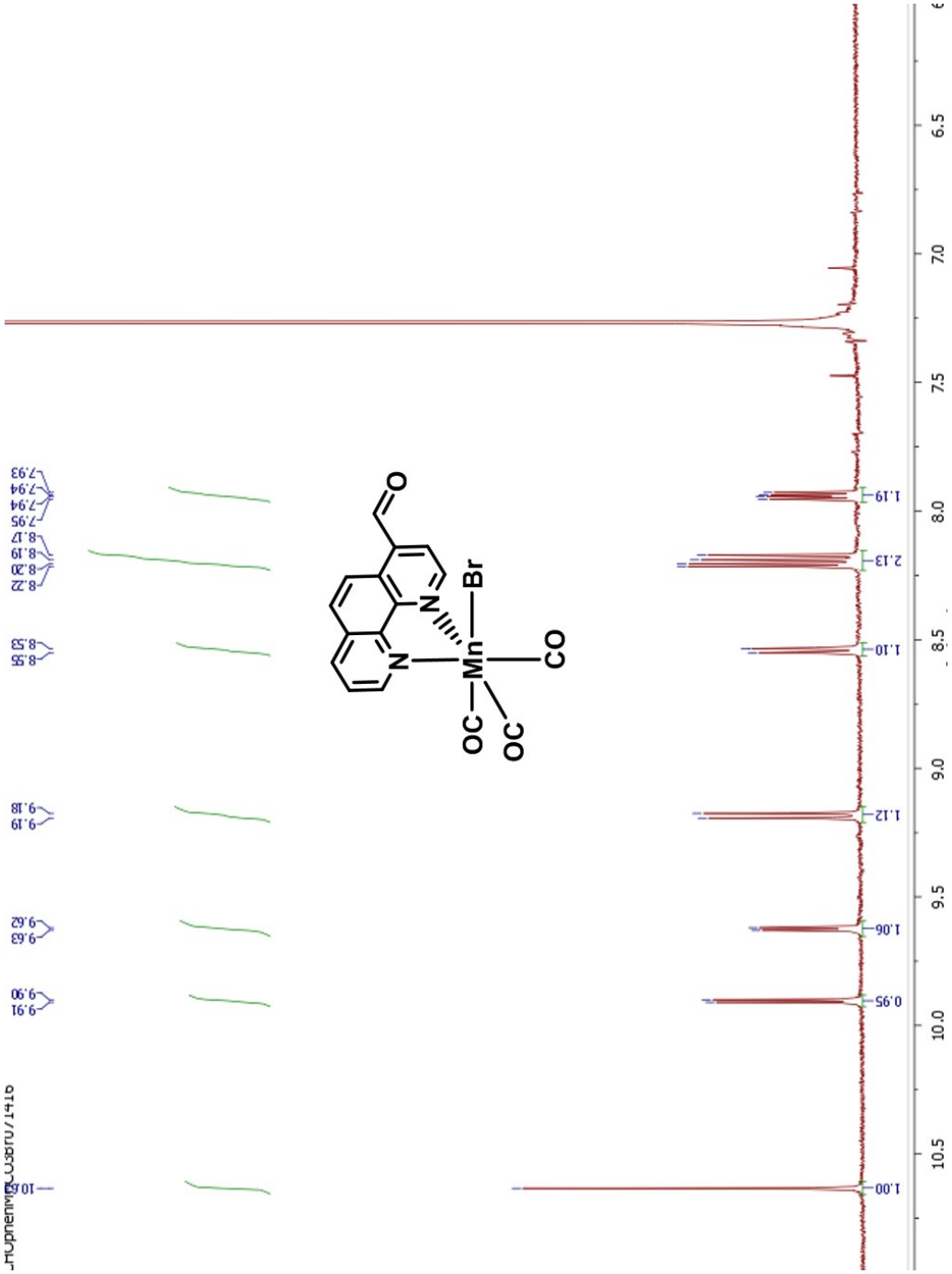

Figure 3.6 $Mn(CO)_3(phenCHO)Br$ ^1H NMR (500 MHz, $CDCl_3$, ppm) δ = 10.63 (s, 1H), 9.90 (d, J(H,H) = 4.9 Hz, 1H), 9.62 (d, J(H,H) = 5.1 Hz, 1H), 9.18 (d, J(H,H) = 9.1, 1H), 8.54 (d, J(H,H) = 8.2, Hz, 1H), 8.20 (d, J(H,H) = 5.1 Hz, 1H), 8.17 (d, J(H,H) = 9.2 Hz, 1H), 7.93 (dd, J(H,H) = 8.2, 5.1 Hz, 1H).

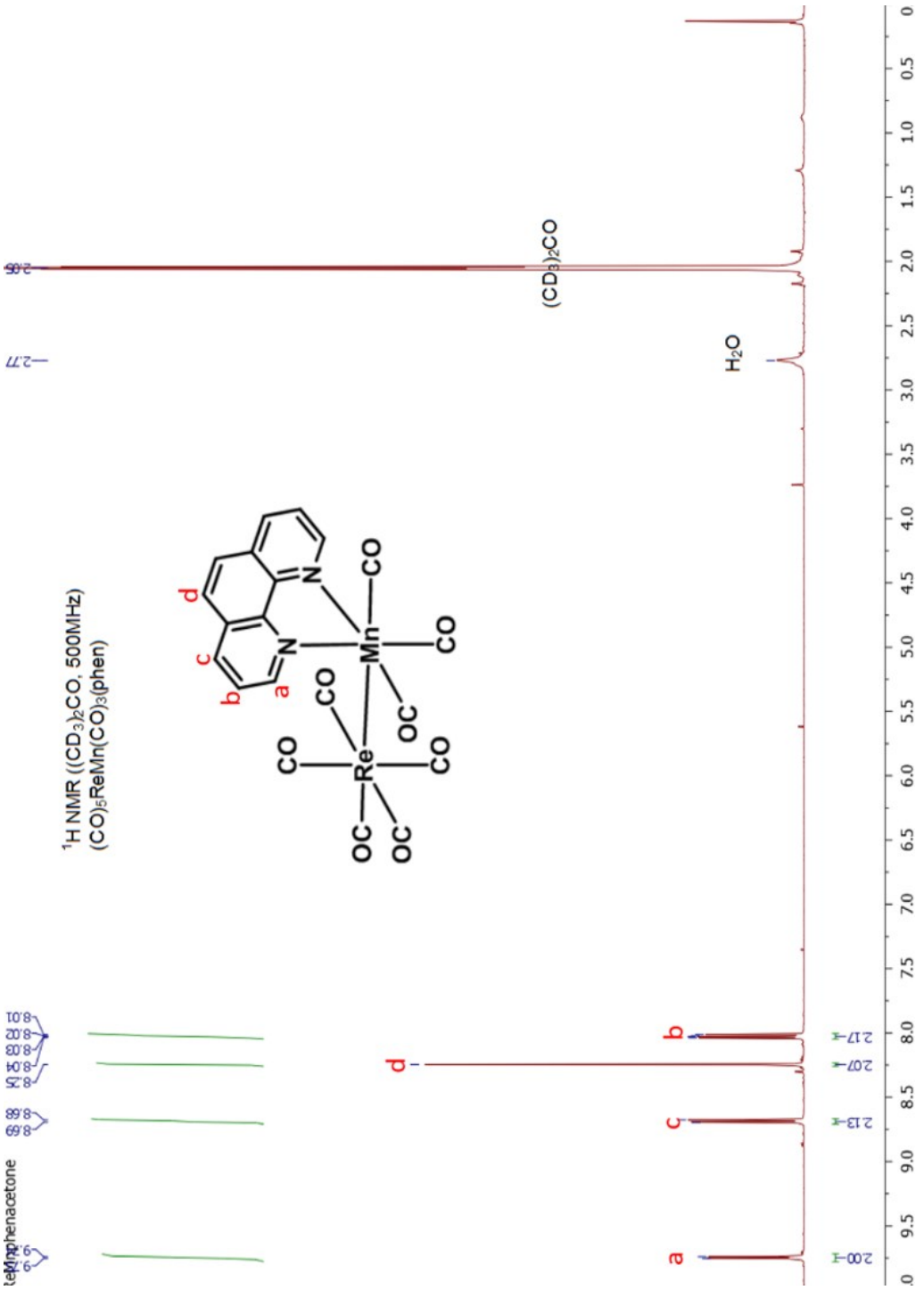

Figure 3.7 $(CO)_5ReMn(CO)_3(phen)$ ^{1}H NMR (500 MHz, $((CD_3)_2CO$, ppm) δ = 9.75 (d, J(H,H) = 6.3 Hz, 2H), 8.69 (dd, J(H,H) = 8.0, 1.1 Hz, 2H), 8.25 (s, 2H), 8.03 (dd, J(H,H) = 8.0, 5.3 Hz, 2H).

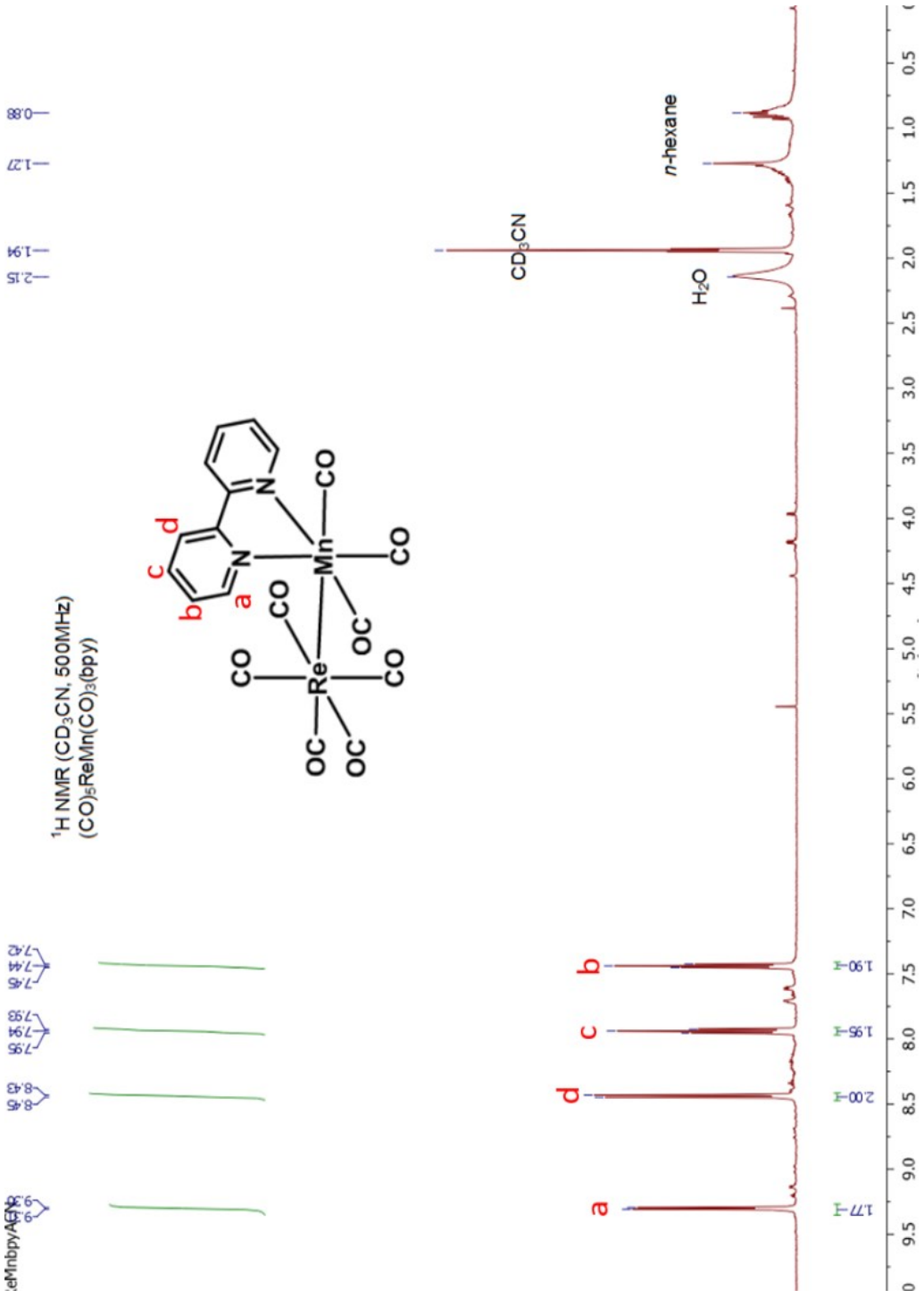

Figure 3.8 $(CO)_5ReMn(CO)_3(bpy)$ ^{1}H NMR (500 MHz, CD_3CN, ppm) δ = 9.30 (d, J(H,H) = 5.4 Hz, 2H), 8.44 (d, J(H,H) = 8.2 Hz, 2H), 7.94 (td, J(H,H) = 8.2, 1.4 Hz, 2H), 7.44 (ddd, J(H,H) = 7.1, 5.8, 1.2 Hz, 2H).

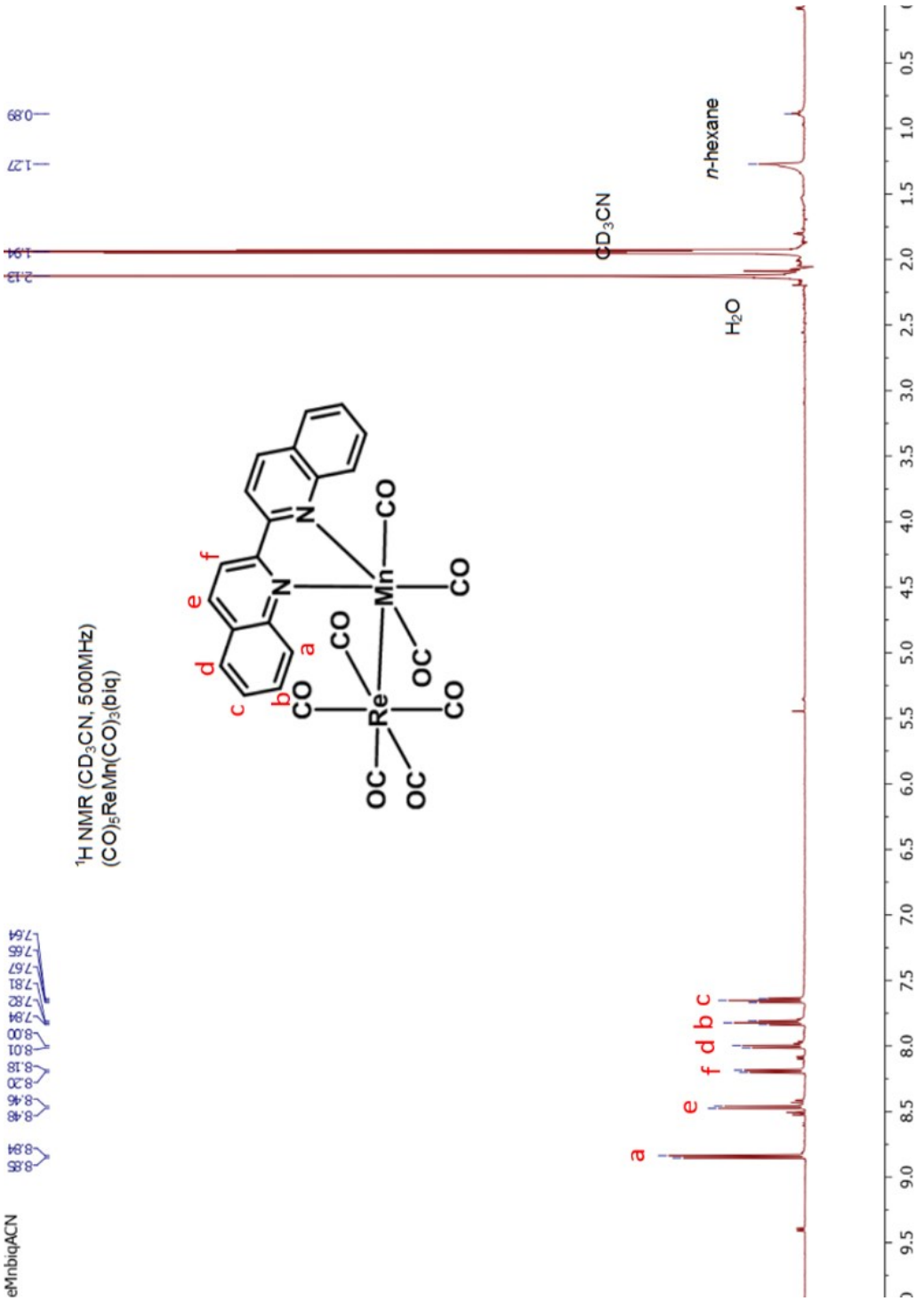

Figure 3.9 $(CO)_5ReMn(CO)_3(biq)$ ^{1}H NMR (500 MHz, CD_3CN, ppm) δ = 8.84 (d, J(H,H) = 8.6 Hz, 2H), 8.47 (d, J(H,H) = 8.6 Hz, 2H), 8.19 (d, J(H,H) = 8.5 Hz, 2H), 8.0 (d, J(H,H) = 8.1 Hz, 2H), 7.82 (ddd, J(H,H) = 8.4, 6.9, 1.4 Hz, 2H), 7.65 (ddd, J(H,H) = 8.1, 6.9, 1.2 Hz, 2H).

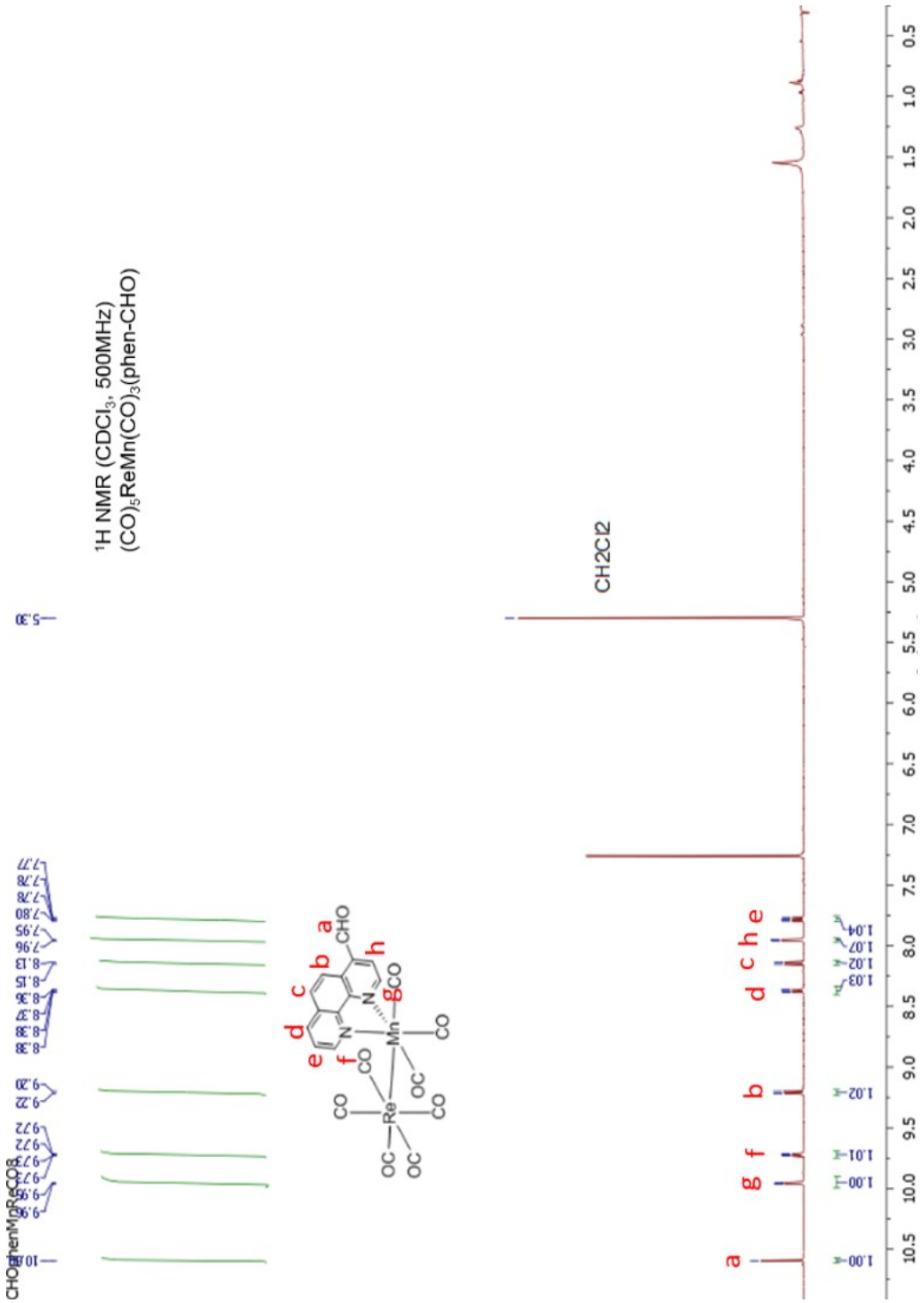

Figure 3.10 $(CO)_5ReMn(CO)_3(phen\text{-}CHO)$ ^{1}H NMR (500MHz, $CDCl_3$, ppm) δ = 10.60 (s, 1H), 9.96 (d, J(H,H) = 5.6 Hz, 1H), 9.72 (dd, J(H,H) = 5.4, 1.1 Hz, 1H), 9.21 (d, J(H,H) = 9.2, 1H), 8.37 (dd, J(H,H) = 8.0, 1.1 Hz, 1H), 8.14 (d, J(H,H) = 9.2, Hz, 1H), 7.95 (d, J(H,H) = 5.6 Hz, 1H), 7.78 (dd, J(H,H) = 7.9, 5.4 Hz, 1H).

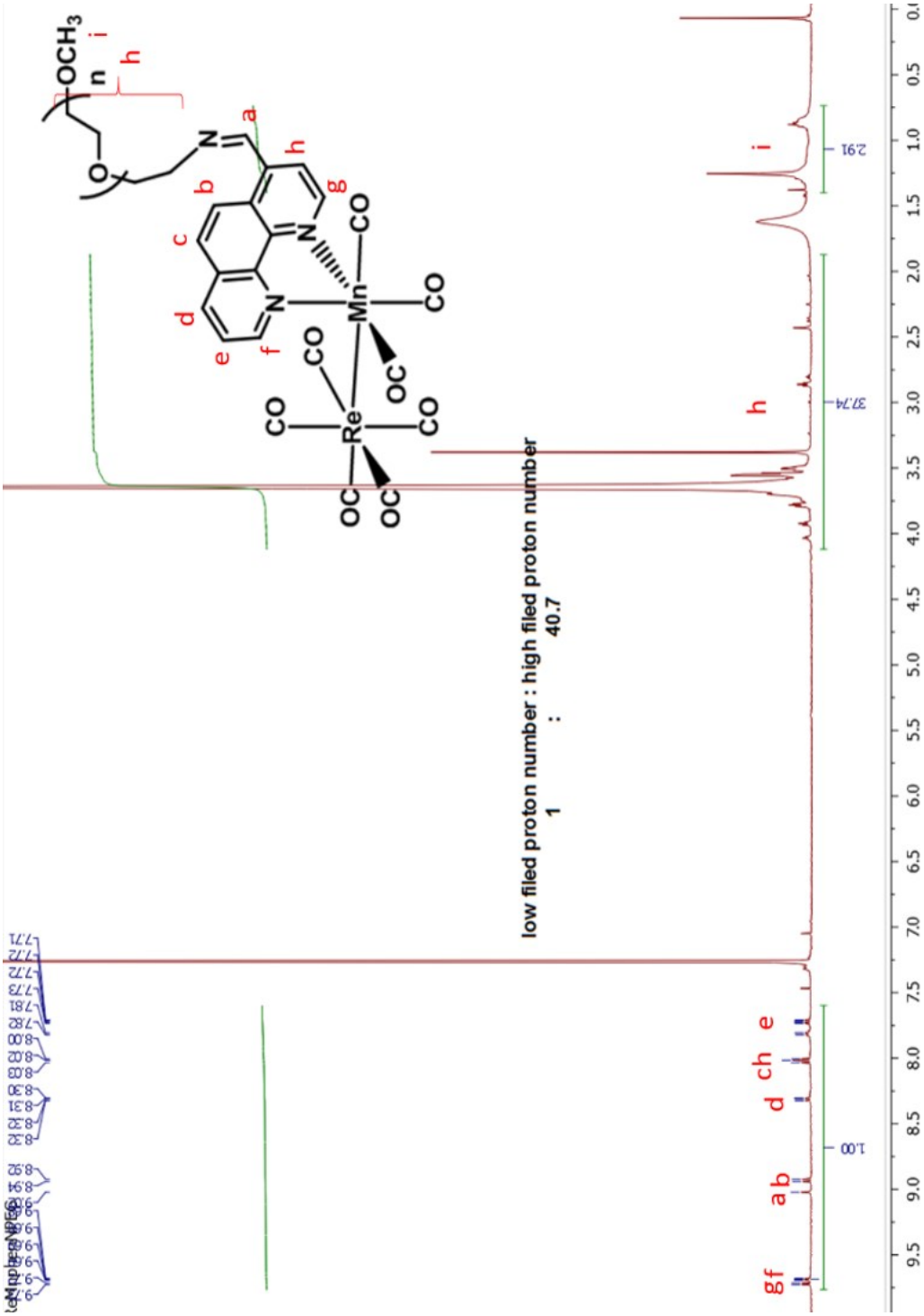

Figure 3.11 imine PEG conjugate (**5**) ^{1}H NMR (500 MHz, $CDCl_3$, ppm) δ = 9.72 (d, J(H,H) = 5.6Hz, 1H), 9.69 (d, J(H,H) = 5.3 Hz, 1H), 9.02 (s, 1H), 8.93 (d, J(H,H) = 9.2, 1H), 8.31 (dd, J(H,H) = 8.0, 1.1 Hz, 1H), 8.03 (d, J(H,H) = 7.6 Hz, 1H), 8.01 (d, J(H,H) = 4.2 Hz, 1H), 7.72 (dd, J(H,H) = 8.0, 5.4 Hz, 1H), 3.64 (m, 284H), 3.38 (s, 3H).

B. ATR-IR spectra

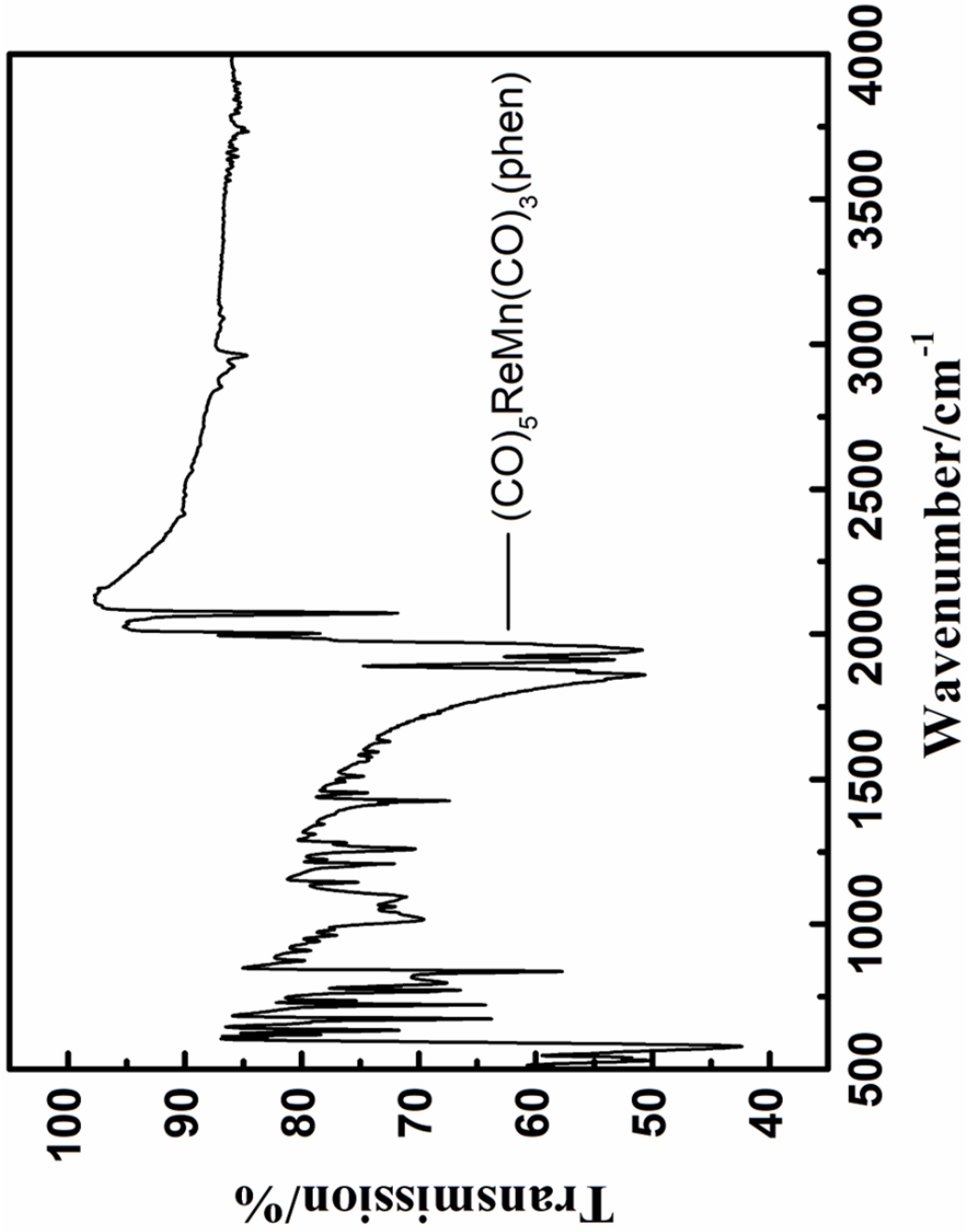

Figure 3.12 ATR-IR spectrum of compound **1** in solid state

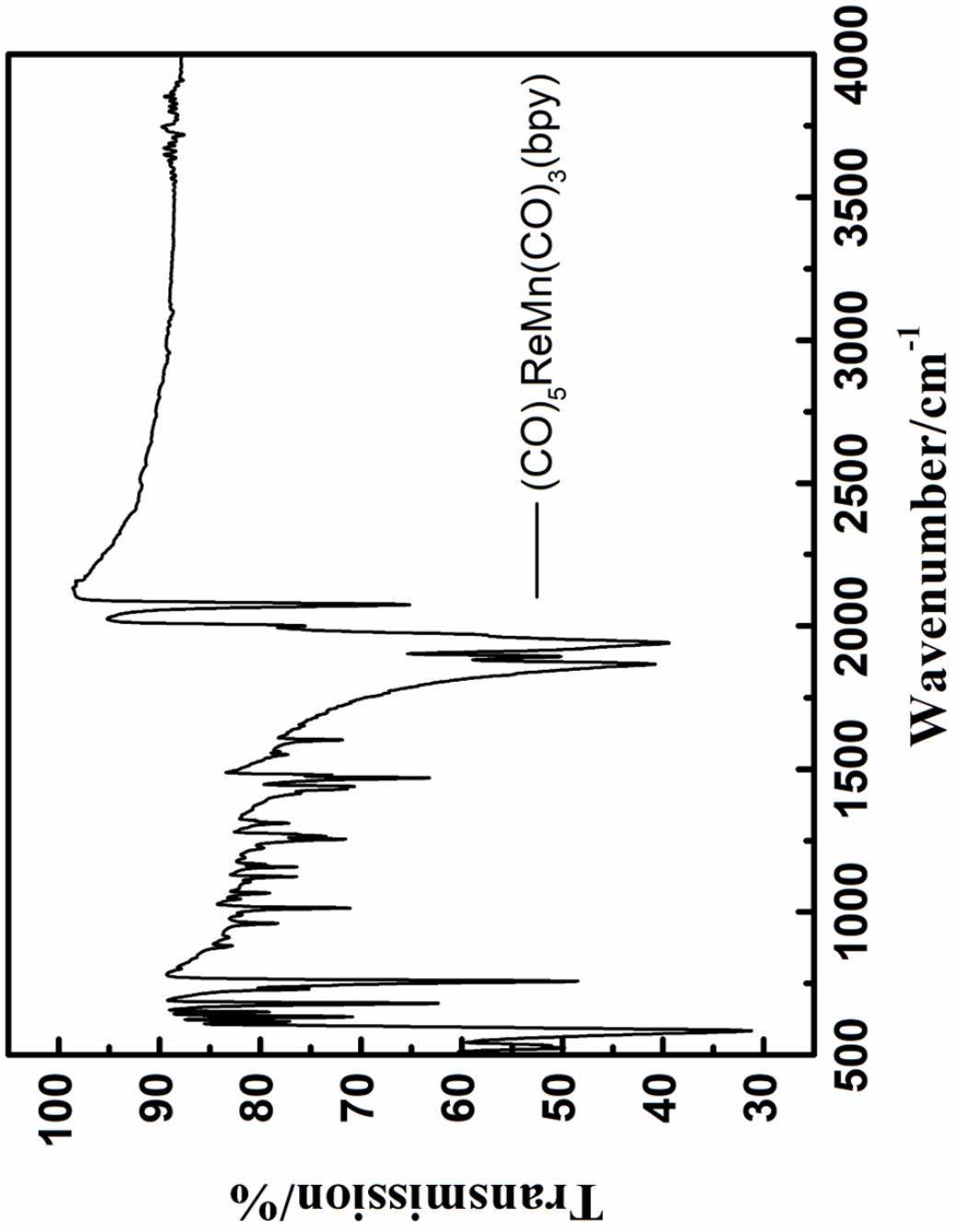

Figure 3.13 ATR-IR spectrum of compound **2** in solid state

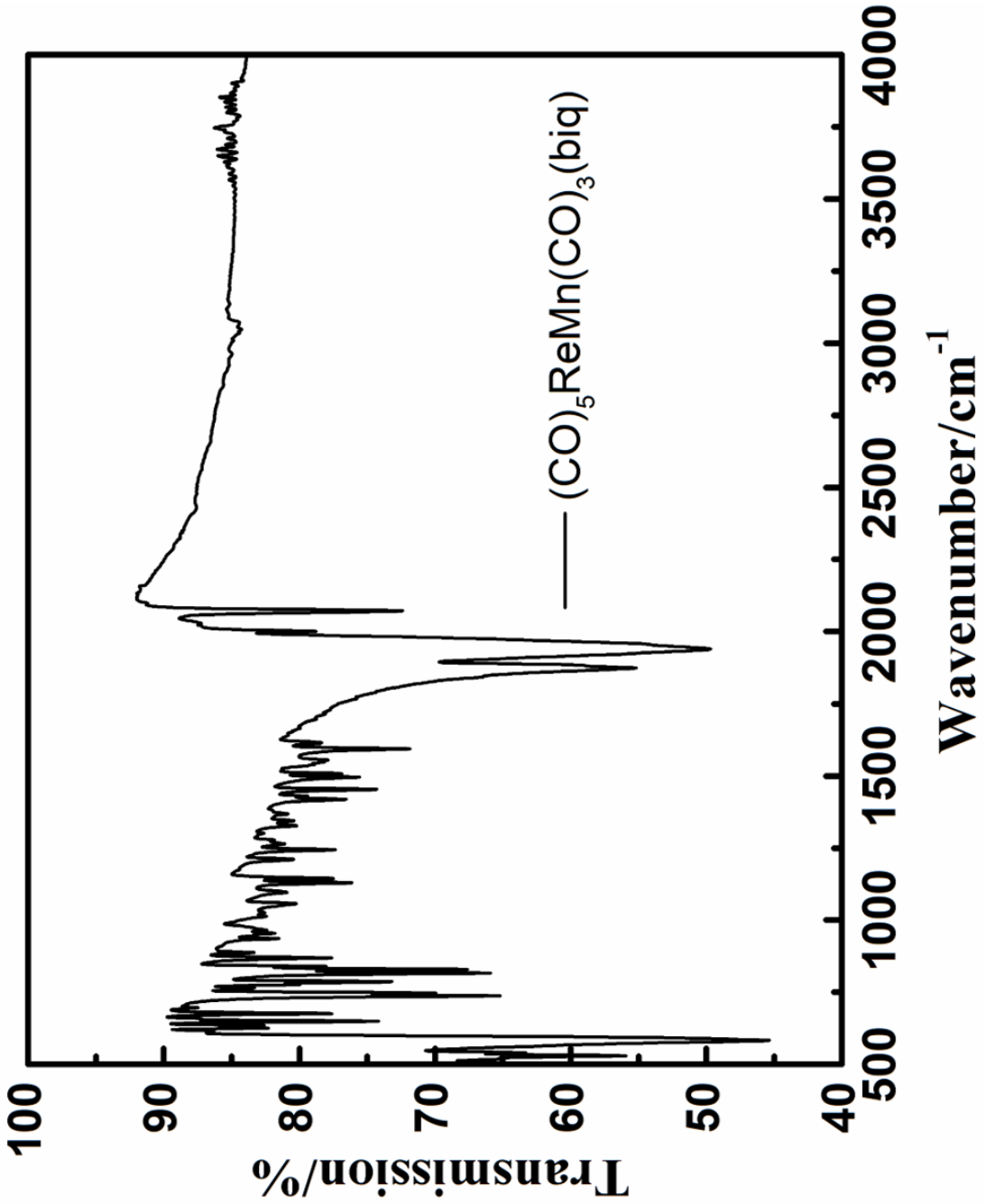

Figure 3.14 ATR-IR spectrum of compound **3** in solid state

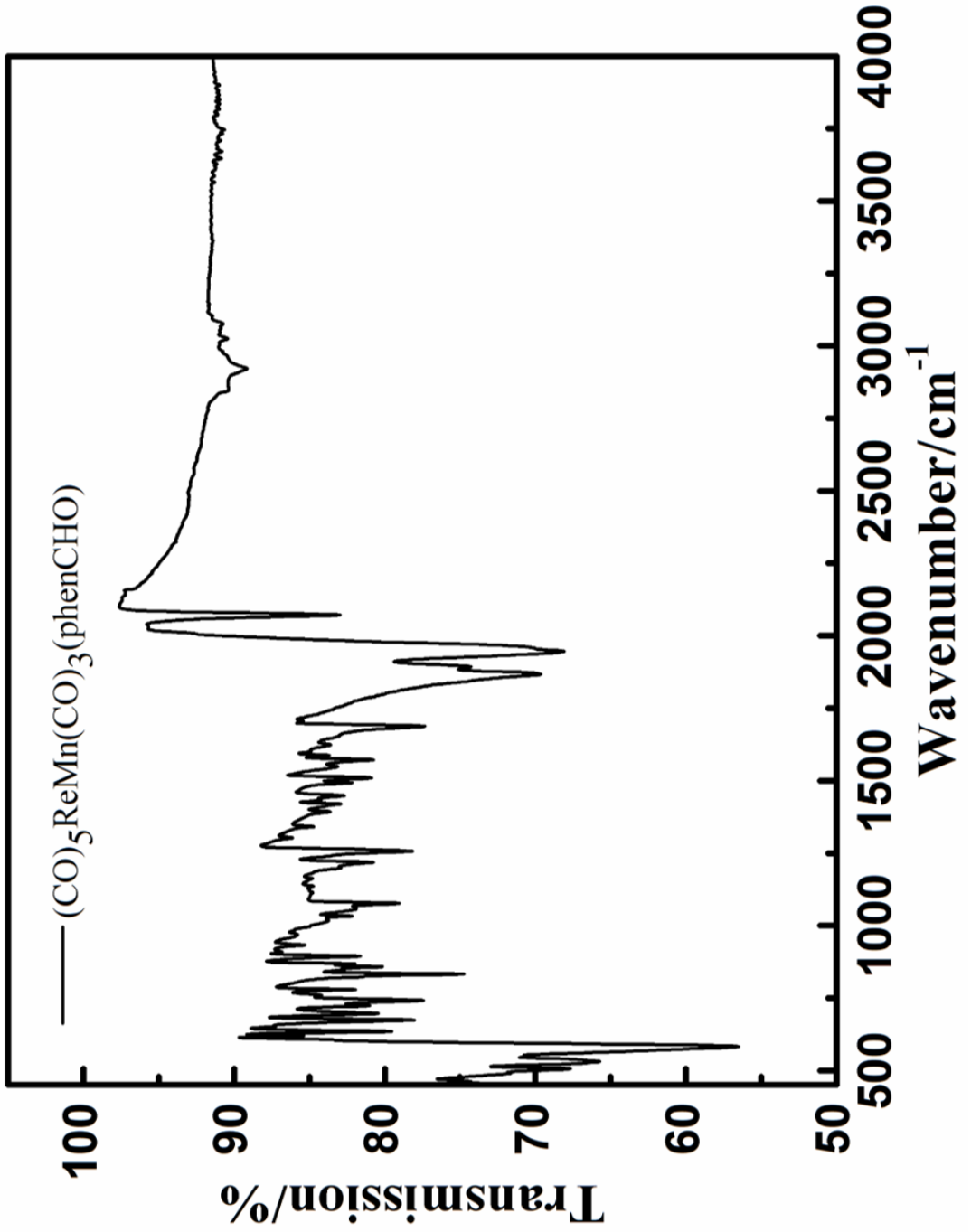

Figure 3.15 ATR-IR spectrum of **4** in solid state

Table 3.1 Solid state attenuated total reflectance (ATR)-IR absorption data for compounds **1**-**4**

Compound	IR absorption peak maxima in cm^{-1}
1	2072 (s), 2003 (m), 1980 (m), 1967 (m), 1944 (s), 1912 (s), 1873 (s), 1861 (s), 1426 (w), 1260 (w), 1209 (w), 1095 (w), 1016 (w), 837 (m), 772 (m), 722 (m), 674 (m), 634 (w), 579 (s)
2	2074 (s), 2002 (m), 1969 (m), 1943 (s), 1894 (m), 1867 (s), 1602 (w), 1469 (m), 1439 (w), 1255 (w), 1158 (w), 1124 (w), 1067 (w), 1014 (w), 961 (w), 758 (s), 730 (s), 680 (m), 650 (w), 634 (m), 617 (w), 585 (s)
3	2072 (s), 2001 (w), 1957 (m), 1940 (s), 1883 (m), 1875 (s), 1594 (w), 1496 (w), 1454 (w), 1419 (w), 1244 (w), 1145 (w), 1130 (w), 869 (w), 840 (w), 829 (m), 817 (m), 787 (w), 747 (m), 738 (m), 676 (w), 649 (w), 583 (s)
4	2072 (s), 1956 (s), 1946 (s), 1947 (s), 1893 (s), 1868 (s), 1688 (m), 1573 (m), 1549 (w), 1510 (m), 1493 (w), 1449 (w), 1420 (w), 1393 (w), 1342 (w), 1302 (w), 1257 (s), 1218 (m), 1077 (m), 1033 (w), 933 (w), 894 (m), 858 (m), 833 (s), 779 (w), 742 (m), 697 (m), 674 (m), 634 (m), 583 (m), 531 (m), 505 (m)

C. Mass spectra

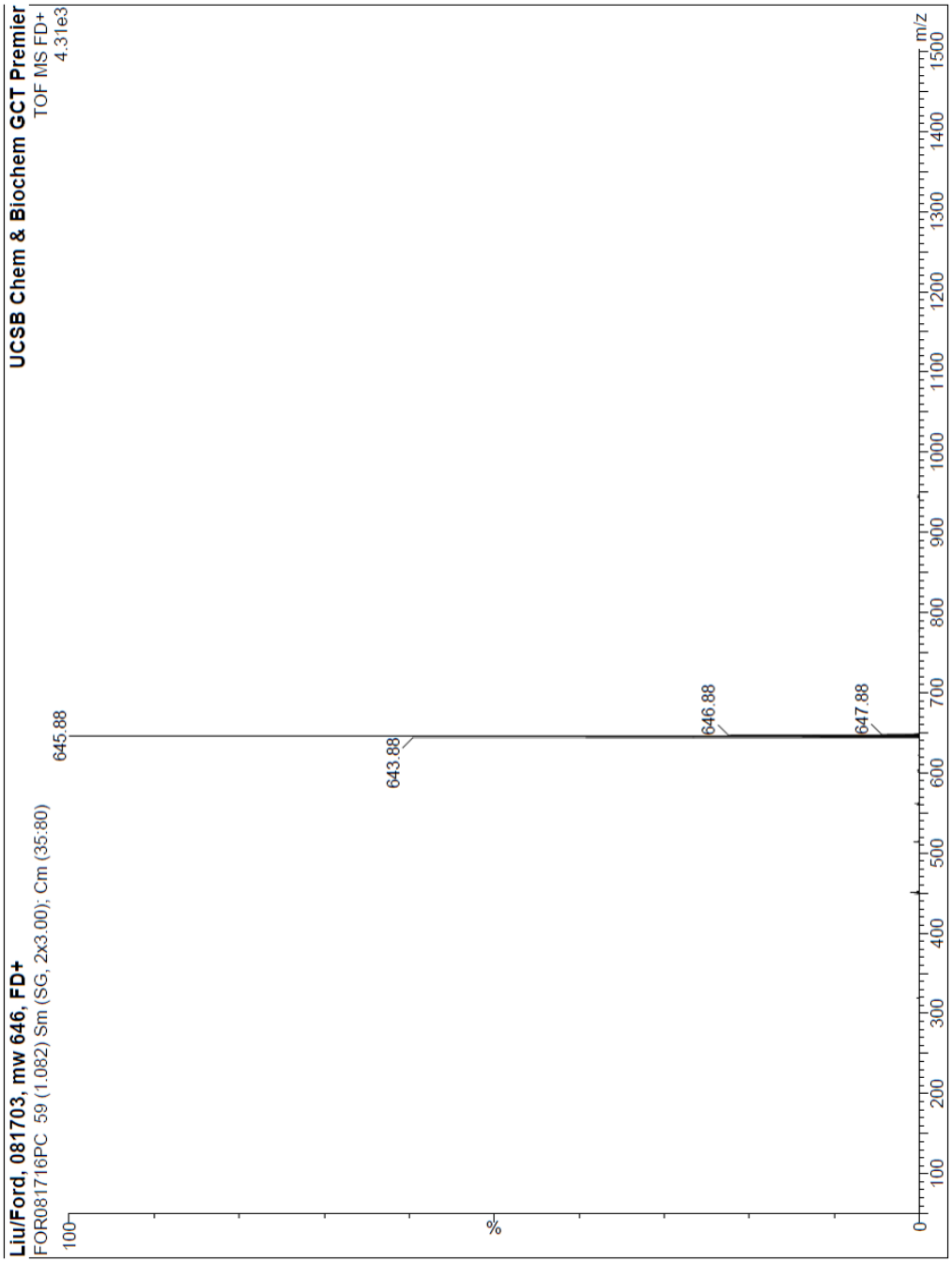

Figure 3.16 FD+ Mass spectrum of **1.** Molar mass: 645.88 m/z; Calculated: 645.92 m/z.

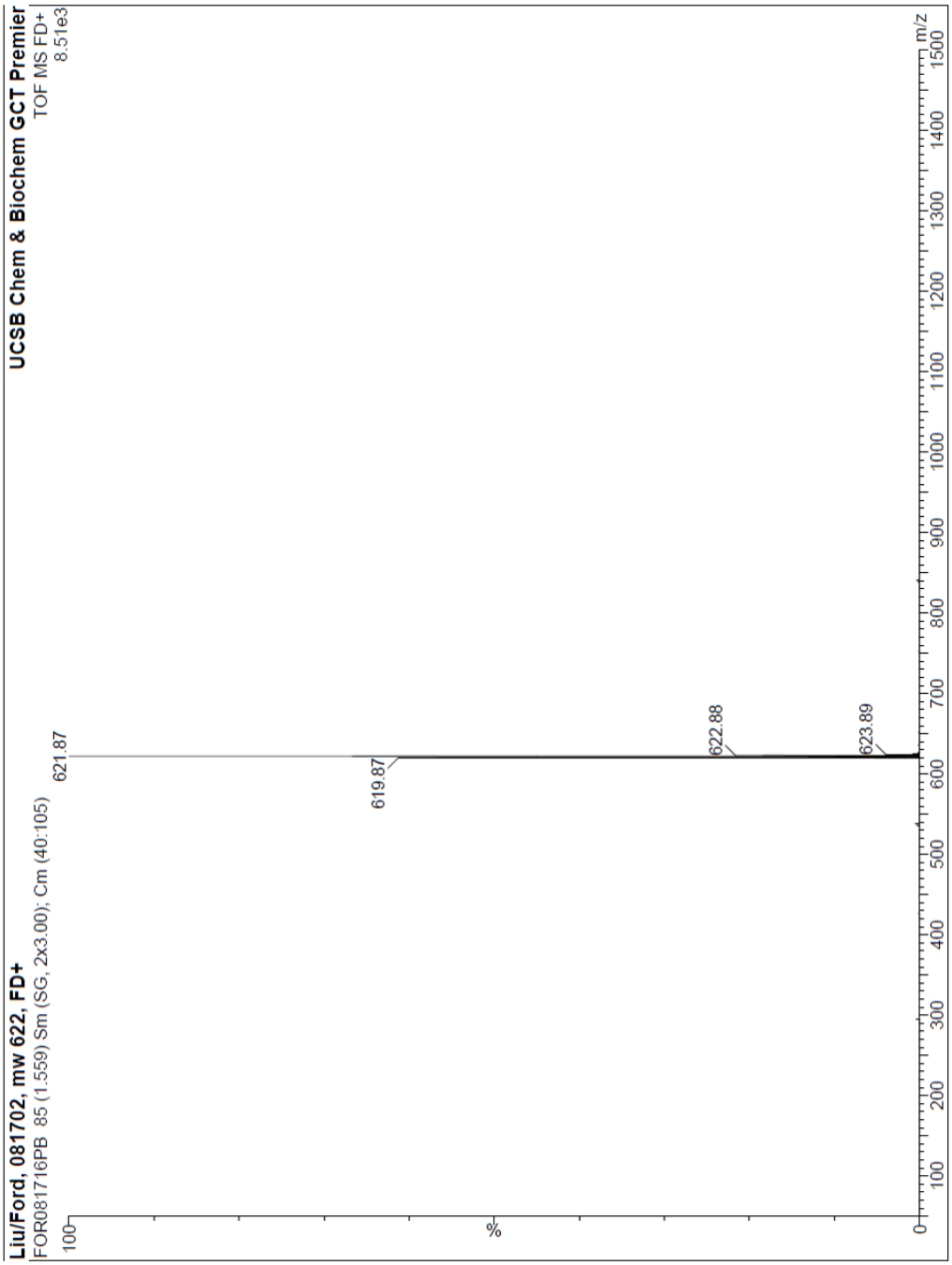

Figure 3.17 FD+ Mass spectrum of **2**. Molar mass: 621.87 m/z; Calculated: 621.92 m/z.

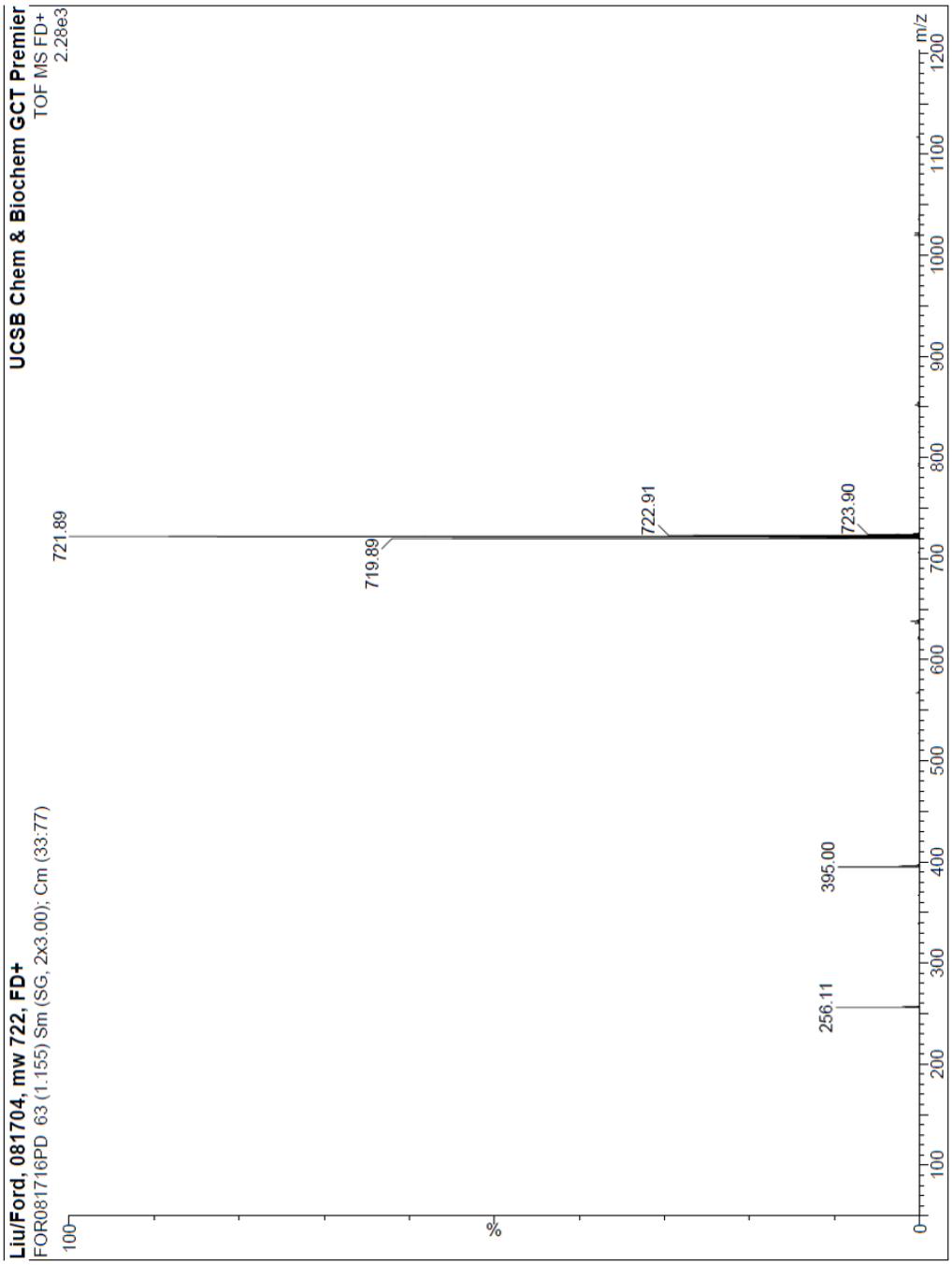

Figure 3.18 FD+ Mass spectrum of **3**. Molar mass: 721.89 m/z; Calculated: 721.95 m/z.

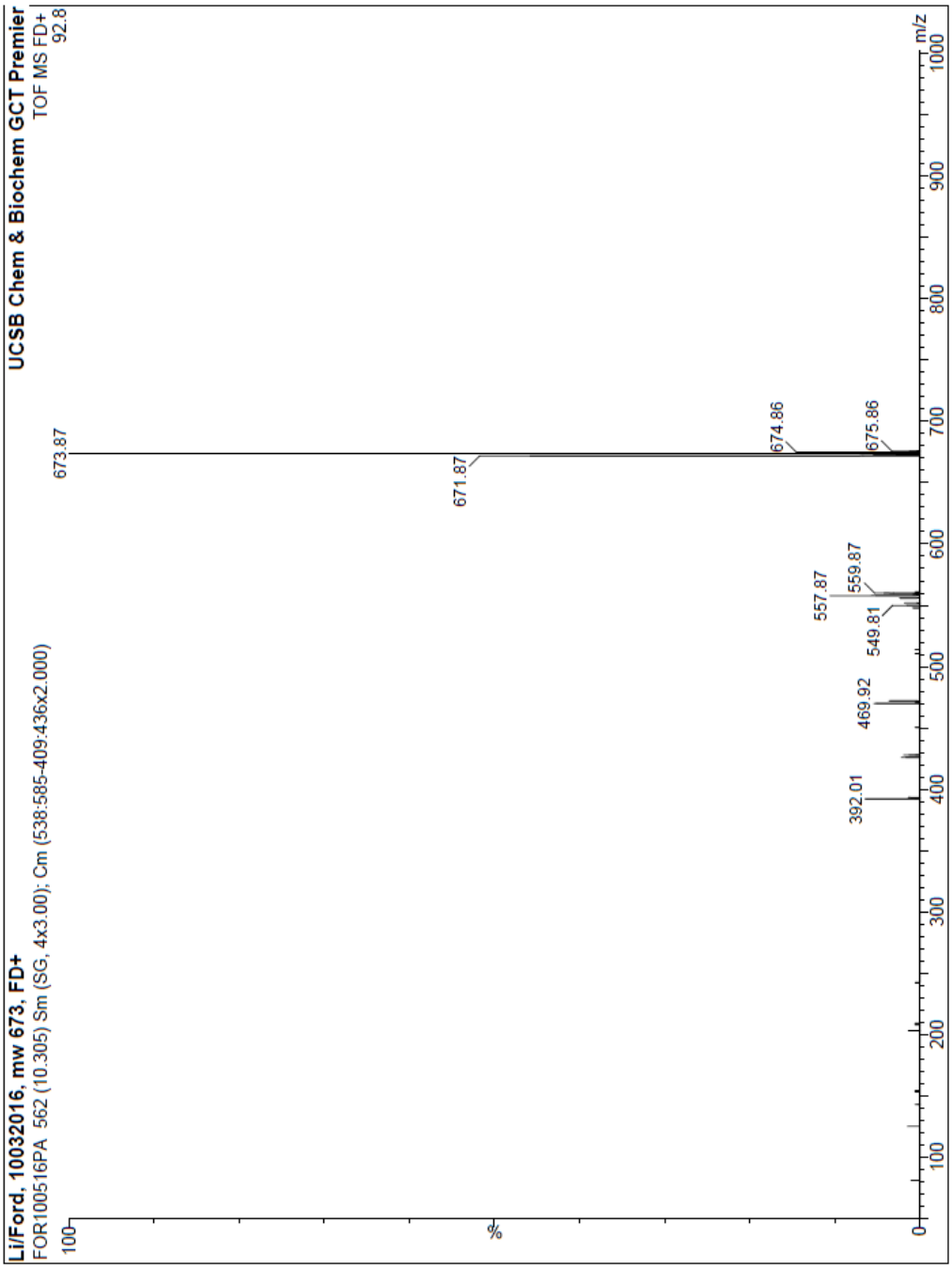

Figure 3.19 FD+ Mass spectrum of **4**. Molar mass: 673.87 m/z; Calculated: 673.92 m/z

D. Electronic absorption spectra

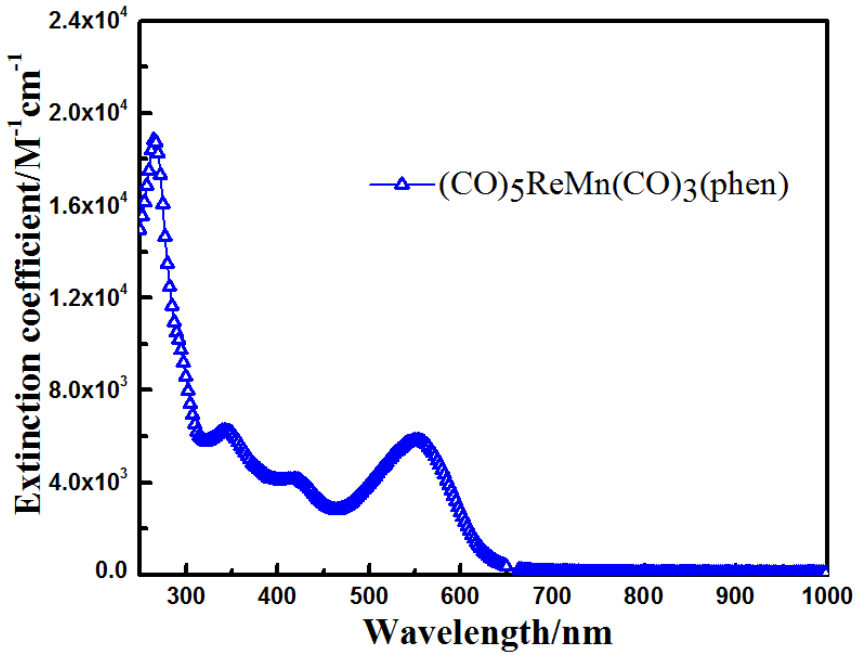

Figure 3.20 The visible absorption spectra of **1** in ambient temperature, aerobic MeCN. The MMLCT λ_{max} extinction coefficient is 5.8 x10^3 M^{-1} cm^{-1}.

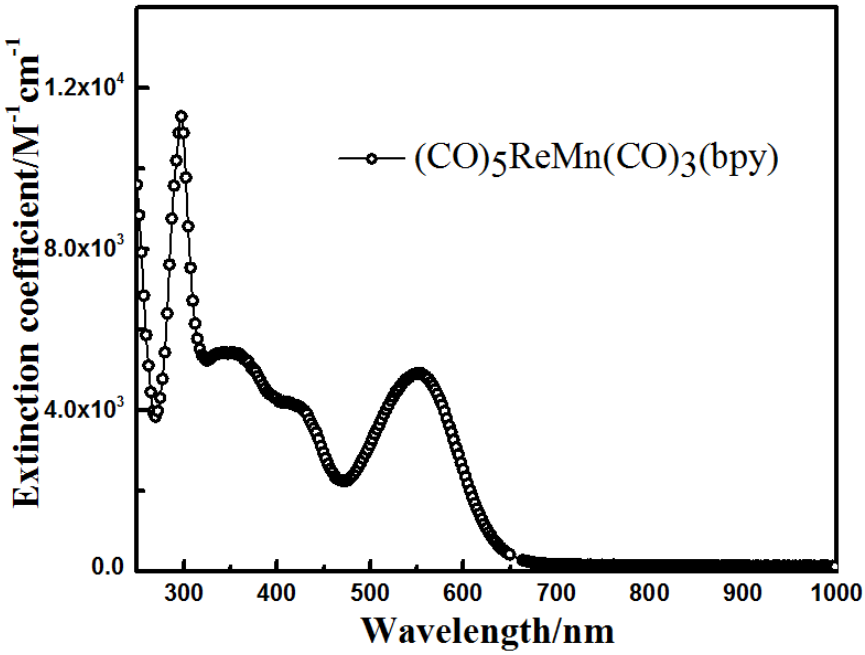

Figure 3.21 The visible absorption spectra of complexes **2** in ambient temperature, aerobic MeCN. The MMLCT λ_{max} extinction coefficient is 4.9 x10^3 M^{-1} cm^{-1}.

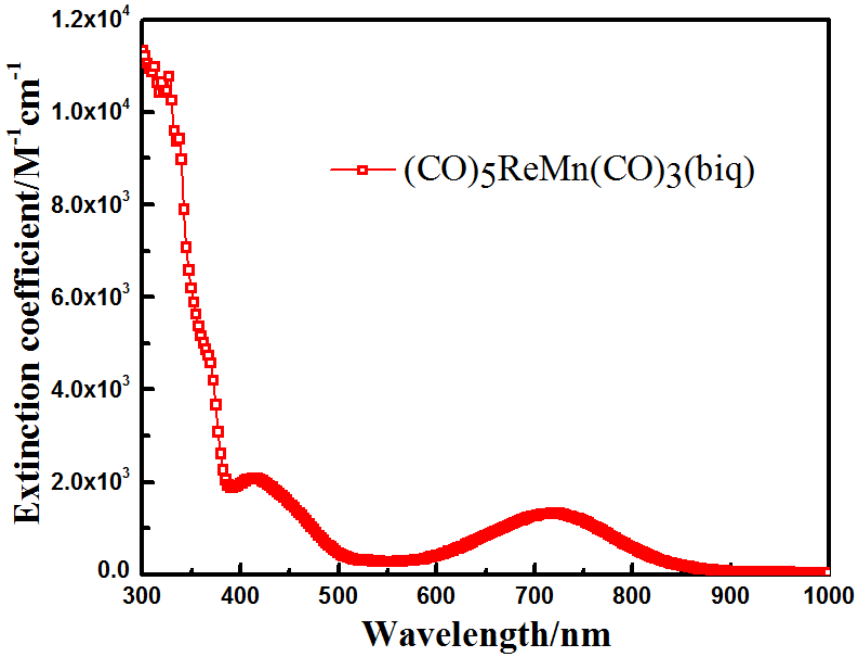

Figure 3.22 The visible absorption spectra of complexes **3** in ambient temperature, aerobic MeCN. The MMLCT λ_{max} extinction coefficient is 1.3 x10^3 M^{-1} cm^{-1}.

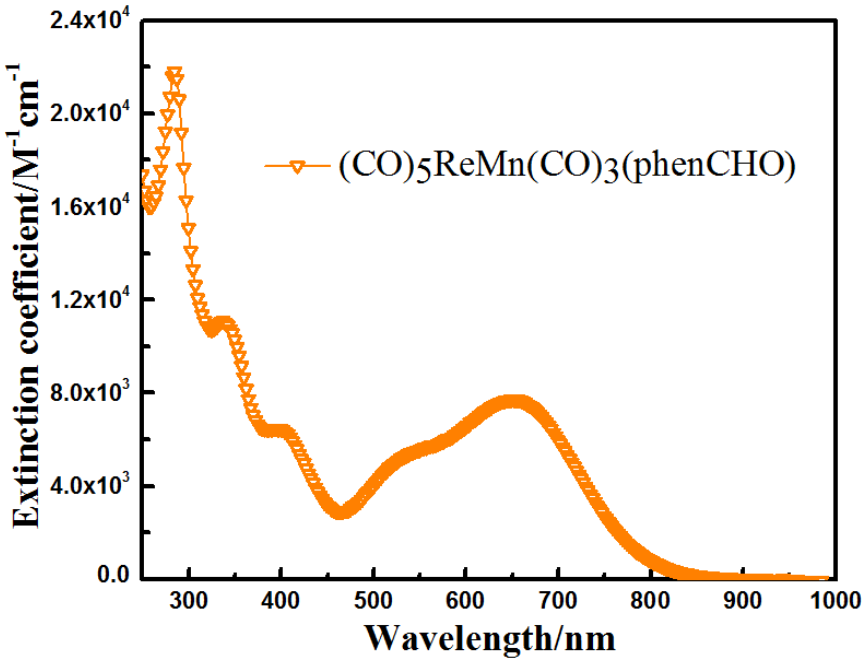

Figure 3.23 The visible absorption spectra of complexes **4** in ambient temperature, aerobic MeCN showing MMLCT λ_{max} extinction coefficient is 7.6 x 10^3 M^{-1} cm^{-1}.

Table 3.2 Uv-vis absorption data for compounds **1**-**4**[a]

Compound	Uv-vis absorption λ_{max} in nm (ε in $M^{-1}cm^{-1}$)
1	341 (6260), 417 (4125), 550 (5824)
2	341 (5427), 415 (4130), 550 (4904)
3	366 (4788), 415 (2095), 719 (1330)
4	286 (21808), 338 (11092), 399 (6446), 543 (5462), 652 (7658)

[a] Solvent: acetonitrile

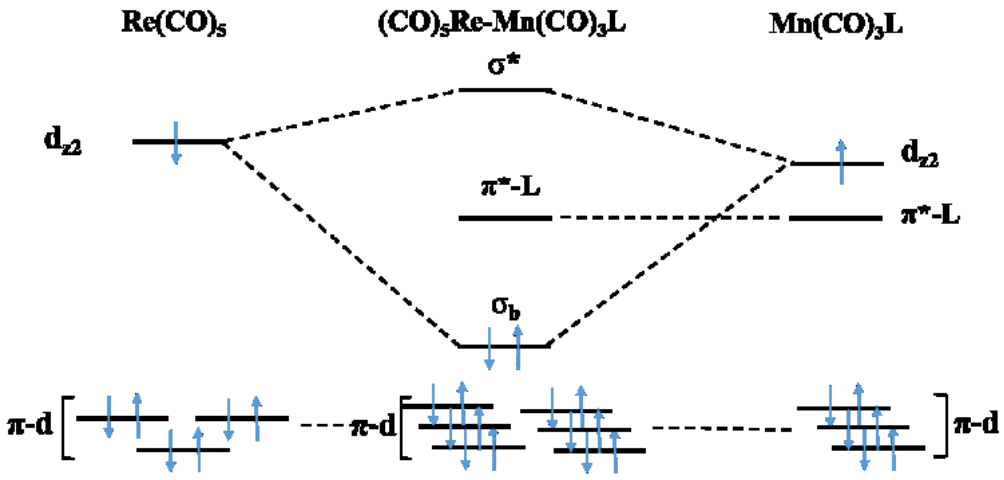

Figure 3.24 Qualitative molecular orbital diagram for dinuclear metal carbonyls.[24]

To explain the electronic transitions difference between **1** and **4**, which have similar chemical structures, DFT and TD-DFT computations were performed with Spartan'14 software packages at unrestricted B3LYP/6-31G* (LANL2DZ>Kr) level of theory without symmetry constraints (Fig 3.25 to 3.28).

TD-DFT calculation of **1** shows that the strong absorption band at 560 nm is corresponding to HOMO to LUMO transition. From Fig. 3.26, it is confirmed that the nature of HOMO to LUMO transition is $\sigma_{MM} \rightarrow \pi_L^*$. The HOMO is centered between Re and Mn

bond and the LUMO is localized on phenanthroline ligand. Compound **4** has similar HOMO (σ_{MM}) to **1** but has two π antibonding orbitals with large energy difference due to aldehyde group substitution. The higher energy π antibonding orbital (LUMO+1) is localized on phen moiety while lower one (LUMO) is more on the aldehyde (Fig. 3.28). Therefore 543 nm band is corresponding to the HOMO to LUMO+1 transition while 652 nm is the HOMO to LUMO transition.

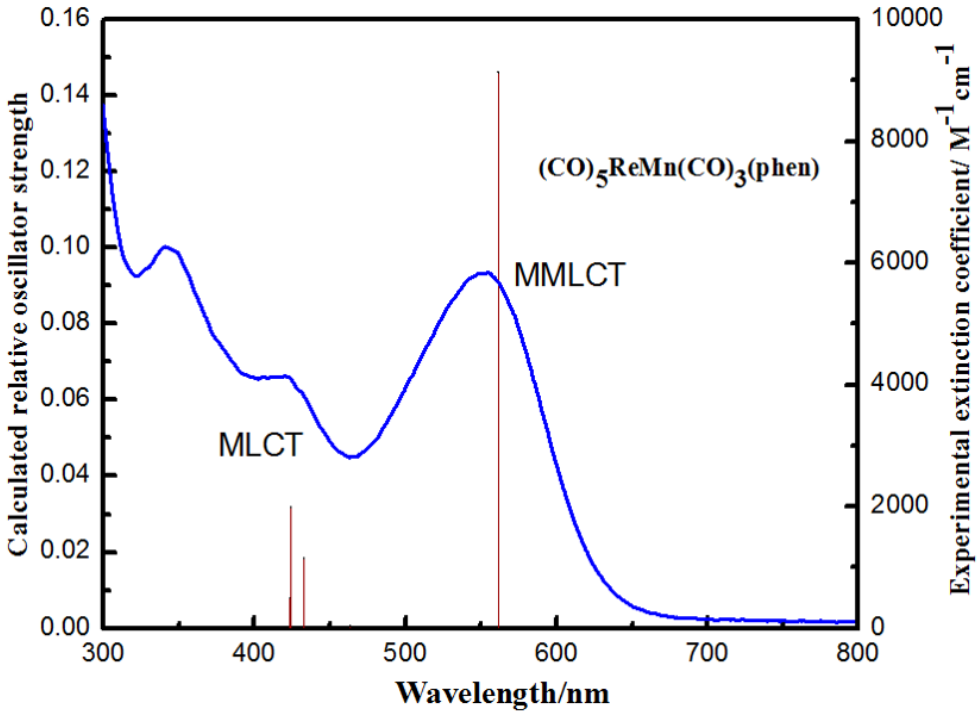

Figure 3.25 Experimental electronic absorption spectrum of **1** (blue) and its TD-DFT calculated electronic transition (red lines).

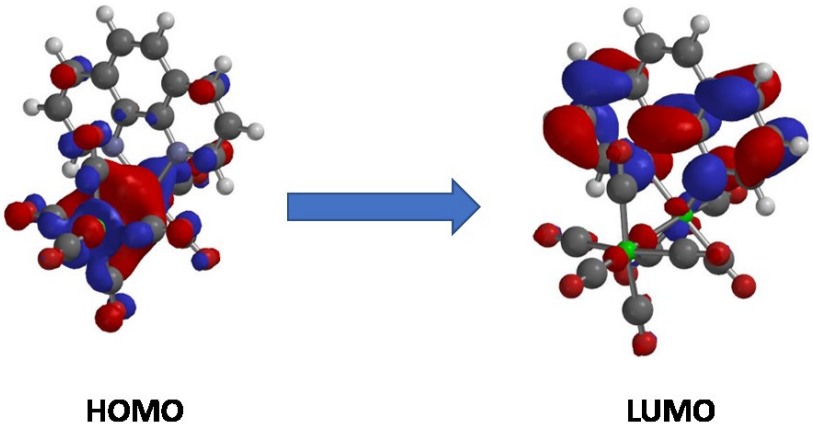

Figure 3.26 TD-DFT calculation of the HOMO and LUMO orbitals of compound **1**

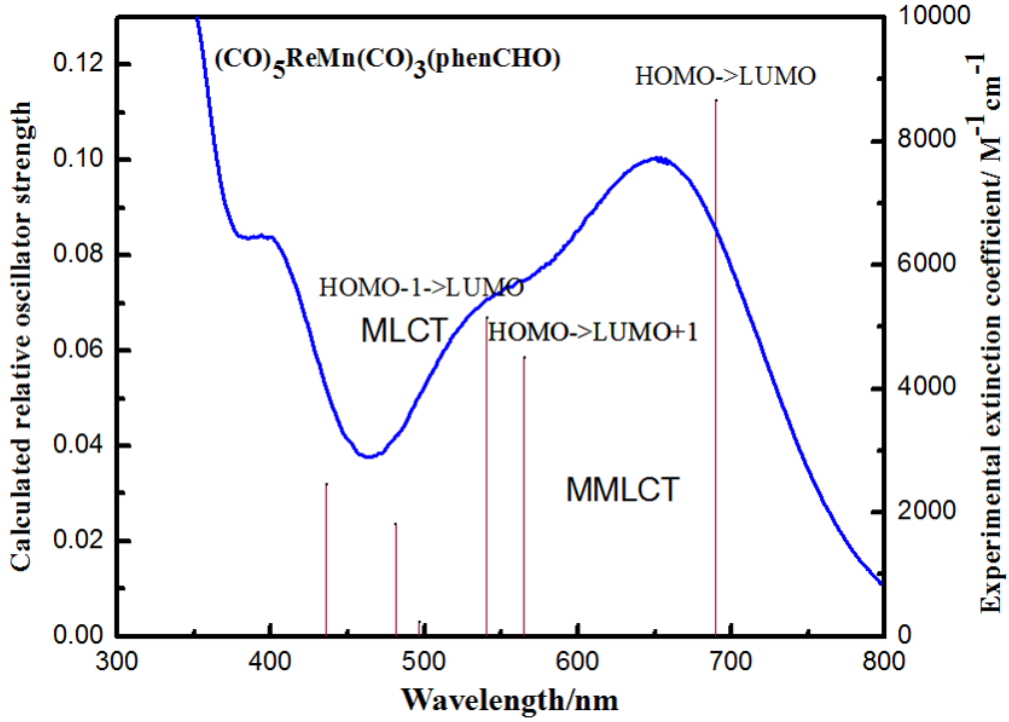

Figure 3.27 Experimental electronic absorption spectrum of **4** (blue) and its TD-DFT calculated electronic transition (red lines).

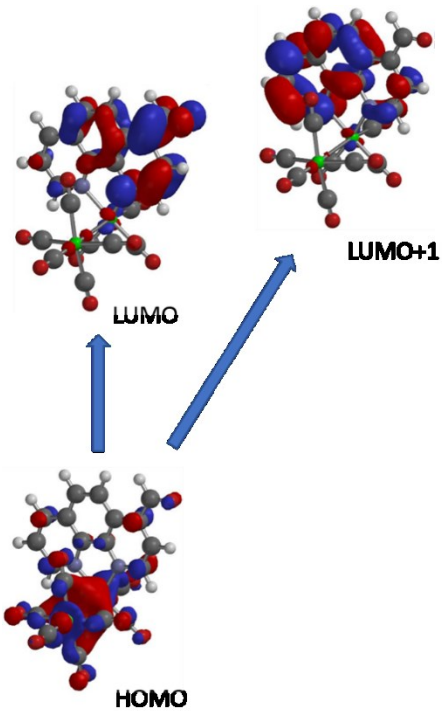

Figure 3.28 TD-DFT calculation of the HOMO, LUMO and LUMO+1 orbitals of compound **4**

E. Crystal structures

The solid state crystal structures of $(CO)_5ReMn(CO)_3(phen)$ (**1**), $(CO)_5ReMn(CO)_3(bpy)$ (**2**), $(CO)_5ReMn(CO)_3(biq)$ (**3**), and $(CO)_5ReMn(CO)_3(phen\text{-}CHO)$ (**4**) were determined by X-ray diffraction on a Kappa Apex II single-crystal diffractometer.

X-ray suitable crystals of compound **1**-**4** were grown by dissolving the complex in a minimal amount of acetonitrile, and slowly evaporating to dryness. Crystals of **2** are simple orthorhombic, while those of **1**,**3** and **4** are triclinic. The structures determined from these studies are shown in Figure 3.29 to 3.32. Bond lengths and angles are summarized in Appendix A-D. For each complex, the three carbonyls on the Mn are in the *facial* configuration. The bpy and phen ligands are coplanar with the coordinating Mn; however, the

structure of **3** shows the plane of biq bending toward metal-metal bond, perhaps to relieve steric crowding. Notably, the Re-Mn bond length in **3** (3.066 Å) is somewhat longer than those in **1**, **2** and **4** at 3.005 Å (ave), 3.020 Å (ave) and 2.998 Å, respectively.

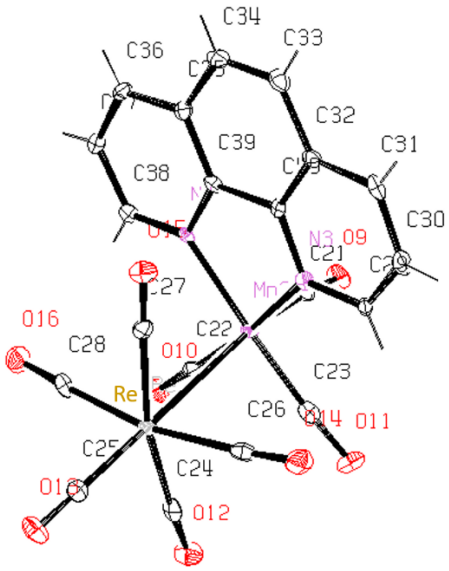

Figure 3.29a. ORTEP drawing of the x-ray structure of $(CO)_5ReMn(CO)_3(phen)$ (**1**) (Shown with 50% thermal ellipsoids)

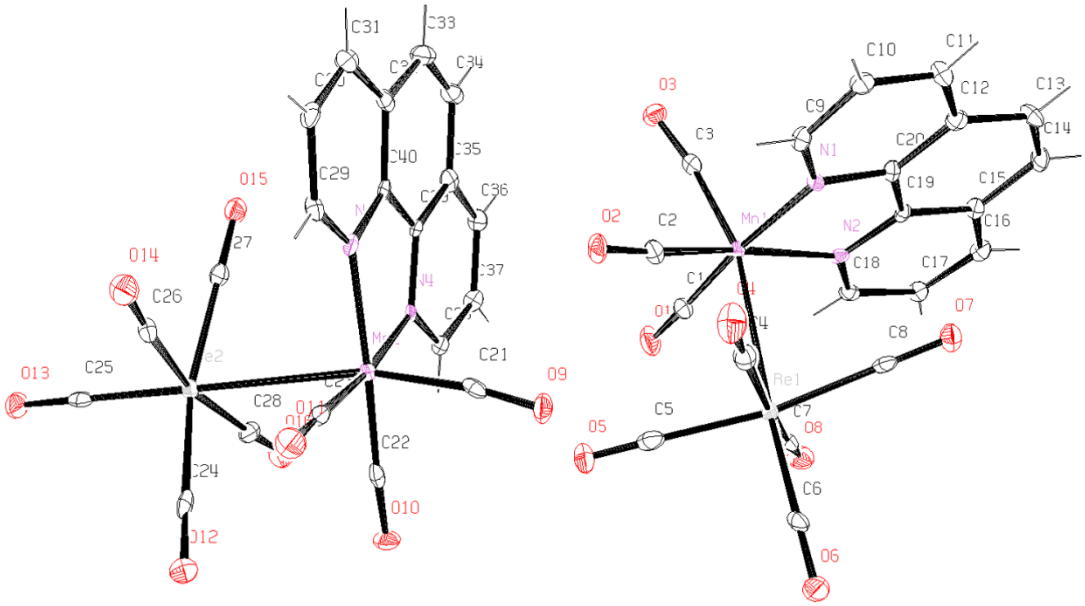

Figure 3.29b Unit cell ORTEP drawing of the x-ray structures of $(CO)_5ReMn(CO)_3(phen)$ (**1**) (Shown with 50% thermal ellipsoids and unit cell includes two independent molecules)

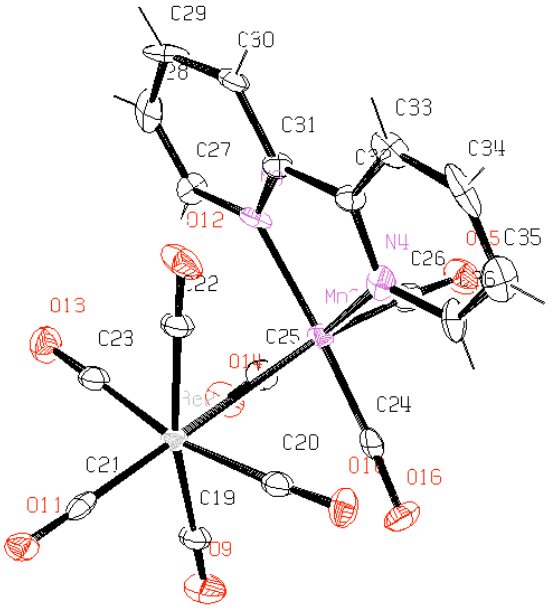

Figure 3.30a ORTEP drawing of the x-ray structures of $(CO)_5ReMn(CO)_3(bpy)$ (**2**) (Shown with 50% thermal ellipsoids).

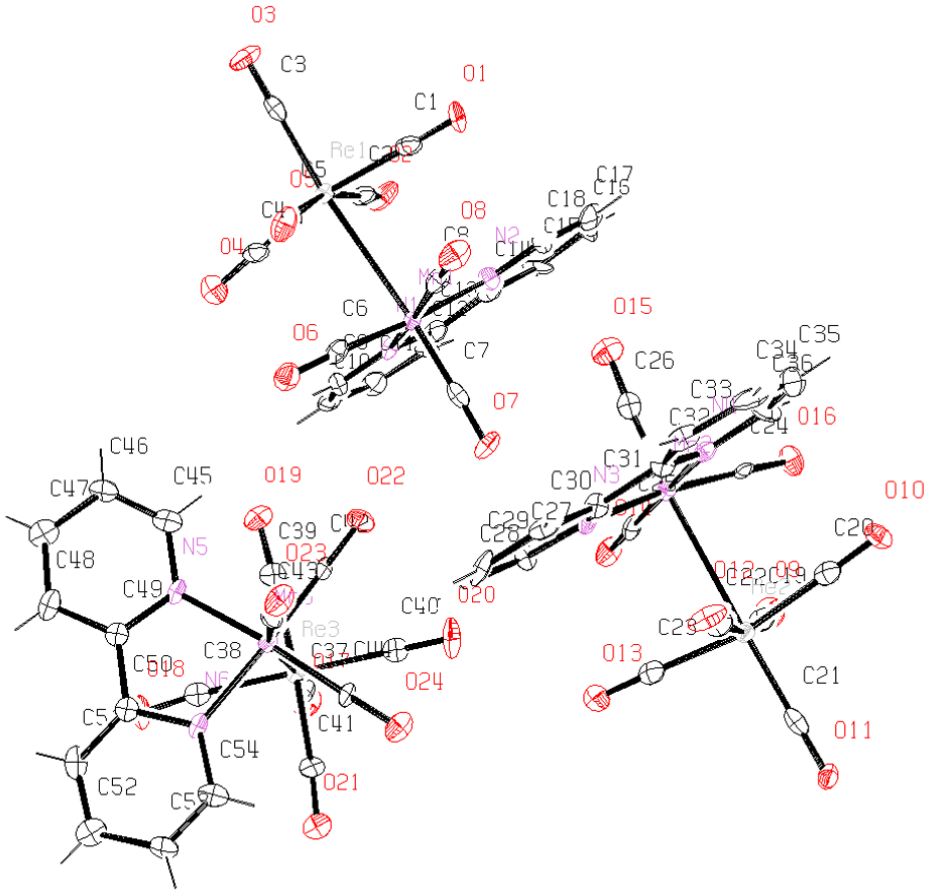

Figure 3.30b Unit cell ORTEP drawing of the x-ray structure of $(CO)_5ReMn(CO)_3(bpy)$ (**2**) (Shown with 50% thermal ellipsoids and unit cell includes three independent molecules)

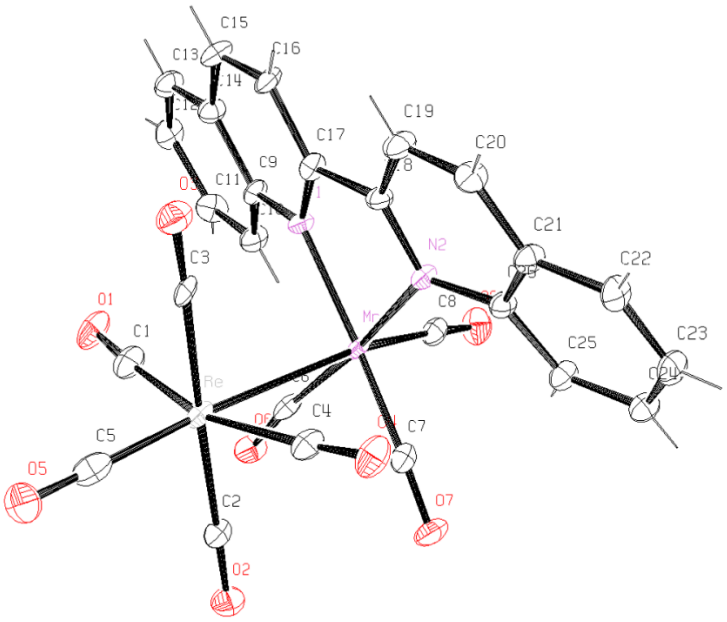

Figure 3.31 ORTEP drawing of the x-ray structures of $(CO)_5ReMn(CO)_3$(biq) (**3**) (with 50% thermal ellipsoids).

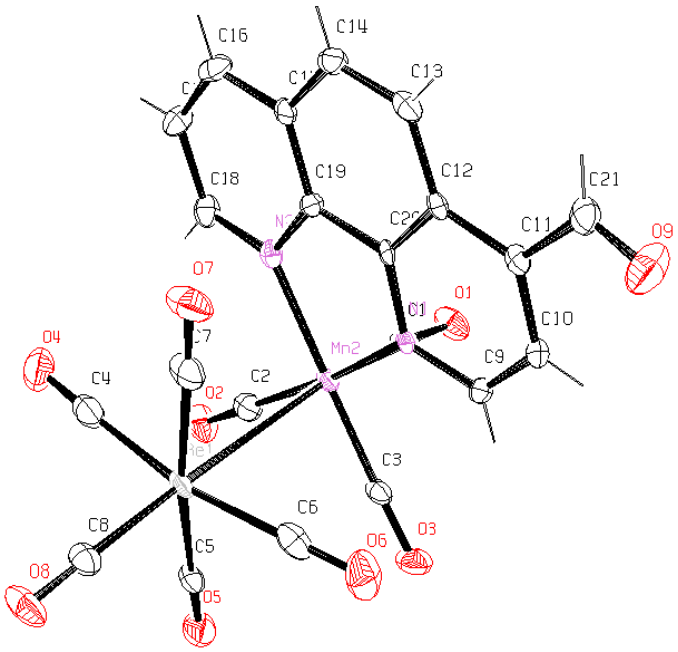

Figure 3.32 ORTEP drawing of $(CO)_5ReMn(CO)_3$(phenCHO) (**4**) (with 50% thermal ellipsoids).

IV. Photochemical study of 1-5

A. Stability in dark

Aerobic MeCN solutions of **1**, **2** and **4** show good stability at 37 ºC when kept in the dark. This was evidenced by very small (≤ 6%) changes of the MMLCT absorbance of **1** and **2** over a 16 h period and less than 20% change in **4** over 12 h period in either aerobic or anaerobic solution (Fig. 3.33 to 3.37). In contrast, an aerobic MeCN solution of the biq complex **3** proved to be less stable with the absorbance at the MMLCT λ_{max} decreasing about 50% over 16 h time period at 37 ºC. In anaerobic solution, however, the change is smaller (19%) over the same time period. This instability may be the result of the extra crowding from the sterically more bulky biq ligand, a feature that was also reflected in the longer Re-Mn bond (3.066 Å).

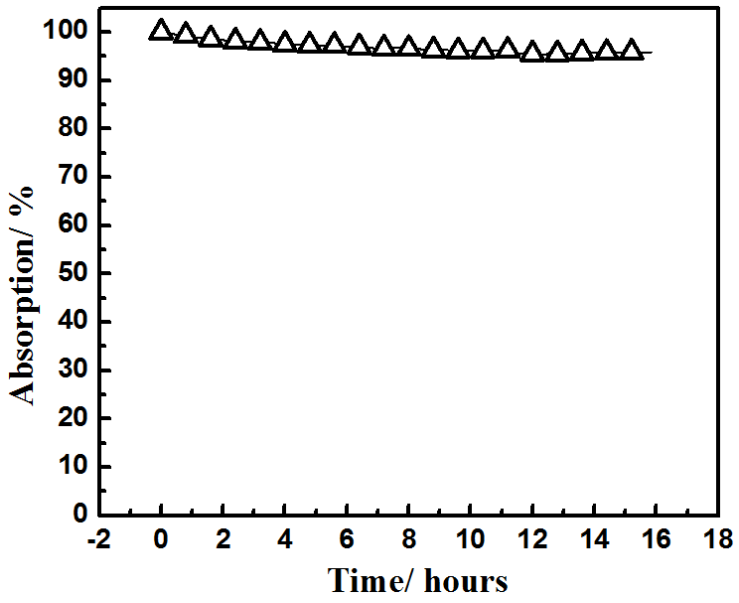

Figure 3.33 Normalized absorbance at the λ_{max} for the MMLCT band of aerobic **1** in MeCN at ~37 ºC over the course of 16 hours (95% remained after 16 hours).

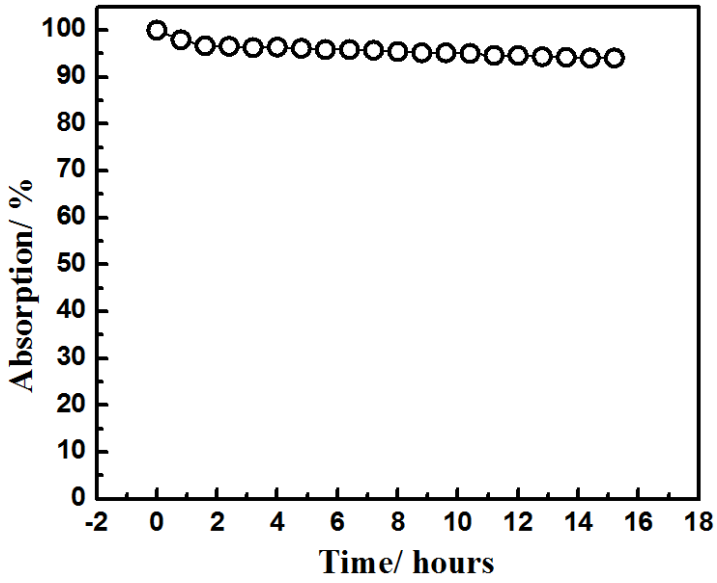

Figure 3.34 Normalized absorbance at the λ_{max} for the MMLCT band of aerobic **2** in MeCN at ~37 ºC over the course of 16 hours (94% remained after 16 hours).

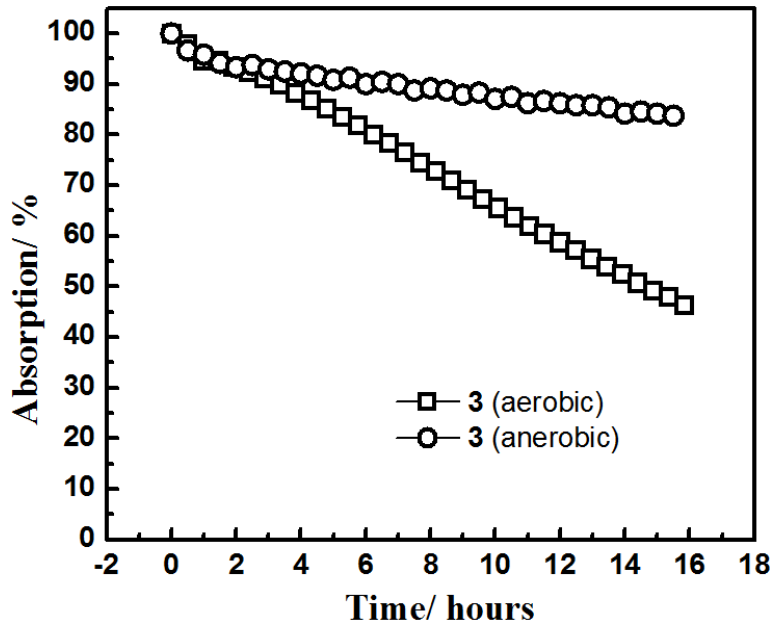

Figure 3.35 Normalized absorbance at the λ_{max} for the MMLCT band of aerobic **3** (rectangle) and anaerobic **3** (circle) in MeCN at ~37 ºC over the course of 16 h (46% remained for aerobic and 84% for anaerobic after 16 hours).

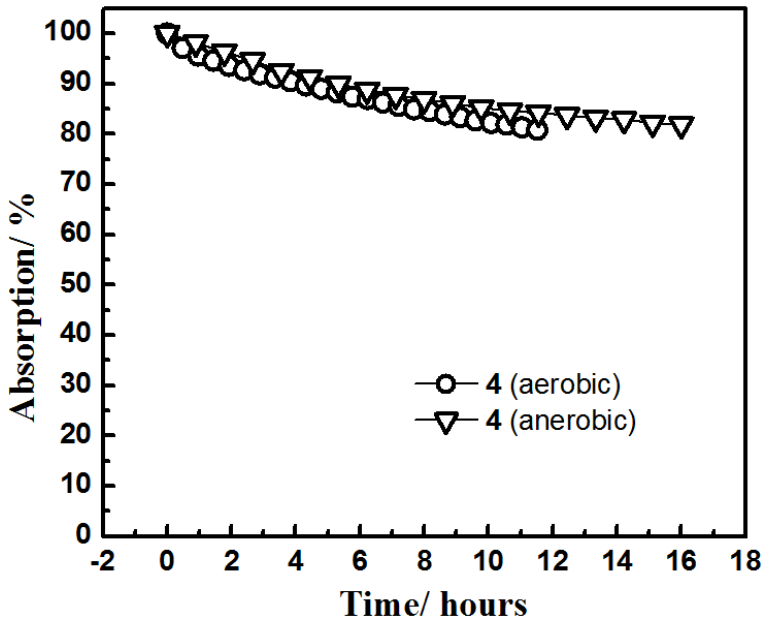

Figure 3.36 Normalized absorbance at the λ_{max} for the MMLCT band of aerobic **4** (circle) and anaerobic **4** (triangle) in MeCN at ~37 ^{o}C over the course of 12-16 h (81% remained for aerobic and 84% for anaerobic after 12 hours).

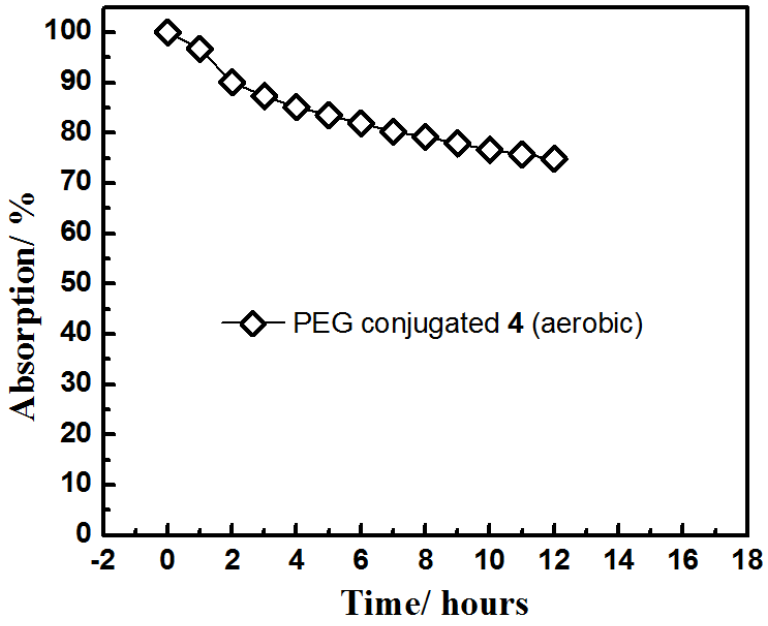

Figure 3.37 Normalized absorbance at the λ_{max} for the MMLCT band of PEG conjugated **4** in aerobic pH 7.4 PBS solution over the course of 12 h (75% remained after 12 hours).

B. Photochemical studies of $(CO)_5ReMn(CO)_3(phen)$ (1)

Initial photochemical experiments largely focused on the phen complex **1.** The MMLCT band (λ_{max} 550 nm) of **1** tails to longer wavelengths, so its photochemistry could be investigated using a deep red LED operating at 659 nm (Chapter 2, Fig. 2.5 and table 2.2), where the extinction coefficient (ε_{659}) for **1** is 315 M^{-1} cm^{-1} in MeCN. Exhaustive 659 nm photolysis of **1** in aerobic solution fully bleached the MMLCT band (Fig. 3.38) as well as bands at 341 and 417 nm attributed to $\sigma_{MM} \rightarrow \sigma_{MM}^*$ and $d\pi \rightarrow \pi_L^*$ transitions. The final color of the solution was a faint yellow. When the photolysis was conducted in a Schlenk cuvette,[10] and the gas phase was sampled after exhaustive photolysis, GC-TCD analysis indicated the release of CO. However, owing to the lower sensitivity of this technique, quantitative CO analysis was done with much higher concentrations.

When analogous 659 nm photolysis of **1** was carried out in anaerobic MeCN solution, the pattern of spectral changes was considerably different (Fig. 3.39). Although the MMLCT band at 550 nm disappeared, a new, longer wavelength band appeared at ~761 nm. Based on the literatures, this observation suggests the formation of the dimanganese compound $Mn_2(CO)_6(phen)_2$ (**6**) via photoinduced cleavage of the Re-Mn bond in **1** followed by homonuclear coupling of $Mn(CO)_3(phen)$ radicals (Scheme 3.1).[26,27] The 761 nm MMLCT band of the putative $Mn_2(CO)_6(phen)_2$ (**6**) remained unchanged under further 659 nm irradiation, suggesting that photolytic cleavage of **6** is followed by a rapid back reaction. The

other expected homonuclear coupling product $Re_2(CO)_{10}$ does not display a visible range absorbance (Fig. 3.40) and would not be susceptible to secondary photolysis at 659 nm. These results clearly imply that, in aerobic solutions, dioxygen efficiently traps such free radicals and therefore prevents reformation of M-M bonds.

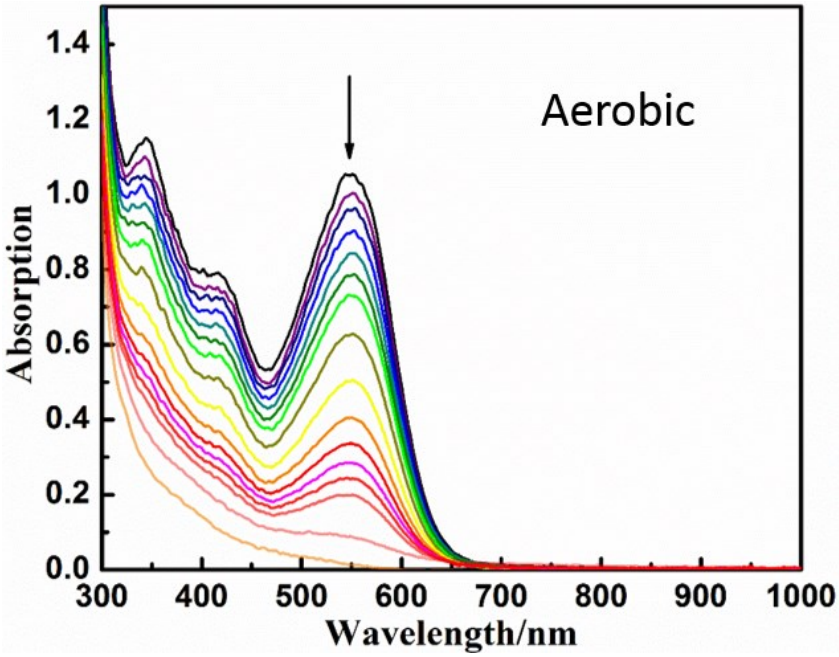

Figure 3.38 Absorption changes resulting from 659 nm photolysis of (25 mW) of dinuclear compound **1** (1.65×10^{-4} M) in aerobic MeCN.

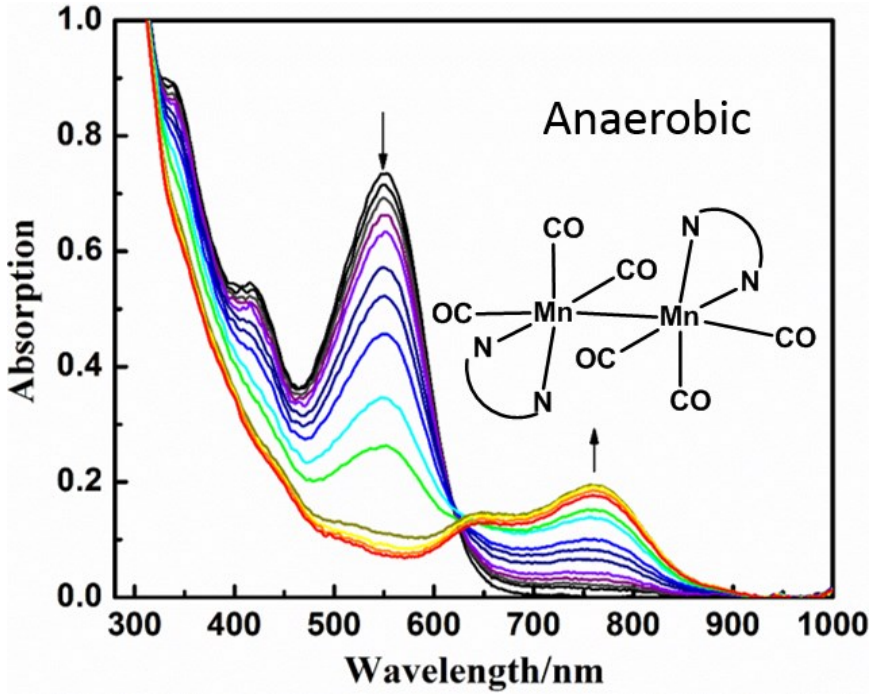

Figure 3.39 Absorption changes resulting from 659 nm photolysis (25 mW) of compound **1** (1.22×10^{-4} M) in anaerobic MeCN.

Scheme 3.1 Proposed redistribution of dinuclear species after MMLCT excitation of **1** at 659 nm. the Mn dimer remains susceptible to photolysis at this λ_{irr} while the Re dimer does not absorb at this longer wavelength.

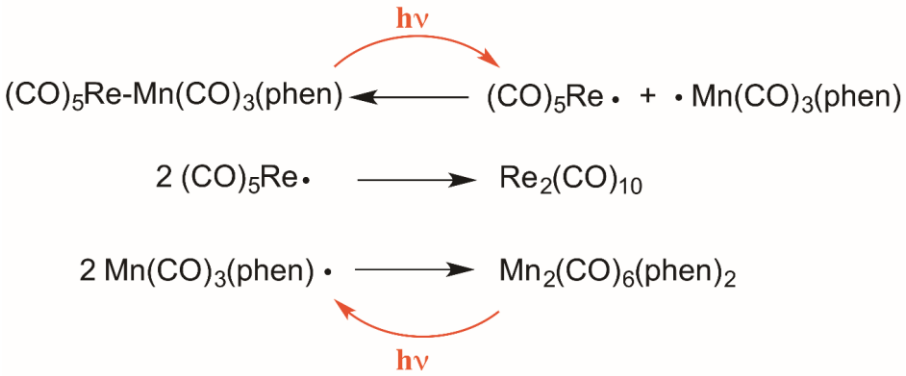

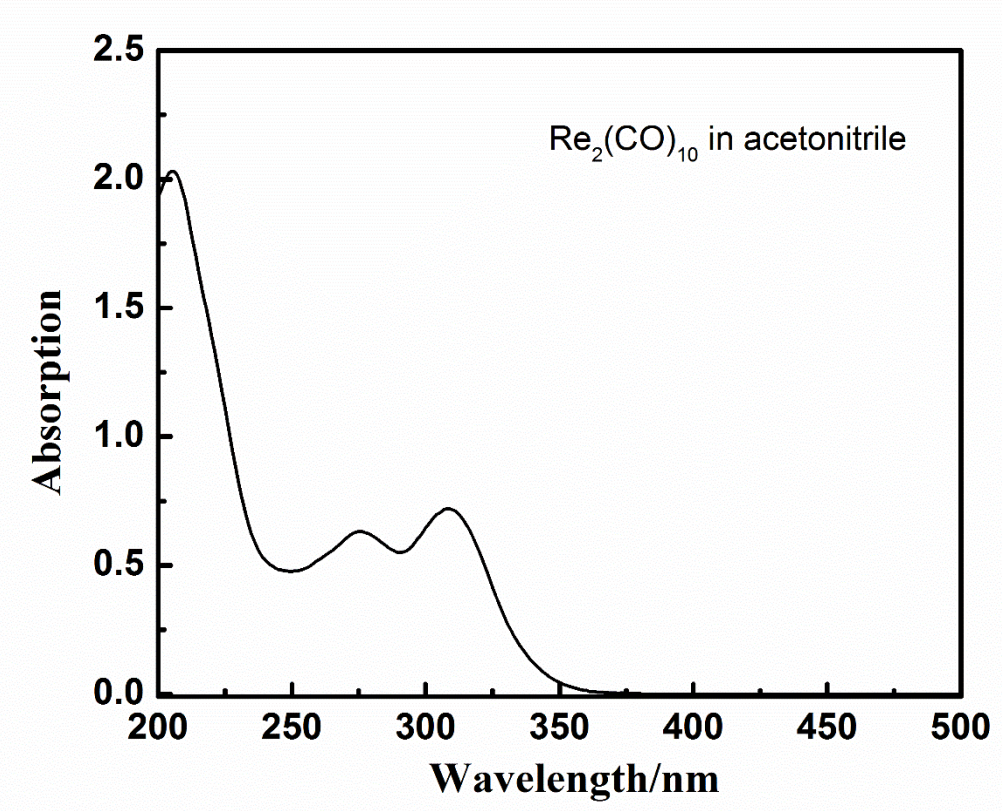

Figure 3.40 Electronic spectrum of $Re_2(CO)_{10}$ (4.6×10^{-4} M) in acetonitrile.

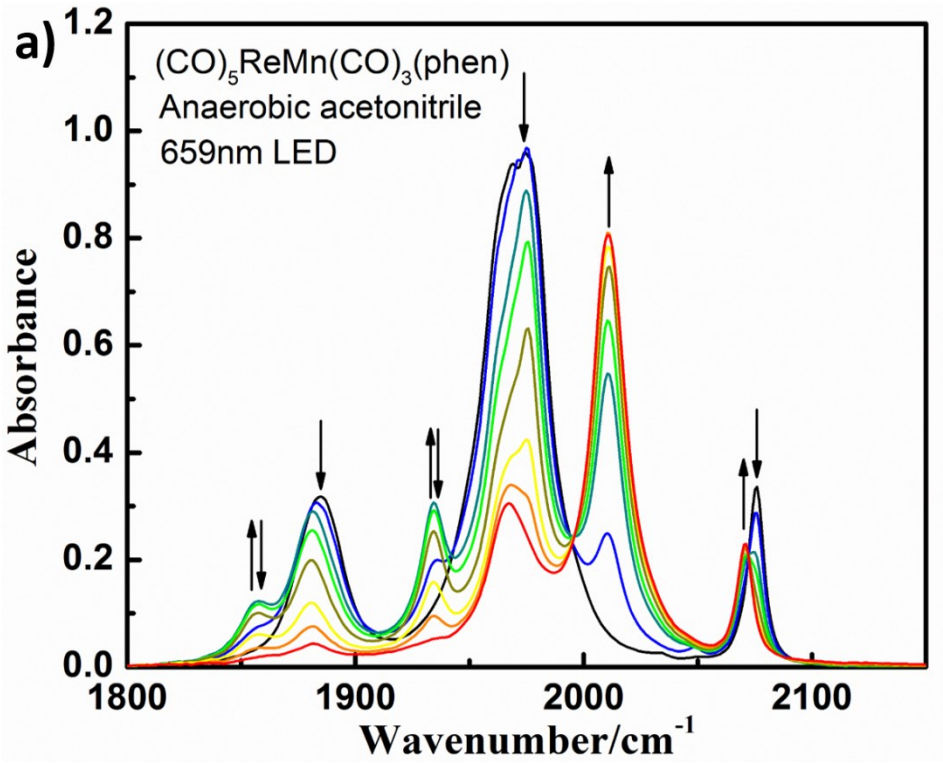

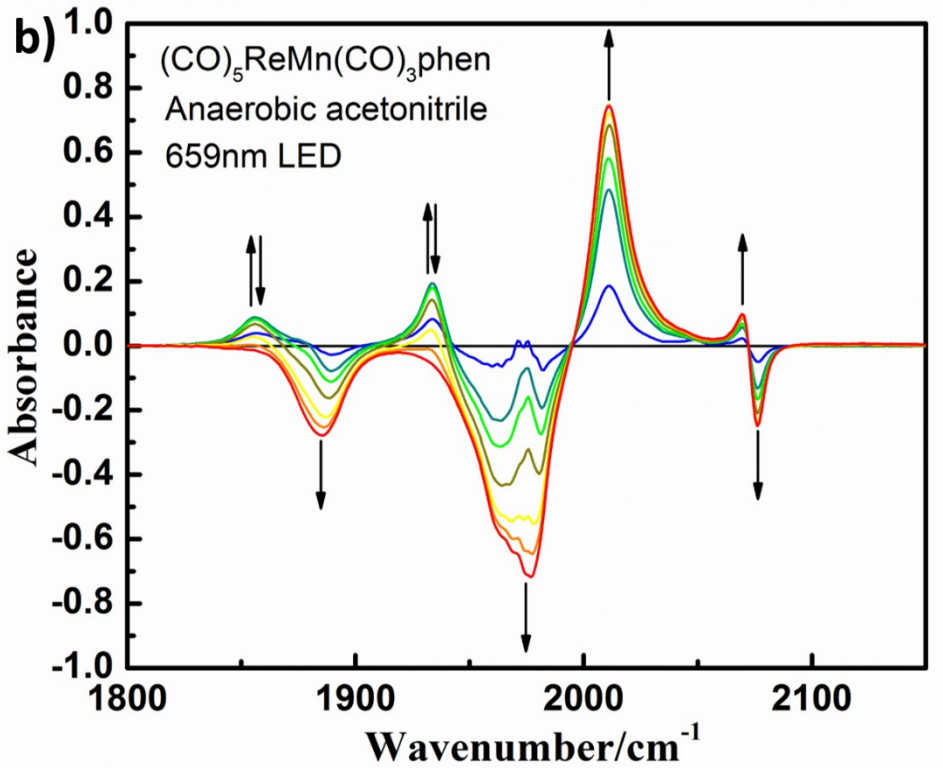

Figure 3.41 IR a) spectral changes and b) difference spectra upon 659 nm photolysis of **1** (4.6 mM) in anaerobic MeCN in a 0.1 cm pathlength KBr cell.

The $Mn_2(CO)_6(phen)_2$ photoproduct was better characterized by examining infrared spectral changes. A freeze-pump-thaw deaerated MeCN solution of **1** (4.6 mM) was transferred under argon to a KBr IR cell, which was then sealed with Teflon plugs in an inert atmosphere glove box. This solution was then photolyzed with the 659 nm LED, and the IR spectral changes were periodically recorded (Fig. 3.41a). Before photolysis, the spectrum of **1** displayed ν_{CO} bands at 1884, 1975 and 2076 cm^{-1}. During irradiation at 659 nm, new bands characteristic of $Re_2(CO)_{10}$ appeared at 1968, 2009 and 2070 cm^{-1} that remained unchanged upon further photolysis (Fig. 3.41b). Synchronously, two lower frequency ν_{CO} bands appeared at 1857 and 1934 cm^{-1} that are close to bands previously observed in 2-methyl tetrahydrofuran for a species identified *in situ* as $Mn_2(CO)_6(phen)_2$.[21] The lower frequency ν_{CO} bands in the

homonuclear dimer relative to **1** may be attributed to Re having a higher electronegativity than Mn,[28] leading to polarization of the Re-Mn bond that draws electron density away from the Mn center in **1**. The latter two ν_{CO} bands did eventually disappear upon standing, an observation attributed to the imperfect seal of the IR cell and slow leakage of air into the system.

The assignment of $Mn_2(CO)_6(phen)_2$ draws further support from the 659 nm photolysis of **1** in deaerated CD_3CN solution in a sealed J Young NMR tube (Chapter 2: Figure 2.3). The ^1H NMR spectra were recorded before and after photolysis (Fig. 3.42) show that the four ^1H resonances characteristic of coordinated phenanthroline for the photolyzed product were all shifted to higher field compared to the analogous peaks in the spectrum of **1**. Only one new set of phen resonances is seen: δ = 7.98 ppm (d, J(H,H) = 7.8 Hz, 2H), 7.92 ppm (d, J(H,H) = 5.2 Hz, 2H), 7.76 ppm (s, 2H), 6.94 ppm (dd, J(H,H) = 7.4, 5.9 Hz, 2H), consistent with the formation of a symmetrical homonuclear dimer, and the upfield shift is consistent with greater Mn-to-phen backbonding in this product.

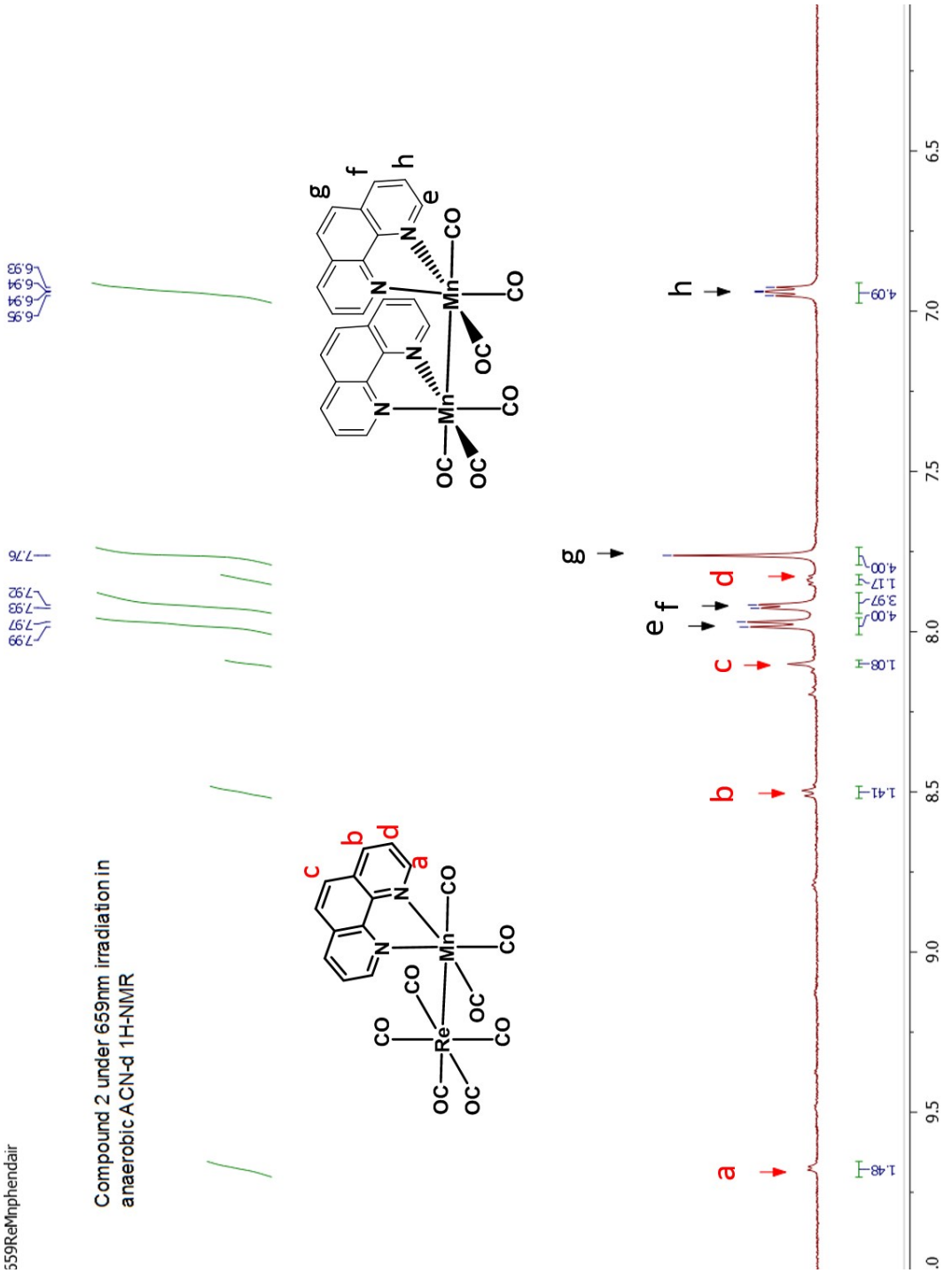

Figure 3.42 ^{1}H NMR spectrum (500 MHz, acetonitrile-d_3) of products in anaerobic CD_3CN after 659 nm photolysis (~30 mW) of **1** (2.31 mM) for 20 min. New set of protons resonance characteristic of **6**: δ = 7.98 ppm (d, J(H,H) = 7.8 Hz, 2H), 7.92 ppm (d, J(H,H) = 5.2 Hz, 2H), 7.76 ppm (s, 2H), 6.94 ppm (dd, J(H,H) = 7.4, 5.9 Hz, 2H).

In aerobic solution, 659 nm photolysis of **1** (2.8 mM) in an IR cell gave somewhat different results. The ν_{CO} bands for **1** decreased while those for $Re_2(CO)_{10}$ and $Mn_2(CO)_6(phen)_2$ appeared, but the latter were less intense than in anaerobic solution (Fig. 3.43). Differences included broadening of the bands at ~1867 cm^{-1} and appearance of a weak band at ~2120 cm^{-1}. Thus, under these conditions, O_2 trapping of radicals occurs but is incomplete presumably because the O_2 initially present in the sealed KBr cell (~1.7 mM)[29] is depleted in the early stages and not replenished.

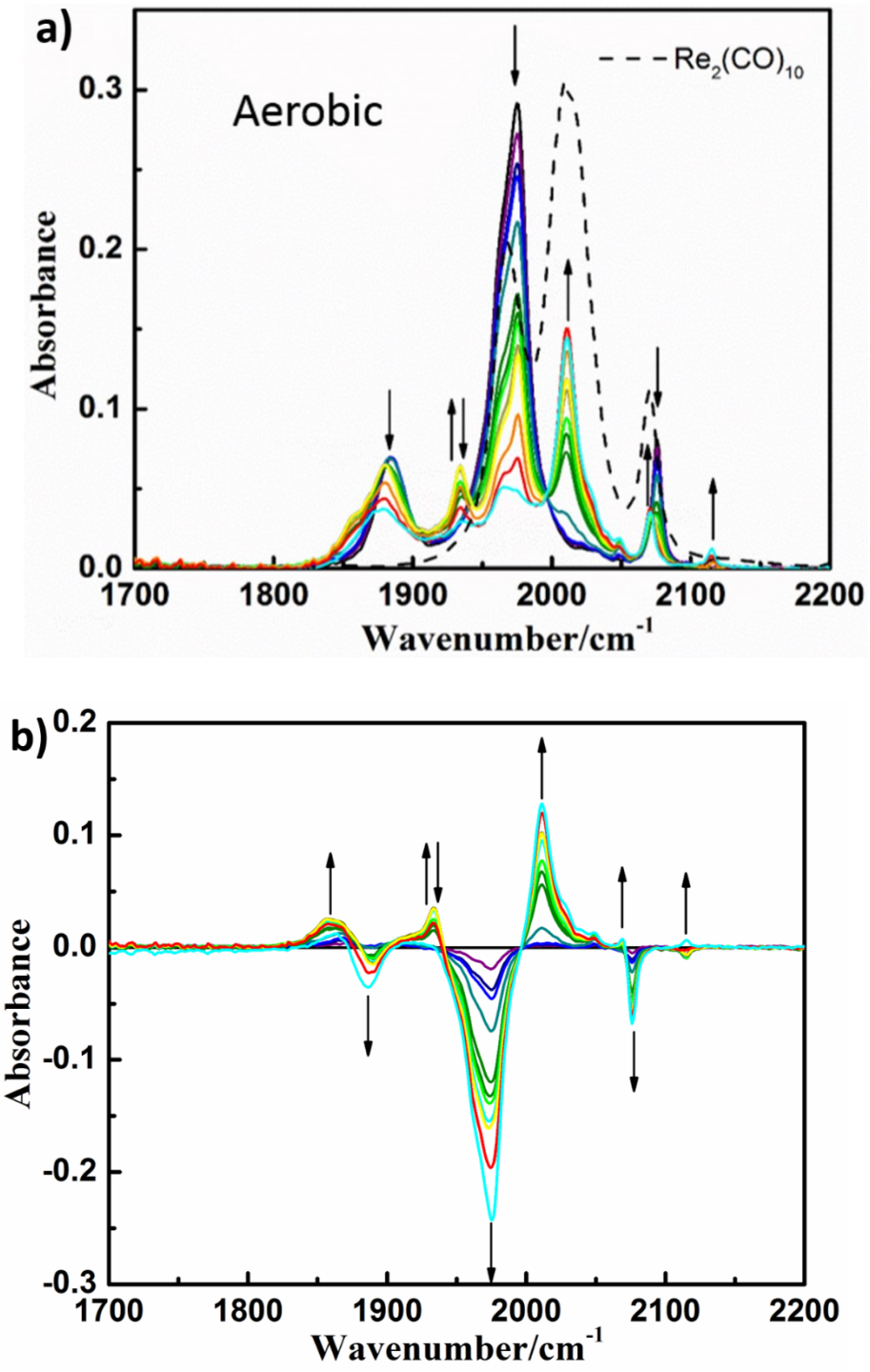

Figure 3.43 a) *Colored solid lines*: IR spectral changes upon 659 nm photolysis of **1** (2.75 mM) in aerobic MeCN in a 0.1 cm pathlength KBr cell. *Dashed line*: IR spectral of $Re_2(CO)_{10}$ in aerobic MeCN in a 0.1 cm pathlength KBr cell; b) Difference spectra of data displayed in a).

Fig. 3.44 illustrates the optical spectrum changes when the analogous photolysis of **1** was carried out in deaerated 90:10 MeCN:chloroform. Similar to the experiment under aerobic conditions, the MMLCT band at 550 nm was depleted, but no bands indicating formation of new dinuclear species were observed. These observations are consistent with Scheme 2; however, in this case, the radicals formed by photolytic cleavage of the Re-Mn bond would be trapped by the $CHCl_3$ (Scheme 3.2).[30] The absorption bands at 417 nm decreased in intensity but did not disappear, which would be expected, since the $d\pi \rightarrow \pi_L^*$ transition of $Mn(CO)_3(phen)Cl$ is also around 420 nm.[14] Although second order rate constants for the recombination d^7 metal carbonyl radicals are several orders of magnitude higher than those for trapping by halocarbons, the high chloroform concentration (~1.3 M) makes such trapping efficient.[30–32]

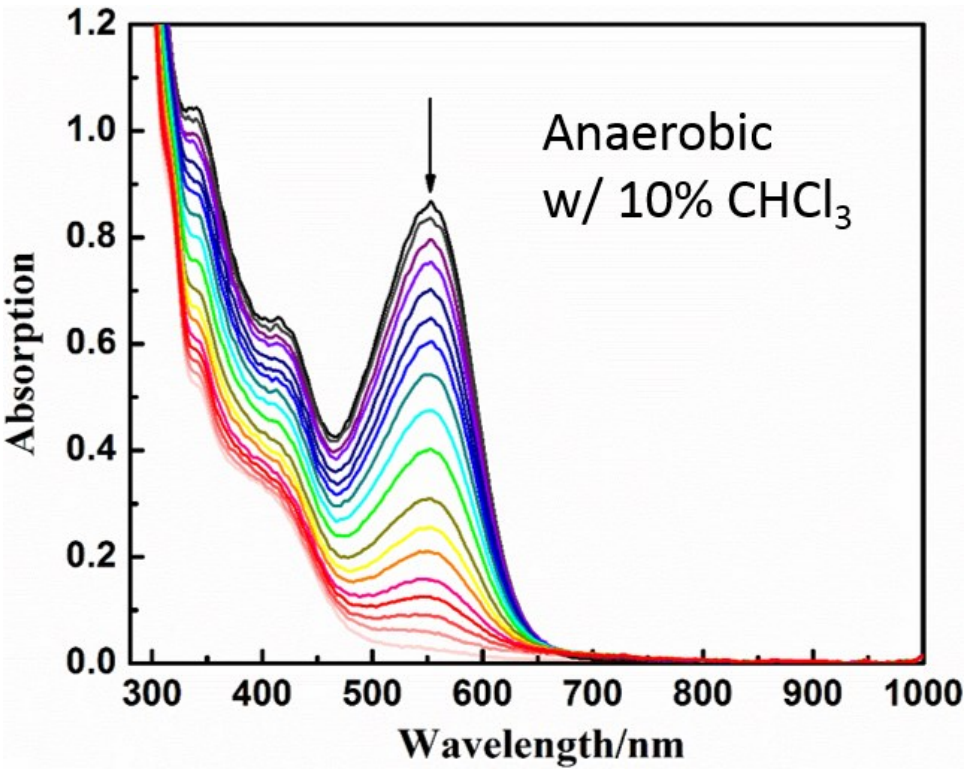

Figure 3.44 Absorption change upon photolysis of **1** (0.135 mM) at 659 nm (25 mW) in anaerobic 90:10 MeCN:$CHCl_3$.

Scheme 3.2 Photolysis of the MMLCT band of **1** in solutions containing $CHCl_3$ leads to trapping of the radicals formed by Re-Mn bond cleavage.

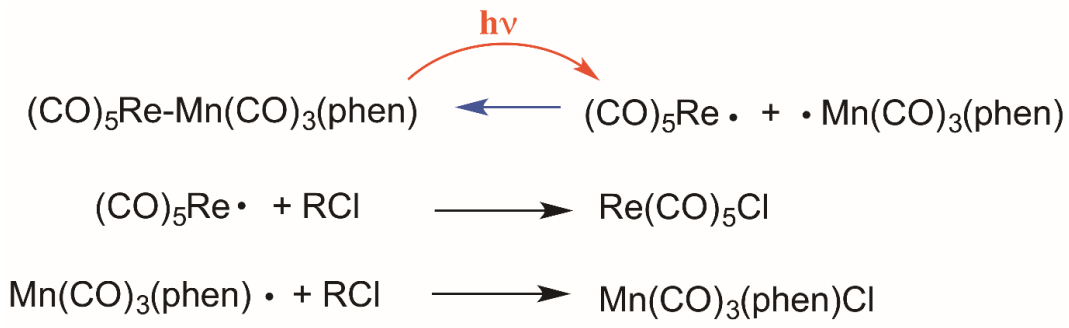

The temporal absorbance changes at the MMLCT λ_{max} upon photolysis (Fig. 3.38, 3.39 and 3.44) were used to determine quantum yields (Φ_{MM}) for disappearance of **1** as calculated from slopes of $N_{reacted}$ vs N_{abs} plots (e.g. Fig. 3.45). The Φ_{MM} value determined thus for 659 nm photolysis of **1** in aerobic acetonitrile was 0.41 ± 0.01 (3 independent measurements). This plot was essentially indistinguishable from that obtained for 659 nm photolysis under anaerobic conditions in 90:10 MeCN:$CHCl_3$ (Φ_{MM} = 0.39 ± 0.01). Thus, it appears that the photolysis generated radicals were efficiently trapped, either by O_2 in aerobic solution or by $CHCl_3$ in the latter solution (Scheme 3.2).

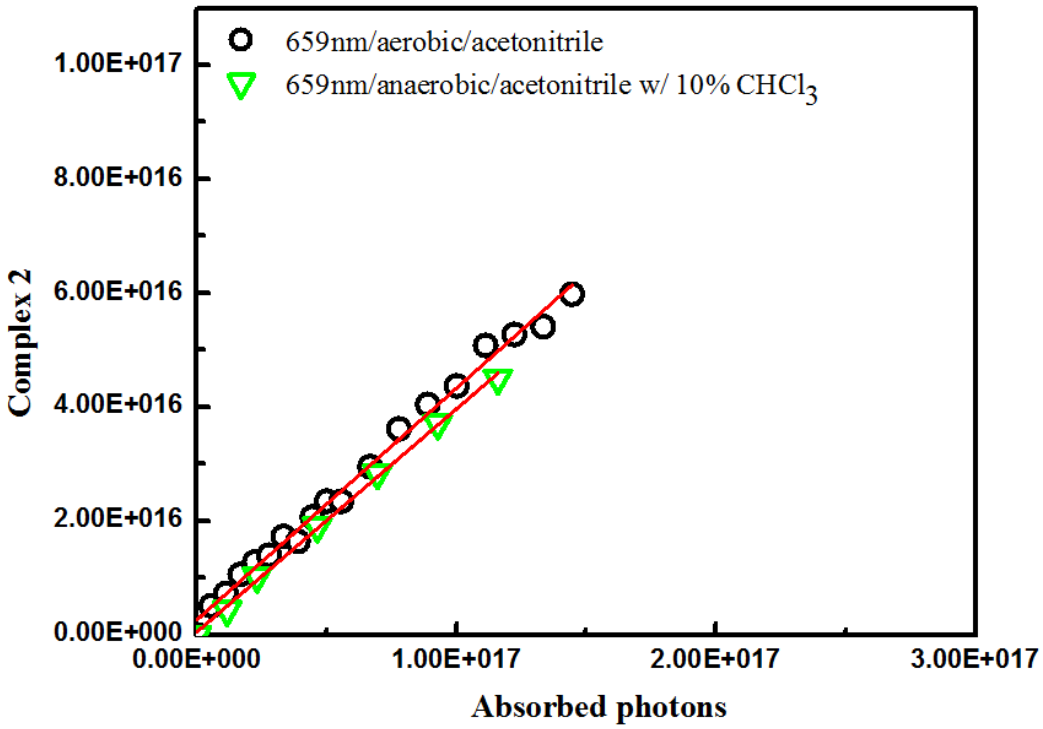

Figure 3.45 Quantum yield (Φ_{MM}) measurements. black circles: 659 nm photolysis of **1** (0.165 mM) in aerobic MeCN; green triangles: 659 nm photolysis of **1** (0.135 mM) in anaerobic 9:1 MeCN:$CHCl_3$

Consistent with this conclusion is the Φ_{MM} (0.38 ± 0.01, Fig. 3.47) determined for the 659 nm photolysis of **1** in MeCN saturated with pure O_2 (~8.1 mM),[29] which is essentially the same as that measured in air equilibrated solution. Notably, 453 nm photolysis in aerobic MeCN solution also gave an equivalent value of Φ_{MM} (0.39 ± 0.01, Fig. 3.48) suggesting that internal conversion/intersystem crossing from the state(s) initially populated by higher energy excitation to those responsible for M-M cleavage is very efficient. In contrast, the value determined in anaerobic MeCN (Φ_{MM} = 0.26 ± 0.01) was lower (Fig 3.49), a result that can be attributed to the radical recombination outlined in Scheme 3.1.

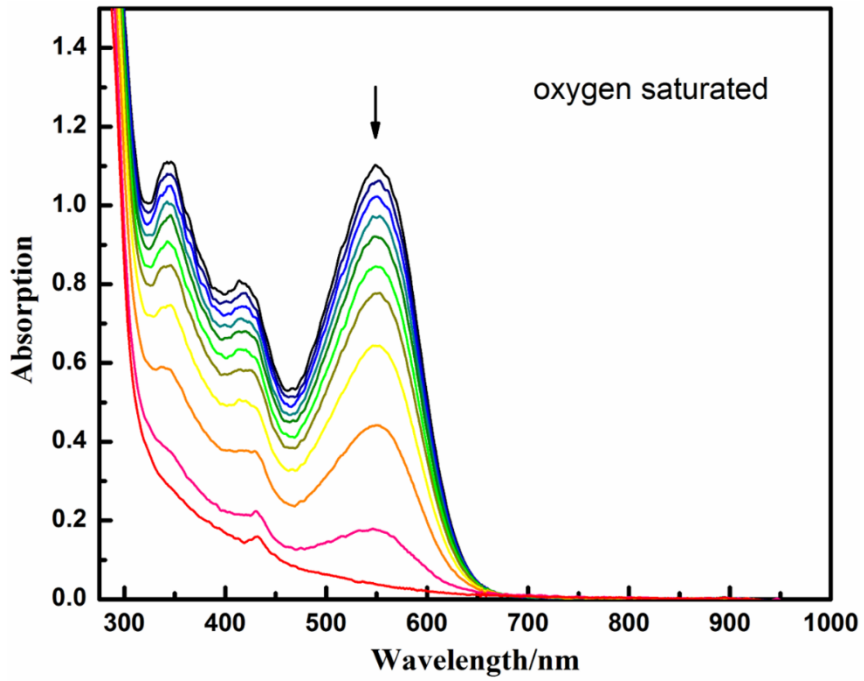

Figure 3.46 Absorption changes upon 659 nm photolysis (22 mW) of **1** (1.65×10^{-4} M) in oxygen saturated MeCN.

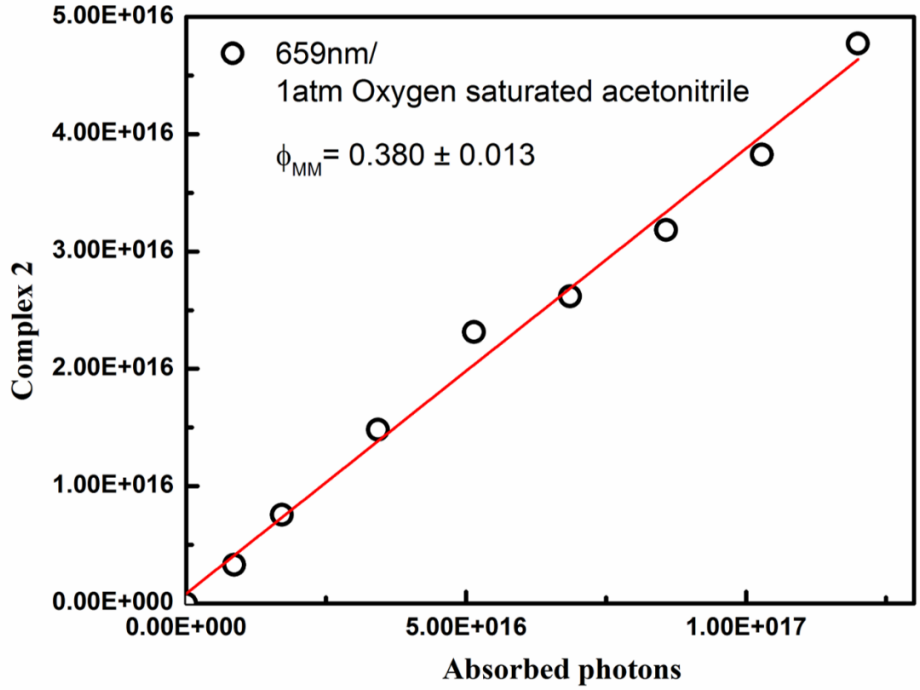

Figure 3.47 Quantum yield measurement for 659 nm photolysis of **1** (Φ_{MM} = 0.165) in O_2 saturated MeCN

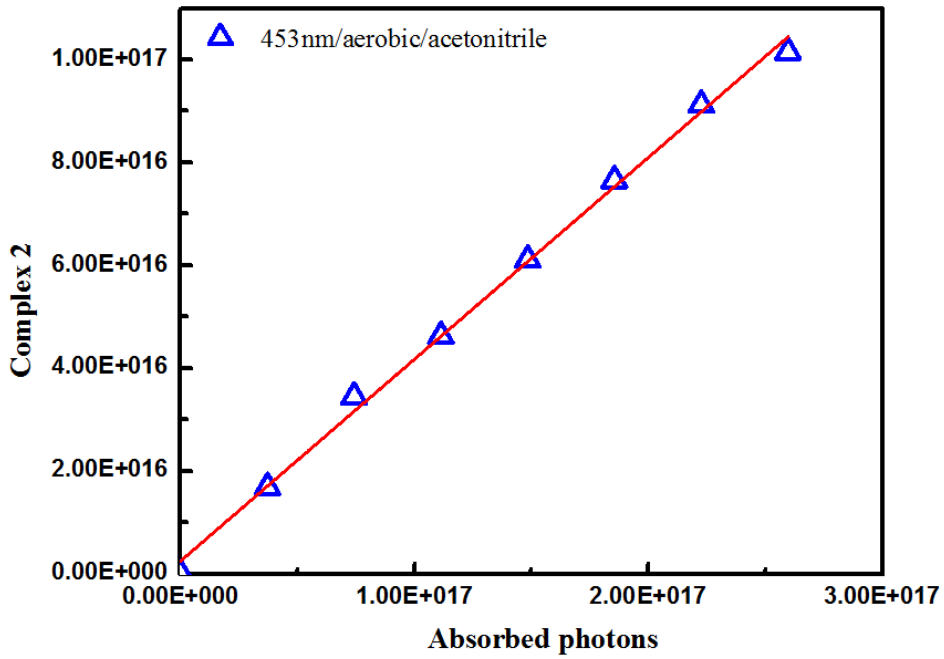

Figure 3.48 Quantum yield (Φ_{MM}) measurements: 435 nm photolysis of **1** (0.165 mM) in aerobic MeCN.

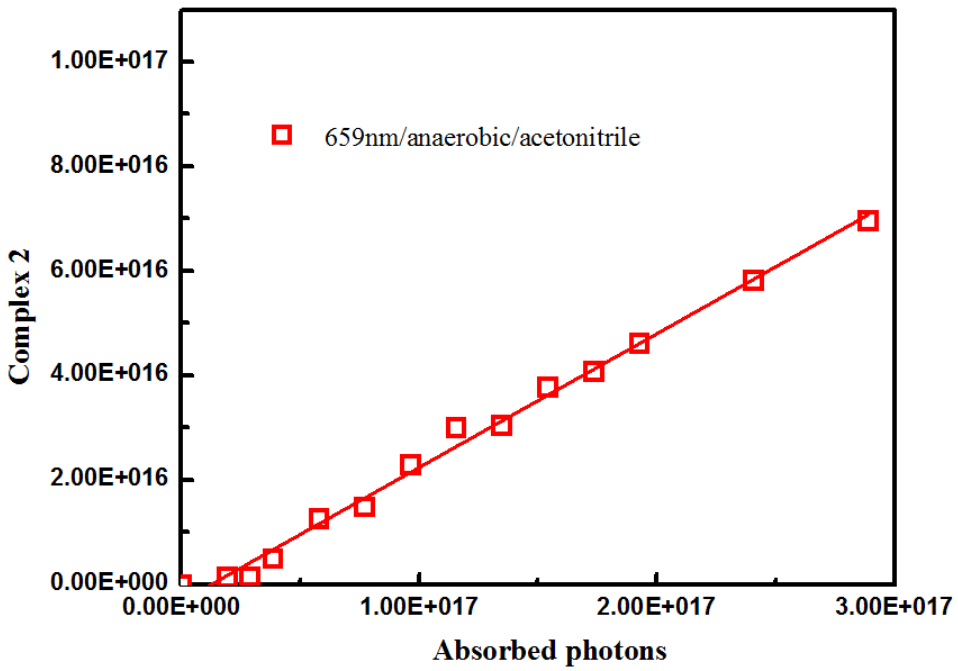

Figure 3.49 Quantum yield (Φ_{MM}) measurements: 659 nm photolysis of **1** (0.122 mM) in anaerobic MeCN

C. Photolyses of complexes 2, 3 and 4

Values of Φ_{MM} were also measured for 659 nm photolyses of the bpy, biq and phenCHO complexes in aerobic acetonitrile. The Φ_{MM} for **2** was 0.39 ± 0.01 (Fig. 3.50 and 3.51), very close to that for **1** under analogous conditions, while a Φ_{MM} of 0.24 ± 0.02 was found for biq complex **3** (Fig. 3.52 and 3.53). In neither case was the nature of the products explored further. Surprisingly, under 659 nm photolysis the phenCHO complex **4** displays a much smaller Φ_{MM} value of 0.0153 ± 0.0004 (Fig. 3.54 and 3.55), although it should be noted that the extinction coefficient of **4** at this wavelength (ε_{659} = 7.7 x 10^3 M^{-1} cm^{-1}) is ~24 fold higher than that of **1**. Since the rate of the photochemical reaction equals Φ_{MM} x I_{abs} (where I_{abs} is the intensity of the light *absorbed*),[7] the much larger extinction coefficient for **4** at this wavelength makes up in large part for the lower quantum yield.

The MMLCT absorption bands of both **3** and **4** extend into the NIR region where transmission of light through tissue is optimal. Photolysis of **4** (ε_{794} = 940 M^{-1} cm^{-1}) at 794 nm with a NIR diode laser led to complete bleaching of the MMLCT band and with Φ_{MM} value of 0.0165 ± 0.0002 in aerobic MeCN (Fig. 3.56 and 3.57). Similarly, 794 nm photolysis of **3** (ε_{794} = 646 M^{-1} cm^{-1}) gave Φ_{MM} = 0.170 ± 0.002 about 30% lower than that under 659 nm irradiation (Fig. 3.58 and 3.59).

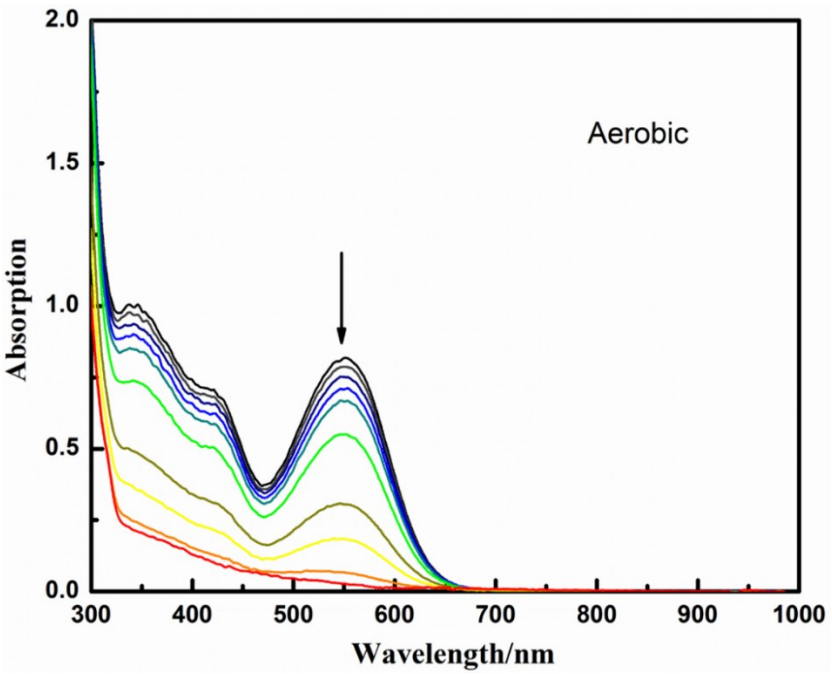

Figure 3.50 Absorption changes resulting from 659 nm photolysis (26 mW) of **2** (1.65×10^{-4} M) in aerobic MeCN

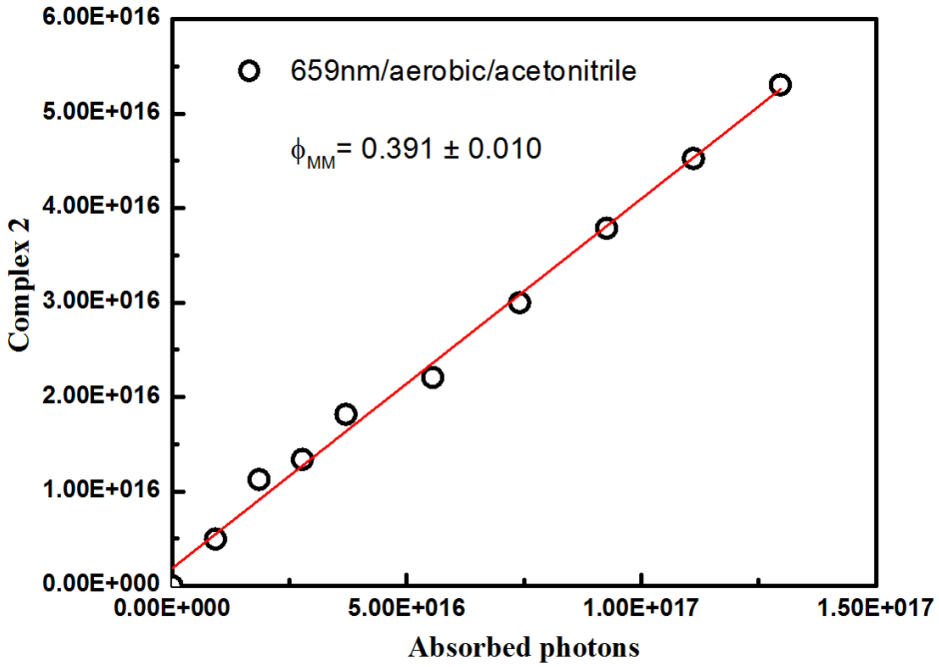

Figure 3.51 Quantum yield measurement for 659 nm photolysis (26 mW) of **2** (1.65×10^{-4} M) in aerobic MeCN (Φ_{MM} = 0.391).

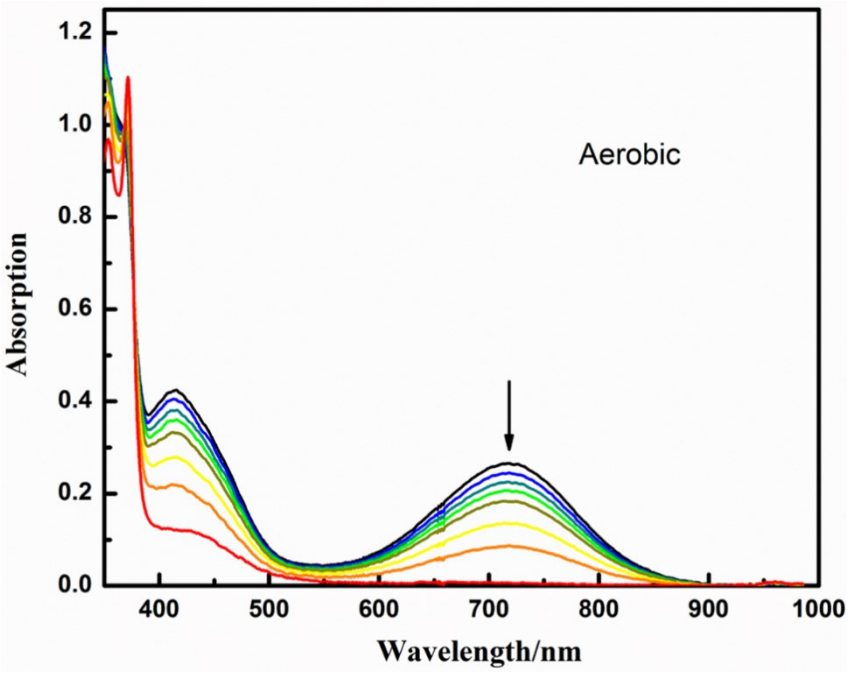

Figure 3.52 Absorption changes resulting from 659 nm photolysis (24 mW) of **3** (1.65×10^{-4} M) in aerobic MeCN

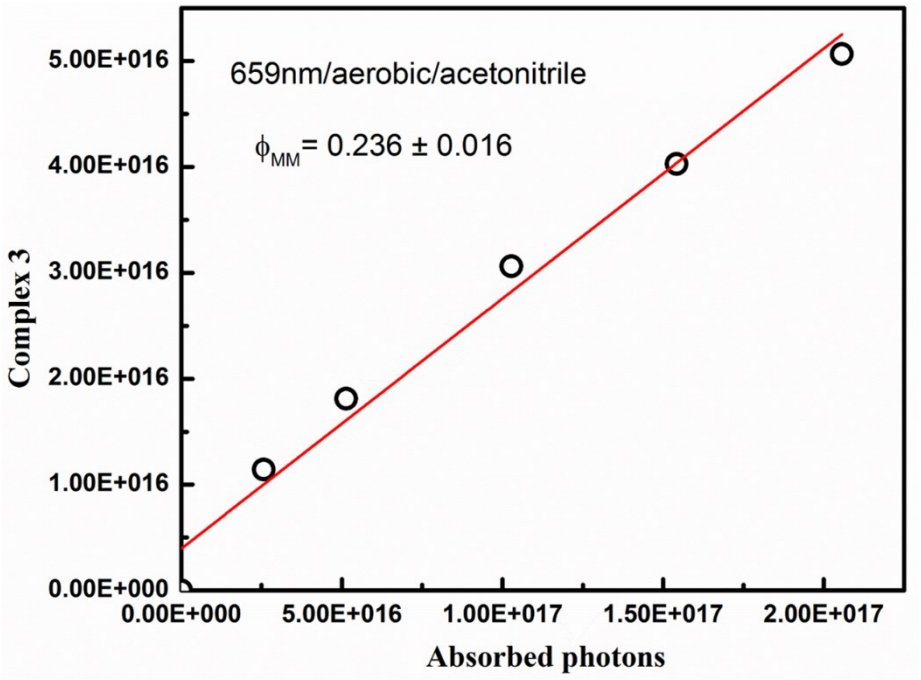

Figure 3.53 Quantum yield measurement for 659 nm photolysis (24 mW) of **3** (1.65×10^{-4} M) in aerobic MeCN (Φ_{MM} = 0.236).

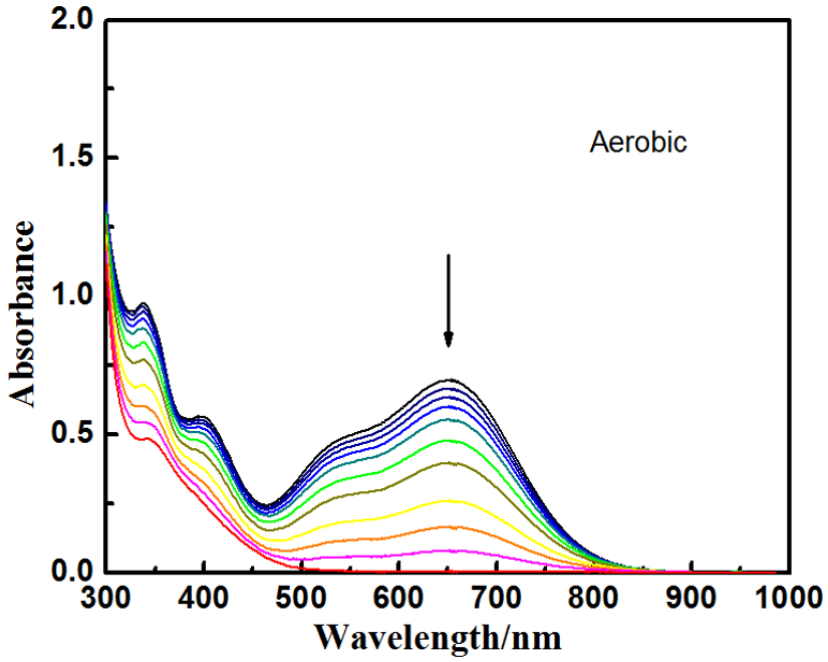

Figure 3.54 Optical spectral changes upon 659 nm photolysis (203 mW) of **4** (initially 9.3×10^{-5} M) in aerobic MeCN.

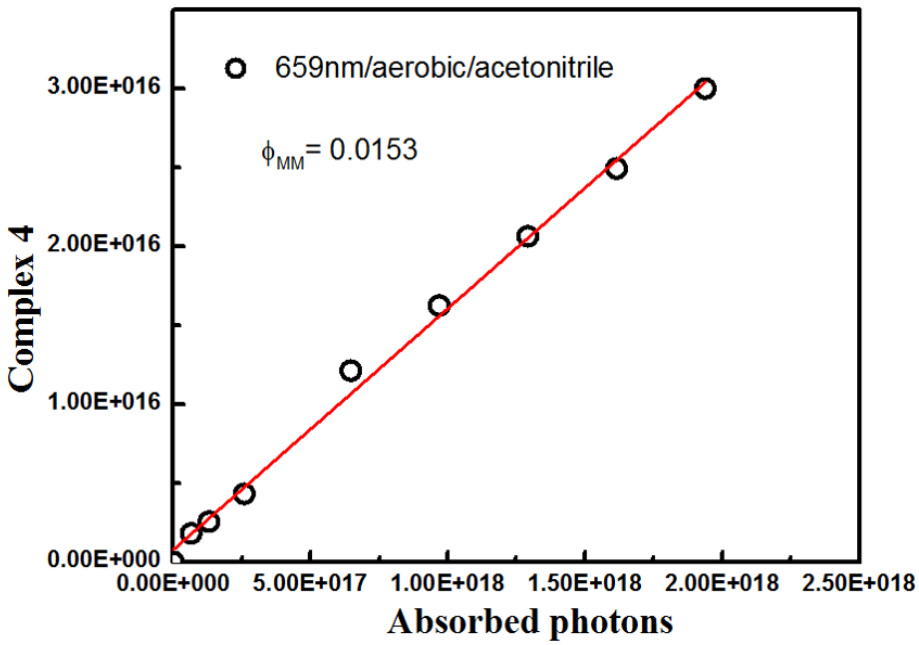

Figure 3.55 Quantum yield measurement for 659 nm photolysis (203 mW) of **4** (initially 9.3×10^{-5} M) in aerobic MeCN (Φ_{MM} = 0.015).

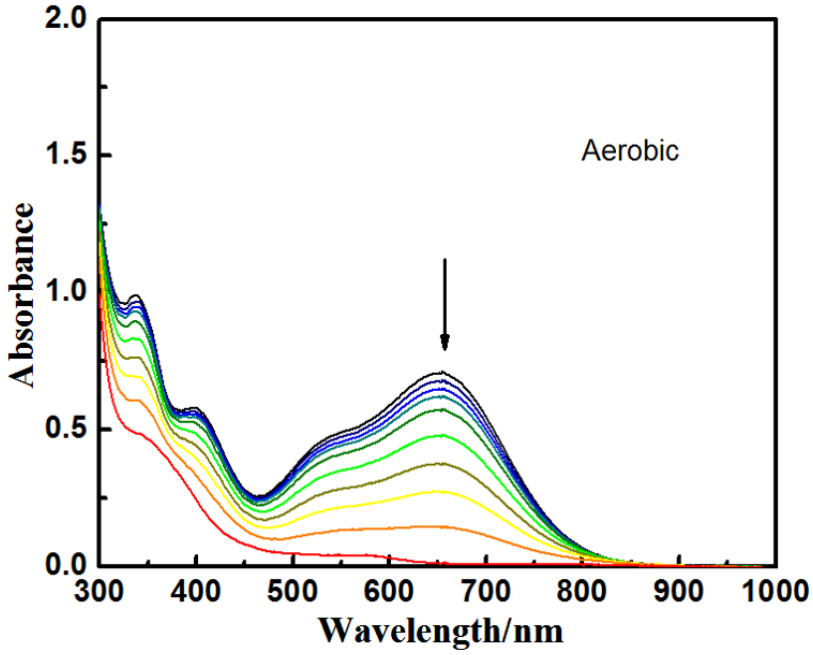

Figure 3.56 Optical spectral changes upon 794 nm photolysis (203 mW) of **4** (initially 9.3×10^{-5} M) in aerobic MeCN.

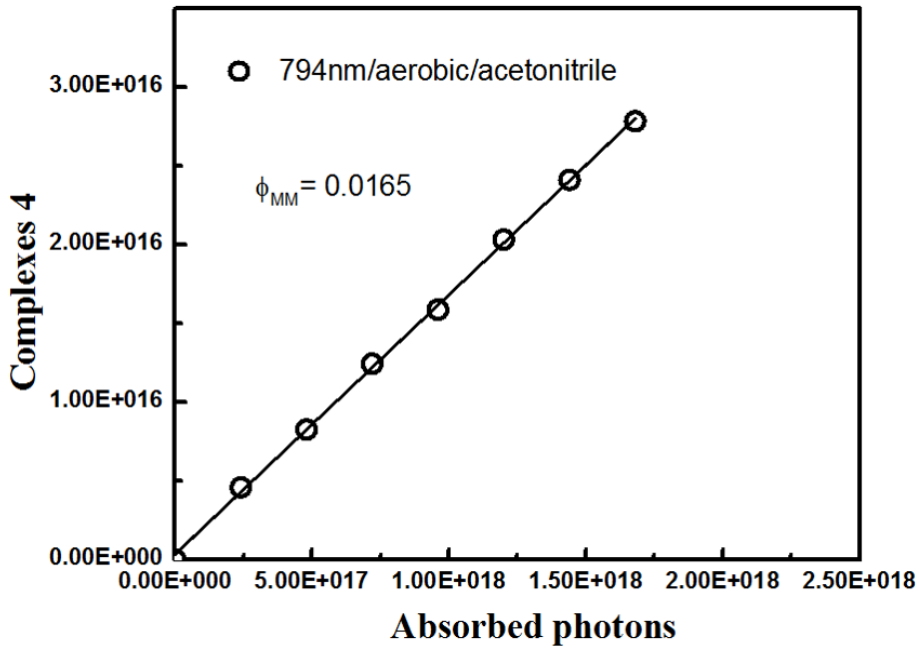

Figure 3.57 Quantum yield measurement for 794 nm photolysis (203 mW) of **4** (initially 9.3×10^{-5} M) in aerobic MeCN (Φ_{MM} = 0.0165).

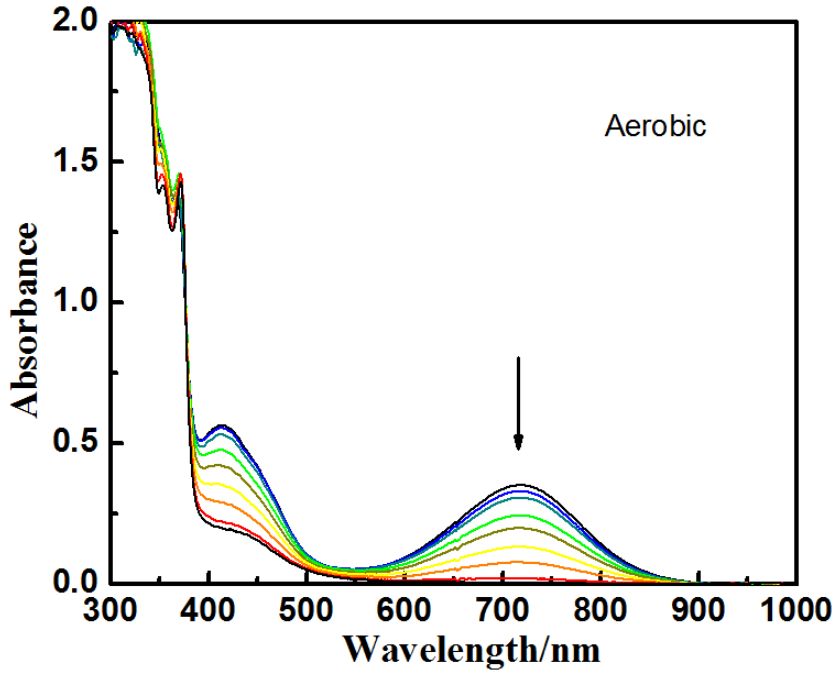

Figure 3.58 Optical spectral changes upon 794 nm photolysis (50 mW) of **3** (initially 2.64×10^{-4} M) in aerobic ACN.

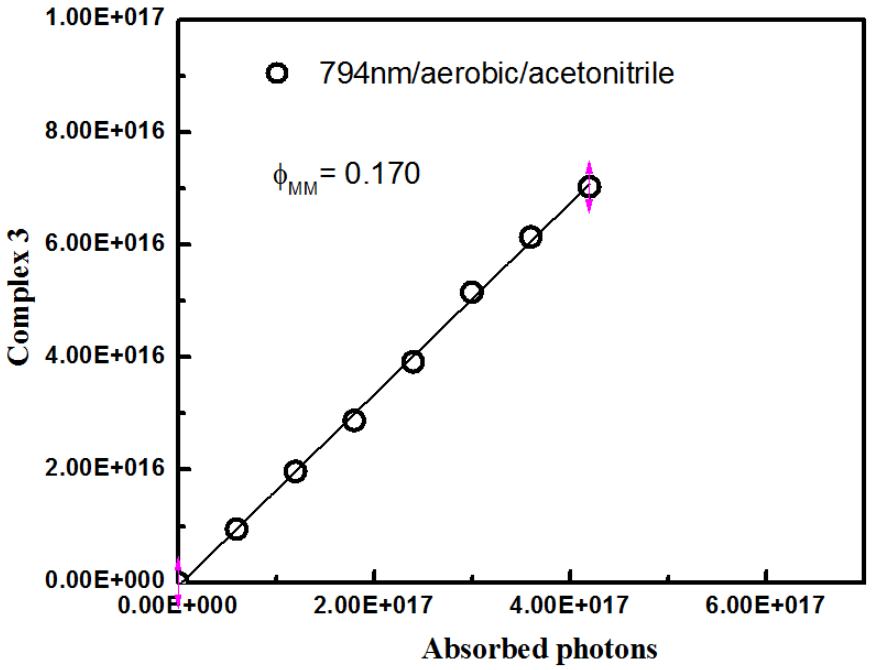

Figure 3.59 Quantum yield measurement for 794 nm photolysis (50 mW) of **3** (initially 2.64×10^{-4} M) in aerobic ACN (Φ_{MM} = 0.17).

D. CO release under photolysis

Table 3.3 summarizes the quantitative CO release measured by GC-TCD analysis of the gas phase after exhaustive photolysis of solutions of **1** and **2** in a Schlenk cuvette. As noted above, these experiments used a relatively high substrate concentration (~2.75 mM) owing to the lower sensitivity of the GC-TCD analysis. The key observation is that 659 nm photolysis in aerobic solution led to CO release in each case; however, no CO was detected when analogous photolysis was conducted either in anaerobic MeCN or in 90:10 MeCN:$CHCl_3$. Given that the principal photoreaction pathway upon MMLCT excitation is Re-Mn bond cleavage, there is clearly a direct correlation between the trapping of these radicals by O_2 and the uncaging of CO. Exhaustive photolysis with the deep-red LED in aerobic solution led to the release of ~2 moles of CO per mole of **1** for two very different substrate concentrations (2.75 mM and 0.13 mM). A somewhat higher value of 2.3 moles CO per mole **1** was seen for photolysis with a blue LED (λ_{irr} = 453 nm) in aerobic media. This may be the result of secondary photolysis Re-Mn bond cleavage products, since there was residual absorbance at 453 nm after exhaustive photolysis at 659 nm. CO release was also observed for the photolysis of **1** in aerobic dichloromethane. Since CH_2Cl_2 is a much less effective radical trapping agent than is $CHCl_3$,[30] it is likely that O_2 trapping of the photolysis generated radicals predominates in this case as well. Compound **2** has similar CO releasing results compared to compound **1** but CO_2 releasing have not been measured yet.

Table 3.3 CO release upon exhaustive photolysis of compound **1** and **2** under various conditions**.**

Complex	**Atmosphere**	**Solvent(s)**	**λ_{irr}**	**CO per Complex (moles/mole)**	**CO_2 per Complex (moles/mole)**
1	Aerobic	MeCN	453 nm[a]	2.28	0.52
			659 nm[a]	2.01	0.81
			659 nm[b]	1.96	0.78
	Anaerobic		659 nm[a]	<0.09	<0.06
		90:10 MeCN:$CHCl_3$	659 nm[a]	<0.07	<0.05
	Aerobic	DCM	659 nm[a]	1.87	0.24
2	Aerobic	MeCN	453nm[a]	2.47	Not measured
			659nm[a]	1.92	Not measured
		DCM	659nm[a]	1.72	Not measured

a. [**1**] = 2.75 mM. b: [**1**] = 0.13 mM.

In each case, CO_2 was also generated during irradiation in aerobic solution (Table 1). A similar observation was made when the tungsten carbonyl complex $W(CO)_5(L')^{3-}$ (L' = tris(sulphonatophenyl)phosphine trianion) was photolyzed in aerated aqueous solution.[10] In that case, CO_2 formation was attributed to CO oxidation by redox active intermediates formed upon O_2 reactions with low valent metal carbonyl centers.

Quantum yields for CO release (Φ_{CO}) in aerobic MeCN were determined with high concentrations of **1** (2.75 mM) in order to use GC-TCD analysis to measure the CO released

at several time points during the photolysis. The value of Φ_{CO} (0.4 ± 0.1) for irradiation at 659 nm was determined from the plot of N_{CO} (molecules of CO released) vs. N_{abs} (Fig. 3.60). Given that, under these condition ~2 moles of CO are released per mole of substrate upon exhaustive photolysis, this value of Φ_{CO} is less than might be expected. One possible explanation would be a less efficient net photolytic cleavage at this concentration which are ~17 fold higher than that used to determine the Φ_{MM} values reported (see above). The greater absorbance at the 659 nm λ_{irr} leads to a higher flux of transient radicals. Since the O_2 in air-saturated MeCN is < ~1.7 mM, radical recombination may play a greater role, thereby giving a lower Φ_{MM}, although exhaustive photolysis would still have the same 2 / 1 Φ_{co} / Φ_{MM} ratio, owing to the reservoir of O_2 in the gas phase of the Schlenk cuvette. This argument is consistent with the IR experiment in aerobic MeCN where 659 nm photolysis of **1** at a comparable concentration **(**2.75 mM) where radical recombination products were evident. Using the same method, NIR (794 nm) irradiation of **4** (2.5 mM in MeCN) gave the Φ_{CO} value 0.015 ± 0.001 (Fig. 3.61), and exhaustive 794 nm photolysis of **4** led to the release of ~1.5 moles of CO per mole of substrate.

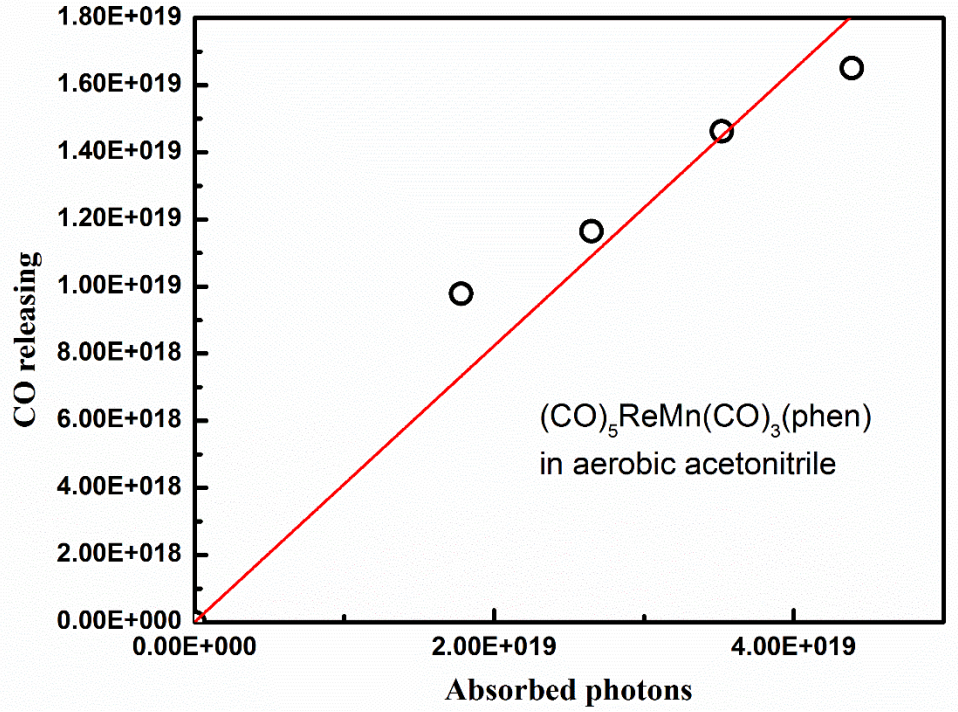

Figure 3.60 Φ_{CO} measurements for the 659 nm photolysis of **1** (2.75 mM) in aerobic MeCN (Red line is the fitting of experiment data).

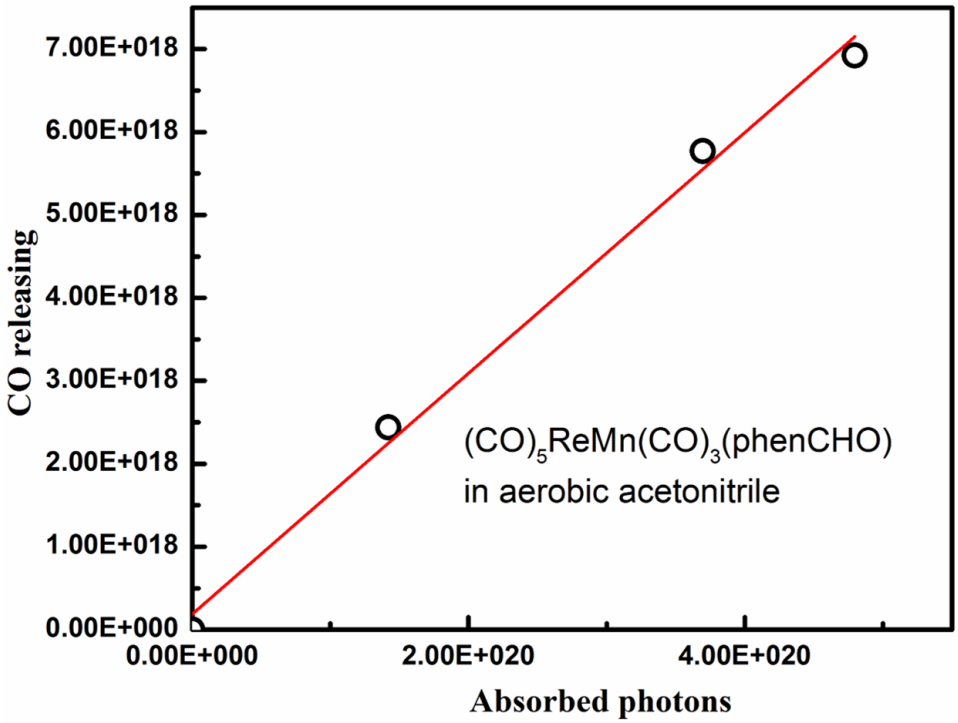

Figure 3.61 Φ_{CO} measurement for the 794 nm photolysis of **4** (2.5 mM) in aerobic MeCN.

E. Studies in aqueous solution

While complexes **1-4** provide a proof-of-principle for using long-wavelength MMLCT excitation of dinuclear metal carbonyls to trigger photochemical CO release in aerobic media, they are not soluble in aqueous solution. In some cases, the hydrophobic nature of these complexes may be an advantage, for example, when used in a biocompatible polymer disk as an implant[33–35] or with an amphiphilic polymer-based water-soluble nanocarriers[4] and micelles.[36,37] We are indeed pursuing both options with these photoCORMs. On the other hand, substituents on the phenanthroline ligands offer possible modifications to enhance aqueous solubility.

One such substituent is the carboxaldehyde on **4**. Reaction of $(CO)_5ReMn(CO)_3$(phen-CHO) with an amine terminated poly(ethylene glycol) PG1-AM-2k (average mol. wt = 3135 Da) gave a water soluble conjugate linked through an imine bond (eq. 1). The product $(CO)_5ReMn(CO)_3$(phen-CHNPEG) (**5**) was characterized by proton NMR spectroscopy (Fig 3.11), where it was shown that the aldehyde proton disappears and the ratio between phen ligand and PEG moiety is approximately 1:1 which confirms its structure. This material displayed a broad absorption band with a λ_{max} at ~ 569 nm with a broad shoulder at 700 nm with absorbance extending beyond 800 nm, presumably the MMLCT transition(s) (Fig 3.62). In aerobic pH 7.4 phosphate buffer saline (PBS) solution at 37 ^oC, **5** demonstrated moderate stability with the absorbance at the MMLCT λ_{max} diminishing about 20% over 12 h; Fig. 3.37)

$$(CO)_5ReMn(CO)_3(phen\text{-}CHO) + H_2N\text{-}PEG \longrightarrow (CO)_5ReMn(CO)_3(phen\text{-}CHNPEG) + H_2O \quad (1)$$

NIR photolysis did demonstrate **5** to be photoactive in aerobic, pH 7.4 PBS solution as evidenced by decreases of the MMLCT absorption (Fig 3.63). However, the quantum yield

measured upon irradiation of such solutions with 794 nm light from a diode laser proved to be quite modest (Φ_{MM} = (1.0 ± 01) x 10^{-3}).

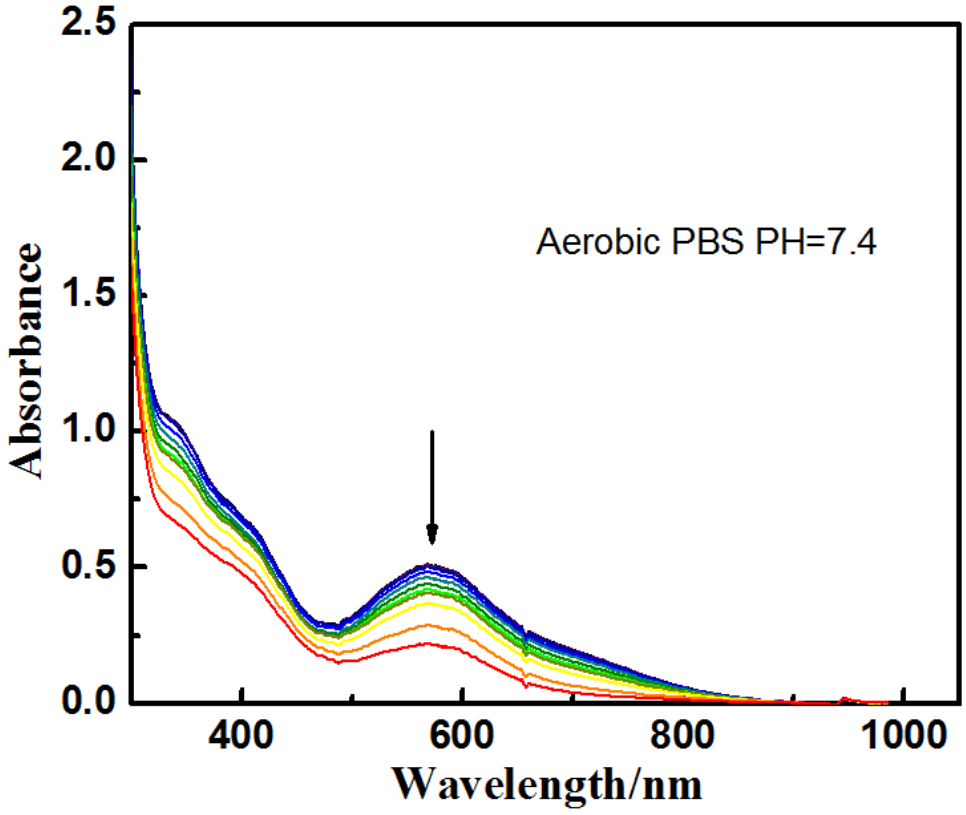

Figure 3.62 Absorption changes upon 794 nm photolysis (203 mW) of the PEG conjugate **5** (initially ~1.0×10^{-4} M) in aerobic pH 7.4 PBS solution.

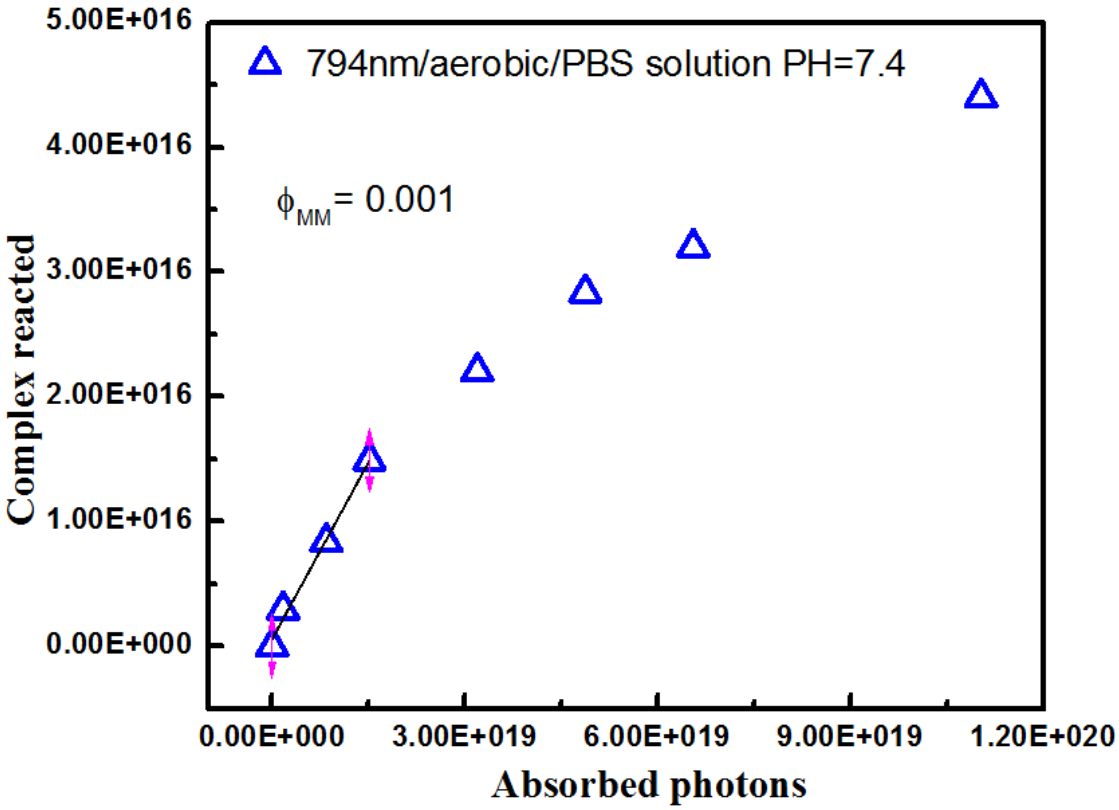

Figure 3.63 Quantum yield measurement from absorption changes upon 794 nm photolysis (203 mW) of the PEG conjugate **6** (initially ~1.0×10^{-4} M) in aerobic pH 7.4 PBS solution.

F. Potential mechanism

Neither CO nor CO_2 were observed upon MMLCT photolysis of **1** in deaerated MeCN (Table 3.3). This result argues that the radicals initially formed by cleaving the Re-Mn bond are not sufficiently substitution labile to generate relevant quantities of CO before recombining (Scheme 3.1) or being trapped by $CHCl_3$ (Scheme 3.2). Thus, the CO (and CO_2) released (or formed) upon longer wavelength excitation under aerobic conditions must involve the dioxygen trapping of such metal centered radicals. In this context, we note earlier studies that used σ_{MM} --> σ_{MM}* excitation of the complexes $M_2(CO)_{10}$ (M = Mn or Re) in 10 K Ar/O_2

matrices and IR spectroscopy to identify the peroxo-bridged adducts $(CO)_5M(\mu\text{-}O_2)M(CO)_5$ formed presumably via eqs. 2 and 3.[11,38–40]

$$\cdot M(CO)_5 + O_2 \rightleftharpoons \cdot O_2M(CO)_5 \quad (2)$$

$$\cdot M(CO)_5 + \cdot O_2M(CO)_5 \rightleftharpoons (CO)_5M(\mu\text{-}O_2)M(CO)_5 \quad (3)$$

The mechanistic sequence proposed in Scheme 3.3 for the photolysis of **1** in aerobic media begins with MMLCT excitation to trigger homolytic cleavage of the Re-Mn linkage. The resulting Re and Mn radicals can recouple in several ways (Scheme 3.3) or be trapped by O_2 to form the intermediates $\cdot O_2Mn(CO)_3(phen)$ (***I₁***) and $\cdot O_2Re(CO)_5$ (***I₂***). DFT studies show the latter reactions to be exothermic by –15 and –21 kcal/mol, respectively (Table 3.4). Furthermore, spin density analysis indicates that, while the unpaired electrons of $\cdot Mn(CO)_3(phen)$ and $\cdot Re(CO)_5$ are largely localized on the respective metal centers (Figs. 3.64a and 3.64b), the unpaired electrons of the dioxygen adducts are largely localized on the respective O_2 ligands (Figs 3.64c and 3.64d). Thus, these are superoxide complexes of the M(I) centers and should be very reactive with subsequently generated metal-centered radicals to give the peroxo-bridged species $\{Mn(CO)_3(phen)\}_2(\mu\text{-}O_2)$ (***I₃***), $(CO)_5Re(\mu\text{-}O_2)Mn(CO)_3(phen)$ (***I₄***) and $[(CO)_5Re]_2(\mu\text{-}O_2)$ (***I₅***). The DFT studies show that all such reactions are exothermic (Table 3.4 and Fig. 3.65).

Scheme 3.3 Proposed mechanism of photo-oxidation of complex **1**

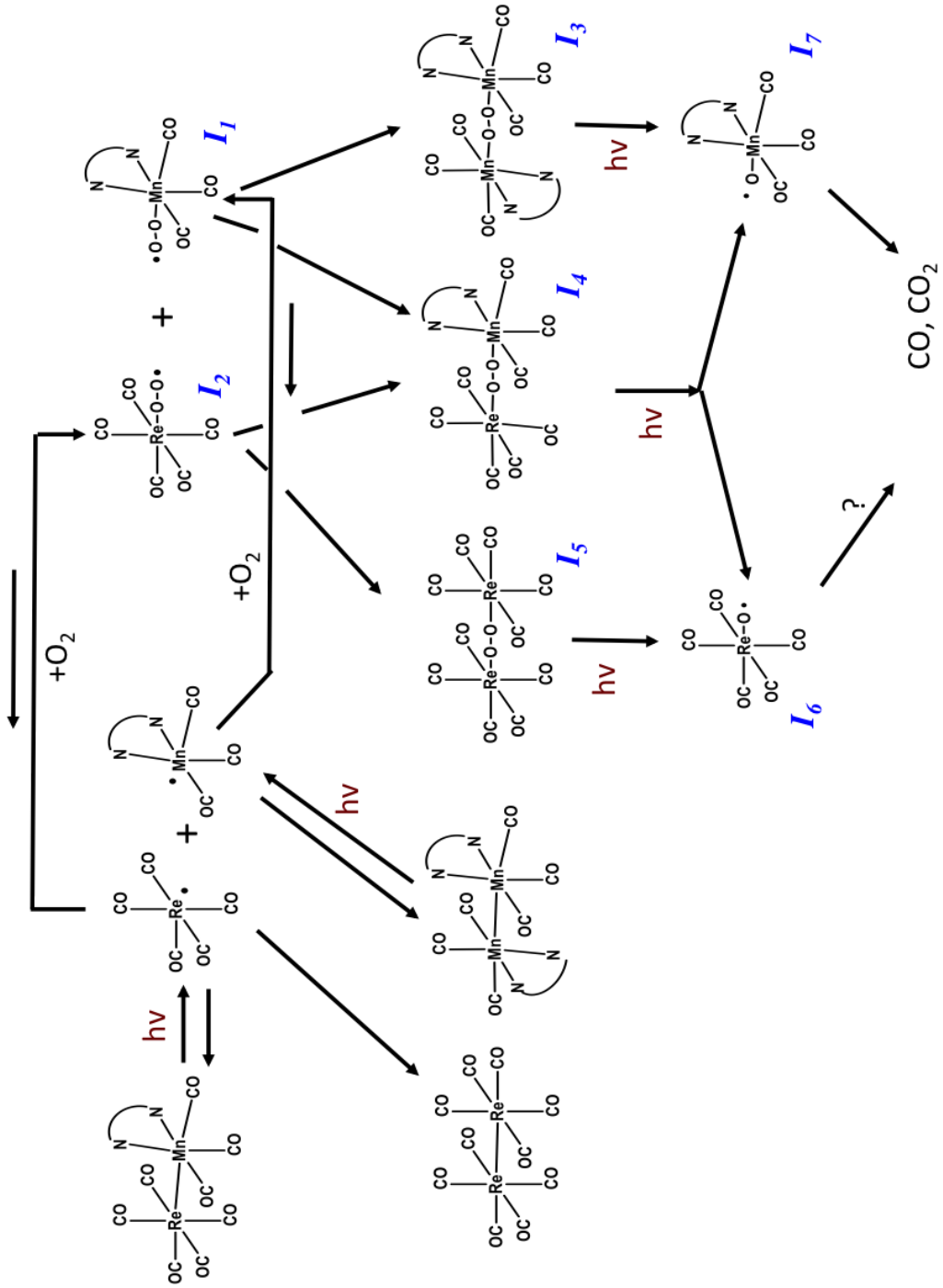

Table 3.4 DFT results-- Energies of reactions and spin-state transitions. Calculations were done at unrestricted B3LYP with base set 6-31G* (6-31G* & LANL2DZ>Kr)[a] without symmetry constraints.

A. Reaction ΔE's (in kcal/mole) for

$Mn(CO)_5 + O_2 \rightleftharpoons O_2Mn(CO)_5$	–10
$Re(CO)_5 + O_2 \rightleftharpoons O_2Re(CO)_5$	–15
$Mn(CO)_3(phen) + O_2 \rightleftharpoons O_2Mn(CO)_3(phen)$	–21
$Mn(CO)_3(phen) + Re(CO)_5 \rightleftharpoons (CO)_5ReMn(CO)_3(phen)$	–35
$2\ Re(CO)_5 \rightleftharpoons Re_2(CO)_{10}$	–44
$2\ Mn(CO)_3(phen) \rightleftharpoons Mn_2(CO)_6(phen)_2$	–20
$Mn(CO)_3(phen) + O_2Mn(CO)_3(phen) \rightleftharpoons [Mn(CO)_3(phen)]_2(\mu\text{-}O_2)$	–28
$Re(CO)_5 + O_2Re(CO)_5 \rightleftharpoons [Re(CO)_5]_2(\mu\text{-}O_2)$	–38
$Re(CO)_5 + O_2Mn(CO)_3(phen) \rightleftharpoons Re(CO)_5(\mu\text{-}O_2)Mn(CO)_3(phen)$	–41
$[Mn(CO)_3(phen)]_2(\mu\text{-}O_2) \rightleftharpoons 2\ ^2[OMn(CO)_3(phen)]$	+35
$[Re(CO)_5]_2(\mu\text{-}O_2) \rightleftharpoons 2\ ^2[ORe(CO)_5]$	+43
$(CO)_5Re\ (\mu\text{-}O_2)Mn(CO)_3(phen) \rightleftharpoons ORe(CO)_5 + OMn(CO)_3(phen)$	+50
$2\ O_2Mn(CO)_3(phen) \rightleftharpoons [Mn(CO)_3(phen)]_2(\mu\text{-}O_4)$	+7

ΔE's for differences in spin states

$^{2}[OMn(CO)_3(phen)] \rightleftharpoons {}^{4}[OMn(CO)_3(phen)]$	+13
$^{2}[OMn(CO)_3(phen)] \rightleftharpoons {}^{6}[OMn(CO)_3(phen)]$	–6
$^{2}[OMn(CO)_5] \rightleftharpoons {}^{4}[OMn(CO)_5] \rightleftharpoons {}^{6}[OMn(CO)_5]$	+41
$^{2}[ORe(CO)_5] \rightleftharpoons {}^{4}[ORe(CO)_5] \rightleftharpoons {}^{6}[ORe(CO)_5]$	+118
$^{6}[OMn(CO)_3(phen)] \rightarrow {}^{6}[Mn(CO)_2(phen)] + CO_2$	–12
$^{2}[OMn(CO)_3(phen)] \rightarrow {}^{2}[OMn(CO)_2(phen)] + CO$	+29
$^{2}[OMn(CO)_3(phen)] \rightarrow {}^{6}OMn(phen) + 3\ CO$	+47
$^{6}[OMn(CO)_3(phen)] \rightarrow {}^{6}OMn(phen) + 3\ CO$	+52
$^{2}[OMn(CO)_3(phen)] \rightarrow {}^{6}Mn(CO_2)(phen) + 2\ CO$	+4
$^{6}[OMn(CO)_3(phen)] \rightarrow {}^{6}Mn(CO_2)(phen) + 2\ CO$	+10
$^{2}[OMn(CO)_5] \rightleftharpoons {}^{6}[OMn(CO)_5]$	+41

[a] for Re

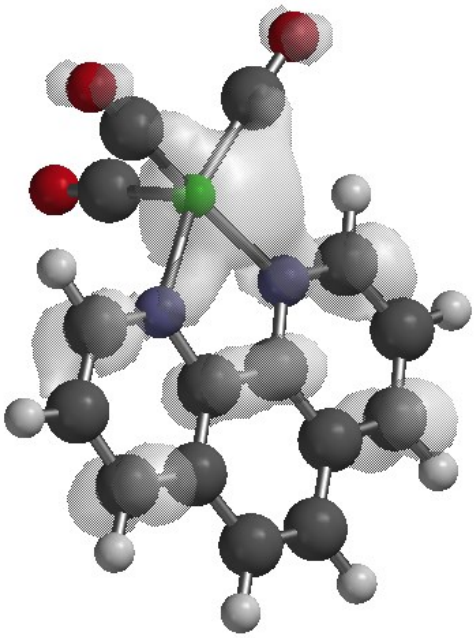

Figure 3.64a. Spin density map of $^2[Mn(CO)_3(phen)]$ from TD-DFT calculation.

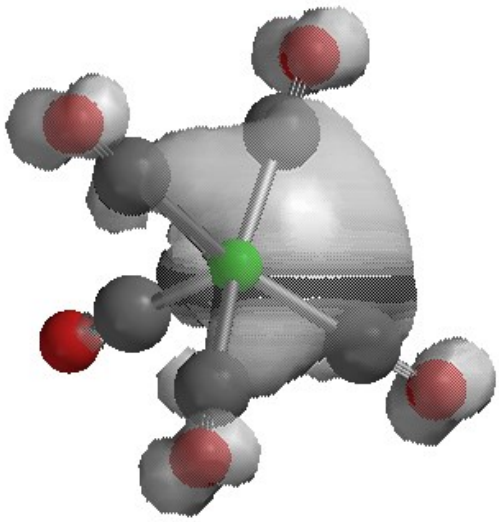

Figure 3.64b Spin density map of $^2[Re(CO)_5]$ from TD-DFT calculation.

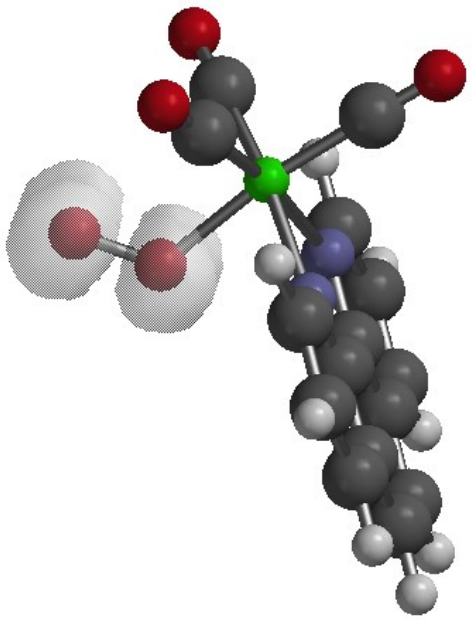

Figure 3.64c Spin density map of $^2[O_2Mn(CO)_3(phen)]$ (***I*****$_1$**) from TD-DFT calculation.

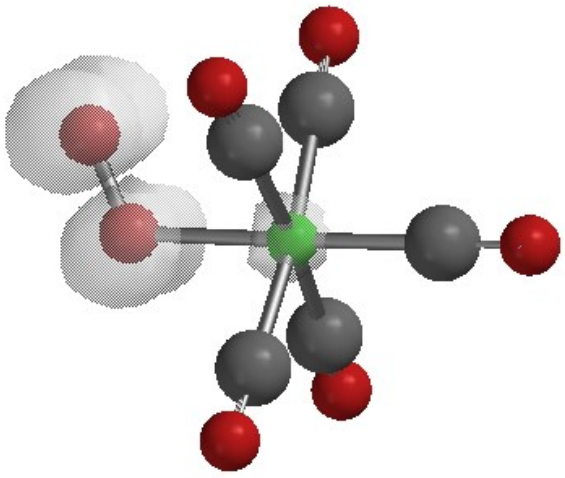

Figure 3.64d Spin density map of $^2[O_2Re(CO)_5]$ (***I*****$_2$**) of from TD-DFT calculation.

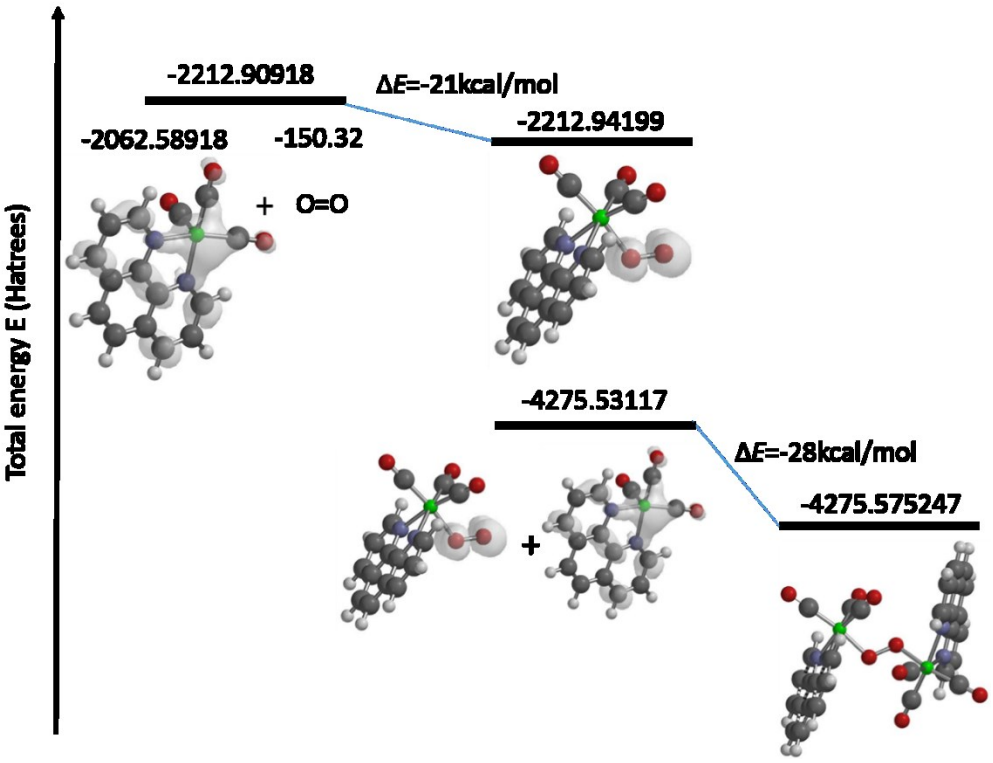

Figure 3.65 Total energies (*E*) of the intermediates $Mn(CO)_3(phen)$, $O_2Mn(CO)_3(phen)$ (***I*****1**) and $\{Mn(CO)_3(phen)\}_2(\mu\text{-}O_2)$ (***I*****3**) calculated by DFT at unrestricted B3LYP/6-31G* level of theory without symmetry constraints.

The peroxo-bridged dirhenium complex ***I*****5** was identified in the IR study noted above[11] as the product of broad band photolysis of $Re_2(CO)_{10}$ in 10 K Ar/O_2 matrices. The same study found that continued broad band photolysis gave a second intermediate suggested to be $ORe(CO)_5$ (***I*****6**) with the eventual products being Re_2O_7, CO and CO_2.

Since ***I*****1 - *I*****5** are all formally d^6, low spin M(I) complexes, one would also not expect any of these to be very labile toward CO release. So the question remains, what pathway is responsible for this labilization? The DFT calculations provide some further insight into this question (Table 3.4). For example, the O-O bonds of the peroxo-bridged dinuclear complexes ***I*****3**, ***I*****4** and ***I*****5** are relatively weak with calculated bond dissociation energies of 35, 50, and 43

kcal/mol, respectively, for spontaneous dissociation to form the doublet mononuclear oxo-complexes (eq. 4). Thermal reactions leading to the latter species are accessible, although not likely to be fast, and certainly would not have played a role in the low T matrix studies with $Re_2(CO)_{10}$ noted above. However, as indicated in that study, this process may also be activated photochemically. In this context, it is notable that TDDFT calculations predict that the spectra of all three peroxo bridged intermediates should display long wavelength visible or NIR transitions involving charge transfer from a (mostly oxygen-oxygen bonding) HOMO (or HOMO-1) to LUMOs largely localized on a phenanthroline, or with ***I*****$_5$**, delocalized on carbonyls (Fig 3.66a-c). The resulting excited states should be more labile to homolytic O-O bond cleavage.

$$(ML_5)_2(\mu\text{-}O_2) \rightleftharpoons 2\ {}^2[OML_5] \qquad (4)$$

Another pathway that might also lead to the formation of metal oxo radicals is shown as below:

$$2\ {}^2[O_2ML_5] \rightleftharpoons (ML_5)_2(\mu\text{-}O_4) \rightleftharpoons 2\ {}^2[OML_5] + O_2 \qquad (5)$$

However, from its DFT calculation (Fig. 3.67), pathway in eq. 5 has shown to contain two steps of endothermic reactions which are certainly not more preferable than the pathway shown in eq. 2-4.

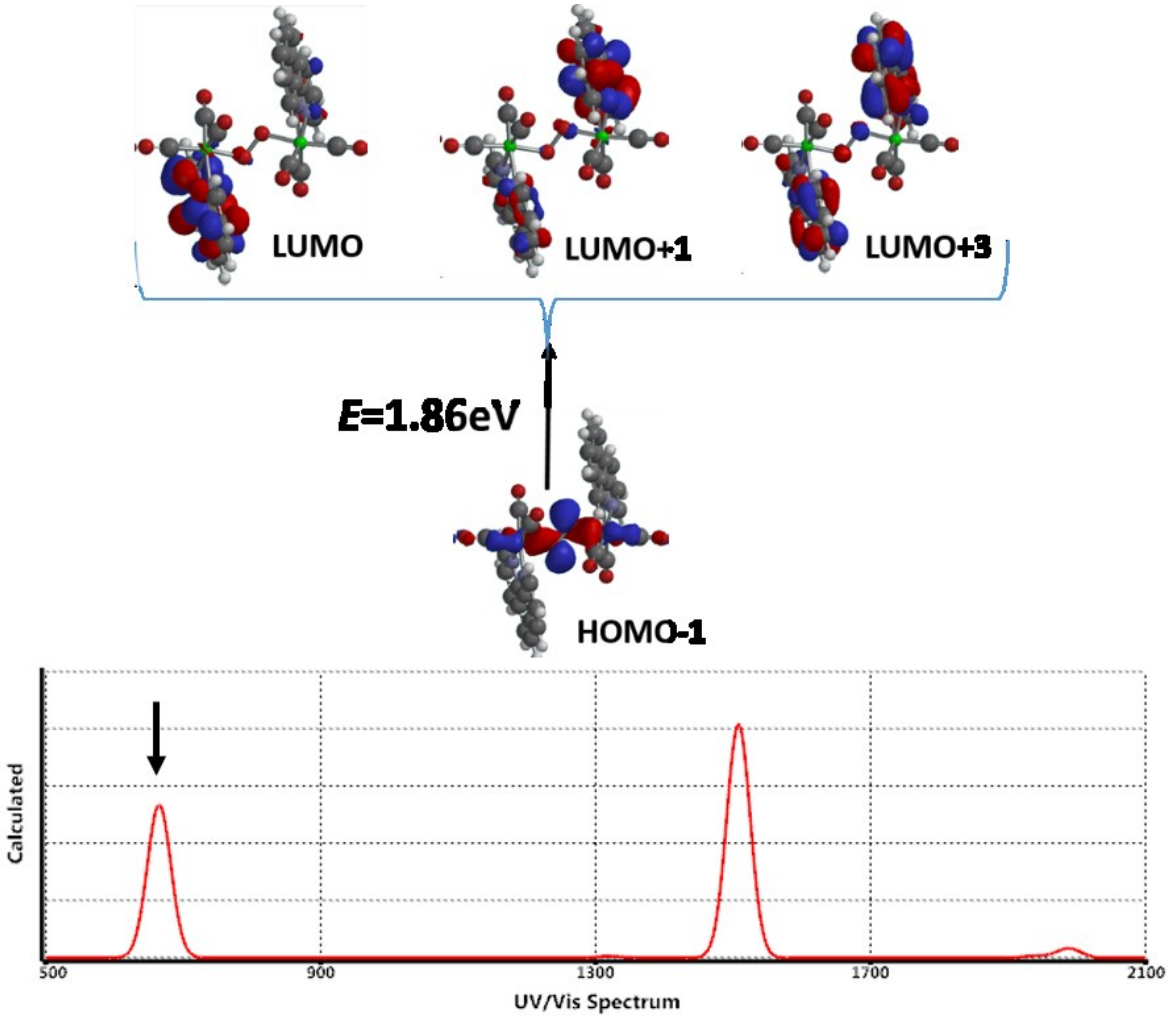

Figure 3.66a. ***Top:*** TD-DFT calculation of the HOMO-1, LUMO, LUMO+1 and LUMO+3 orbitals of (phen)$(CO)_3Mn(\mu\text{-}O_2)Mn(CO)_3$(phen) (***I₃***) based on the calculated ground state geometry. ***Bottom:*** Calculated optical absorption spectrum.

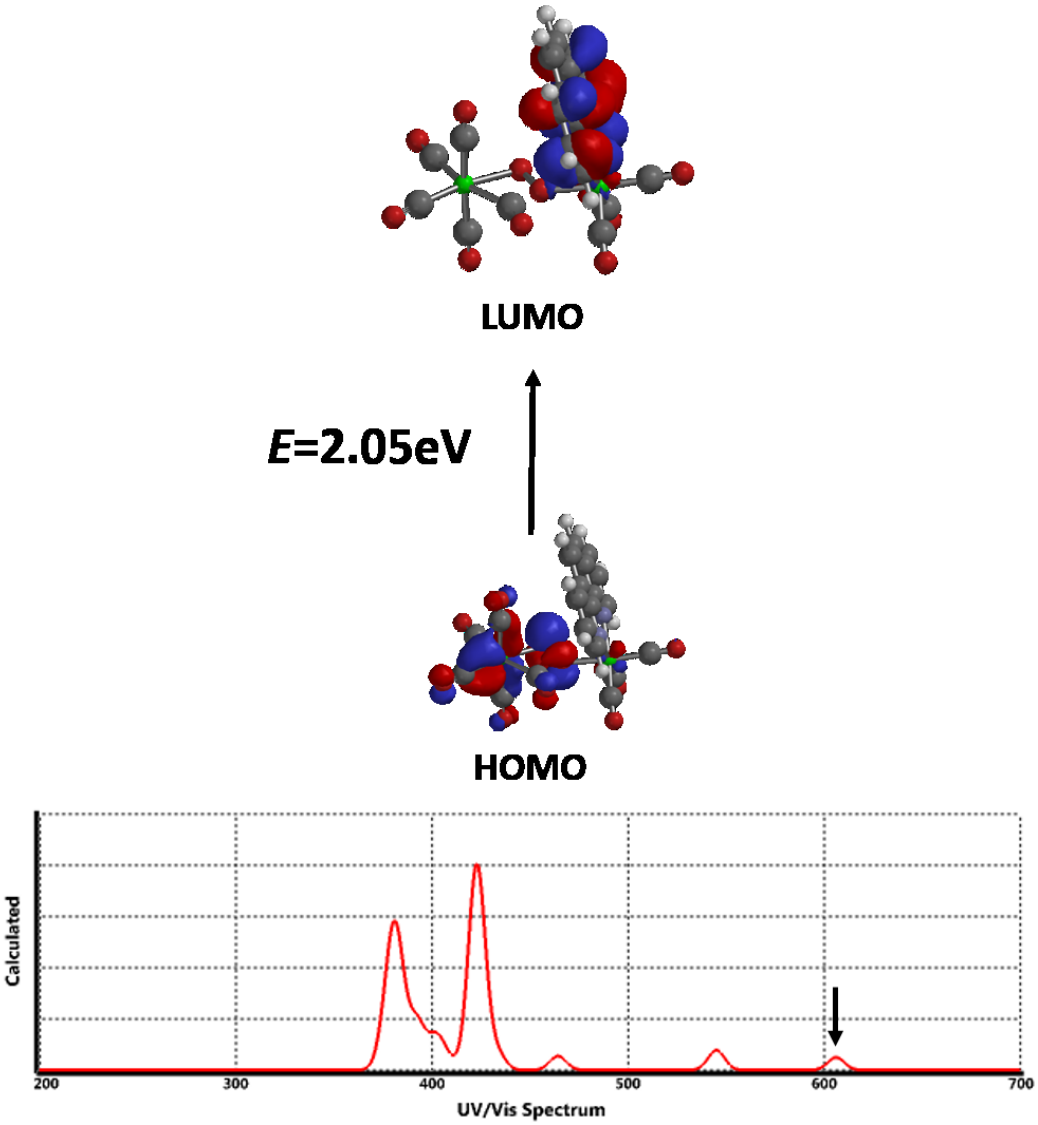

Figure 3.66b ***Top:*** TD-DFT calculation of the HOMO, LUMO orbitals of $(CO)_5Re(\mu\text{-}O_2)Mn(CO)_3(phen)$ (***I4***) based on calculated ground state geometry. ***Bottom:*** Calculated optical absorption spectrum.

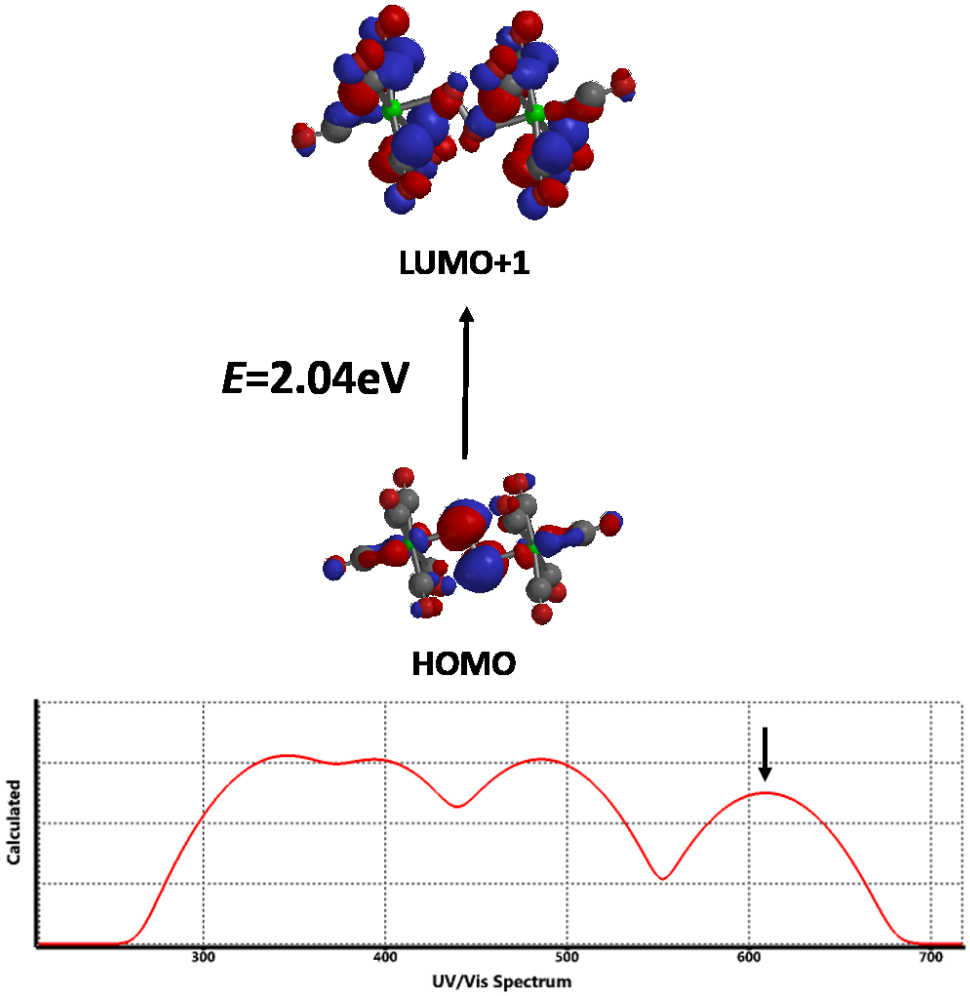

Figure 3.66c ***Top:*** TD-DFT calculation of the HOMO and LUMO+1 orbitals of $[(CO)_5Re]_2(\mu\text{-}O_2)$ (***I*****5**) based on the calculated ground state geometry. ***Bottom:*** Calculated optical absorption spectrum.

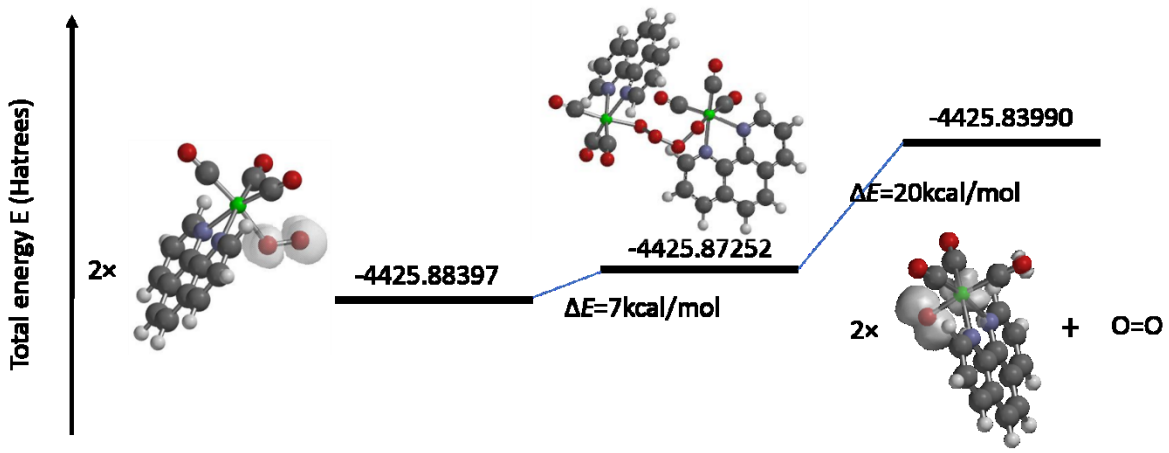

Figure 3.67 Total energies (*E*) of the intermediates $O_2Mn(CO)_3(phen)$, and $\{Mn(CO)_3(phen)\}_2(\mu\text{-}O_4)$ calculated by DFT at unrestricted B3LYP/6-31G* level of theory.

Cleavage of the peroxo bonds of ***I*****3**, ***I*****4** or ***I*****5** would lead initially to the doublet state oxo radical intermediates $^2[ORe(CO)_5]$ (^{2}***I*****6**) and $^2[OMn(CO)_3(phen)]$ (^{2}***I*****7**). In each case, the unpaired spin is largely localized on the oxo ligand (Figs. 3.68a and 3.68b). Notably, for the rhenium intermediate, the doublet (or low spin form) ^{2}***I*****6** is the lowest energy state with the corresponding sextet high spin form dramatically higher in energy as expected for a third row transition metal (Table 3.4). In contrast, for the manganese analog, the sextet is the lower energy state, with ^{6}***I*****7** having a calculated energy 6 kcal/mol lower than ^{2}***I*****7**. Furthermore, the calculated structure of the high spin state is highly distorted, showing the oxo ligand to have moved toward the carbon of an adjacent carbonyl as if to form CO_2 spontaneously and the remaining Mn-CO bonds bent significantly from linear to suggest weakening of the metal-carbonyl bonding (Fig. 3.68c). Thus, ^{6}***I*****7** is primed for the release of two CO's and the formation of carbon dioxide. While there are undoubtedly other mechanisms both for CO release and for CO_2 formation in this complicated system, it is notable that long wavelength

photolysis of **1** in aerobic media generally releases two CO's per complex and nearly one CO_2, as predicted by the calculations.

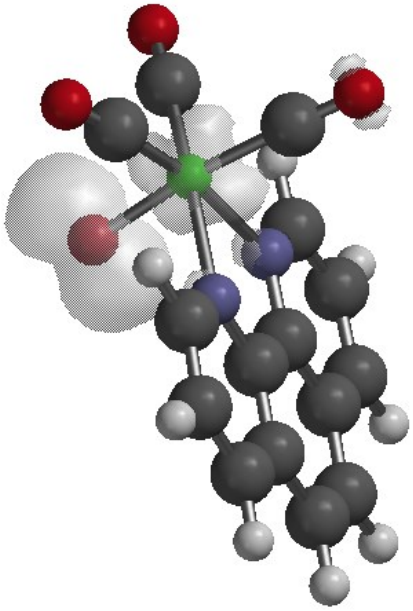

Figure 3.68a. Spin density map of ^{2}[OMn(CO)$_3$(phen)] ($^2\boldsymbol{I}_7$) from TD-DFT calculation.

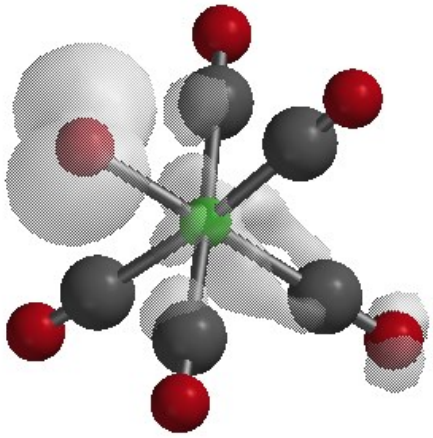

Figure 3.68b. Spin density map of $^{2}[ORe(CO)_5]$ ($^{2}\boldsymbol{I_6}$) from TD-DFT calculation.

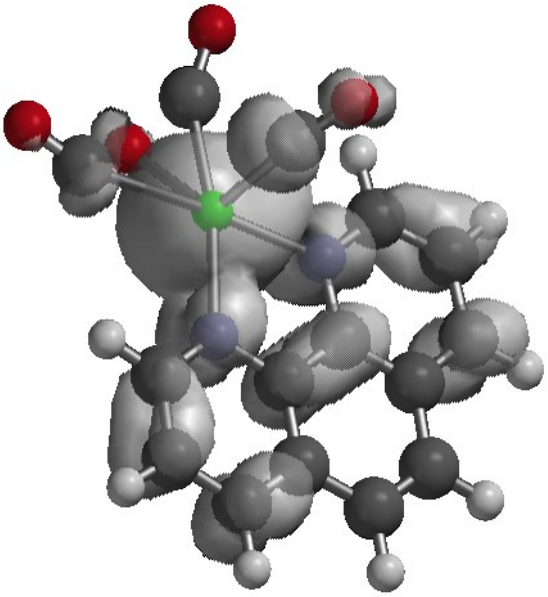

Figure 3.68c. Spin density map of $^{6}[OMn(CO)_3(phen)]$ ($^{6}\boldsymbol{I_7}$) from DFT calculation.

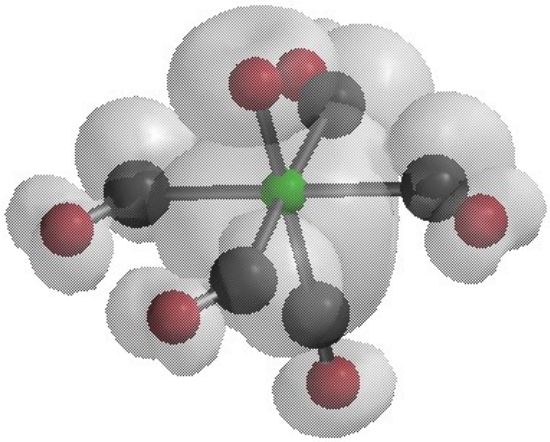

Figure 3.68d. Spin density map of $^{6}[ORe(CO)_5]$ ($^{6}\boldsymbol{I_6}$) from DFT calculation.

V. Biocompatible polymer carriers for photoCORMs delivery

A. Poly(lactic-co-glycolic acid) (PLGA)

To deliver the hydrophobic versions of these dinuclear complexes (**1** to **4**), the biocompatible polymer poly(lactic-co-glycolic acid) (PLGA) was used as a matrix in the form of nano/micro particles. PLGA is a copolymer synthesized by ring-opening polymerization of two monomers, the cyclic dimers of glycolic acid (1,4-dioxane-2,5-diones) and lactic acid in the form of random polymer or block co-polymer (Fig. 3.69). It has been approved by the Food and Drug Administration (FDA) and is widely used in coating of therapeutic devices owing to its biocompatible and biodegradable properties.

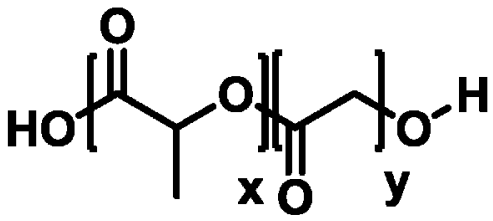

Figure 3.69 General chemical structure of poly(lactic-co-glycolic acid) (PLGA).

Since PLGA has ester group between two monomers, it will be hydrolyzed in aqueous solution in physiological conditions. Its degradation time shows dependence on the ratios between lactic acid and glycolic acid. PLGA degrades the faster with higher content of lactic units. However, an exception is observed that 50:50 ratio of lactic and glycolic gives highest degradation rate (two months). End cap groups also have effect on degradation time: carboxylic acid end-capped ones have shorter degradation time.

After degradation, lactic acid and glycolic acid are the only two products, and these are also products from metabolism in body. Therefore, for PLGA, there is minimal toxicity expected from this biomaterial.

B. Synthesis and characterization of upconverting nanoparticles (UCNPs)

Since photoCORMs **1** and **2** only absorb up to 680 nm, it is necessary to develop strategies to achieve their near infrared light activation (higher penetration in tissue). Previously, our laboratory described a strategy to trigger small molecule release with NIR light using carriers incorporating lanthanide-doped upconverting nanoparticles (UCNPs) which have multi-photon excitation property[4,7,33,42]. Different from organic dyes and quantum dots that simultaneously absorb two or more photons through virtual states, UCNPs sequentially absorb a second photon through long lifetime and ladder like states of lanthanide ions to achieve photon upconversion (anti-Stokes shift emission). Therefore, low power continuous wave irradiation can be used in the UCNPs, and it also has a much higher upconverting efficiency than simultaneous upconversion.

The UCNPs synthesized have following structure: core, $NaYF_4$:Yb/Gd/Nd/Er (30/20/1/0.5%) and shell, $NaGdF_4$:Nd (20%). $NaYF_4$ and $NaGdF_4$ were used as matrix material for their low phonon energy. Nd^{3+} is used as a dopant for near infrared light absorption and Er^{3+} is visible emitter. The shell is used to reduce surface quenching. As shown in scheme 3.4, Nd^{3+} ions absorb 794 nm photons and transfer the energy through Yb^{3+} to Er^{3+}. When Er^{3+} is excited to higher energy states, it emits at 520 nm and 540 nm (Figure 3.70) as well as at other wavelengths. Similar to Er^{3+} doped UCNPs, Tm^{3+} doped UCNPs were also

synthesized with the composition: NaYF4:Yb/Gd/Nd/Tm (30/20/1/0.5%) @NaGdF4:Nd (20%) for shorter wavelength emission (465 nm and 470 nm).

Scheme **3.4** Energy transfer pathway in UCNP: $NaYF_4$:Yb/Gd/Nd/Er (30/20/1/0.5%) @$NaGdF_4$:Nd (20%)

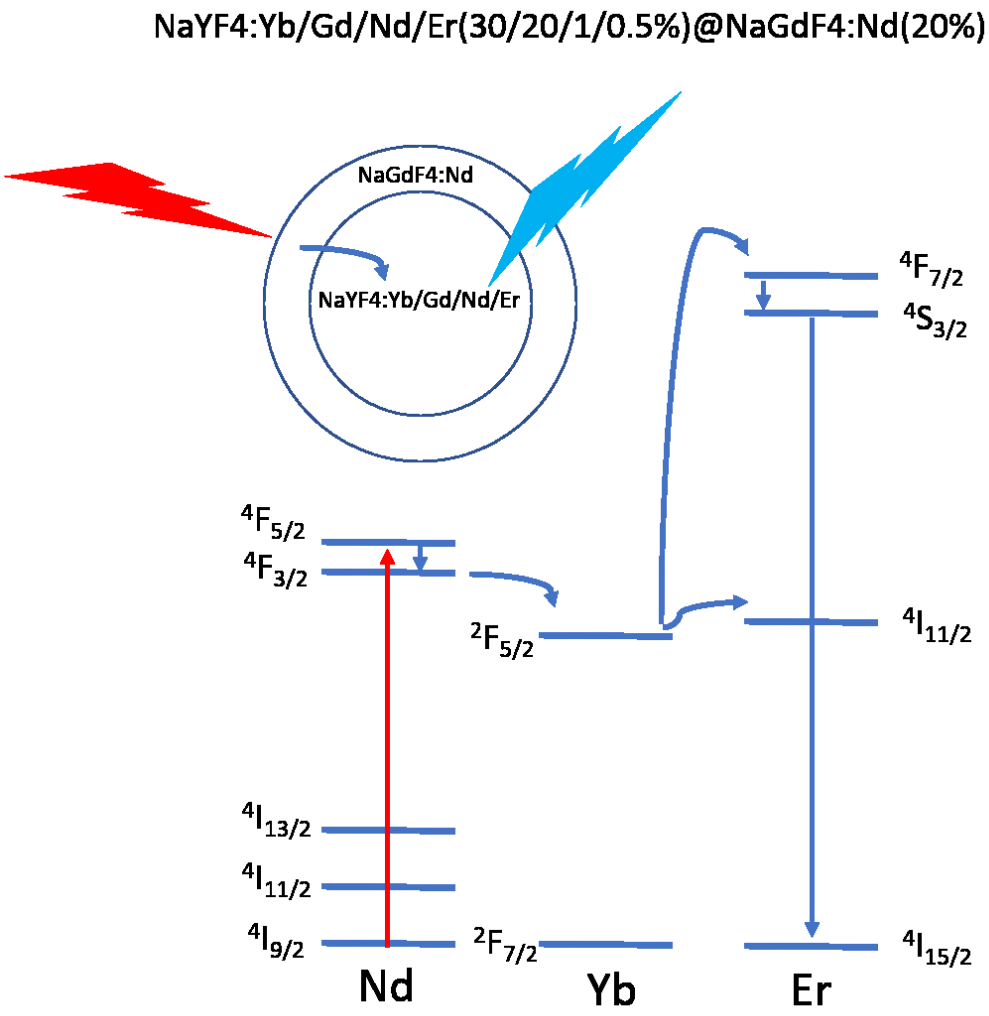

Synthesis of the UCNPs was done using the nanomaterial synthesis robot WANDA (Automated Nanomaterials Discovery and Analysis) at the Molecular Foundry of the Lawrence Berkeley National Lab with Dr. Emory Chan. Stock solution of lanthanide precursors in oleic acid and octadecene (see table 3.5) were heated to 140 °C under vacuum (< 50 mTorr) to remove water and oxygen. Then the flask with stock solution was backfilled with nitrogen and heated to 180 °C. After it was cooled to room temperature, the stock solution was transferred into the glovebox. Na oleate, NH_4F, oleic acid and octadecene were added into the stock solution (see table 3.5). Nucleation was done automatically by the robot with a heating ramp to 310 °C. Active shell with composite ($NaGdF_4$ and Nd (20%)) was synthesized on the Tm and Er-UCNPs.

Table 3.5 Receipts for the UCNPs

Core: $NaYF_4$:Yb/Gd/Nd/Er (30/20/1/0.5%)	**Chemical**	**Mol**	**Mass (g)**	**Volume (ml)**	**Mole fraction**
	stock solution				
	YCl_3	2.43E-04	0.0474		0.485
	$YbCl_3$	1.50E-04	0.0419		0.3
	$NdCl_3$	5.00E-06	0.0013		0.01
	$ErCl_3$	2.50E-06	0.0007		0.005
	$GdCl_3$	1.00E-04	0.0264		0.2
	oleic acid (stock)	9.50E-03	2.6834	3.00	
	ODE (stock)	6.23E-03	1.5730	1.99	
			4.3739		
	add in glovebox				
	Na oleate	1.25E-03	0.3806		
	NH_4F	2.00E-03	0.0741		
	oleic acid	2.00E-03	0.5649	0.63	
	ODE	1.39E-02	3.5000	4.44	
	Total		**13.2673**	**10.06**	

Core: $NaYF_4$:Yb/Gd/Nd/Tm (30/20/1/0.5%)	**Chemical**	**Mol**	**Mass (g)**	**Volume (ml)**	**Mole fraction**
	stock solution				
	YCl_3	2.43E-04	0.0474		0.485
	$YbCl_3$	1.50E-04	0.0419		0.3
	$NdCl_3$	5.00E-06	0.0013		0.01
	$TmCl_3$	2.50E-06	0.0007		0.005
	$GdCl_3$	1.00E-04	0.0264		0.2
	oleic acid (stock)	9.50E-03	2.6834	3.00	0.485
	ODE (stock)	6.23E-03	1.5730	1.99	
			4.3739		
	add in glovebox				
	Na oleate	1.25E-03	0.3806		
	NH_4F	2.00E-03	0.0741		
	oleic acid	2.00E-03	0.5649	0.63	
	ODE	1.39E-02	3.5000	4.44	
	Total		**13.2673**	**10.06**	

Shell: $NaGdF_4$:Nd (20%)	**Chemical**	**Mol**	**Mass (g)**	**Volume (ml)**	**Mole fraction**
	$GdCl_3$	0.0032	0.8436		0.8
	$NdCl_3$	0.0008	0.2006		0.2
	oleic acid (stock)		7.16	8	
	ODE (stock)		9.468	12	
	Core				
	Chemical	**Mol**	**mass (g)**	**volume (ml)**	**Concentration (M)**
	oleic acid (stock)		3.5800	4	
	ODE (stock)		4.7340	6	
	UCNPs				
	NaTFA				0.2

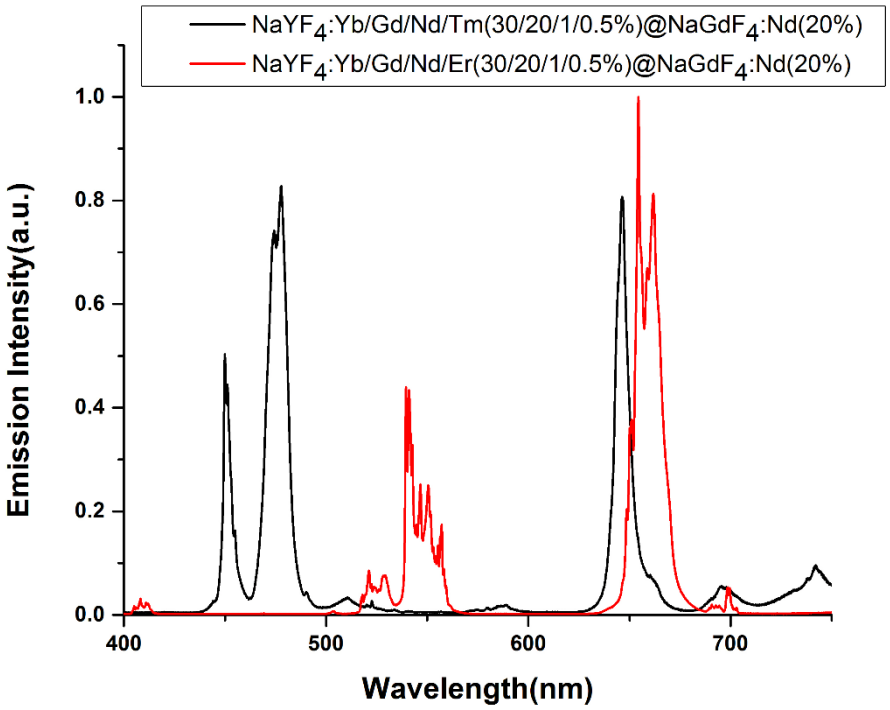

Figure 3.70 Emission spectra of the Er-UCNPs and the Tm-UCNPs with 800nm excitation.

From XRD spectra (Fig. 3.71), both Er-UCNP and Tm-UCNP show estimated particles sizes of 12 ± 2 nm. TEM images of the Tm-UCNPs core and core/shell were also taken which show a core size of 10 ± 2 nm and a core/shell size of 12 ± 2 nm (Fig. 3.72 and Fig. 3.73). Although core-only TEM images were not performed on the Er-UCNPs, it should have ~2nm shell thickness due to using same shell recipe.

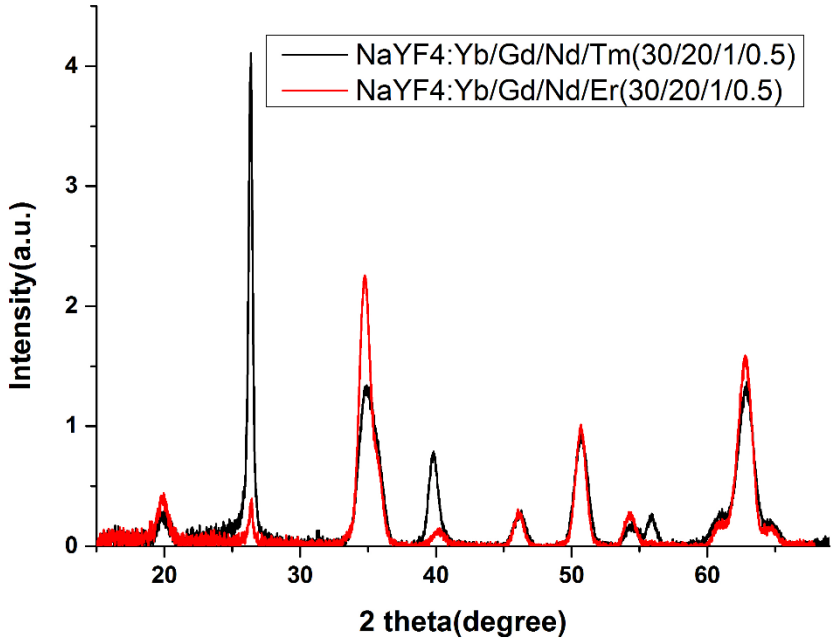

Figure 3.71 X-ray diffraction (XRD) of Er-UCNP and Tm-UCNP.

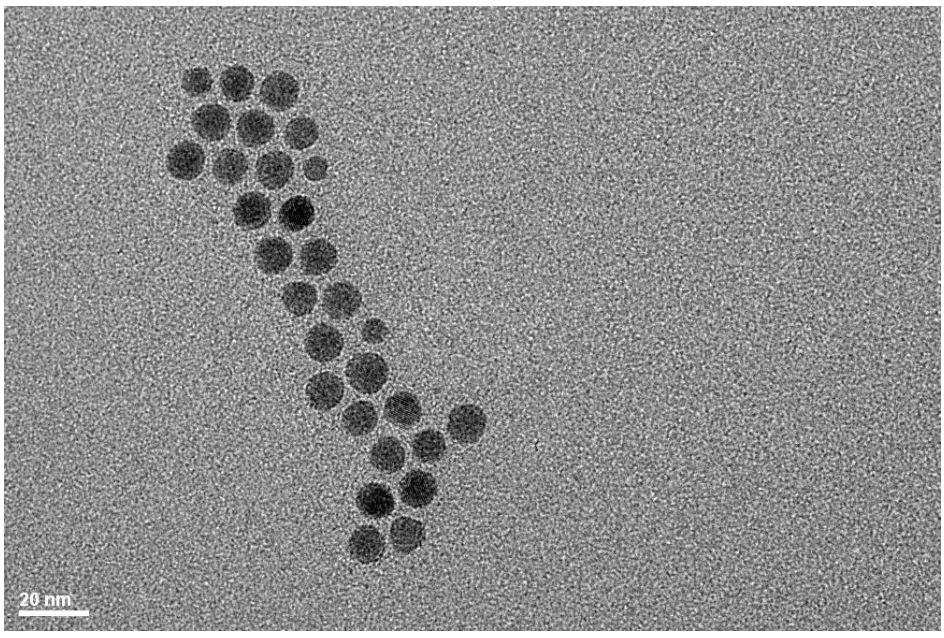

Figure 3.72 Transition electron microscope (TEM) image of the Tm-UCNPs core.

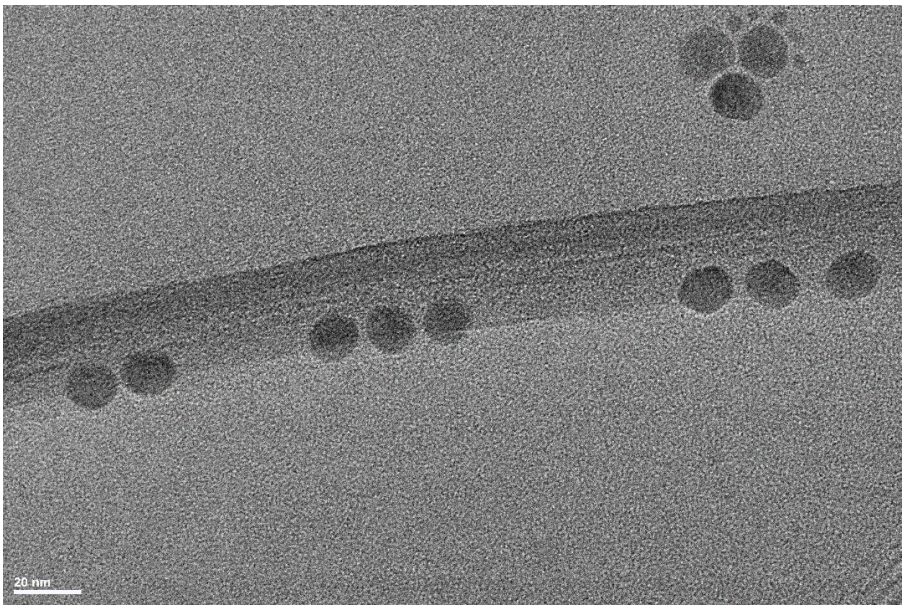

Figure 3.73 Transition electron microscope (TEM) image of the Tm-UCNPs with core/shell structure.

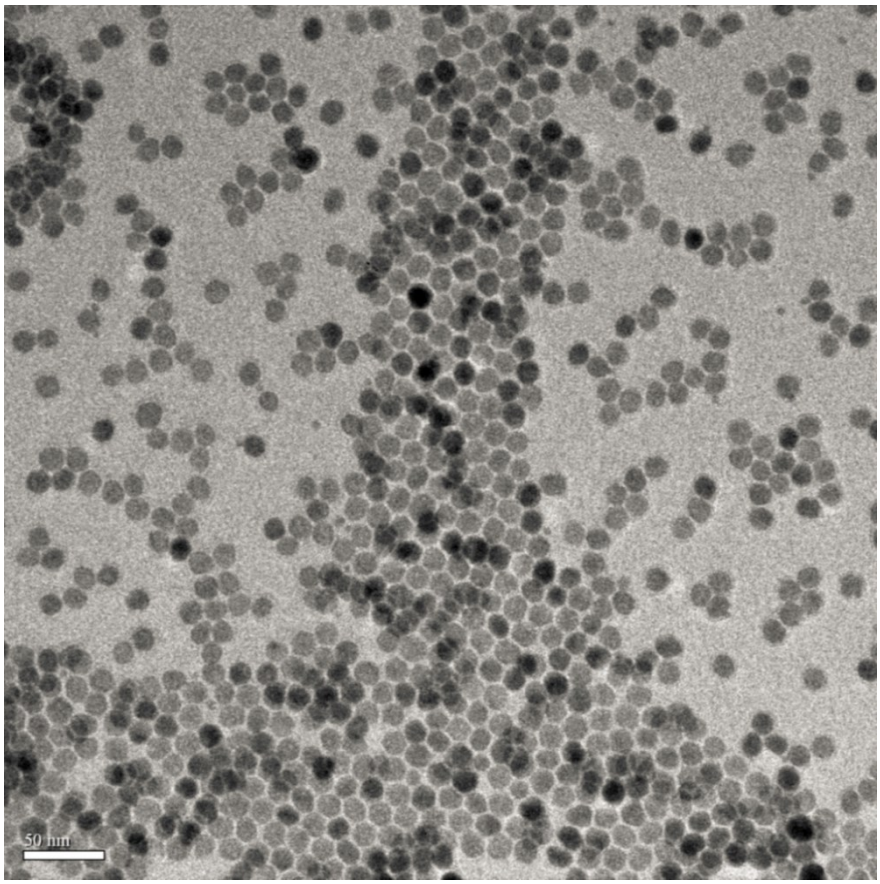

Figure 3.74 Transition electron microscope (TEM) image of the Er-UCNPs with core/shell structure.

C. Synthesis and characterization of PLGA microparticles and nanoparticles with photoCORMs

The PLGA microparticles and nanoparticles were both synthesized using an emulsion solvent evaporation method. To synthesize PLGA microparticles, PLGA (Resomer ® RG 752H Poly (D.L-lactide Co-glycotide)) (100 mg) and compound **1** (26 mg) were dissolved in 2 ml of DCM followed by sonication in room temperature water bath. After PLGA and **1** were dissolved, the solution was added into 100 mL of 1% aqueous polyvinyl alcohol (PVA) solution and the resulting solution was simultaneously sonicated for 30 s. The resulting emulsion was taken out by pipette leaving out floating bulk PLGA on the surface and precipitate at the bottom, and was then allowed to gently stir overnight to evaporate the DCM. The particles were collected by centrifugation at 6000 rpm for 15 mins, and then they particles were washed with nanopure water for 3 times by centrifuging at 6000 rpm to remove PVA. Nanopure water was added and the resulting suspension was centrifuged at 300 rpm and the supernatant was collected to give microparticles with sizes of 6 ± 3 μm according to the optical microscope (Figure 3.75).

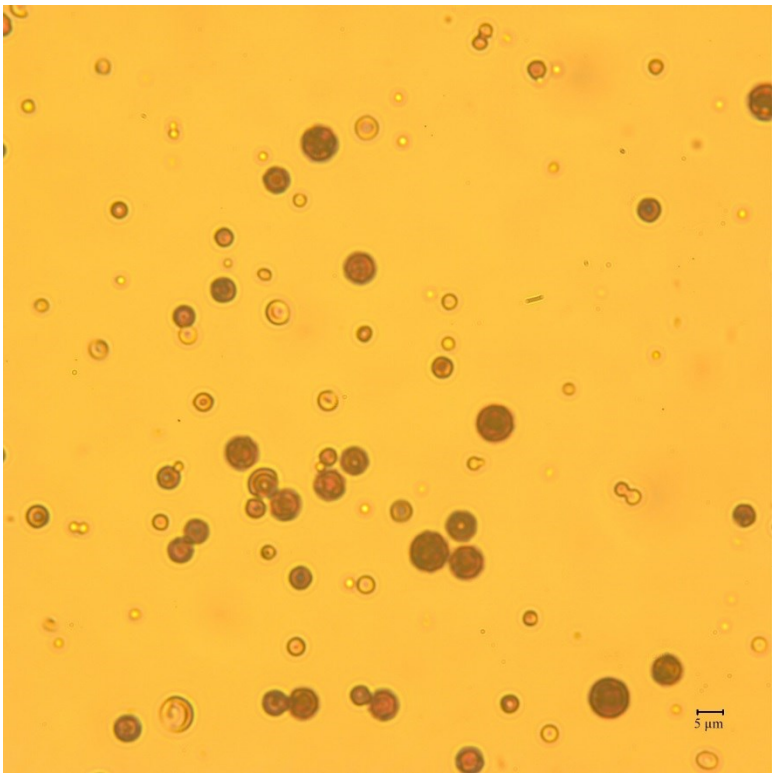

Figure 3.75 Optical microscope image of PLGA microparticles of **1**

In a Schlenk cuvette, gas release from aqueous suspension of compound **1** PLGA microparticles was measured by GC-TCD after 659 nm exhaustive photolysis. Figure 3.76 shows the GC signal of gas in the headspace above the aqueous suspension. Release of CO and CO_2 were observed. Although with sizes of 6 ± 3 μm, the microcarriers could cause clogging in blood vessel, this experimental result serves as a-proof-of-concept that the hydrophobic dinuclear complexes in PLGA microcarriers can be triggered by long wavelength light and release CO from the microcarriers.

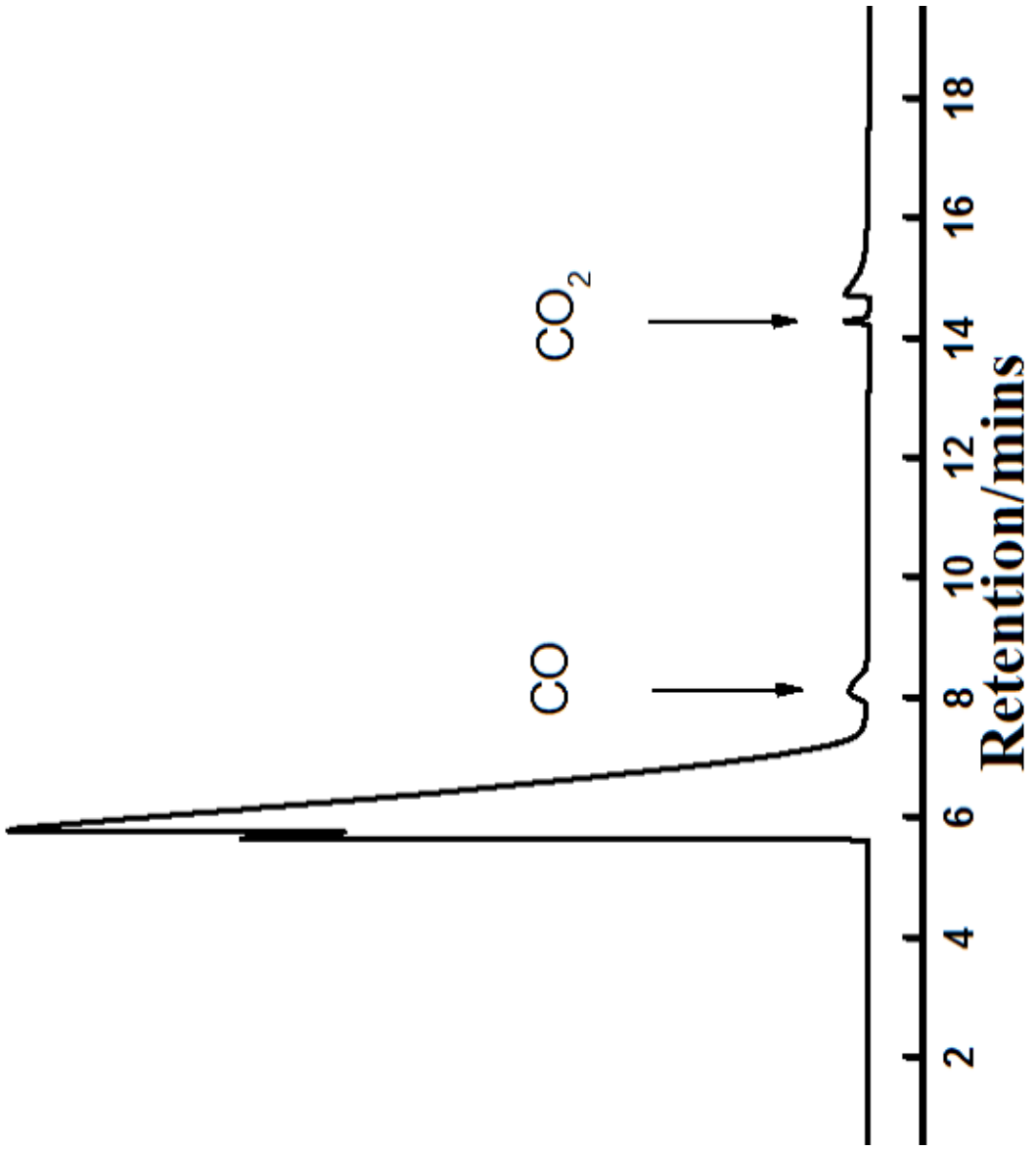

Figure 3.76 GC-TCD analysis of compound **1** PLGA microparticles aqueous suspension after 659 nm exhaustive photolysis.

In order to prepare the PLGA nanoparticles containing UCNPs, PLGA (Resomer ® RG 752H Poly (D.L-lactide Co-glycotide)) (100 mg), compound **1** (14 mg) and Er-UCNPs (10 mg in 0.1 mL hexane) were dissolved in 1.3 mL of DCM followed by sonication in room temperature water bath. After the PLGA and the CO donor dissolved, the solution was added

into 100 mL 2% aqueous polyvinyl alcohol (PVA) solution, and the resulting solution was simultaneously sonicated for 30 s. The emulsion was then allowed to gently stir overnight to evaporate the DCM. In a similar to the microparticle preparation, these nanoparticles were also purified by centrifugation. After centrifuging down at 8000 rpm, these nanoparticles were repeatedly washed (6X) by suspending in nano pure water followed by centrifuging at 8000 rpm to remove supernatant (residue PVA). Then the collected particles were added nanopure water and centrifuged at 4000 rpm (3 times) and the supernatant was collected and dried under vacuum to give particles. SEM was performed on the resulting particles, from which particles show size of 100 nm-250 nm (Fig. 3.77).

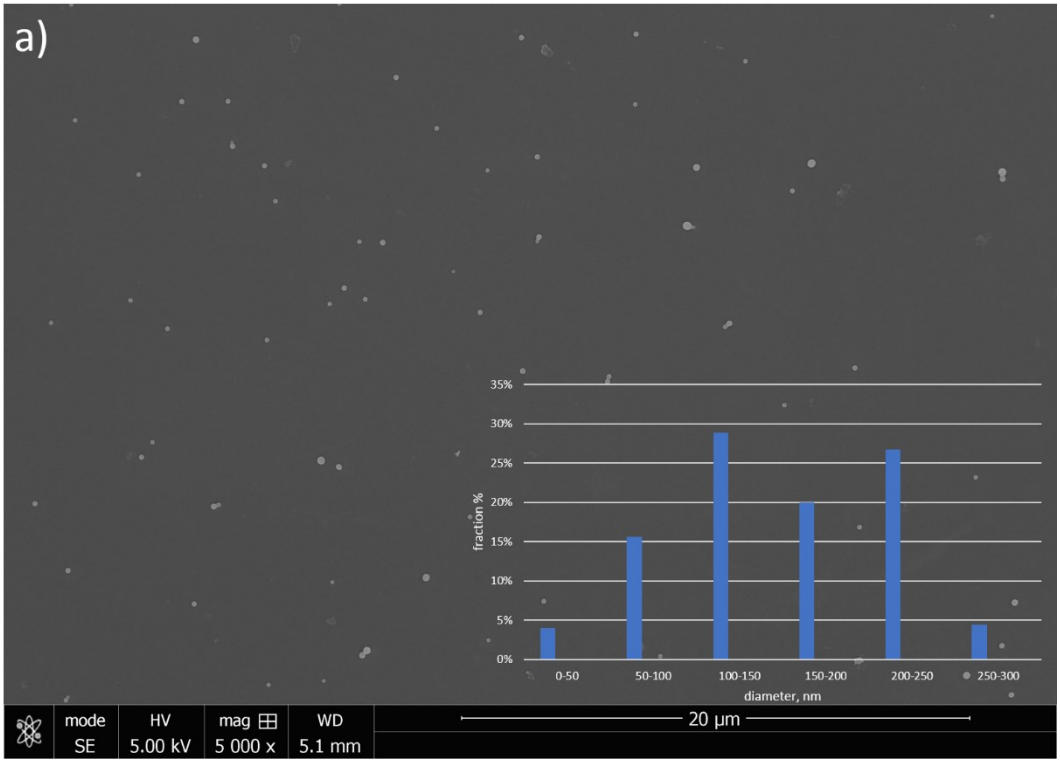

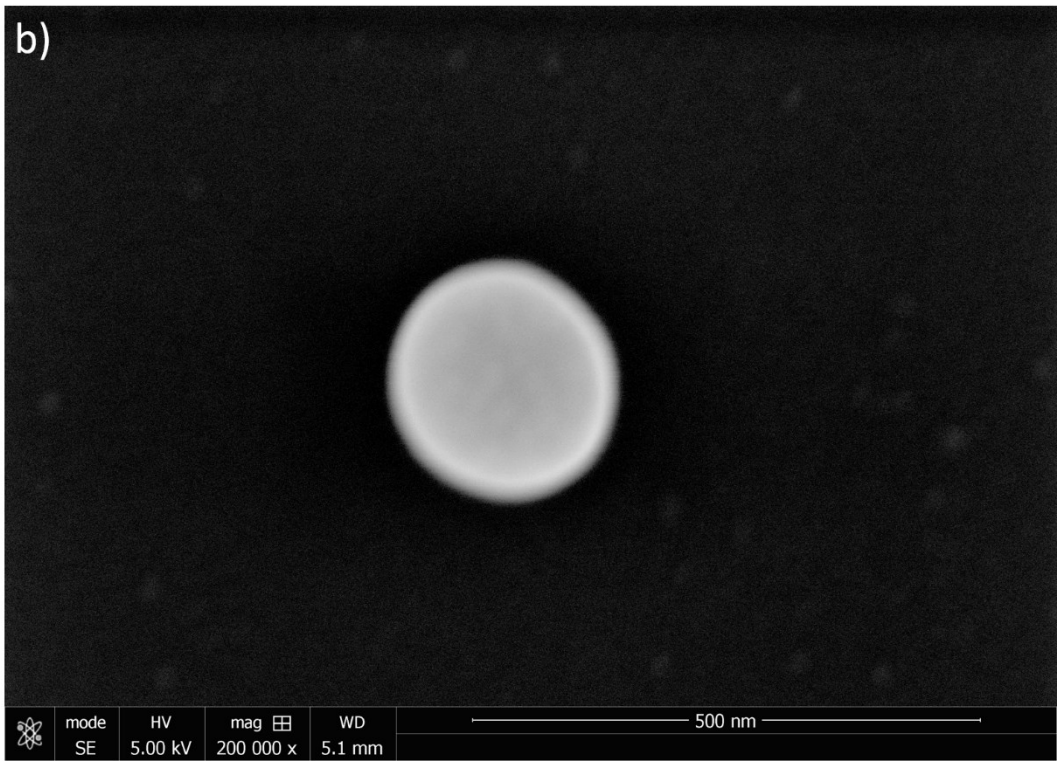

Figure 3.77 SEM images of PLGA nanoparticles with compound **1** and Er-UCNP.

VI. Summary and future study

By exploiting metal-metal bond labilization upon MMLCT excitation of dinuclear rhenium-manganese carbonyls in aerobic media, we have developed a new strategy for photo-uncaging CO by long-wavelength red or NIR light. For complex **1,** deep-red excitation of the $\sigma_{MM} \rightarrow \pi_L^*$ transition leads to homolytic cleavage of the Re-Mn bond. Dioxygen trapping of the resulting $Mn(CO)_3(phen)$ radical results eventually in the release of two CO's and the apparent oxidation of one to CO_2. By rational ligand modification, the MMLCT absorption bands can be extended to the near-infrared (e.g. compounds **3** and **4)** where photochemical reactivity and CO uncaging are seen with 794 nm excitation. Although, the Φ_{CO} values determined at this excitation wavelength are modest, the phenanthroline carboxaldehyde complex **4** illustrates the potential for further functionalization. Not only is this compound photoactive at NIR wavelengths, but it also can be conjugated to an amine-terminated PEG oligomer to give a water soluble derivative. Continuing studies are directed along several related pathways. The most obvious will be to explore using the hydrophobic versions of these dinuclear complexes with biocompatible polymer matrices as their drug delivery systems in the form of nano/micro carriers or as implantable disks. A second will be to exploit ligand modifications to enhance aqueous solubility and/or to attach targeting molecules such as certain peptide oligomers[41] to provide spatio-temporal control of CO delivery to specific cellular types or tissues.

References

1. König, K. Multiphoton Microscopy in Life Sciences. *Journal of Microscopy* **2000**, 200, 83–104.

2. Peng, P.; Wang, C.; Shi, Z.; K. Johns, V.; Ma, L.; Oyer, J.; Copik, A.; Igarashi, R.; Liao, Y. Visible-Light Activatable Organic CO-Releasing Molecules (PhotoCORMs) That Simultaneously Generate Fluorophores. *Organic & Biomolecular Chemistry* **2013**, 11, 6671–6674.

3. Palao, E.; Slanina, T.; Muchová, L.; Šolomek, T.; Vítek, L.; Klán, P. Transition-Metal-Free CO-Releasing BODIPY Derivatives Activatable by Visible to NIR Light as Promising Bioactive Molecules. *J. Am. Chem. Soc.* **2016**, 138, 126–133.

4. Pierri, A. E.; Huang, P.-J.; Garcia, J. V.; Stanfill, J. G.; Chui, M.; Wu, G.; Zheng, N.; Ford, P. C. A photoCORM Nanocarrier for CO Release Using NIR Light. *Chem. Commun*. **2015**, 51, 2072.

5. Kottelat, E.; Ruggi, A.; Zobi, F. Red-Light Activated photoCORMs of Mn(I) Species Bearing Electron Deficient 2,2′-Azopyridines. *Dalton Trans*. **2016**, 45, 6920–6927.

6. Ford, P. C. Polychromophoric Metal Complexes for Generating the Bioregulatory Agent Nitric Oxide by Single- and Two-Photon Excitation. *Acc. Chem. Res*. **2008**, 41, 190–200.

7. Garcia, J. V.; Zhang, F.; Ford, P. C. Multi-Photon Excitation in Uncaging the Small Molecule Bioregulator Nitric Oxide. *Phil. Trans. R. Soc. A* **2013**, 371, 20120129.

8. Wrighton, M.; Bredesen, D. Symmetrical Cleavage of the Metal-Metal Bond in decacarbonyldirhenium(0) by Ultraviolet Irradiation. *Journal of Organometallic Chemistry* **1973**, 50, C35–C38.

9. Morse, D. L.; Wrighton, M. S. Photochemistry of Metal-Metal Bonded Complexes. 5. Cleavage of the M-M Bond in $(OC)_5M$-$M(CO)_3L$ by Irradiation into a Low-Lying M .fwdarw. L Charge-Transfer Band. *J. Am. Chem. Soc*. **1976**, 98, 3931–3934.

10. Rimmer, R. D.; Richter, H.; Ford, P. C. A Photochemical Precursor for Carbon Monoxide Release in Aerated Aqueous Media. *Inorg. Chem*. **2009**, 49, 1180–1185.

11. Almond, M. J.; Orrin, R. H. Photo-Oxidation of $[Re_2(CO)_{10}]$ in Low-Temperature Matrices Containing O_2. *J. Chem. Soc., Dalton Trans*. **1992**, 7, 1229–1234.

12. Sazonov, P. K.; Ivushkin, V. A.; Khrustalev, V. N.; Kolotyrkina, N. G.; Beletskaya, I. P. A Halogenophilic Pathway in the Reactions of Transition Metal Carbonyl Anions with $[(\eta 6\text{-iodobenzene})Cr(CO)_3]$. *Dalton Trans*. **2014**, 43, 13392–13398.

13. Bossmann, S. H.; Ghatlia, N. D.; Ottaviani, M. F.; Turro, C.; Dürr, H.; Turro, N. J. Synthesis and Characterization of Nitroxide-Linked Ruthenium Complexes as Molecular Probes for Microheterogeneous *Environments. Synthesis*, **1996**, 1313–1319.

14. Kurtz, D. A.; Dhakal, B.; Hulme, R. J.; Nichol, G. S.; Felton, G. A. N. Correlations between Photophysical and Electrochemical Properties for a Series of New Mn Carbonyl Complexes Containing Substituted Phenanthroline Ligands. *Inorganica Chimica Acta* **2015**, 427, 22–26.

15. Fei, H.; Sampson, M. D.; Lee, Y.; Kubiak, C. P.; Cohen, S. M. Photocatalytic CO2 Reduction to Formate Using a Mn(I) Molecular Catalyst in a Robust Metal–Organic Framework. *Inorg. Chem*. **2015**, 54, 6821–6828.

16. Bourrez, M.; Molton, F.; Chardon-Noblat, S.; Deronzier, A. [Mn(bipyridyl)$(CO)_3$Br]: An Abundant Metal Carbonyl Complex as Efficient Electrocatalyst for CO_2 Reduction. *Angew. Chem. Int. Ed*. **2011**, 50, 9903–9906.

17. Dessy, R. E.; Weissman, P. M. Organometallic Electrochemistry. VIII. The Formation of Metal-Metal Bonds. *J. Am. Chem. Soc*. **1966**, 88, 5124–5129.

18. Morse, D. L.; Wrighton, M. S. Reaction of Pentacarbonyl-Manganese(-1) and -Rhenium(-1) with Metal Carbonyl Halide Derivatives. *Journal of Organometallic Chemistry* **1977**, 125, 71–77.

19. Staal, L. H.; Van Koten, G.; Vrieze, K. Binuclear Metal Carbonyl Dab Complexes : II. The Syntheses and Coordination Properties of Mn(CO)5M′(CO)3DAB (M′ = Mn, Re; DAB = 1,4-Diazabutadiene). *Journal of Organometallic Chemistry* **1979**, 175, 73–86.

20. Male, J. L.; Lindfors, B. E.; Covert, K. J.; Tyler, D. R. The Effect of Radical Size and Mass on the Cage Recombination Efficiency of Photochemically Generated Radical Cage Pairs. *J. Am. Chem. Soc*. **1998**, 120, 13176–13186.

21. Oelkers, A. B.; Tyler, D. R. Radical Cage Effects: A Method for Measuring Recombination Efficiencies of Secondary Geminate Radical Cage Pairs Using Pump–probe Transient Absorption Methods. *Photochem. Photobiol. Sci*. **2008**, 7, 1386–1390.

22. Kokkes, M. W.; Snoeck, T. L.; Stufkens, D. J.; Oskam, A.; Cristophersen, M.; Stam, C. H. Structural and Spectroscopic Properties of [(CO)5MM′ (CO)3(R-DAB)] (M,M′=Mn,Re; R-DAB=1,4-Diaza-1,3-Butadiene Complexes. X-Ray Structure of [(CO)5ReMn(CO)3-(I-Pr-DAB)] and Infrared and Resonance Raman Spectra of [(CO)5MM′(CO)3(R-DAB)]. *Journal of Molecular Structure* **1985**, 131, 11–29.

23. Van Outersterp, J. W. M.; Hartl, F.; Stufkens, D. J. Variable Temperature IR Spectroelectrochemical Investigation of the Stability of the Metal-Metal-Bonded Radical Anions [(CO)5MnRe(CO)3(L)].bul.- (L = 2,2'-Bipyridine (BPY), 2,2'-Bipyrimidine (BPYM), 2,3-Bis(2-Pyridyl)pyrazine (DPP)) and [(CO)5MnRe(CO)3(L)Re(Br)(CO)3].bul.- (L = BPYM, DPP) Controlled by the Lowest .pi. (.alpha.-Diimine) Orbital Energy. *Organometallics* **1995**, 14, 3303–3310.

24. Geoffroy, G. L.; Wrighton, M. S. Organometallic Photochemistry; Academic Press, New York, **1979**.

25. Luong, J. C.; Faltynek, R. A.; Wrighton, M. S. Competitive Radiative Decay and Metal-Metal Bond Cleavage from the Lowest Excited State of Triphenyltin- and Triphenylgermanium tricarbonyl(1,10-Phenanthroline)rhenium. *J. Am. Chem. Soc*. **1979**, 101, 1597–1598.

26. McCullen, S. B.; Brown, T. L. Photochemical Reaction of Decacarbonyldimanganese with Pyridine: Evidence for a Radical Pathway. *Inorg. Chem*. **1981**, 20, 3528–3533.

27. Kokkes, M. W.; Stufkens, D. J.; Oskam, A. Photochemistry of Metal-Metal-Bonded Complexes. 1. MLCT Photolysis of (CO)5MM'(CO)3(.alpha.-Diimine) (M, M' = Mn, Re) in 2-MeTHF between 133 and 230 K. *Inorg. Chem*. **1985**, 24, 2934–2942.

28. Greenwood, N. N.; Earnshaw, A. Chemistry of the Elements; Pergamon Press, Oxford, UK, **1993**.

29. Achord, J. M.; Hussey, C. L. Determination of Dissolved Oxygen in Nonaqueous Electrochemical Solvents. *Anal. Chem*. **1980**, 52, 601–602.

30. Laine, R. M.; Ford, P. C. Reactivity of Metal Radicals Generated Photochemically. Effects of Solvent and of Trapping Agent Concentrations on Quantum Yields for Photolysis of Hexacarbonylbis(.pi.-cyclopentadienyl)ditungsten(I), [.pi.-CpW(CO)3]2. *Inorg. Chem*. **1977**, 16 (2), 388–391.

31. Church, S. P.; Poliakoff, M.; Timney, J. A.; Turner, J. J. Synthesis and Characterization of the pentacarbonylmanganese(0) Radical, Mn(CO)5, in Low-Temperature Matrixes. *J. Am. Chem. Soc*. **1981**, 103, 7515–7520.

32. Church, S. P.; Hermann, H.; Grevels, F.-W.; Schaffner, K. The Primary Photoproducts of Mn2(CO)10: Direct I.r. Observation and Decay Kinetics of Mn(CO)5 and Mn2(CO)9 in Hydrocarbon Solution at Room Temperature. J. Chem. Soc., *Chem. Commun*. **1984**, 12, 785–786.

33. Burks, P. T.; Garcia, J. V.; GonzalezIrias, R.; Tillman, J. T.; Niu, M.; Mikhailovsky, A. A.; Zhang, J.; Zhang, F.; Ford, P. C. Nitric Oxide Releasing Materials Triggered

by Near-Infrared Excitation Through Tissue Filters. *J. Am. Chem. Soc*. **2013**, 135, 18145–18152.

34. Timko, B. P.; Arruebo, M.; Shankarappa, S. A.; McAlvin, J. B.; Okonkwo, O. S.; Mizrahi, B.; Stefanescu, C. F.; Gomez, L.; Zhu, J.; Zhu, A.; Santamaria, J.; Langer, R.; Kohane, D. S. Near-Infrared–actuated Devices for Remotely Controlled Drug Delivery. *Proc Natl Acad Sci* U S A **2014**, 111, 1349–1354.

35. D. Mase, J.; O. Razgoniaev, A.; K. Tschirhart, M.; D. Ostrowski, A. Light-Controlled Release of Nitric Oxide from Solid Polymer Composite Materials Using Visible and near Infra-Red Light. *Photochemical & Photobiological Sciences* **2015**, 14, 775–785.

36. Sugahara, K. N.; Teesalu, T.; Karmali, P. P.; Kotamraju, V. R.; Agemy, L.; Girard, O. M.; Hanahan, D.; Mattrey, R. F.; Ruoslahti, E. Tissue-Penetrating Delivery of Compounds and Nanoparticles into Tumors. *Cancer Cell* **2009**, 16, 510–520.

37. Chung, E. J.; Cheng, Y.; Morshed, R.; Nord, K.; Han, Y.; Wegscheid, M. L.; Auffinger, B.; Wainwright, D. A.; Lesniak, M. S.; Tirrell, M. V. Fibrin-Binding, Peptide Amphiphile Micelles for Targeting Glioblastoma. *Biomaterials* **2014**, 35, 1249–1256.

38. Fieldhouse, S. A.; Fullam, B. W.; Neilson, G. W.; Symons, M. C. R. Reaction of Metal Carbonyls with Oxygen. *J. Chem. Soc., Dalton Trans*. **1974**, 6, 567–569.

39. Mach, K.; Nováková, J.; Raynor, J. B. Electron Spin Resonance Spectroscopy of Mn(CO)5 · Radicals Generated in the Gas Phase Thermolysis of $Mn_2(CO)_{10}$. *Journal of Organometallic Chemistry* **1992**, 439, 341–345.

40. Lindsell, W. E.; Preston, P. N. Electron Spin Resonance Investigations of the Photo-Oxidation of Decacarbonyldimanganese and Related Complexes. *J. Chem. Soc., Dalton Trans*. **1979**, 6, 1105–1108.

41. S. Levy, E.; P. Morales, D.; V. Garcia, J.; O. Reich, N.; C. Ford, P. Near-IR Mediated Intracellular Uncaging of NO from Cell Targeted Hollow Gold Nanoparticles. *Chemical Communications* **2015**, 51, 17692–17695.

42. Garcia, J. V.; Yang, J.; Shen, D.; Yao, C.; Li, X.; Wang, R.; Stucky, G. D.; Zhao, D.; Ford, P. C.; Zhang, F. NIR-Triggered Release of Caged Nitric Oxide Using Upconverting Nanostructured Materials. *Small* **2012**, 8, 3800–3805.

Appendix

Appendix A Crystallographic parameters crystal data of $(CO)_5ReMn(CO)_3(phen)$ (**1**)

Table A1. Crystal data and structure refinement for **1**.

Identification code	b01302015_0m
Empirical formula	C20 H8 Mn N2 O8 Re
Formula weight	645.42
Temperature	100(2) K
Wavelength	0.71073 Å
Crystal system	Triclinic
Space group	P-1
Unit cell dimensions	a = 9.6988(9) Å □α = 88.928(2)°. b = 11.1599(10) Å □β = 84.634(3)°. c = 18.8156(16) Å γ = 74.441(2)°. □□□□□□□□□□□□□□□□□□
Volume	1953.3(3) $Å^3$
Z	4
Density (calculated)	2.195 Mg/m^3
Absorption coefficient	6.892 mm^{-1}
F(000)	1224
Crystal size	0.200 x 0.100 x 0.050 mm^3
Theta range for data collection	1.087 to 28.279°.
Index ranges	-8<=h<=12, -14<=k<=14, -25<=l<=25
Reflections collected	21418
Independent reflections	9653 [R(int) = 0.0402]
Completeness to theta = 25.242°	100.0 %
Absorption correction	Semi-empirical from equivalents
Max. and min. transmission	0.7457 and 0.5219
Refinement method	Full-matrix least-squares on F^2
Data / restraints / parameters	9653 / 0 / 577
Goodness-of-fit on F^2	0.988
Final R indices [I>2sigma(I)]	R1 = 0.0297, wR2 = 0.0612
R indices (all data)	R1 = 0.0429, wR2 = 0.0660
Extinction coefficient	n/a
Largest diff. peak and hole	1.197 and -1.361 $e.Å^{-3}$

Table A2. Atomic coordinates (x 104) and equivalent isotropic displacement parameters (Å2x 103)
for **1**. U(eq) is defined as one third of the trace of the orthogonalized Uij tensor.

	x	y	z	U(eq)
C(1)	4708(5)	6828(4)	5992(2)	14(1)
C(2)	5509(4)	6590(4)	7275(2)	13(1)
C(3)	4083(5)	8632(4)	6841(2)	10(1)
C(4)	8511(5)	5211(4)	7187(2)	16(1)
C(5)	6697(5)	4213(4)	6362(2)	18(1)
C(6)	9684(5)	3799(4)	5880(2)	14(1)
C(7)	7435(5)	5533(4)	5181(2)	13(1)
C(8)	9222(5)	6489(4)	5985(2)	13(1)
C(9)	7262(4)	8448(4)	7678(2)	12(1)
C(10)	8008(5)	9216(4)	7943(2)	14(1)
C(11)	8546(5)	10011(4)	7499(2)	15(1)
C(12)	8308(5)	10041(4)	6776(2)	13(1)
C(13)	8807(5)	10825(4)	6260(2)	14(1)
C(14)	8533(5)	10820(4)	5563(2)	15(1)
C(15)	7703(4)	10030(4)	5319(2)	11(1)
C(16)	7392(5)	9971(4)	4613(2)	13(1)
C(17)	6571(4)	9199(4)	4443(2)	12(1)
C(18)	6065(4)	8499(4)	4981(2)	12(1)
C(19)	7188(4)	9269(4)	5825(2)	9(1)
C(20)	7506(4)	9260(4)	6547(2)	10(1)
C(21)	5953(5)	3101(4)	8225(2)	12(1)
C(22)	4579(4)	1748(4)	7766(2)	12(1)
C(23)	5185(5)	1584(4)	9083(2)	13(1)
C(24)	3261(5)	21(4)	8718(2)	15(1)
C(25)	200(5)	959(4)	9096(2)	13(1)
C(26)	2267(5)	1719(4)	9881(2)	15(1)
C(27)	752(5)	3466(4)	9023(2)	12(1)
C(28)	1492(5)	1880(4)	7839(2)	14(1)
C(29)	3868(4)	3943(4)	10020(2)	11(1)
C(30)	3418(5)	4921(4)	10512(2)	14(1)
C(31)	2721(5)	6097(4)	10297(2)	14(1)
C(32)	2457(4)	6279(4)	9573(2)	12(1)
C(33)	1751(5)	7459(4)	9272(2)	15(1)
C(34)	1488(5)	7567(4)	8587(2)	15(1)
C(35)	1904(4)	6509(4)	8114(2)	12(1)
C(36)	1672(4)	6558(4)	7387(2)	12(1)
C(37)	2142(4)	5488(4)	6981(2)	12(1)
C(38)	2832(4)	4372(4)	7295(2)	12(1)
C(39)	2617(4)	5349(4)	8384(2)	9(1)
C(40)	2906(4)	5240(4)	9115(2)	8(1)

Mn(1)	5736(1)	7544(1)	6515(1)	9(1)
Mn(2)	4257(1)	2794(1)	8514(1)	9(1)
N(1)	6989(4)	8450(3)	6989(2)	9(1)
N(2)	6372(4)	8499(3)	5658(2)	10(1)
N(3)	3619(4)	4076(3)	9327(2)	10(1)
N(4)	3079(4)	4279(3)	7983(2)	8(1)
O(1)	3983(4)	6448(3)	5649(2)	23(1)
O(2)	5302(3)	6041(3)	7780(2)	17(1)
O(3)	2965(3)	9210(3)	7080(2)	16(1)
O(4)	8756(4)	5221(3)	7762(2)	26(1)
O(5)	5891(4)	3630(3)	6461(2)	23(1)
O(6)	10609(4)	2954(3)	5707(2)	21(1)
O(7)	9863(3)	7199(3)	5887(2)	17(1)
O(8)	7066(3)	5723(3)	4627(2)	19(1)
O(9)	7086(3)	3168(3)	8015(2)	18(1)
O(10)	4822(3)	1102(3)	7265(2)	17(1)
O(11)	5831(3)	849(3)	9455(2)	20(1)
O(12)	4123(3)	-893(3)	8642(2)	21(1)
O(13)	-747(3)	538(3)	9230(2)	19(1)
O(14)	2506(4)	1824(3)	10453(2)	21(1)
O(15)	195(3)	4487(3)	9129(2)	18(1)
O(16)	1281(4)	2057(3)	7252(2)	22(1)
Re(1)	8111(1)	5227(1)	6157(1)	10(1)
Re(2)	1790(1)	1668(1)	8873(1)	10(1)

Table A3. Bond lengths [Å] and angles [°] for **1**.

C(1)-O(1)	1.159(5)
C(1)-Mn(1)	1.801(4)
C(2)-O(2)	1.151(5)
C(2)-Mn(1)	1.800(4)
C(3)-O(3)	1.158(5)
C(3)-Mn(1)	1.794(4)
C(4)-O(4)	1.129(5)
C(4)-Re(1)	2.011(4)
C(5)-O(5)	1.144(5)
C(5)-Re(1)	2.008(5)
C(6)-O(6)	1.142(5)
C(6)-Re(1)	1.928(4)
C(7)-O(8)	1.132(5)
C(7)-Re(1)	1.999(4)
C(8)-O(7)	1.134(5)
C(8)-Re(1)	1.995(4)
C(9)-N(1)	1.347(5)

C(9)-C(10)	1.387(6)
C(9)-H(9)	0.9500
C(10)-C(11)	1.377(6)
C(10)-H(10)	0.9500
C(11)-C(12)	1.400(6)
C(11)-H(11)	0.9500
C(12)-C(20)	1.411(6)
C(12)-C(13)	1.432(6)
C(13)-C(14)	1.361(6)
C(13)-H(13)	0.9500
C(14)-C(15)	1.450(6)
C(14)-H(14)	0.9500
C(15)-C(16)	1.395(6)
C(15)-C(19)	1.408(5)
C(16)-C(17)	1.381(6)
C(16)-H(16)	0.9500
C(17)-C(18)	1.399(5)
C(17)-H(17)	0.9500
C(18)-N(2)	1.335(5)
C(18)-H(18)	0.9500
C(19)-N(2)	1.372(5)
C(19)-C(20)	1.421(5)
C(20)-N(1)	1.377(5)
C(21)-O(9)	1.154(5)
C(21)-Mn(2)	1.801(4)
C(22)-O(10)	1.165(5)
C(22)-Mn(2)	1.795(4)
C(23)-O(11)	1.157(5)
C(23)-Mn(2)	1.804(4)
C(24)-O(12)	1.134(5)
C(24)-Re(2)	2.008(5)
C(25)-O(13)	1.145(5)
C(25)-Re(2)	1.924(4)
C(26)-O(14)	1.137(5)
C(26)-Re(2)	1.999(4)
C(27)-O(15)	1.135(5)
C(27)-Re(2)	2.002(4)
C(28)-O(16)	1.145(5)
C(28)-Re(2)	1.994(4)
C(29)-N(3)	1.345(5)
C(29)-C(30)	1.395(6)
C(29)-H(29)	0.9500
C(30)-C(31)	1.378(6)
C(30)-H(30)	0.9500
C(31)-C(32)	1.409(6)
C(31)-H(31)	0.9500

C(32)-C(40)	1.404(6)
C(32)-C(33)	1.445(6)
C(33)-C(34)	1.335(6)
C(33)-H(33)	0.9500
C(34)-C(35)	1.437(6)
C(34)-H(34)	0.9500
C(35)-C(39)	1.405(5)
C(35)-C(36)	1.406(6)
C(36)-C(37)	1.375(6)
C(36)-H(36)	0.9500
C(37)-C(38)	1.395(5)
C(37)-H(37)	0.9500
C(38)-N(4)	1.334(5)
C(38)-H(38)	0.9500
C(39)-N(4)	1.371(5)
C(39)-C(40)	1.426(5)
C(40)-N(3)	1.370(5)
Mn(1)-N(1)	2.047(3)
Mn(1)-N(2)	2.054(3)
Mn(1)-Re(1)	3.0039(7)
Mn(2)-N(4)	2.046(3)
Mn(2)-N(3)	2.050(3)
Mn(2)-Re(2)	3.0071(7)

O(1)-C(1)-Mn(1)	175.3(4)
O(2)-C(2)-Mn(1)	175.8(4)
O(3)-C(3)-Mn(1)	171.7(4)
O(4)-C(4)-Re(1)	178.3(4)
O(5)-C(5)-Re(1)	178.3(4)
O(6)-C(6)-Re(1)	179.0(4)
O(8)-C(7)-Re(1)	178.6(4)
O(7)-C(8)-Re(1)	179.5(4)
N(1)-C(9)-C(10)	123.0(4)
N(1)-C(9)-H(9)	118.5
C(10)-C(9)-H(9)	118.5
C(11)-C(10)-C(9)	120.8(4)
C(11)-C(10)-H(10)	119.6
C(9)-C(10)-H(10)	119.6
C(10)-C(11)-C(12)	118.6(4)
C(10)-C(11)-H(11)	120.7
C(12)-C(11)-H(11)	120.7
C(11)-C(12)-C(20)	117.5(4)
C(11)-C(12)-C(13)	124.1(4)
C(20)-C(12)-C(13)	118.3(4)
C(14)-C(13)-C(12)	121.5(4)
C(14)-C(13)-H(13)	119.2

C(12)-C(13)-H(13)	119.2
C(13)-C(14)-C(15)	121.0(4)
C(13)-C(14)-H(14)	119.5
C(15)-C(14)-H(14)	119.5
C(16)-C(15)-C(19)	118.1(4)
C(16)-C(15)-C(14)	124.0(4)
C(19)-C(15)-C(14)	117.9(4)
C(17)-C(16)-C(15)	119.0(4)
C(17)-C(16)-H(16)	120.5
C(15)-C(16)-H(16)	120.5
C(16)-C(17)-C(18)	119.4(4)
C(16)-C(17)-H(17)	120.3
C(18)-C(17)-H(17)	120.3
N(2)-C(18)-C(17)	123.6(4)
N(2)-C(18)-H(18)	118.2
C(17)-C(18)-H(18)	118.2
N(2)-C(19)-C(15)	123.1(4)
N(2)-C(19)-C(20)	116.2(3)
C(15)-C(19)-C(20)	120.7(4)
N(1)-C(20)-C(12)	123.8(4)
N(1)-C(20)-C(19)	115.7(4)
C(12)-C(20)-C(19)	120.5(4)
O(9)-C(21)-Mn(2)	172.8(4)
O(10)-C(22)-Mn(2)	177.0(4)
O(11)-C(23)-Mn(2)	176.1(4)
O(12)-C(24)-Re(2)	177.6(4)
O(13)-C(25)-Re(2)	179.9(4)
O(14)-C(26)-Re(2)	175.9(4)
O(15)-C(27)-Re(2)	177.4(4)
O(16)-C(28)-Re(2)	176.8(4)
N(3)-C(29)-C(30)	122.9(4)
N(3)-C(29)-H(29)	118.5
C(30)-C(29)-H(29)	118.5
C(31)-C(30)-C(29)	120.4(4)
C(31)-C(30)-H(30)	119.8
C(29)-C(30)-H(30)	119.8
C(30)-C(31)-C(32)	118.4(4)
C(30)-C(31)-H(31)	120.8
C(32)-C(31)-H(31)	120.8
C(40)-C(32)-C(31)	117.7(4)
C(40)-C(32)-C(33)	117.8(4)
C(31)-C(32)-C(33)	124.4(4)
C(34)-C(33)-C(32)	121.8(4)
C(34)-C(33)-H(33)	119.1
C(32)-C(33)-H(33)	119.1
C(33)-C(34)-C(35)	121.2(4)

C(33)-C(34)-H(34)	119.4
C(35)-C(34)-H(34)	119.4
C(39)-C(35)-C(36)	117.1(4)
C(39)-C(35)-C(34)	118.7(4)
C(36)-C(35)-C(34)	124.2(4)
C(37)-C(36)-C(35)	119.2(4)
C(37)-C(36)-H(36)	120.4
C(35)-C(36)-H(36)	120.4
C(36)-C(37)-C(38)	119.9(4)
C(36)-C(37)-H(37)	120.0
C(38)-C(37)-H(37)	120.0
N(4)-C(38)-C(37)	123.2(4)
N(4)-C(38)-H(38)	118.4
C(37)-C(38)-H(38)	118.4
N(4)-C(39)-C(35)	123.9(4)
N(4)-C(39)-C(40)	116.2(3)
C(35)-C(39)-C(40)	119.9(4)
N(3)-C(40)-C(32)	123.8(3)
N(3)-C(40)-C(39)	115.6(4)
C(32)-C(40)-C(39)	120.6(4)
C(3)-Mn(1)-C(2)	87.93(18)
C(3)-Mn(1)-C(1)	88.18(19)
C(2)-Mn(1)-C(1)	92.14(19)
C(3)-Mn(1)-N(1)	93.80(16)
C(2)-Mn(1)-N(1)	95.00(16)
C(1)-Mn(1)-N(1)	172.65(16)
C(3)-Mn(1)-N(2)	100.73(15)
C(2)-Mn(1)-N(2)	170.00(17)
C(1)-Mn(1)-N(2)	93.11(16)
N(1)-Mn(1)-N(2)	79.57(13)
C(3)-Mn(1)-Re(1)	164.54(13)
C(2)-Mn(1)-Re(1)	78.90(14)
C(1)-Mn(1)-Re(1)	84.30(14)
N(1)-Mn(1)-Re(1)	95.37(10)
N(2)-Mn(1)-Re(1)	93.17(10)
C(22)-Mn(2)-C(21)	87.12(18)
C(22)-Mn(2)-C(23)	92.10(18)
C(21)-Mn(2)-C(23)	88.90(18)
C(22)-Mn(2)-N(4)	94.53(16)
C(21)-Mn(2)-N(4)	94.10(15)
C(23)-Mn(2)-N(4)	172.85(17)
C(22)-Mn(2)-N(3)	172.40(16)
C(21)-Mn(2)-N(3)	98.16(16)
C(23)-Mn(2)-N(3)	93.45(16)
N(4)-Mn(2)-N(3)	79.71(13)
C(22)-Mn(2)-Re(2)	81.82(13)

C(21)-Mn(2)-Re(2)	166.36(13)
C(23)-Mn(2)-Re(2)	83.57(13)
N(4)-Mn(2)-Re(2)	94.71(9)
N(3)-Mn(2)-Re(2)	93.65(9)
C(9)-N(1)-C(20)	116.3(3)
C(9)-N(1)-Mn(1)	129.1(3)
C(20)-N(1)-Mn(1)	114.3(3)
C(18)-N(2)-C(19)	116.8(3)
C(18)-N(2)-Mn(1)	129.1(3)
C(19)-N(2)-Mn(1)	114.0(2)
C(29)-N(3)-C(40)	116.7(3)
C(29)-N(3)-Mn(2)	129.1(3)
C(40)-N(3)-Mn(2)	114.1(2)
C(38)-N(4)-C(39)	116.8(3)
C(38)-N(4)-Mn(2)	129.0(3)
C(39)-N(4)-Mn(2)	113.8(3)
C(6)-Re(1)-C(8)	96.26(17)
C(6)-Re(1)-C(7)	95.17(17)
C(8)-Re(1)-C(7)	89.96(16)
C(6)-Re(1)-C(5)	93.63(18)
C(8)-Re(1)-C(5)	170.06(17)
C(7)-Re(1)-C(5)	88.12(17)
C(6)-Re(1)-C(4)	95.36(17)
C(8)-Re(1)-C(4)	88.00(17)
C(7)-Re(1)-C(4)	169.43(18)
C(5)-Re(1)-C(4)	92.11(17)
C(6)-Re(1)-Mn(1)	176.37(12)
C(8)-Re(1)-Mn(1)	80.81(12)
C(7)-Re(1)-Mn(1)	82.73(12)
C(5)-Re(1)-Mn(1)	89.27(13)
C(4)-Re(1)-Mn(1)	86.71(13)
C(25)-Re(2)-C(28)	94.40(17)
C(25)-Re(2)-C(26)	95.51(17)
C(28)-Re(2)-C(26)	169.06(17)
C(25)-Re(2)-C(27)	99.00(17)
C(28)-Re(2)-C(27)	88.54(17)
C(26)-Re(2)-C(27)	85.35(17)
C(25)-Re(2)-C(24)	94.82(17)
C(28)-Re(2)-C(24)	93.32(17)
C(26)-Re(2)-C(24)	90.45(18)
C(27)-Re(2)-C(24)	165.88(17)
C(25)-Re(2)-Mn(2)	179.39(13)
C(28)-Re(2)-Mn(2)	85.13(12)
C(26)-Re(2)-Mn(2)	84.93(12)
C(27)-Re(2)-Mn(2)	80.60(12)
C(24)-Re(2)-Mn(2)	85.60(12)

Symmetry transformations used to generate equivalent atoms:

Table A4. Anisotropic displacement parameters (Å2x 103) for **1**. The anisotropic displacement factor exponent takes the form: -2□2[h2 a*2U11 + ... + 2 h k a* b* U12]

	U11	U22	U33	U23	U13	U12
C(1)	16(2)	10(2)	16(2)	2(2)	1(2)	-4(2)
C(2)	8(2)	10(2)	22(2)	3(2)	-3(2)	-2(2)
C(3)	17(2)	10(2)	5(2)	4(1)	-3(2)	-5(2)
C(4)	14(2)	14(2)	19(2)	3(2)	-1(2)	-4(2)
C(5)	21(2)	12(2)	15(2)	0(2)	3(2)	4(2)
C(6)	22(2)	9(2)	11(2)	1(2)	1(2)	-6(2)
C(7)	14(2)	7(2)	18(2)	0(2)	2(2)	-4(2)
C(8)	12(2)	10(2)	12(2)	-2(2)	2(2)	3(2)
C(9)	14(2)	14(2)	8(2)	4(2)	0(2)	-4(2)
C(10)	18(2)	16(2)	7(2)	-1(2)	-1(2)	-6(2)
C(11)	16(2)	14(2)	17(2)	1(2)	-4(2)	-8(2)
C(12)	13(2)	10(2)	14(2)	1(2)	1(2)	-1(2)
C(13)	21(2)	9(2)	16(2)	3(2)	-5(2)	-7(2)
C(14)	16(2)	13(2)	15(2)	5(2)	2(2)	-6(2)
C(15)	9(2)	6(2)	16(2)	5(2)	0(2)	1(2)
C(16)	15(2)	12(2)	10(2)	4(2)	0(2)	-1(2)
C(17)	15(2)	9(2)	9(2)	5(2)	-1(2)	-1(2)
C(18)	11(2)	9(2)	15(2)	-1(2)	-2(2)	-1(2)
C(19)	6(2)	9(2)	10(2)	2(1)	1(2)	0(2)
C(20)	9(2)	11(2)	11(2)	2(2)	0(2)	-3(2)
C(21)	21(2)	8(2)	9(2)	0(1)	-5(2)	-5(2)
C(22)	8(2)	11(2)	18(2)	5(2)	-2(2)	-5(2)
C(23)	12(2)	14(2)	13(2)	-4(2)	4(2)	-5(2)
C(24)	9(2)	23(2)	15(2)	1(2)	2(2)	-10(2)
C(25)	17(2)	11(2)	10(2)	-5(2)	-1(2)	-2(2)
C(26)	16(2)	12(2)	17(2)	2(2)	3(2)	-6(2)
C(27)	12(2)	14(2)	10(2)	2(2)	0(2)	-4(2)
C(28)	11(2)	17(2)	14(2)	-5(2)	1(2)	-7(2)
C(29)	13(2)	13(2)	9(2)	3(2)	-5(2)	-8(2)
C(30)	17(2)	21(2)	6(2)	0(2)	1(2)	-11(2)
C(31)	13(2)	18(2)	15(2)	-4(2)	-1(2)	-9(2)
C(32)	9(2)	10(2)	17(2)	1(2)	-1(2)	-5(2)
C(33)	13(2)	14(2)	18(2)	-5(2)	-1(2)	-3(2)
C(34)	10(2)	10(2)	23(2)	-1(2)	-1(2)	-1(2)
C(35)	6(2)	13(2)	17(2)	2(2)	-2(2)	-3(2)

C(36)	12(2)	12(2)	12(2)	4(2)	-3(2)	-2(2)
C(37)	10(2)	16(2)	10(2)	1(2)	-2(2)	-3(2)
C(38)	12(2)	12(2)	10(2)	-1(2)	2(2)	-5(2)
C(39)	8(2)	10(2)	10(2)	-2(2)	4(2)	-5(2)
C(40)	4(2)	13(2)	8(2)	2(1)	0(1)	-4(2)
Mn(1)	10(1)	8(1)	8(1)	1(1)	0(1)	-3(1)
Mn(2)	10(1)	8(1)	9(1)	1(1)	0(1)	-3(1)
N(1)	10(2)	6(2)	12(2)	1(1)	0(1)	-1(1)
N(2)	12(2)	6(2)	9(2)	0(1)	1(1)	1(1)
N(3)	10(2)	13(2)	8(2)	1(1)	2(1)	-5(1)
N(4)	7(2)	9(2)	9(2)	1(1)	1(1)	-6(1)
O(1)	27(2)	28(2)	19(2)	-1(1)	-1(1)	-20(2)
O(2)	18(2)	16(2)	18(2)	9(1)	1(1)	-6(1)
O(3)	17(2)	14(2)	15(2)	1(1)	1(1)	-1(1)
O(4)	26(2)	38(2)	20(2)	7(2)	-6(2)	-15(2)
O(5)	22(2)	20(2)	29(2)	4(1)	4(1)	-11(2)
O(6)	22(2)	12(2)	24(2)	4(1)	5(1)	-1(1)
O(7)	16(2)	17(2)	19(2)	4(1)	0(1)	-7(1)
O(8)	24(2)	18(2)	14(2)	-2(1)	-2(1)	-6(1)
O(9)	15(2)	22(2)	18(2)	0(1)	3(1)	-12(1)
O(10)	18(2)	15(2)	18(2)	-8(1)	1(1)	-5(1)
O(11)	21(2)	16(2)	20(2)	6(1)	-3(1)	0(1)
O(12)	18(2)	16(2)	25(2)	-1(1)	4(1)	-2(1)
O(13)	19(2)	22(2)	19(2)	-4(1)	4(1)	-13(2)
O(14)	31(2)	21(2)	14(2)	3(1)	-2(1)	-8(2)
O(15)	14(2)	16(2)	21(2)	2(1)	4(1)	-3(1)
O(16)	26(2)	27(2)	16(2)	3(1)	-4(1)	-11(2)
Re(1)	11(1)	8(1)	10(1)	1(1)	1(1)	-2(1)
Re(2)	11(1)	10(1)	10(1)	1(1)	0(1)	-5(1)

Table A5. Hydrogen coordinates (x 104) and isotropic displacement parameters (Å2x 10 3) for **1**.

	x	y	z	U(eq)
H(9)	6928	7895	7997	14
H(10)	8151	9193	8436	16
H(11)	9068	10529	7680	18
H(13)	9341	11361	6407	17
H(14)	8892	11342	5233	18
H(16)	7741	10456	4255	16

H(17)	6350	9143	3966	14
H(18)	5472	7996	4858	14
H(29)	4372	3148	10181	13
H(30)	3593	4775	10998	16
H(31)	2425	6769	10628	17
H(33)	1467	8178	9570	19
H(34)	1017	8359	8408	18
H(36)	1196	7320	7177	15
H(37)	1996	5508	6489	15
H(38)	3142	3644	7006	14

Table A6. Torsion angles [°] for **1**.

N(1)-C(9)-C(10)-C(11)	-1.6(7)
C(9)-C(10)-C(11)-C(12)	0.8(7)
C(10)-C(11)-C(12)-C(20)	0.9(6)
C(10)-C(11)-C(12)-C(13)	179.9(4)
C(11)-C(12)-C(13)-C(14)	-179.5(4)
C(20)-C(12)-C(13)-C(14)	-0.5(6)
C(12)-C(13)-C(14)-C(15)	1.0(7)
C(13)-C(14)-C(15)-C(16)	-179.5(4)
C(13)-C(14)-C(15)-C(19)	0.0(6)
C(19)-C(15)-C(16)-C(17)	1.5(6)
C(14)-C(15)-C(16)-C(17)	-179.0(4)
C(15)-C(16)-C(17)-C(18)	0.3(6)
C(16)-C(17)-C(18)-N(2)	-2.3(6)
C(16)-C(15)-C(19)-N(2)	-1.5(6)
C(14)-C(15)-C(19)-N(2)	178.9(4)
C(16)-C(15)-C(19)-C(20)	178.1(4)
C(14)-C(15)-C(19)-C(20)	-1.5(6)
C(11)-C(12)-C(20)-N(1)	-2.1(6)
C(13)-C(12)-C(20)-N(1)	178.9(4)
C(11)-C(12)-C(20)-C(19)	178.2(4)
C(13)-C(12)-C(20)-C(19)	-0.9(6)
N(2)-C(19)-C(20)-N(1)	1.8(5)
C(15)-C(19)-C(20)-N(1)	-177.9(4)
N(2)-C(19)-C(20)-C(12)	-178.4(4)
C(15)-C(19)-C(20)-C(12)	1.9(6)
N(3)-C(29)-C(30)-C(31)	-1.9(6)
C(29)-C(30)-C(31)-C(32)	0.9(6)
C(30)-C(31)-C(32)-C(40)	0.9(6)
C(30)-C(31)-C(32)-C(33)	-179.4(4)
C(40)-C(32)-C(33)-C(34)	1.9(6)
C(31)-C(32)-C(33)-C(34)	-177.7(4)
C(32)-C(33)-C(34)-C(35)	-0.3(7)

C(33)-C(34)-C(35)-C(39)	-0.8(6)
C(33)-C(34)-C(35)-C(36)	-179.4(4)
C(39)-C(35)-C(36)-C(37)	0.1(6)
C(34)-C(35)-C(36)-C(37)	178.8(4)
C(35)-C(36)-C(37)-C(38)	0.3(6)
C(36)-C(37)-C(38)-N(4)	-0.4(6)
C(36)-C(35)-C(39)-N(4)	-0.5(6)
C(34)-C(35)-C(39)-N(4)	-179.3(4)
C(36)-C(35)-C(39)-C(40)	179.0(4)
C(34)-C(35)-C(39)-C(40)	0.3(6)
C(31)-C(32)-C(40)-N(3)	-2.1(6)
C(33)-C(32)-C(40)-N(3)	178.3(4)
C(31)-C(32)-C(40)-C(39)	177.3(4)
C(33)-C(32)-C(40)-C(39)	-2.4(6)
N(4)-C(39)-C(40)-N(3)	0.3(5)
C(35)-C(39)-C(40)-N(3)	-179.3(4)
N(4)-C(39)-C(40)-C(32)	-179.1(4)
C(35)-C(39)-C(40)-C(32)	1.4(6)
C(10)-C(9)-N(1)-C(20)	0.5(6)
C(10)-C(9)-N(1)-Mn(1)	-172.7(3)
C(12)-C(20)-N(1)-C(9)	1.3(6)
C(19)-C(20)-N(1)-C(9)	-178.9(4)
C(12)-C(20)-N(1)-Mn(1)	175.6(3)
C(19)-C(20)-N(1)-Mn(1)	-4.7(5)
C(17)-C(18)-N(2)-C(19)	2.3(6)
C(17)-C(18)-N(2)-Mn(1)	180.0(3)
C(15)-C(19)-N(2)-C(18)	-0.4(6)
C(20)-C(19)-N(2)-C(18)	-180.0(4)
C(15)-C(19)-N(2)-Mn(1)	-178.4(3)
C(20)-C(19)-N(2)-Mn(1)	2.0(4)
C(30)-C(29)-N(3)-C(40)	0.8(6)
C(30)-C(29)-N(3)-Mn(2)	177.0(3)
C(32)-C(40)-N(3)-C(29)	1.2(6)
C(39)-C(40)-N(3)-C(29)	-178.2(4)
C(32)-C(40)-N(3)-Mn(2)	-175.6(3)
C(39)-C(40)-N(3)-Mn(2)	5.1(4)
C(37)-C(38)-N(4)-C(39)	0.0(6)
C(37)-C(38)-N(4)-Mn(2)	-172.4(3)
C(35)-C(39)-N(4)-C(38)	0.5(6)
C(40)-C(39)-N(4)-C(38)	-179.1(3)
C(35)-C(39)-N(4)-Mn(2)	174.0(3)
C(40)-C(39)-N(4)-Mn(2)	-5.5(4)

Appendix B Crystallographic parameters crystal data of $(CO)_5ReMn(CO)_3(bpy)$ (**2**)

Table B1. Crystal data and structure refinement for **2**.

Identification code	new_0m	
Empirical formula	C18 H8 Mn N2 O8 Re	
Formula weight	621.40	
Temperature	100(2) K	
Wavelength	0.71073 Å	
Crystal system	Orthorhombic	
Space group	$P2_12_12_1$	
Unit cell dimensions	a = 9.0583(5) Å	□= 90°.
	b = 13.8780(8) Å	□= 90°.
	c = 45.661(3) Å	□= 90°.
Volume	5740.0(6) $Å^3$	
Z	12	
Density (calculated)	2.157 Mg/m^3	
Absorption coefficient	7.031 mm^{-1}	
F(000)	3528	
Crystal size	0.200 x 0.100 x 0.050 mm^3	
Theta range for data collection	0.892 to 26.821°.	
Index ranges	-11<=h<=11, -17<=k<=15, -57<=l<=56	
Reflections collected	28567	
Independent reflections	12147 [R(int) = 0.1055]	
Completeness to theta = 25.242°	99.4 %	
Absorption correction	Semi-empirical from equivalents	
Max. and min. transmission	0.7454 and 0.4707	
Refinement method	Full-matrix least-squares on F^2	
Data / restraints / parameters	12147 / 0 / 668	
Goodness-of-fit on F^2	0.933	
Final R indices [I>2sigma(I)]	R1 = 0.0531, wR2 = 0.1118	
R indices (all data)	R1 = 0.0795, wR2 = 0.1242	
Absolute structure parameter	-0.012(13)	
Extinction coefficient	0.00021(4)	
Largest diff. peak and hole	3.404 and -2.671 $e.Å^{-3}$	

Table B2. Atomic coordinates (x 10^4) and equivalent isotropic displacement parameters ($Å^2$x 10^3) for **2**. U(eq) is defined as one third of the trace of the orthogonalized U^{ij} tensor.

	x	y	z	U(eq)
C(1)	4030(30)	6478(15)	7645(5)	22(3)
C(2)	1220(30)	6631(15)	7908(4)	22(3)
C(3)	3050(20)	8360(15)	7768(4)	19(3)
C(4)	2500(20)	7626(15)	8353(5)	22(3)
C(5)	5340(30)	7445(13)	8133(4)	19(5)
C(6)	4370(20)	6007(14)	8559(5)	21(3)
C(7)	4280(20)	4217(15)	8476(4)	19(3)
C(8)	5410(20)	5288(14)	8092(5)	21(3)
C(9)	1060(20)	5647(14)	8691(4)	22(3)
C(10)	-350(20)	5585(15)	8790(5)	24(5)
C(11)	-1390(30)	5074(15)	8621(5)	27(5)
C(12)	-930(20)	4636(14)	8370(4)	19(4)
C(13)	560(20)	4736(14)	8281(5)	21(2)
C(14)	1100(20)	4346(15)	8009(5)	21(2)
C(15)	270(30)	3835(16)	7807(5)	27(5)
C(16)	880(30)	3495(15)	7556(5)	28(6)
C(17)	2410(30)	3643(16)	7521(5)	30(6)
C(18)	3170(30)	4135(13)	7724(4)	22(3)
C(19)	6110(30)	-881(14)	8697(5)	21(2)
C(20)	8820(30)	-1007(14)	8392(5)	21(2)
C(21)	8760(20)	-1611(15)	8983(4)	19(3)
C(22)	10260(20)	125(14)	8773(5)	21(2)
C(23)	7630(20)	301(14)	9097(5)	21(2)
C(24)	6660(20)	406(13)	8183(4)	17(4)
C(25)	5890(20)	1314(14)	8617(5)	20(5)
C(26)	6800(30)	2240(15)	8173(4)	22(4)
C(27)	8230(20)	2619(13)	8919(4)	17(4)
C(28)	9110(30)	3162(15)	9091(5)	31(6)
C(29)	10650(20)	3260(14)	9019(5)	23(5)
C(30)	11130(20)	2835(13)	8764(5)	20(4)
C(31)	10150(20)	2282(14)	8592(5)	17(2)
C(32)	10600(20)	1826(14)	8324(5)	17(2)
C(33)	12020(20)	1894(15)	8196(5)	23(5)
C(34)	12290(30)	1419(17)	7943(6)	37(7)
C(35)	11160(30)	913(16)	7799(5)	31(6)
C(36)	9790(30)	880(16)	7938(5)	26(5)
C(37)	1790(30)	3965(13)	9960(5)	22(5)
C(38)	3880(20)	5428(14)	10138(5)	20(2)
C(39)	3340(20)	5265(14)	9540(5)	20(2)

C(40)	4100(20)	3265(15)	9566(5)	20(2)
C(41)	4790(20)	3567(14)	10165(5)	17(4)
C(42)	6320(20)	4824(12)	9371(4)	14(3)
C(43)	8760(30)	5254(13)	9613(4)	19(4)
C(44)	7260(20)	3784(13)	9774(4)	14(3)
C(45)	6000(20)	7011(15)	9508(5)	20(3)
C(46)	5730(20)	7966(15)	9525(5)	20(3)
C(47)	5720(20)	8413(16)	9801(5)	23(4)
C(48)	6080(20)	7886(14)	10045(5)	23(5)
C(49)	6450(20)	6893(14)	10014(4)	17(2)
C(50)	6980(20)	6310(14)	10257(4)	17(2)
C(51)	7130(20)	6577(15)	10547(5)	23(5)
C(52)	7680(20)	5970(15)	10754(5)	23(4)
C(53)	8040(20)	5031(15)	10660(4)	20(3)
C(54)	7820(20)	4765(16)	10382(4)	20(3)
Mn(1)	3653(3)	5256(2)	8288(1)	14(1)
Mn(2)	7524(4)	1304(2)	8406(1)	16(1)
Mn(3)	6915(3)	5050(2)	9742(1)	13(1)
N(1)	1535(17)	5254(10)	8440(4)	15(2)
N(2)	2567(18)	4516(12)	7968(4)	19(4)
N(3)	8741(18)	2162(11)	8669(4)	18(4)
N(4)	9510(20)	1302(12)	8198(4)	20(4)
N(5)	6370(17)	6452(10)	9744(4)	15(2)
N(6)	7276(16)	5365(10)	10172(4)	15(2)
O(1)	4456(19)	6085(11)	7443(4)	32(4)
O(2)	128(17)	6338(11)	7859(4)	32(4)
O(3)	2966(18)	9069(10)	7640(4)	32(4)
O(4)	1952(16)	7897(11)	8581(3)	27(3)
O(5)	6515(18)	7534(10)	8196(4)	30(4)
O(6)	4920(17)	6472(10)	8750(4)	29(4)
O(7)	4730(17)	3548(10)	8604(4)	25(4)
O(8)	6475(16)	5296(10)	7973(4)	30(4)
O(9)	4925(19)	-1082(12)	8664(4)	34(4)
O(10)	9291(16)	-1308(11)	8162(3)	24(3)
O(11)	9108(16)	-2295(9)	9115(3)	21(3)
O(12)	11374(16)	443(10)	8767(4)	31(4)
O(13)	7248(17)	755(11)	9301(3)	28(4)
O(14)	4789(16)	1329(10)	8757(4)	25(2)
O(15)	6304(17)	2815(11)	8017(4)	31(4)
O(16)	6017(17)	-187(10)	8049(3)	27(4)
O(17)	656(18)	3792(11)	10018(4)	29(4)
O(18)	3887(16)	6007(10)	10320(3)	23(3)
O(19)	3057(16)	5822(10)	9357(3)	23(3)
O(20)	4283(18)	2657(12)	9405(4)	38(5)
O(21)	5356(16)	3145(10)	10363(3)	23(3)
O(22)	6009(16)	4678(10)	9128(3)	22(3)

O(23)	9938(16)	5334(10)	9517(4)	25(2)
O(24)	7534(16)	2977(10)	9785(3)	25(2)
Re(1)	3252(1)	7182(1)	7990(1)	16(1)
Re(2)	8232(1)	-482(1)	8766(1)	16(1)
Re(3)	3836(1)	4348(1)	9858(1)	14(1)

Table B3. Bond lengths [Å] and angles [°] for **2**.

C(1)-O(1)	1.14(3)
C(1)-Re(1)	1.98(2)
C(2)-O(2)	1.09(3)
C(2)-Re(1)	2.03(2)
C(3)-O(3)	1.15(3)
C(3)-Re(1)	1.93(2)
C(4)-O(4)	1.21(3)
C(4)-Re(1)	1.90(2)
C(5)-O(5)	1.11(3)
C(5)-Re(1)	2.04(2)
C(6)-O(6)	1.20(3)
C(6)-Mn(1)	1.74(2)
C(7)-O(7)	1.17(3)
C(7)-Mn(1)	1.77(2)
C(8)-O(8)	1.11(2)
C(8)-Mn(1)	1.82(2)
C(9)-N(1)	1.34(2)
C(9)-C(10)	1.35(3)
C(9)-H(9)	0.9500
C(10)-C(11)	1.41(3)
C(10)-H(10)	0.9500
C(11)-C(12)	1.36(3)
C(11)-H(11)	0.9500
C(12)-C(13)	1.41(3)
C(12)-H(12)	0.9500
C(13)-N(1)	1.35(3)
C(13)-C(14)	1.44(3)
C(14)-N(2)	1.36(3)
C(14)-C(15)	1.39(3)
C(15)-C(16)	1.35(3)
C(15)-H(15)	0.9500
C(16)-C(17)	1.41(3)
C(16)-H(16)	0.9500
C(17)-C(18)	1.35(3)
C(17)-H(17)	0.9500

C(18)-N(2)	1.35(3)
C(18)-H(18)	0.9500
C(19)-O(9)	1.11(3)
C(19)-Re(2)	2.03(2)
C(20)-O(10)	1.21(3)
C(20)-Re(2)	1.93(2)
C(21)-O(11)	1.17(3)
C(21)-Re(2)	1.91(2)
C(22)-O(12)	1.10(2)
C(22)-Re(2)	2.02(2)
C(23)-O(13)	1.18(3)
C(23)-Re(2)	1.94(2)
C(24)-O(16)	1.18(2)
C(24)-Mn(2)	1.79(2)
C(25)-O(14)	1.19(2)
C(25)-Mn(2)	1.76(2)
C(26)-O(15)	1.16(3)
C(26)-Mn(2)	1.80(2)
C(27)-C(28)	1.35(3)
C(27)-N(3)	1.38(2)
C(27)-H(27)	0.9500
C(28)-C(29)	1.43(3)
C(28)-H(28)	0.9500
C(29)-C(30)	1.38(3)
C(29)-H(29)	0.9500
C(30)-C(31)	1.41(3)
C(30)-H(30)	0.9500
C(31)-N(3)	1.34(3)
C(31)-C(32)	1.44(3)
C(32)-N(4)	1.36(3)
C(32)-C(33)	1.41(3)
C(33)-C(34)	1.35(3)
C(33)-H(33)	0.9500
C(34)-C(35)	1.40(4)
C(34)-H(34)	0.9500
C(35)-C(36)	1.40(3)
C(35)-H(35)	0.9500
C(36)-N(4)	1.35(3)
C(36)-H(36)	0.9500
C(37)-O(17)	1.09(3)
C(37)-Re(3)	1.98(2)
C(38)-O(18)	1.16(2)
C(38)-Re(3)	1.97(2)
C(39)-O(19)	1.17(2)
C(39)-Re(3)	1.98(2)
C(40)-O(20)	1.13(3)

C(40)-Re(3)	2.02(2)
C(41)-O(21)	1.19(2)
C(41)-Re(3)	1.97(2)
C(42)-O(22)	1.17(2)
C(42)-Mn(3)	1.80(2)
C(43)-O(23)	1.16(3)
C(43)-Mn(3)	1.79(2)
C(44)-O(24)	1.15(2)
C(44)-Mn(3)	1.791(18)
C(45)-C(46)	1.35(3)
C(45)-N(5)	1.37(3)
C(45)-H(45)	0.9500
C(46)-C(47)	1.40(3)
C(46)-H(46)	0.9500
C(47)-C(48)	1.37(3)
C(47)-H(47)	0.9500
C(48)-C(49)	1.42(3)
C(48)-H(48)	0.9500
C(49)-N(5)	1.38(3)
C(49)-C(50)	1.46(3)
C(50)-C(51)	1.38(3)
C(50)-N(6)	1.40(2)
C(51)-C(52)	1.36(3)
C(51)-H(51)	0.9500
C(52)-C(53)	1.41(3)
C(52)-H(52)	0.9500
C(53)-C(54)	1.34(3)
C(53)-H(53)	0.9500
C(54)-N(6)	1.36(3)
C(54)-H(54)	0.9500
Mn(1)-N(2)	2.039(17)
Mn(1)-N(1)	2.041(16)
Mn(1)-Re(1)	3.021(3)
Mn(2)-N(3)	2.019(17)
Mn(2)-N(4)	2.034(19)
Mn(2)-Re(2)	3.042(3)
Mn(3)-N(5)	2.007(15)
Mn(3)-N(6)	2.037(17)
Mn(3)-Re(3)	3.002(3)

O(1)-C(1)-Re(1)	178(2)
O(2)-C(2)-Re(1)	178.7(19)
O(3)-C(3)-Re(1)	178(2)
O(4)-C(4)-Re(1)	176.8(18)
O(5)-C(5)-Re(1)	174.7(18)
O(6)-C(6)-Mn(1)	175.7(18)

O(7)-C(7)-Mn(1)	177.8(19)
O(8)-C(8)-Mn(1)	179(2)
N(1)-C(9)-C(10)	124(2)
N(1)-C(9)-H(9)	117.8
C(10)-C(9)-H(9)	117.8
C(9)-C(10)-C(11)	118(2)
C(9)-C(10)-H(10)	120.8
C(11)-C(10)-H(10)	120.8
C(12)-C(11)-C(10)	119(2)
C(12)-C(11)-H(11)	120.6
C(10)-C(11)-H(11)	120.6
C(11)-C(12)-C(13)	119(2)
C(11)-C(12)-H(12)	120.4
C(13)-C(12)-H(12)	120.4
N(1)-C(13)-C(12)	121(2)
N(1)-C(13)-C(14)	116.2(19)
C(12)-C(13)-C(14)	122.3(19)
N(2)-C(14)-C(15)	122(2)
N(2)-C(14)-C(13)	112.6(18)
C(15)-C(14)-C(13)	125(2)
C(16)-C(15)-C(14)	121(2)
C(16)-C(15)-H(15)	119.4
C(14)-C(15)-H(15)	119.4
C(15)-C(16)-C(17)	116(2)
C(15)-C(16)-H(16)	121.8
C(17)-C(16)-H(16)	121.8
C(18)-C(17)-C(16)	120(2)
C(18)-C(17)-H(17)	120.0
C(16)-C(17)-H(17)	120.0
C(17)-C(18)-N(2)	124(2)
C(17)-C(18)-H(18)	117.9
N(2)-C(18)-H(18)	117.9
O(9)-C(19)-Re(2)	178(2)
O(10)-C(20)-Re(2)	175.4(19)
O(11)-C(21)-Re(2)	178.8(19)
O(12)-C(22)-Re(2)	177(2)
O(13)-C(23)-Re(2)	178.2(18)
O(16)-C(24)-Mn(2)	175.3(19)
O(14)-C(25)-Mn(2)	179(2)
O(15)-C(26)-Mn(2)	177.6(19)
C(28)-C(27)-N(3)	123(2)
C(28)-C(27)-H(27)	118.7
N(3)-C(27)-H(27)	118.7
C(27)-C(28)-C(29)	119(2)
C(27)-C(28)-H(28)	120.3
C(29)-C(28)-H(28)	120.3

C(30)-C(29)-C(28)	118(2)
C(30)-C(29)-H(29)	121.2
C(28)-C(29)-H(29)	121.2
C(29)-C(30)-C(31)	120(2)
C(29)-C(30)-H(30)	119.9
C(31)-C(30)-H(30)	119.9
N(3)-C(31)-C(30)	121.4(19)
N(3)-C(31)-C(32)	116.2(18)
C(30)-C(31)-C(32)	122.4(19)
N(4)-C(32)-C(33)	121(2)
N(4)-C(32)-C(31)	113.0(18)
C(33)-C(32)-C(31)	125.6(19)
C(34)-C(33)-C(32)	119(2)
C(34)-C(33)-H(33)	120.4
C(32)-C(33)-H(33)	120.4
C(33)-C(34)-C(35)	121(2)
C(33)-C(34)-H(34)	119.7
C(35)-C(34)-H(34)	119.7
C(36)-C(35)-C(34)	117(2)
C(36)-C(35)-H(35)	121.6
C(34)-C(35)-H(35)	121.6
N(4)-C(36)-C(35)	124(2)
N(4)-C(36)-H(36)	118.1
C(35)-C(36)-H(36)	118.1
O(17)-C(37)-Re(3)	177.2(19)
O(18)-C(38)-Re(3)	174.3(18)
O(19)-C(39)-Re(3)	178.4(19)
O(20)-C(40)-Re(3)	178.1(19)
O(21)-C(41)-Re(3)	175.7(18)
O(22)-C(42)-Mn(3)	176.7(18)
O(23)-C(43)-Mn(3)	175.4(18)
O(24)-C(44)-Mn(3)	176.7(18)
C(46)-C(45)-N(5)	123.7(19)
C(46)-C(45)-H(45)	118.2
N(5)-C(45)-H(45)	118.2
C(45)-C(46)-C(47)	119.1(19)
C(45)-C(46)-H(46)	120.5
C(47)-C(46)-H(46)	120.5
C(48)-C(47)-C(46)	119(2)
C(48)-C(47)-H(47)	120.3
C(46)-C(47)-H(47)	120.3
C(47)-C(48)-C(49)	119(2)
C(47)-C(48)-H(48)	120.3
C(49)-C(48)-H(48)	120.3
N(5)-C(49)-C(48)	120.5(18)
N(5)-C(49)-C(50)	116.9(16)

C(48)-C(49)-C(50)	122.6(18)
C(51)-C(50)-N(6)	120.1(18)
C(51)-C(50)-C(49)	128.0(19)
N(6)-C(50)-C(49)	111.8(17)
C(52)-C(51)-C(50)	122(2)
C(52)-C(51)-H(51)	118.8
C(50)-C(51)-H(51)	118.8
C(51)-C(52)-C(53)	117(2)
C(51)-C(52)-H(52)	121.7
C(53)-C(52)-H(52)	121.7
C(54)-C(53)-C(52)	121(2)
C(54)-C(53)-H(53)	119.7
C(52)-C(53)-H(53)	119.7
C(53)-C(54)-N(6)	124(2)
C(53)-C(54)-H(54)	118.2
N(6)-C(54)-H(54)	118.2
C(6)-Mn(1)-C(7)	91.3(9)
C(6)-Mn(1)-C(8)	90.4(10)
C(7)-Mn(1)-C(8)	88.7(9)
C(6)-Mn(1)-N(2)	171.7(9)
C(7)-Mn(1)-N(2)	95.2(8)
C(8)-Mn(1)-N(2)	94.7(8)
C(6)-Mn(1)-N(1)	96.3(9)
C(7)-Mn(1)-N(1)	97.8(8)
C(8)-Mn(1)-N(1)	170.5(8)
N(2)-Mn(1)-N(1)	77.9(7)
C(6)-Mn(1)-Re(1)	80.5(7)
C(7)-Mn(1)-Re(1)	167.6(6)
C(8)-Mn(1)-Re(1)	82.1(6)
N(2)-Mn(1)-Re(1)	93.8(5)
N(1)-Mn(1)-Re(1)	92.4(4)
C(25)-Mn(2)-C(24)	87.2(10)
C(25)-Mn(2)-C(26)	90.6(10)
C(24)-Mn(2)-C(26)	90.3(9)
C(25)-Mn(2)-N(3)	97.4(8)
C(24)-Mn(2)-N(3)	171.0(8)
C(26)-Mn(2)-N(3)	97.3(8)
C(25)-Mn(2)-N(4)	174.8(9)
C(24)-Mn(2)-N(4)	96.7(8)
C(26)-Mn(2)-N(4)	92.8(8)
N(3)-Mn(2)-N(4)	78.3(7)
C(25)-Mn(2)-Re(2)	83.6(7)
C(24)-Mn(2)-Re(2)	80.3(6)
C(26)-Mn(2)-Re(2)	169.2(7)
N(3)-Mn(2)-Re(2)	92.5(5)
N(4)-Mn(2)-Re(2)	93.7(5)

C(44)-Mn(3)-C(43)	91.1(9)
C(44)-Mn(3)-C(42)	87.6(9)
C(43)-Mn(3)-C(42)	89.9(9)
C(44)-Mn(3)-N(5)	173.4(8)
C(43)-Mn(3)-N(5)	94.5(8)
C(42)-Mn(3)-N(5)	95.8(7)
C(44)-Mn(3)-N(6)	95.9(8)
C(43)-Mn(3)-N(6)	97.6(8)
C(42)-Mn(3)-N(6)	171.6(8)
N(5)-Mn(3)-N(6)	80.0(6)
C(44)-Mn(3)-Re(3)	80.1(6)
C(43)-Mn(3)-Re(3)	167.1(6)
C(42)-Mn(3)-Re(3)	80.4(6)
N(5)-Mn(3)-Re(3)	94.9(5)
N(6)-Mn(3)-Re(3)	92.7(4)
C(9)-N(1)-C(13)	117.7(18)
C(9)-N(1)-Mn(1)	126.5(14)
C(13)-N(1)-Mn(1)	115.5(14)
C(18)-N(2)-C(14)	116.0(19)
C(18)-N(2)-Mn(1)	126.4(15)
C(14)-N(2)-Mn(1)	117.5(14)
C(31)-N(3)-C(27)	118.6(18)
C(31)-N(3)-Mn(2)	116.0(13)
C(27)-N(3)-Mn(2)	125.4(14)
C(36)-N(4)-C(32)	117.9(19)
C(36)-N(4)-Mn(2)	125.4(16)
C(32)-N(4)-Mn(2)	116.5(14)
C(45)-N(5)-C(49)	117.7(16)
C(45)-N(5)-Mn(3)	127.1(14)
C(49)-N(5)-Mn(3)	115.1(12)
C(54)-N(6)-C(50)	116.5(18)
C(54)-N(6)-Mn(3)	127.3(13)
C(50)-N(6)-Mn(3)	116.1(13)
C(4)-Re(1)-C(3)	98.7(8)
C(4)-Re(1)-C(1)	169.3(8)
C(3)-Re(1)-C(1)	91.9(8)
C(4)-Re(1)-C(2)	87.5(9)
C(3)-Re(1)-C(2)	98.0(8)
C(1)-Re(1)-C(2)	89.6(9)
C(4)-Re(1)-C(5)	89.7(9)
C(3)-Re(1)-C(5)	95.9(8)
C(1)-Re(1)-C(5)	90.6(9)
C(2)-Re(1)-C(5)	166.1(8)
C(4)-Re(1)-Mn(1)	86.4(6)
C(3)-Re(1)-Mn(1)	175.0(6)
C(1)-Re(1)-Mn(1)	83.0(6)

C(2)-Re(1)-Mn(1)	81.8(6)
C(5)-Re(1)-Mn(1)	84.4(6)
C(21)-Re(2)-C(20)	94.6(8)
C(21)-Re(2)-C(23)	97.2(8)
C(20)-Re(2)-C(23)	167.9(8)
C(21)-Re(2)-C(22)	96.0(9)
C(20)-Re(2)-C(22)	85.4(9)
C(23)-Re(2)-C(22)	90.5(9)
C(21)-Re(2)-C(19)	95.4(8)
C(20)-Re(2)-C(19)	91.4(9)
C(23)-Re(2)-C(19)	90.4(9)
C(22)-Re(2)-C(19)	168.3(8)
C(21)-Re(2)-Mn(2)	177.4(6)
C(20)-Re(2)-Mn(2)	83.6(6)
C(23)-Re(2)-Mn(2)	84.5(6)
C(22)-Re(2)-Mn(2)	82.0(6)
C(19)-Re(2)-Mn(2)	86.5(5)
C(38)-Re(3)-C(41)	87.1(8)
C(38)-Re(3)-C(37)	94.0(8)
C(41)-Re(3)-C(37)	95.5(8)
C(38)-Re(3)-C(39)	89.5(8)
C(41)-Re(3)-C(39)	166.8(9)
C(37)-Re(3)-C(39)	97.5(9)
C(38)-Re(3)-C(40)	172.1(8)
C(41)-Re(3)-C(40)	90.5(8)
C(37)-Re(3)-C(40)	93.8(8)
C(39)-Re(3)-C(40)	91.2(8)
C(38)-Re(3)-Mn(3)	81.4(6)
C(41)-Re(3)-Mn(3)	84.1(6)
C(37)-Re(3)-Mn(3)	175.3(6)
C(39)-Re(3)-Mn(3)	82.8(6)
C(40)-Re(3)-Mn(3)	90.9(6)

Symmetry transformations used to generate equivalent atoms:

Table B4. Anisotropic displacement parameters ($Å^2 x\ 10^3$) for **2**. The anisotropic displacement factor exponent takes the form: $-2\pi^2[h^2 a^{*2} U^{11} + ... + 2 h k a^* b^* U^{12}]$

	U^{11}	U^{22}	U^{33}	U^{23}	U^{13}	U^{12}
C(1)	24(7)	22(6)	20(7)	7(5)	-8(6)	-4(5)
C(2)	24(7)	22(6)	20(7)	7(5)	-8(6)	-4(5)
C(3)	10(6)	30(7)	16(6)	-9(5)	1(5)	-7(5)
C(4)	24(7)	22(6)	20(7)	7(5)	-8(6)	-4(5)
C(5)	36(14)	13(10)	9(11)	-6(7)	4(10)	4(9)
C(6)	16(8)	16(7)	31(9)	3(6)	-2(7)	-1(6)
C(7)	10(6)	30(7)	16(6)	-9(5)	1(5)	-7(5)
C(8)	16(8)	16(7)	31(9)	3(6)	-2(7)	-1(6)
C(9)	29(9)	19(7)	17(8)	-4(5)	1(7)	-1(7)
C(10)	35(13)	19(10)	18(11)	6(9)	8(10)	15(10)
C(11)	26(14)	24(11)	32(13)	3(9)	-11(11)	-2(9)
C(12)	20(11)	24(11)	12(10)	7(8)	0(9)	-6(9)
C(13)	20(4)	18(4)	26(5)	4(3)	-5(4)	-7(4)
C(14)	20(4)	18(4)	26(5)	4(3)	-5(4)	-7(4)
C(15)	30(14)	39(14)	11(12)	11(9)	-13(10)	-7(11)
C(16)	43(16)	23(12)	17(12)	-10(8)	4(11)	-8(10)
C(17)	34(14)	21(12)	35(15)	3(9)	13(12)	15(10)
C(18)	29(9)	19(7)	17(8)	-4(5)	1(7)	-1(7)
C(19)	20(4)	18(4)	26(5)	4(3)	-5(4)	-7(4)
C(20)	20(4)	18(4)	26(5)	4(3)	-5(4)	-7(4)
C(21)	10(6)	30(7)	16(6)	-9(5)	1(5)	-7(5)
C(22)	20(4)	18(4)	26(5)	4(3)	-5(4)	-7(4)
C(23)	20(4)	18(4)	26(5)	4(3)	-5(4)	-7(4)
C(24)	22(11)	12(9)	16(10)	6(7)	1(10)	8(9)
C(25)	22(13)	14(10)	25(12)	-1(8)	1(10)	7(8)
C(26)	17(10)	24(10)	25(12)	-4(9)	2(11)	-2(10)
C(27)	10(9)	23(10)	19(11)	-5(8)	8(10)	5(9)
C(28)	53(17)	18(11)	22(13)	6(9)	-8(12)	18(11)
C(29)	8(10)	8(9)	53(16)	-1(9)	-3(10)	-1(8)
C(30)	15(10)	19(10)	27(12)	10(9)	-5(10)	-8(9)
C(31)	9(5)	20(5)	21(6)	0(4)	2(4)	-2(4)
C(32)	9(5)	20(5)	21(6)	0(4)	2(4)	-2(4)
C(33)	7(11)	27(11)	36(14)	13(9)	2(10)	5(8)
C(34)	41(16)	34(14)	35(16)	24(11)	22(13)	15(12)
C(35)	36(14)	29(12)	28(13)	-1(9)	10(12)	13(11)
C(36)	25(12)	38(13)	14(12)	4(9)	8(10)	6(10)
C(37)	21(12)	13(9)	31(13)	2(7)	14(11)	4(10)
C(38)	7(6)	27(6)	24(6)	3(5)	3(6)	1(5)
C(39)	7(6)	27(6)	24(6)	3(5)	3(6)	1(5)
C(40)	7(6)	27(6)	24(6)	3(5)	3(6)	1(5)
C(41)	12(10)	23(10)	17(11)	5(9)	10(9)	2(8)

C(42)	12(7)	10(6)	20(8)	-1(5)	11(6)	3(5)
C(43)	24(12)	20(10)	13(10)	-1(7)	4(10)	7(9)
C(44)	12(7)	10(6)	20(8)	-1(5)	11(6)	3(5)
C(45)	8(7)	33(8)	19(8)	5(6)	2(6)	-7(6)
C(46)	11(8)	32(8)	19(8)	4(6)	-6(6)	-6(6)
C(47)	7(7)	29(8)	33(10)	4(6)	0(7)	1(6)
C(48)	11(10)	16(10)	41(14)	-4(8)	-5(10)	-1(9)
C(49)	9(5)	20(5)	21(6)	0(4)	2(4)	-2(4)
C(50)	9(5)	20(5)	21(6)	0(4)	2(4)	-2(4)
C(51)	12(12)	25(11)	32(13)	-10(9)	13(10)	-2(8)
C(52)	7(7)	29(8)	33(10)	4(6)	0(7)	1(6)
C(53)	11(8)	32(8)	19(8)	4(6)	-6(6)	-6(6)
C(54)	8(7)	33(8)	19(8)	5(6)	2(6)	-7(6)
Mn(1)	14(2)	12(1)	17(2)	0(1)	0(1)	1(1)
Mn(2)	18(2)	12(2)	17(2)	0(1)	0(1)	0(1)
Mn(3)	10(2)	12(1)	15(2)	1(1)	1(1)	1(1)
N(1)	6(5)	10(4)	27(6)	-1(4)	-1(4)	-1(3)
N(2)	17(9)	22(9)	19(9)	-2(7)	-3(8)	-1(7)
N(3)	17(9)	10(7)	26(10)	1(6)	7(8)	-4(7)
N(4)	24(10)	16(9)	20(10)	3(7)	-4(8)	10(7)
N(5)	6(5)	10(4)	27(6)	-1(4)	-1(4)	-1(3)
N(6)	6(5)	10(4)	27(6)	-1(4)	-1(4)	-1(3)
O(1)	48(11)	24(8)	25(10)	-14(7)	6(8)	3(7)
O(2)	22(9)	20(8)	53(12)	11(7)	-14(8)	-1(7)
O(3)	34(10)	20(8)	42(10)	16(7)	8(8)	5(7)
O(4)	17(8)	34(8)	30(9)	-4(7)	-3(7)	-5(7)
O(5)	20(10)	19(7)	50(11)	-2(6)	2(8)	-7(6)
O(6)	30(9)	23(8)	33(10)	0(7)	-11(8)	2(7)
O(7)	24(9)	13(7)	39(10)	6(6)	-1(7)	-1(6)
O(8)	17(9)	29(8)	45(10)	8(7)	6(8)	9(6)
O(9)	31(10)	30(9)	42(11)	1(7)	1(8)	-12(8)
O(10)	24(9)	33(9)	16(8)	-2(6)	4(7)	2(7)
O(11)	25(9)	13(7)	24(8)	-2(5)	-1(7)	1(6)
O(12)	21(9)	27(8)	45(10)	20(7)	-8(8)	-4(7)
O(13)	33(9)	28(8)	23(9)	-1(6)	2(7)	3(7)
O(14)	15(4)	23(5)	39(6)	3(4)	6(4)	8(4)
O(15)	27(9)	29(8)	36(9)	7(7)	-1(8)	1(7)
O(16)	28(9)	28(8)	26(9)	-9(6)	-5(8)	-6(7)
O(17)	23(9)	24(8)	40(10)	6(7)	8(8)	-11(7)
O(18)	10(7)	23(7)	36(9)	-15(6)	2(7)	-4(6)
O(19)	15(8)	24(8)	31(8)	9(6)	12(7)	-4(6)
O(20)	32(10)	28(9)	54(12)	-24(8)	3(9)	5(7)
O(21)	12(7)	26(8)	31(9)	4(6)	-2(7)	-3(6)
O(22)	18(8)	31(8)	18(8)	0(6)	-2(7)	0(6)
O(23)	15(4)	23(5)	39(6)	3(4)	6(4)	8(4)
O(24)	15(4)	23(5)	39(6)	3(4)	6(4)	8(4)

Re(1)	17(1)	13(1)	17(1)	0(1)	0(1)	0(1)
Re(2)	17(1)	13(1)	17(1)	1(1)	-2(1)	-1(1)
Re(3)	10(1)	13(1)	19(1)	1(1)	1(1)	-1(1)

Table B5. Hydrogen coordinates (x 10^4) and isotropic displacement parameters ($Å^2$x 10^3) for **2**.

	x	y	z	U(eq)
H(9)	1749	5991	8807	26
H(10)	-626	5879	8970	29
H(11)	-2389	5036	8680	33
H(12)	-1596	4267	8256	22
H(15)	-745	3720	7845	32
H(16)	302	3175	7412	33
H(17)	2897	3395	7353	36
H(18)	4199	4221	7694	26
H(27)	7224	2549	8971	21
H(28)	8721	3476	9259	37
H(29)	11303	3605	9142	28
H(30)	12126	2915	8703	25
H(33)	12773	2268	8286	28
H(34)	13257	1429	7861	44
H(35)	11322	607	7616	37
H(36)	9012	542	7844	31
H(45)	5940	6710	9321	24
H(46)	5544	8330	9353	25
H(47)	5467	9074	9819	28
H(48)	6085	8180	10233	27
H(51)	6847	7209	10603	27
H(52)	7808	6168	10951	28
H(53)	8442	4583	10796	25
H(54)	8066	4123	10327	24

Table B6. Torsion angles [°] for **2**.

N(1)-C(9)-C(10)-C(11)	0(3)
C(9)-C(10)-C(11)-C(12)	2(3)
C(10)-C(11)-C(12)-C(13)	-2(3)
C(11)-C(12)-C(13)-N(1)	0(3)
C(11)-C(12)-C(13)-C(14)	-175.8(19)
N(1)-C(13)-C(14)-N(2)	4(3)
C(12)-C(13)-C(14)-N(2)	-179.3(19)
N(1)-C(13)-C(14)-C(15)	-177(2)
C(12)-C(13)-C(14)-C(15)	-1(3)
N(2)-C(14)-C(15)-C(16)	-1(3)
C(13)-C(14)-C(15)-C(16)	-180(2)
C(14)-C(15)-C(16)-C(17)	3(3)
C(15)-C(16)-C(17)-C(18)	-3(3)
C(16)-C(17)-C(18)-N(2)	0(3)
N(3)-C(27)-C(28)-C(29)	-1(3)
C(27)-C(28)-C(29)-C(30)	4(3)
C(28)-C(29)-C(30)-C(31)	-3(3)
C(29)-C(30)-C(31)-N(3)	1(3)
C(29)-C(30)-C(31)-C(32)	180.0(19)
N(3)-C(31)-C(32)-N(4)	-3(3)
C(30)-C(31)-C(32)-N(4)	177.9(18)
N(3)-C(31)-C(32)-C(33)	177.1(19)
C(30)-C(31)-C(32)-C(33)	-2(3)
N(4)-C(32)-C(33)-C(34)	-1(3)
C(31)-C(32)-C(33)-C(34)	180(2)
C(32)-C(33)-C(34)-C(35)	4(3)
C(33)-C(34)-C(35)-C(36)	-4(3)
C(34)-C(35)-C(36)-N(4)	0(3)
N(5)-C(45)-C(46)-C(47)	-4(3)
C(45)-C(46)-C(47)-C(48)	4(3)
C(46)-C(47)-C(48)-C(49)	0(3)
C(47)-C(48)-C(49)-N(5)	-3(3)
C(47)-C(48)-C(49)-C(50)	174.1(19)
N(5)-C(49)-C(50)-C(51)	-179(2)
C(48)-C(49)-C(50)-C(51)	4(3)
N(5)-C(49)-C(50)-N(6)	-2(2)
C(48)-C(49)-C(50)-N(6)	-179.4(18)
N(6)-C(50)-C(51)-C(52)	5(3)
C(49)-C(50)-C(51)-C(52)	-178.2(19)
C(50)-C(51)-C(52)-C(53)	-2(3)
C(51)-C(52)-C(53)-C(54)	-1(3)
C(52)-C(53)-C(54)-N(6)	1(3)
C(10)-C(9)-N(1)-C(13)	-2(3)
C(10)-C(9)-N(1)-Mn(1)	-176.5(15)

C(12)-C(13)-N(1)-C(9)	2(3)
C(14)-C(13)-N(1)-C(9)	178.4(18)
C(12)-C(13)-N(1)-Mn(1)	177.0(15)
C(14)-C(13)-N(1)-Mn(1)	-7(2)
C(17)-C(18)-N(2)-C(14)	2(3)
C(17)-C(18)-N(2)-Mn(1)	179.3(16)
C(15)-C(14)-N(2)-C(18)	-2(3)
C(13)-C(14)-N(2)-C(18)	177.2(17)
C(15)-C(14)-N(2)-Mn(1)	-178.9(16)
C(13)-C(14)-N(2)-Mn(1)	0(2)
C(30)-C(31)-N(3)-C(27)	2(3)
C(32)-C(31)-N(3)-C(27)	-177.3(17)
C(30)-C(31)-N(3)-Mn(2)	-177.6(15)
C(32)-C(31)-N(3)-Mn(2)	3(2)
C(28)-C(27)-N(3)-C(31)	-2(3)
C(28)-C(27)-N(3)-Mn(2)	178.0(15)
C(35)-C(36)-N(4)-C(32)	3(3)
C(35)-C(36)-N(4)-Mn(2)	178.5(16)
C(33)-C(32)-N(4)-C(36)	-3(3)
C(31)-C(32)-N(4)-C(36)	176.8(18)
C(33)-C(32)-N(4)-Mn(2)	-178.6(15)
C(31)-C(32)-N(4)-Mn(2)	1(2)
C(46)-C(45)-N(5)-C(49)	1(3)
C(46)-C(45)-N(5)-Mn(3)	-176.2(15)
C(48)-C(49)-N(5)-C(45)	3(3)
C(50)-C(49)-N(5)-C(45)	-174.3(17)
C(48)-C(49)-N(5)-Mn(3)	-179.6(15)
C(50)-C(49)-N(5)-Mn(3)	3(2)
C(53)-C(54)-N(6)-C(50)	2(3)
C(53)-C(54)-N(6)-Mn(3)	179.4(16)
C(51)-C(50)-N(6)-C(54)	-5(3)
C(49)-C(50)-N(6)-C(54)	177.9(16)
C(51)-C(50)-N(6)-Mn(3)	177.4(15)
C(49)-C(50)-N(6)-Mn(3)	0(2)

Symmetry transformations used to generate equivalent atoms:

Appendix C Crystallographic parameters crystal data of $(CO)_5ReMn(CO)_3$(biq) (**3**)

Table C1. Crystal data and structure refinement for **3**.

Identification code	l06052015_0m	
Empirical formula	C26 H12 Mn N2 O8 Re	
Formula weight	721.52	
Temperature	100(2) K	
Wavelength	0.71073 Å	
Crystal system	Triclinic	
Space group	P-1	
Unit cell dimensions	a = 9.0494(15) Å	□= 83.744(5)°.
	b = 9.3772(14) Å	□= 81.785(5)°.
	c = 14.4945(19) Å	□ = 75.337(5)°.
Volume	1174.3(3) $Å^3$	
Z	2	
Density (calculated)	2.041 Mg/m^3	
Absorption coefficient	5.744 mm^{-1}	
F(000)	692	
Crystal size	0.300 x 0.050 x 0.050 mm^3	
Theta range for data collection	1.424 to 27.152°.	
Index ranges	-11<=h<=11, -12<=k<=11, -18<=l<=18	
Reflections collected	9396	
Independent reflections	5186 [R(int) = 0.0400]	
Completeness to theta = 25.242°	100.0 %	
Absorption correction	Semi-empirical from equivalents	
Max. and min. transmission	0.7455 and 0.4235	
Refinement method	Full-matrix least-squares on F^2	
Data / restraints / parameters	5186 / 0 / 343	
Goodness-of-fit on F^2	0.998	
Final R indices [I>2sigma(I)]	R1 = 0.0403, wR2 = 0.1025	
R indices (all data)	R1 = 0.0491, wR2 = 0.1077	
Extinction coefficient	n/a	
Largest diff. peak and hole	3.026 and -3.600 $e.Å^{-3}$	

Table C2. Atomic coordinates (x 10^4) and equivalent isotropic displacement parameters ($Å^2$x 10^3) for **3**. U(eq) is defined as one third of the trace of the orthogonalized U^{ij} tensor.

	x	y	z	U(eq)
C(1)	7257(7)	5961(7)	8951(4)	21(1)
C(2)	8434(7)	3704(6)	7658(4)	16(1)
C(3)	8795(7)	7801(7)	7777(4)	15(1)
C(4)	9419(7)	5938(7)	6378(4)	18(1)
C(5)	10536(8)	4992(7)	8252(5)	25(1)
C(6)	5219(7)	5276(7)	7838(4)	17(1)
C(7)	6362(7)	5193(6)	6239(4)	16(1)
C(8)	3647(7)	6867(7)	6608(4)	18(1)
C(9)	3824(6)	8676(6)	8566(4)	14(1)
C(10)	2909(7)	7649(7)	8883(4)	19(1)
C(11)	1902(7)	7835(7)	9691(4)	21(1)
C(12)	1749(7)	9028(7)	10227(4)	22(1)
C(13)	2580(7)	10058(7)	9928(4)	21(1)
C(14)	3611(7)	9912(7)	9102(4)	17(1)
C(15)	4427(7)	11019(7)	8761(4)	19(1)
C(16)	5325(7)	10874(6)	7927(4)	17(1)
C(17)	5488(6)	9628(6)	7422(4)	14(1)
C(18)	6315(7)	9499(6)	6484(4)	15(1)
C(19)	7146(7)	10549(7)	6050(4)	19(1)
C(20)	7846(7)	10401(7)	5167(4)	19(1)
C(21)	7624(7)	9297(7)	4649(4)	17(1)
C(22)	8214(7)	9174(7)	3689(4)	19(1)
C(23)	7898(7)	8152(7)	3200(4)	21(1)
C(24)	6966(7)	7200(7)	3636(4)	20(1)
C(25)	6394(7)	7275(7)	4570(4)	16(1)
C(26)	6754(6)	8290(6)	5110(4)	15(1)
Mn	5517(1)	6713(1)	6951(1)	11(1)
N(1)	4831(5)	8505(5)	7755(3)	13(1)
N(2)	6221(5)	8340(5)	6053(3)	14(1)
O(1)	6453(6)	6161(6)	9622(3)	29(1)
O(2)	8386(5)	2510(5)	7591(3)	23(1)
O(3)	8964(5)	8976(5)	7802(3)	24(1)
O(4)	9837(5)	6129(5)	5609(3)	26(1)
O(5)	11671(5)	4531(6)	8574(4)	31(1)
O(6)	5033(5)	4267(5)	8338(3)	21(1)
O(7)	6823(5)	4142(5)	5824(3)	23(1)
O(8)	2443(5)	6862(5)	6439(3)	26(1)
Re	8618(1)	5752(1)	7740(1)	15(1)

Table C3. Bond lengths [Å] and angles [°] for **3**.

C(1)-O(1)	1.131(8)
C(1)-Re	1.993(6)
C(2)-O(2)	1.147(7)
C(2)-Re	1.987(6)
C(3)-O(3)	1.156(7)
C(3)-Re	1.975(6)
C(4)-O(4)	1.134(7)
C(4)-Re	2.008(6)
C(5)-O(5)	1.153(8)
C(5)-Re	1.923(7)
C(6)-O(6)	1.160(7)
C(6)-Mn	1.802(6)
C(7)-O(7)	1.164(7)
C(7)-Mn	1.796(6)
C(8)-O(8)	1.152(7)
C(8)-Mn	1.799(6)
C(9)-N(1)	1.378(7)
C(9)-C(10)	1.422(8)
C(9)-C(14)	1.423(8)
C(10)-C(11)	1.374(8)
C(10)-H(10)	0.9500
C(11)-C(12)	1.398(9)
C(11)-H(11)	0.9500
C(12)-C(13)	1.367(9)
C(12)-H(12)	0.9500
C(13)-C(14)	1.406(8)
C(13)-H(13)	0.9500
C(14)-C(15)	1.428(8)
C(15)-C(16)	1.356(8)
C(15)-H(15)	0.9500
C(16)-C(17)	1.410(8)
C(16)-H(16)	0.9500
C(17)-N(1)	1.348(7)
C(17)-C(18)	1.458(8)
C(18)-N(2)	1.337(7)
C(18)-C(19)	1.427(7)
C(19)-C(20)	1.349(8)
C(19)-H(19)	0.9500
C(20)-C(21)	1.412(8)
C(20)-H(20)	0.9500
C(21)-C(22)	1.423(8)
C(21)-C(26)	1.431(8)
C(22)-C(23)	1.359(9)
C(22)-H(22)	0.9500

C(23)-C(24)	1.418(8)
C(23)-H(23)	0.9500
C(24)-C(25)	1.381(8)
C(24)-H(24)	0.9500
C(25)-C(26)	1.420(8)
C(25)-H(25)	0.9500
C(26)-N(2)	1.384(7)
Mn-N(2)	2.061(5)
Mn-N(1)	2.064(5)
Mn-Re	3.0663(10)

O(1)-C(1)-Re	176.1(6)
O(2)-C(2)-Re	177.2(5)
O(3)-C(3)-Re	177.1(5)
O(4)-C(4)-Re	176.0(5)
O(5)-C(5)-Re	178.8(6)
O(6)-C(6)-Mn	173.3(5)
O(7)-C(7)-Mn	174.0(5)
O(8)-C(8)-Mn	174.2(5)
N(1)-C(9)-C(10)	121.2(5)
N(1)-C(9)-C(14)	121.6(5)
C(10)-C(9)-C(14)	117.2(5)
C(11)-C(10)-C(9)	120.7(6)
C(11)-C(10)-H(10)	119.6
C(9)-C(10)-H(10)	119.6
C(10)-C(11)-C(12)	121.4(6)
C(10)-C(11)-H(11)	119.3
C(12)-C(11)-H(11)	119.3
C(13)-C(12)-C(11)	119.4(6)
C(13)-C(12)-H(12)	120.3
C(11)-C(12)-H(12)	120.3
C(12)-C(13)-C(14)	120.8(6)
C(12)-C(13)-H(13)	119.6
C(14)-C(13)-H(13)	119.6
C(13)-C(14)-C(9)	120.5(5)
C(13)-C(14)-C(15)	121.1(6)
C(9)-C(14)-C(15)	118.4(5)
C(16)-C(15)-C(14)	118.7(5)
C(16)-C(15)-H(15)	120.7
C(14)-C(15)-H(15)	120.7
C(15)-C(16)-C(17)	120.5(5)
C(15)-C(16)-H(16)	119.7
C(17)-C(16)-H(16)	119.7
N(1)-C(17)-C(16)	122.5(5)
N(1)-C(17)-C(18)	115.2(5)
C(16)-C(17)-C(18)	122.2(5)

N(2)-C(18)-C(19)	122.4(5)
N(2)-C(18)-C(17)	115.3(5)
C(19)-C(18)-C(17)	122.4(5)
C(20)-C(19)-C(18)	119.7(5)
C(20)-C(19)-H(19)	120.1
C(18)-C(19)-H(19)	120.1
C(19)-C(20)-C(21)	119.7(5)
C(19)-C(20)-H(20)	120.2
C(21)-C(20)-H(20)	120.2
C(20)-C(21)-C(22)	122.3(5)
C(20)-C(21)-C(26)	118.2(5)
C(22)-C(21)-C(26)	119.6(5)
C(23)-C(22)-C(21)	120.4(6)
C(23)-C(22)-H(22)	119.8
C(21)-C(22)-H(22)	119.8
C(22)-C(23)-C(24)	120.6(5)
C(22)-C(23)-H(23)	119.7
C(24)-C(23)-H(23)	119.7
C(25)-C(24)-C(23)	120.5(6)
C(25)-C(24)-H(24)	119.7
C(23)-C(24)-H(24)	119.7
C(24)-C(25)-C(26)	120.4(5)
C(24)-C(25)-H(25)	119.8
C(26)-C(25)-H(25)	119.8
N(2)-C(26)-C(25)	120.6(5)
N(2)-C(26)-C(21)	120.9(5)
C(25)-C(26)-C(21)	118.4(5)
C(7)-Mn-C(8)	91.6(3)
C(7)-Mn-C(6)	83.7(2)
C(8)-Mn-C(6)	90.2(3)
C(7)-Mn-N(2)	97.5(2)
C(8)-Mn-N(2)	100.5(2)
C(6)-Mn-N(2)	169.2(2)
C(7)-Mn-N(1)	172.5(2)
C(8)-Mn-N(1)	95.2(2)
C(6)-Mn-N(1)	99.2(2)
N(2)-Mn-N(1)	78.32(18)
C(7)-Mn-Re	82.75(19)
C(8)-Mn-Re	166.77(19)
C(6)-Mn-Re	77.37(18)
N(2)-Mn-Re	92.14(13)
N(1)-Mn-Re	91.16(13)
C(17)-N(1)-C(9)	117.9(5)
C(17)-N(1)-Mn	113.6(4)
C(9)-N(1)-Mn	128.5(4)
C(18)-N(2)-C(26)	118.0(5)

C(18)-N(2)-Mn	113.5(4)
C(26)-N(2)-Mn	128.0(4)
C(5)-Re-C(3)	90.8(3)
C(5)-Re-C(2)	90.2(3)
C(3)-Re-C(2)	178.1(2)
C(5)-Re-C(1)	97.2(3)
C(3)-Re-C(1)	88.8(2)
C(2)-Re-C(1)	92.6(2)
C(5)-Re-C(4)	99.4(3)
C(3)-Re-C(4)	86.3(2)
C(2)-Re-C(4)	92.0(2)
C(1)-Re-C(4)	162.8(3)
C(5)-Re-Mn	175.41(19)
C(3)-Re-Mn	93.69(17)
C(2)-Re-Mn	85.29(17)
C(1)-Re-Mn	82.01(18)
C(4)-Re-Mn	81.81(17)

Symmetry transformations used to generate equivalent atoms:

Table C4. Anisotropic displacement parameters ($Å^2 x\ 10^3$) for **3**. The anisotropic displacement factor exponent takes the form: $-2\pi^2[h^2 a^{*2} U^{11} + ... + 2 h k a^* b^* U^{12}]$

	U^{11}	U^{22}	U^{33}	U^{23}	U^{13}	U^{12}
C(1)	25(3)	23(3)	20(3)	-4(2)	-1(3)	-14(3)
C(2)	20(3)	17(3)	13(3)	-1(2)	1(2)	-9(2)
C(3)	20(3)	21(3)	5(2)	-4(2)	2(2)	-8(2)
C(4)	20(3)	18(3)	21(3)	-5(2)	-1(2)	-12(2)
C(5)	27(3)	24(3)	27(3)	-10(3)	3(3)	-12(3)
C(6)	17(3)	21(3)	15(3)	-10(2)	4(2)	-8(2)
C(7)	21(3)	18(3)	12(3)	0(2)	0(2)	-11(2)
C(8)	21(3)	20(3)	13(3)	-3(2)	1(2)	-8(2)
C(9)	14(3)	18(3)	9(2)	-5(2)	3(2)	-3(2)
C(10)	23(3)	20(3)	14(3)	-3(2)	4(2)	-7(3)
C(11)	18(3)	22(3)	22(3)	0(2)	6(2)	-6(3)
C(12)	21(3)	29(3)	13(3)	-3(2)	6(2)	-4(3)
C(13)	23(3)	22(3)	16(3)	-8(2)	3(2)	-3(3)
C(14)	19(3)	17(3)	16(3)	-3(2)	1(2)	-5(2)
C(15)	23(3)	18(3)	20(3)	-10(2)	1(2)	-8(3)
C(16)	26(3)	16(3)	13(3)	-5(2)	-1(2)	-11(2)
C(17)	10(3)	19(3)	13(3)	-4(2)	2(2)	-4(2)
C(18)	18(3)	11(3)	15(3)	-2(2)	-1(2)	-5(2)
C(19)	25(3)	16(3)	19(3)	-4(2)	0(2)	-10(3)
C(20)	24(3)	17(3)	17(3)	1(2)	2(2)	-11(3)
C(21)	18(3)	18(3)	15(3)	-3(2)	3(2)	-5(2)
C(22)	19(3)	25(3)	12(3)	0(2)	4(2)	-6(3)
C(23)	22(3)	26(3)	12(3)	-4(2)	4(2)	-3(3)
C(24)	21(3)	21(3)	16(3)	-5(2)	1(2)	-2(3)
C(25)	18(3)	19(3)	14(3)	-3(2)	2(2)	-8(2)
C(26)	16(3)	15(3)	13(3)	-2(2)	1(2)	-4(2)
Mn	16(1)	12(1)	8(1)	-4(1)	3(1)	-8(1)
N(1)	15(2)	11(2)	13(2)	-3(2)	2(2)	-4(2)
N(2)	15(2)	14(2)	12(2)	-4(2)	1(2)	-6(2)
O(1)	37(3)	38(3)	13(2)	-9(2)	5(2)	-15(2)
O(2)	25(2)	19(2)	25(2)	-3(2)	-2(2)	-7(2)
O(3)	30(2)	22(2)	22(2)	-4(2)	-1(2)	-10(2)
O(4)	28(2)	36(3)	17(2)	-7(2)	4(2)	-13(2)
O(5)	18(2)	35(3)	42(3)	-8(2)	-13(2)	-2(2)
O(6)	29(2)	17(2)	17(2)	0(2)	6(2)	-11(2)
O(7)	33(3)	18(2)	19(2)	-8(2)	3(2)	-8(2)
O(8)	25(2)	34(3)	26(2)	1(2)	-7(2)	-15(2)
Re	17(1)	16(1)	12(1)	-5(1)	2(1)	-8(1)

Table C5. Hydrogen coordinates (x 10^4) and isotropic displacement parameters ($Å^2$x 10^3) for **3**.

	x	y	z	U(eq)
H(10)	2994	6826	8533	22
H(11)	1298	7139	9888	26
H(12)	1074	9121	10794	27
H(13)	2458	10883	10283	25
H(15)	4343	11841	9111	23
H(16)	5849	11617	7680	20
H(19)	7206	11349	6380	23
H(20)	8485	11036	4895	23
H(22)	8832	9811	3388	23
H(23)	8305	8073	2561	25
H(24)	6733	6506	3283	24
H(25)	5757	6645	4853	20

Table C6. Torsion angles [°] for **3**.

N(1)-C(9)-C(10)-C(11)	-179.7(6)
C(14)-C(9)-C(10)-C(11)	-2.0(9)
C(9)-C(10)-C(11)-C(12)	-0.3(10)
C(10)-C(11)-C(12)-C(13)	2.1(10)
C(11)-C(12)-C(13)-C(14)	-1.6(9)
C(12)-C(13)-C(14)-C(9)	-0.7(9)
C(12)-C(13)-C(14)-C(15)	176.9(6)
N(1)-C(9)-C(14)-C(13)	-179.8(5)
C(10)-C(9)-C(14)-C(13)	2.5(8)
N(1)-C(9)-C(14)-C(15)	2.5(9)
C(10)-C(9)-C(14)-C(15)	-175.3(5)
C(13)-C(14)-C(15)-C(16)	-175.4(6)
C(9)-C(14)-C(15)-C(16)	2.3(9)
C(14)-C(15)-C(16)-C(17)	-2.1(9)
C(15)-C(16)-C(17)-N(1)	-3.1(9)
C(15)-C(16)-C(17)-C(18)	173.8(6)
N(1)-C(17)-C(18)-N(2)	4.5(7)
C(16)-C(17)-C(18)-N(2)	-172.6(5)
N(1)-C(17)-C(18)-C(19)	-176.4(5)
C(16)-C(17)-C(18)-C(19)	6.5(9)
N(2)-C(18)-C(19)-C(20)	1.3(9)
C(17)-C(18)-C(19)-C(20)	-177.7(6)
C(18)-C(19)-C(20)-C(21)	6.3(9)
C(19)-C(20)-C(21)-C(22)	174.0(6)

C(19)-C(20)-C(21)-C(26)	-4.9(9)
C(20)-C(21)-C(22)-C(23)	-176.1(6)
C(26)-C(21)-C(22)-C(23)	2.9(9)
C(21)-C(22)-C(23)-C(24)	0.6(9)
C(22)-C(23)-C(24)-C(25)	-1.5(9)
C(23)-C(24)-C(25)-C(26)	-1.1(9)
C(24)-C(25)-C(26)-N(2)	-178.1(5)
C(24)-C(25)-C(26)-C(21)	4.4(9)
C(20)-C(21)-C(26)-N(2)	-3.8(8)
C(22)-C(21)-C(26)-N(2)	177.2(5)
C(20)-C(21)-C(26)-C(25)	173.7(6)
C(22)-C(21)-C(26)-C(25)	-5.3(8)
C(16)-C(17)-N(1)-C(9)	7.8(8)
C(18)-C(17)-N(1)-C(9)	-169.3(5)
C(16)-C(17)-N(1)-Mn	-171.9(4)
C(18)-C(17)-N(1)-Mn	11.1(6)
C(10)-C(9)-N(1)-C(17)	170.3(5)
C(14)-C(9)-N(1)-C(17)	-7.4(8)
C(10)-C(9)-N(1)-Mn	-10.2(8)
C(14)-C(9)-N(1)-Mn	172.2(4)
C(19)-C(18)-N(2)-C(26)	-9.9(8)
C(17)-C(18)-N(2)-C(26)	169.2(5)
C(19)-C(18)-N(2)-Mn	163.1(4)
C(17)-C(18)-N(2)-Mn	-17.8(6)
C(25)-C(26)-N(2)-C(18)	-166.4(5)
C(21)-C(26)-N(2)-C(18)	11.0(8)
C(25)-C(26)-N(2)-Mn	21.7(8)
C(21)-C(26)-N(2)-Mn	-160.8(4)

Symmetry transformations used to generate equivalent atoms:

Appendix D Crystallographic parameters crystal data of $(CO)_5ReMn(CO)_3(phenCHO)$ (**4**)

Table D1. Crystal data and structure refinement for **4**.

Identification code	05052016_0m	
Empirical formula	C21.50 H9 Cl Mn N2 O9 Re	
Formula weight	715.90	
Temperature	99(2) K	
Wavelength	0.71073 Å	
Crystal system	Triclinic	
Space group	P-1	
Unit cell dimensions	a = 9.888(3) Å	a= 111.712(8)°.
	b = 10.582(3) Å	b= 90.526(8)°.
	c = 12.887(4) Å	g = 114.312(8)°.
Volume	1120.8(6) $Å^3$	
Z	2	
Density (calculated)	2.121 Mg/m^3	
Absorption coefficient	6.136 mm^{-1}	
F(000)	682	
Crystal size	0.150 x 0.150 x 0.050 mm^3	
Theta range for data collection	1.733 to 28.467°.	
Index ranges	-13<=h<=12, -14<=k<=14, -16<=l<=17	
Reflections collected	8923	
Independent reflections	5413 [R(int) = 0.0351]	
Completeness to theta = 25.242°	98.3 %	
Refinement method	Full-matrix least-squares on F^2	
Data / restraints / parameters	5413 / 2 / 320	
Goodness-of-fit on F^2	1.035	
Final R indices [I>2sigma(I)]	R1 = 0.0425, wR2 = 0.0989	
R indices (all data)	R1 = 0.0539, wR2 = 0.1047	
Extinction coefficient	n/a	
Largest diff. peak and hole	3.717 and -2.449 $e.Å^{-3}$	

Table D2. Atomic coordinates (x 10^4) and equivalent isotropic displacement parameters ($Å^2$x 10^3) for **4**. U(eq) is defined as one third of the trace of the orthogonalized U^{ij} tensor.

	x	y	z	U(eq)
C(22)	9080(30)	4320(60)	5230(17)	270(30)
C(1)	8364(7)	340(6)	9684(5)	17(1)
C(2)	7881(7)	-1809(7)	7743(5)	20(1)
C(3)	5774(7)	-1094(6)	8479(5)	16(1)
C(4)	7779(8)	-2015(7)	5398(5)	26(1)
C(5)	4967(7)	-3404(7)	6052(5)	20(1)
C(6)	4641(8)	-761(7)	6513(5)	24(1)
C(7)	7351(8)	547(8)	5852(5)	26(1)
C(8)	4987(7)	-2409(7)	4269(5)	22(1)
C(9)	6325(6)	2197(6)	8996(4)	14(1)
C(10)	6367(7)	3607(7)	9248(5)	16(1)
C(11)	7596(7)	4760(6)	9124(4)	14(1)
C(12)	8819(6)	4479(6)	8737(4)	14(1)
C(13)	10166(7)	5555(6)	8571(5)	17(1)
C(14)	11310(6)	5198(7)	8226(5)	17(1)
C(15)	11196(6)	3716(6)	8016(4)	14(1)
C(16)	12366(7)	3319(7)	7683(5)	20(1)
C(17)	12139(7)	1855(7)	7491(5)	20(1)
C(18)	10766(7)	829(7)	7617(5)	18(1)
C(19)	9872(6)	2636(6)	8138(4)	13(1)
C(20)	8681(6)	3012(6)	8505(4)	13(1)
C(21)	7624(7)	6261(7)	9428(5)	21(1)
Re(1)	6072(1)	-1506(1)	5817(1)	16(1)
Cl(1)	8871(4)	3250(4)	3774(3)	33(1)
Cl(2)	9114(5)	4191(6)	4171(4)	49(1)
Mn(2)	7635(1)	-86(1)	8251(1)	13(1)
N(1)	7462(5)	1869(5)	8603(4)	12(1)
N(2)	9641(5)	1188(5)	7930(4)	14(1)
O(1)	8742(5)	513(5)	10595(4)	26(1)
O(2)	8036(6)	-2891(5)	7460(4)	26(1)
O(3)	4609(5)	-1720(5)	8677(4)	27(1)
O(4)	8773(6)	-2270(7)	5175(4)	37(1)
O(5)	4347(6)	-4465(5)	6212(4)	30(1)
O(6)	3808(6)	-317(6)	6929(4)	36(1)
O(7)	8089(6)	1706(6)	5861(4)	34(1)
O(8)	4343(6)	-2969(6)	3362(4)	33(1)
O(9)	6499(6)	6465(6)	9565(5)	38(1)

Table D3. Bond lengths [Å] and angles [°] for **4**.

C(22)-Cl(2)#1	1.742(14)
C(22)-Cl(1)	1.754(10)
C(1)-O(1)	1.153(7)
C(1)-Mn(2)	1.796(6)
C(2)-O(2)	1.142(8)
C(2)-Mn(2)	1.815(6)
C(3)-O(3)	1.154(7)
C(3)-Mn(2)	1.799(6)
C(4)-O(4)	1.135(9)
C(4)-Re(1)	1.995(7)
C(5)-O(5)	1.134(8)
C(5)-Re(1)	1.992(7)
C(6)-O(6)	1.152(8)
C(6)-Re(1)	1.962(7)
C(7)-O(7)	1.135(9)
C(7)-Re(1)	1.997(7)
C(8)-O(8)	1.135(7)
C(8)-Re(1)	1.937(6)
C(9)-N(1)	1.357(7)
C(9)-C(10)	1.387(8)
C(10)-C(11)	1.385(8)
C(11)-C(12)	1.413(8)
C(11)-C(21)	1.476(8)
C(12)-C(20)	1.414(8)
C(12)-C(13)	1.433(8)
C(13)-C(14)	1.363(9)
C(14)-C(15)	1.444(8)
C(15)-C(19)	1.396(8)
C(15)-C(16)	1.405(9)
C(16)-C(17)	1.392(9)
C(17)-C(18)	1.403(9)
C(18)-N(2)	1.337(8)
C(19)-N(2)	1.371(8)
C(19)-C(20)	1.424(8)
C(20)-N(1)	1.359(7)
C(21)-O(9)	1.220(8)
Re(1)-Mn(2)	2.9991(12)
Cl(2)-C(22)#1	1.742(14)
Cl(2)-Cl(2)#1	2.307(9)
Mn(2)-N(1)	2.029(5)
Mn(2)-N(2)	2.036(5)
Cl(2)#1-C(22)-Cl(1)	112.7(12)
O(1)-C(1)-Mn(2)	174.9(5)

O(2)-C(2)-Mn(2)	177.7(5)
O(3)-C(3)-Mn(2)	176.9(5)
O(4)-C(4)-Re(1)	178.4(6)
O(5)-C(5)-Re(1)	178.4(5)
O(6)-C(6)-Re(1)	179.5(6)
O(7)-C(7)-Re(1)	179.0(7)
O(8)-C(8)-Re(1)	178.5(6)
N(1)-C(9)-C(10)	122.2(6)
C(11)-C(10)-C(9)	121.0(6)
C(10)-C(11)-C(12)	118.8(5)
C(10)-C(11)-C(21)	119.7(6)
C(12)-C(11)-C(21)	121.5(6)
C(11)-C(12)-C(20)	116.3(5)
C(11)-C(12)-C(13)	125.3(6)
C(20)-C(12)-C(13)	118.4(5)
C(14)-C(13)-C(12)	121.2(6)
C(13)-C(14)-C(15)	120.7(6)
C(19)-C(15)-C(16)	118.9(5)
C(19)-C(15)-C(14)	118.8(5)
C(16)-C(15)-C(14)	122.3(6)
C(17)-C(16)-C(15)	117.8(6)
C(16)-C(17)-C(18)	119.8(6)
N(2)-C(18)-C(17)	123.1(6)
N(2)-C(19)-C(15)	123.2(5)
N(2)-C(19)-C(20)	116.4(5)
C(15)-C(19)-C(20)	120.5(5)
N(1)-C(20)-C(12)	125.0(5)
N(1)-C(20)-C(19)	114.7(5)
C(12)-C(20)-C(19)	120.3(5)
O(9)-C(21)-C(11)	122.8(6)
C(8)-Re(1)-C(6)	95.3(3)
C(8)-Re(1)-C(5)	93.3(3)
C(6)-Re(1)-C(5)	89.8(3)
C(8)-Re(1)-C(4)	95.3(3)
C(6)-Re(1)-C(4)	169.2(2)
C(5)-Re(1)-C(4)	91.8(3)
C(8)-Re(1)-C(7)	96.3(3)
C(6)-Re(1)-C(7)	88.9(3)
C(5)-Re(1)-C(7)	170.4(2)
C(4)-Re(1)-C(7)	87.7(3)
C(8)-Re(1)-Mn(2)	177.5(2)
C(6)-Re(1)-Mn(2)	82.20(17)
C(5)-Re(1)-Mn(2)	86.29(17)
C(4)-Re(1)-Mn(2)	87.25(18)
C(7)-Re(1)-Mn(2)	84.14(17)
C(22)#1-Cl(2)-Cl(2)#1	34.7(12)

C(1)-Mn(2)-C(3)	88.2(3)
C(1)-Mn(2)-C(2)	90.1(3)
C(3)-Mn(2)-C(2)	90.7(3)
C(1)-Mn(2)-N(1)	96.7(2)
C(3)-Mn(2)-N(1)	94.8(2)
C(2)-Mn(2)-N(1)	171.4(2)
C(1)-Mn(2)-N(2)	95.9(2)
C(3)-Mn(2)-N(2)	173.3(2)
C(2)-Mn(2)-N(2)	94.5(2)
N(1)-Mn(2)-N(2)	79.6(2)
C(1)-Mn(2)-Re(1)	167.29(19)
C(3)-Mn(2)-Re(1)	83.79(17)
C(2)-Mn(2)-Re(1)	80.20(19)
N(1)-Mn(2)-Re(1)	93.81(12)
N(2)-Mn(2)-Re(1)	93.05(13)
C(9)-N(1)-C(20)	116.7(5)
C(9)-N(1)-Mn(2)	127.7(4)
C(20)-N(1)-Mn(2)	115.5(4)
C(18)-N(2)-C(19)	117.2(5)
C(18)-N(2)-Mn(2)	128.9(4)
C(19)-N(2)-Mn(2)	113.8(4)

Symmetry transformations used to generate equivalent atoms:
#1 -x+2,-y+1,-z+1

Table D4. Anisotropic displacement parameters ($Å^2 x\ 10^3$) for **4**. The anisotropic displacement factor exponent takes the form: $-2p^2[\ h^2\ a^{*2}U^{11} + ... + 2\ h\ k\ a^*\ b^*\ U^{12}\ ]$

	U^{11}	U^{22}	U^{33}	U^{23}	U^{13}	U^{12}
C(1)	15(3)	11(3)	18(3)	6(2)	2(2)	0(2)
C(2)	23(3)	18(3)	14(3)	8(2)	3(2)	4(2)
C(3)	19(3)	14(3)	10(3)	4(2)	0(2)	2(2)
C(4)	30(3)	21(3)	16(3)	4(2)	0(3)	5(3)
C(5)	21(3)	13(3)	18(3)	-1(2)	2(2)	7(2)
C(6)	30(3)	20(3)	17(3)	4(2)	-4(3)	10(3)
C(7)	32(3)	25(3)	14(3)	8(2)	-1(3)	7(3)
C(8)	26(3)	15(3)	18(3)	7(2)	3(2)	5(2)
C(9)	14(2)	16(3)	10(2)	5(2)	4(2)	4(2)
C(10)	16(3)	17(3)	11(3)	3(2)	4(2)	7(2)
C(11)	20(3)	14(3)	8(2)	6(2)	2(2)	7(2)
C(12)	16(3)	15(3)	5(2)	1(2)	-1(2)	5(2)
C(13)	23(3)	12(3)	12(3)	4(2)	0(2)	5(2)
C(14)	14(3)	17(3)	15(3)	6(2)	1(2)	4(2)
C(15)	17(3)	14(3)	7(2)	3(2)	2(2)	4(2)
C(16)	15(3)	26(3)	20(3)	15(2)	5(2)	5(2)
C(17)	18(3)	24(3)	24(3)	12(2)	9(2)	12(2)
C(18)	24(3)	18(3)	17(3)	8(2)	6(2)	12(2)
C(19)	12(2)	15(3)	10(2)	4(2)	2(2)	4(2)
C(20)	14(2)	15(3)	4(2)	-1(2)	1(2)	5(2)
C(21)	27(3)	22(3)	16(3)	9(2)	8(2)	11(3)
Re(1)	21(1)	12(1)	9(1)	1(1)	-1(1)	4(1)
Mn(2)	16(1)	9(1)	8(1)	3(1)	1(1)	2(1)
N(1)	13(2)	13(2)	5(2)	1(2)	1(2)	3(2)
N(2)	17(2)	17(2)	7(2)	5(2)	1(2)	8(2)
O(1)	33(3)	22(2)	15(2)	7(2)	-5(2)	7(2)
O(2)	40(3)	16(2)	24(2)	7(2)	7(2)	15(2)
O(3)	23(2)	22(2)	24(2)	9(2)	2(2)	-2(2)
O(4)	33(3)	53(4)	24(3)	9(2)	10(2)	24(3)
O(5)	34(3)	18(2)	29(3)	6(2)	10(2)	6(2)
O(6)	43(3)	41(3)	30(3)	7(2)	5(2)	32(3)
O(7)	36(3)	23(2)	28(3)	11(2)	-4(2)	-1(2)
O(8)	40(3)	27(3)	17(2)	4(2)	-9(2)	6(2)
O(9)	44(3)	38(3)	54(3)	30(3)	31(3)	27(3)

Table D5. Hydrogen coordinates (x 10^4) and isotropic displacement parameters ($Å^2$x 10^3) for **4**.

	x	y	z	U(eq)
H(9)	5472	1435	9102	17
H(10)	5540	3784	9511	19
H(13)	10264	6537	8704	20
H(14)	12192	5931	8121	20
H(16)	13282	4026	7593	24
H(17)	12911	1552	7274	25
H(18)	10630	-167	7474	22
H(21)	8558	7103	9520	26

Appendix E Discussion of the "first order rate law" observation in photochemical reactions in literatures.

In some photoCORMs literatures[1,2], it has been shown that the solution concentration of a photoCORM ([*M*]) changed exponentially with irradiation time (*t*). In some cases, this behavior was attributed this correlation to a first order rate law for the photochemical reactions for which first order rate constants were reported. However, an obvious argument against above conclusion is that the "first order rate constant" is no longer constant if irradiation power is changed, and, furthermore, when the concentration is high enough to absorb all the excitation light, the rate of the photochemical reaction becomes independent of substrate concentration.

For further illustration, an experiment was carried using 2.5 mM compound **4** in acetonitrile solution using 794 nm irradiation (Fig. A1). In this experiment, I_0 is the incident light intensity (1.2E-6 Einsteins/s) while I_1 is the transmitted intensity (1.0E-6 Einsteins/s) when the cuvette contains only the solvent (acetonitrile). I_2 is the transmitted intensity through a solution of compound **4** solution in the cuvette. I_{abs} was then calculated from $I_{abs} = I_1 - I_2$ (doing this corrects for light reflected and/or scattered by the cell), and the use of power meter here made it possible to monitor I_{abs} change as a function of *t* (Fig. A2).

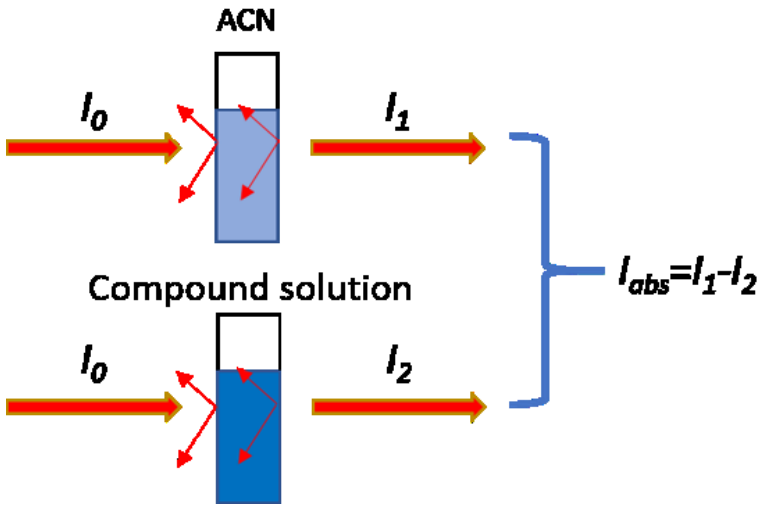

Figure. A1. Illustrative depiction of absorbed light intensity (I_{abs}) measurement: Acetonitrile solution of compound **4** has a concentration of 2.2 mM and irradiation source was 794 nm continuous laser with a power of 180 mW; I_0 was incident light intensity (1.2E-6 Einsteins/s) while I_1 (1.0E-6 Einsteins/s) was transmission light intensity when the cuvette is filled with solvent.

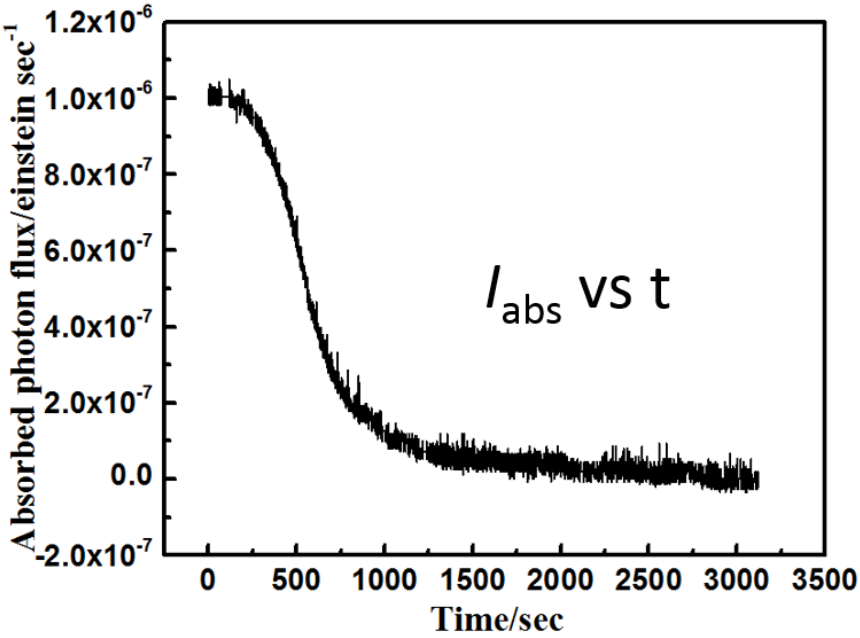

Figure. A2. Absorbed light intensity (I_{abs}) change as function of irradiation time from experiment described in Fig. A1.

The integration of I_{abs} over time gives the amount of light absorbed (N_{abs}, in Einsteins) for a particular period of irradiation (Fig. A3). A high concentration solution of **4** was used, so nearly all the light was absorbed for the early stages of the photolysis, thus N_{abs} was linearly proportional to t. After **4** is significantly depleted, N_{abs} was found to decrease in a near exponential relationship with t before hitting a plateau representing the absorbance of the photoproduct. In this regime, the depletion rate of the substrate **4** is represented by eq. A1

$$- d[\mathbf{4}]/dt = \Phi I_{abs} \quad (\text{or } \Phi N_{abs})$$

where

$$I_{abs} = I_o (1\text{-}10^{\varepsilon c l})$$

and c is [**4**], ε is the extinction coefficient for **4** at the excitation wavelength and l is the pathlength. I_{abs} is absorbed light intensity by unit volume of solution (Einstein $L^{-1}s^{-1}$) and I_o is incident light intensity by unit volume of solution (Einstein $L^{-1}s^{-1}$). Thus, while the curvature of the plot in Figure A2 when the concentration of **4** is relatively low may appear to be an exponential decay, it is obvious that these equations do not integrate to a first order rate law, and that any rate constant derived from such plots is an artifact.

Reference

1. Gonzalez, M. A.; Yim, M. A.; Cheng, S.; Moyes, A.; Hobbs, A. J.; Mascharak, P. K. Manganese Carbonyls Bearing Tripodal Polypyridine Ligands as Photoactive Carbon Monoxide-Releasing Molecules. *Inorg. Chem.* **2012**, 51, 601−608.

2. Chakraborty, I.; Carrington, S. J.; Mascharak, P. K. Photodelivery of CO by Designed PhotoCORMs: Correlation between Absorption in the Visible Region and Metal–CO Bond Labilization in Carbonyl Complexes. *ChemMedChem.* **2014**, 9, 1266 – 1274.

Chapter 4. Visible Light Activated Turn-On Emissive Dinuclear PhotoCORM

I. Introduction

In our previous work on dinuclear photoCORMs[1], we described a new strategy for triggering photochemical release of caged carbon monoxide in aerobic media using long wavelength visible and near infrared (NIR) light. The dinuclear rhenium-manganese carbonyl complexes (**1**-**4**) have high photochemical quantum yields under long wavelength photolysis and competitive thermal stability. Conjugation of **4**, with an amine-terminated polyethylene glycol (PEG) oligomer gives a water-soluble derivative with similar photochemistry. Alternatively, with PLGA microparticles and nanoparticles as carriers, aqueous suspension of compound **1**-**4** can be achieved.

A luminescent photoCORM could also be a imageable reagent that is trackable in biological systems. However, the dinuclear photoCORMs **1**-**4** do not emit nor do their photo products, which is not surprising since those metal carbonyls encounter fast photochemistry reaction (metal-metal bond cleavage) and most $Re(CO)_5X$ only emit at low temperature[2]. Some rhenium tricarbonyl complexes, such as *fac*-$[Re(CO)_3LX]$ and *fac*-$[Re(CO)_3L_2X]$, (L is bidentate or monodentate amine ligand) have been found to be emissive in solution and solid state at room temperature which emission was associated with the radiative decay of ^{3}MLCT (Re to π^* of L charge transfer) excited states. Such compounds have already been used as trackable photoCORMs in the literature.[3–6] In this work, we synthesized a Re-Mn dinuclear photoCORM: $(CO)_5MnRe(CO)_3(bpy)$ (compound **7**) which contains a rhenium tricarbonyl moiety ($-Re(CO)_3(bpy)$). Emission was expected from **7** or its photoproduct to give dinuclear compound bioimaging property.

II. Synthesis

Synthesis of compound **7** was first reported by D. J. Stufkens and coworkers using a method similar to Re-Mn dinuclear carbonyls **1-4** (Scheme 4.1)[7]. However, we found the synthesis depicted in Scheme 4.1 results in a very low reaction yield around 1%. Although reagent $Re(CO)_5Cl$ was replaced by $Re(CO)_5Br$, since -Br is a better leaving group than -Cl, the reaction yield was still only ~1% (Scheme 4.2). One possible explanation of the low reaction yield is that the $Mn(CO)_5^-$ anion is not as strong reducing agent as is the $Re(CO)_5^-$ anion (Scheme 4.4)[8]. Therefore, an alternative synthesis pathway was initiated as shown in scheme 4.3 where the roles of redox reagents were switched. The Re anion was synthesized to reduce the manganese pentacarbonyl bromide to form Re-Mn bond, and a reaction yield of 15% was achieved. It is notable that this reaction yield for the synthesis of is still much lower than that found for the synthesis of its isomer, compound **2** ($(CO)_5ReMn(CO)_3$(bpy).

A. Precursors

***fac*-[Re(CO)$_3$(bpy)Cl]:** This was prepared by a modified literature procedure.[3] Dirhenium decacarbonyl (1.000 g, 1.53 mmol) was refluxed with 2,2'-bipyridine (0.716 g, 4.59 mmol) in 2-chloroethanol (120 mL) for 18 h under Ar atmosphere. After 18 h, the reaction solution was vacuum dried and dissolved in 50 mL of DCM and washed with water (50 ml × 3). A yellow solid was obtained after evaporating the DCM and the solid was dried in vacuum oven at 60 C° for 12 h. Total yield was 1.085 g (76.8%). The ^{1}HNMR spectrum agreed with the literature[9] (500 MHz, $CDCl_3$, ppm) δ = 9.08 (d, J(H,H) = 5.4 Hz, 2H), 8.20 (d, J(H,H) = 8.1 Hz, 2H), 8.09 (td, J(H,H) = 7.9, 1.6 Hz, 2H), 7.56 (ddd, J(H,H) = 7.5, 5.5, 1.2 Hz, 2H).

Na[Re(CO)$_3$(bpy)]: Hg(Na) (3%) (2.4 g) was added to a dry round bottom flask containing ~30 mL dry THF under an argon atmosphere. Under flowing argon, solid Re(CO)$_3$(bpy)Cl (0.150 g, 0.324 mmol) was added to this solution, and it was stirred for 3 h in dark. The initially yellow Re(CO)$_3$(bpy)Cl solution underwent a change to the dark green of Na[Re(CO)$_3$(bpy)]. The Na[Re(CO)$_3$(bpy)] was not isolated; instead the THF solution was kept under an argon atmosphere until being used in its entirety using the same day in each synthetic procedure.

B. (CO)$_5$MnRe(CO)$_3$(bpy) (compound 7)

A THF solution containing the rhenium anion Na[Re(CO)$_3$(bpy)] (0.324 mmol) was carefully transferred via cannula to another round bottom flask containing Mn(CO)$_5$Br (0.100 g, 0.365 mmol) dissolved in 35 mL of dry THF. The solution was then allowed to stir under argon at 40 C°, with the exclusion of light for 12 h. The mixed solution color changed from a yellow color to orange. After 12 h, the solvent was removed under vacuum, and the resulting solid was purified by flash chromatography over activated alumina. The column was washed with one column volume of pure hexanes, then it was eluted with a gradient of DCM/hexanes (0%-50% DCM). The main component from the column chromatography purification was collected and was further purified by recrystallization from DCM by slow vacuum evaporation of solvent giving a final product with a yield of 43 mg (15%).

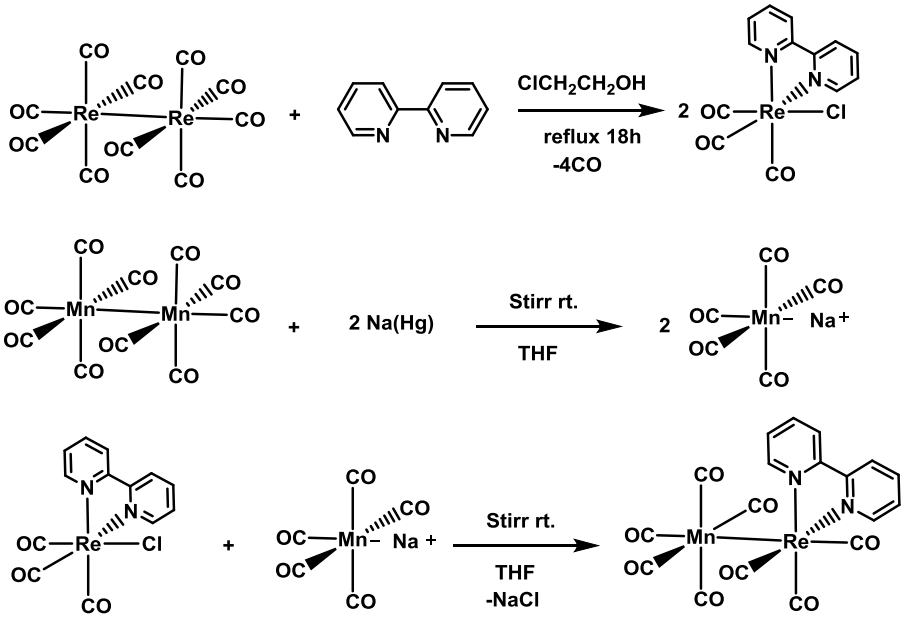

Scheme 4.1 Steps leading to the syntheses of complexes **7** using Mn anion as a reactant.

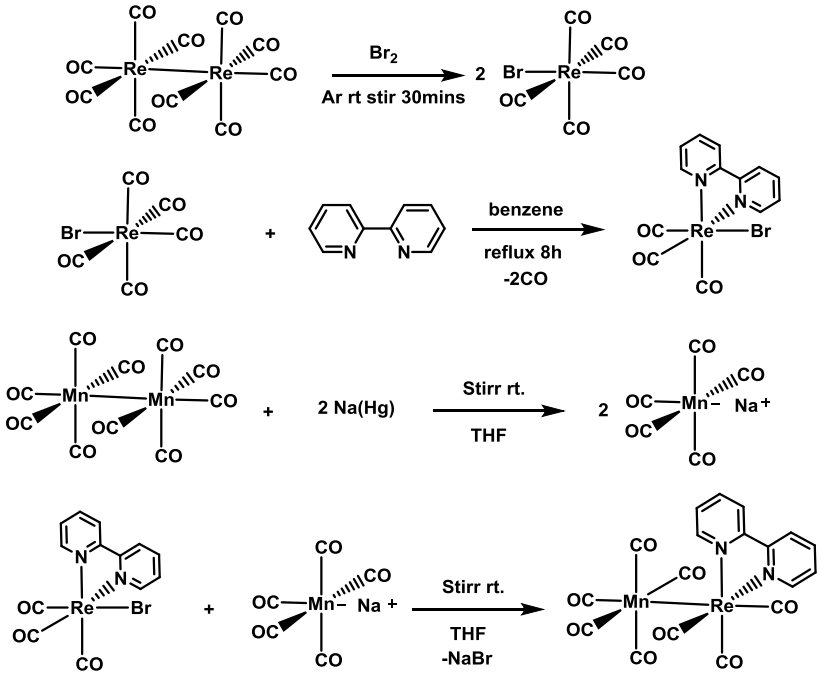

Scheme 4.2 Modified syntheses steps of complexes **7** using $Re(CO)_5Br$ as precursor.

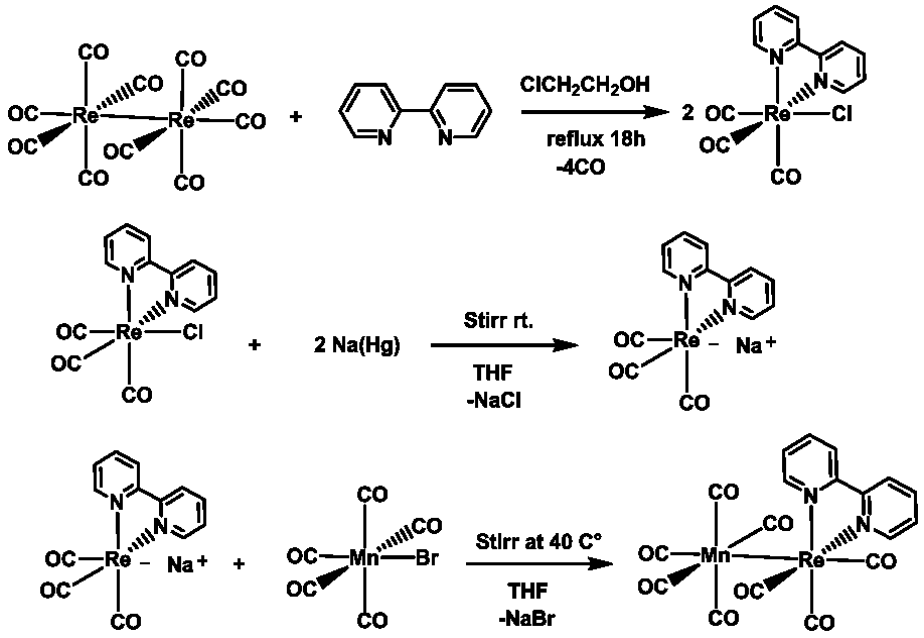

Scheme 4.3 Steps leading to the syntheses of complexes **7** using Re anion as a reactant.

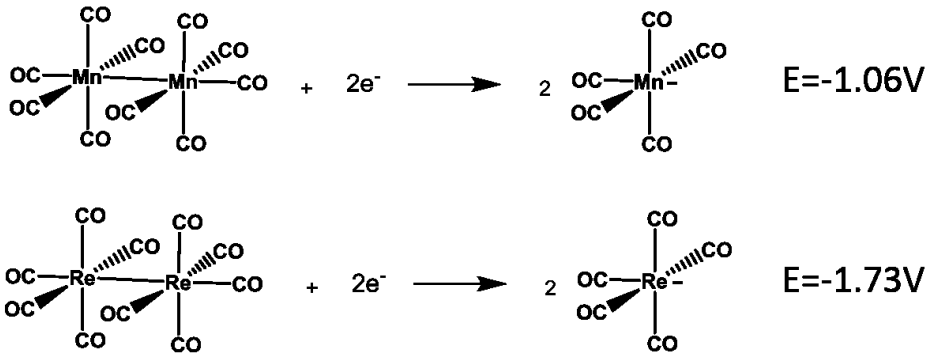

Scheme 4.4 Reduction reactions of $Mn_2(CO)_{10}$ and $Re_2(CO)_{10}$.

III. Characterizations of $(CO)_5MnRe(CO)_3(bpy)$ and precursors

Compound **7** and its precursor *fac*-$[Re(CO)_3(bpy)Cl]$ were identified by ^1H NMR spectrometry (500 MHz, CD_3CN, ppm) (Fig. 4.2 and 4.1). The ^1H NMR spectrum of *fac*-$[Re(CO)_3(bpy)Cl]$ agrees with the literature[9] and the ^1H NMR spectrum of **7** has a set of lower field resonances characteristic of bpy compared to its precursor: δ = 9.12 (d, J(H,H) = 5.6 Hz, 2H), 8.52 (d, J(H,H) = 8.3 Hz, 2H), 8.10 (td, J(H,H) = 8.2, 1.5 Hz, 2H), 7.56 (ddd, J(H,H) = 7.1, 5.7, 1.2 Hz, 2H). In Fig. 4.3, the ATR-IR spectrum of 7 has shown strong ν_{CO} bands at 2053(s), 1984(s), 1949(s), 1922(s), 1875(s), 1860(s) which are listed in Table. 4.1. Molar mass of **7** is determined to be 621.87 m/z by FD+ mass spectrum with a calculated molar mass: 621.92 m/z (Fig. 4.4). Besides the ^1H NMR, IR, mass spectra, the dinuclear compound **7** was also characterized by UV-visible spectroscopy (Fig. 4.5). The UV-visible spectrum of **7** in acetonitrile (MeCN) solution displays an absorption band at 483 nm which is attributed to a MMLCT ($\sigma_{MM} \rightarrow \pi L^*$) transition in analogy to earlier studies with related complexes.

A. ^{1}H NMR spectra

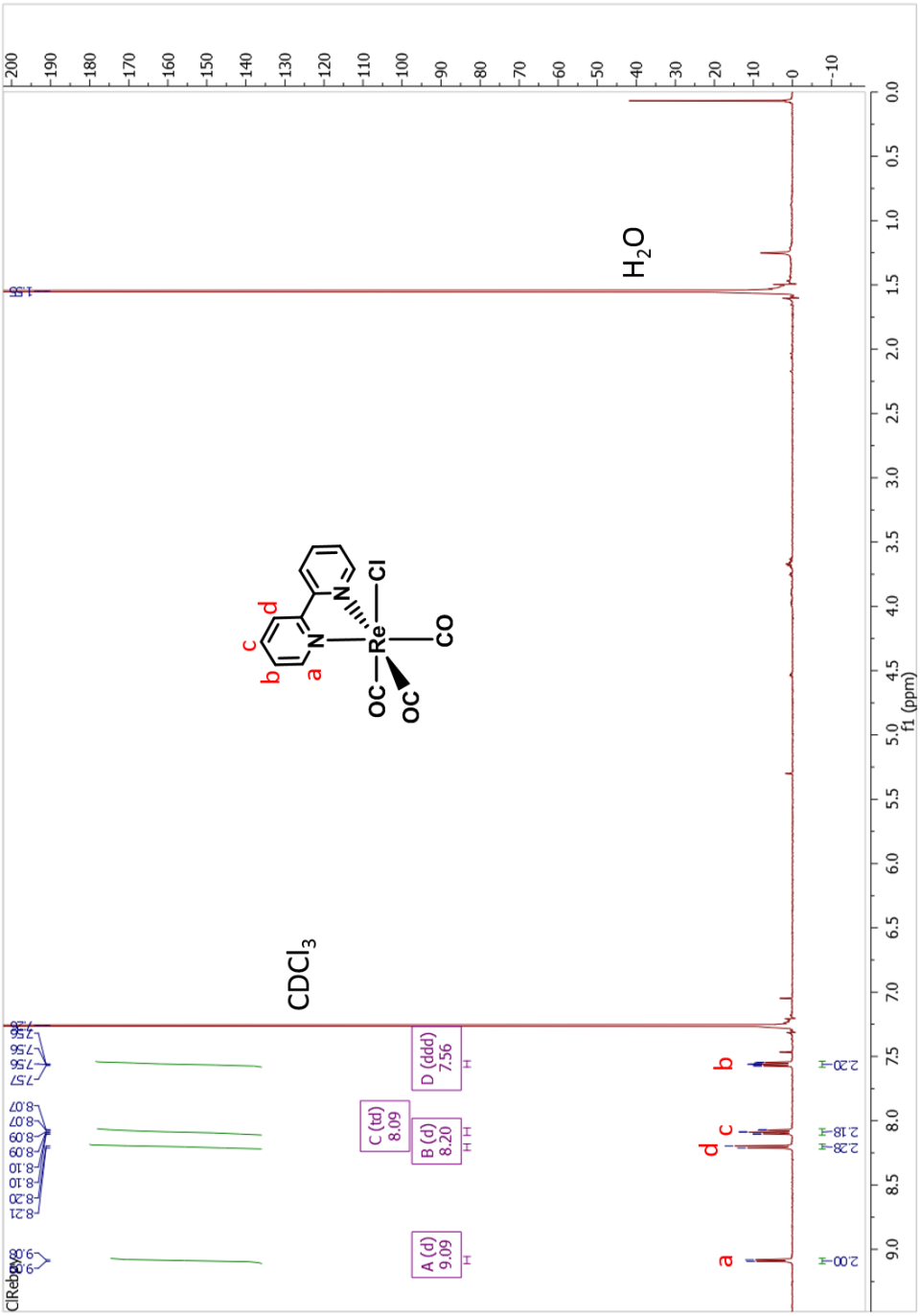

Figure 4.1 ^{1}H NMR spectrum of precursor *fac*-[Re(CO)$_3$(bpy)Cl] agreed with the literature[9] (500 MHz, $CDCl_3$, ppm) δ = 9.08 (d, J(H,H) = 5.4 Hz, 2H), 8.20 (d, J(H,H) = 8.1 Hz, 2H), 8.09 (td, J(H,H) = 7.9, 1.6 Hz, 2H), 7.56 (ddd, J(H,H) = 7.5, 5.5, 1.2 Hz, 2H).

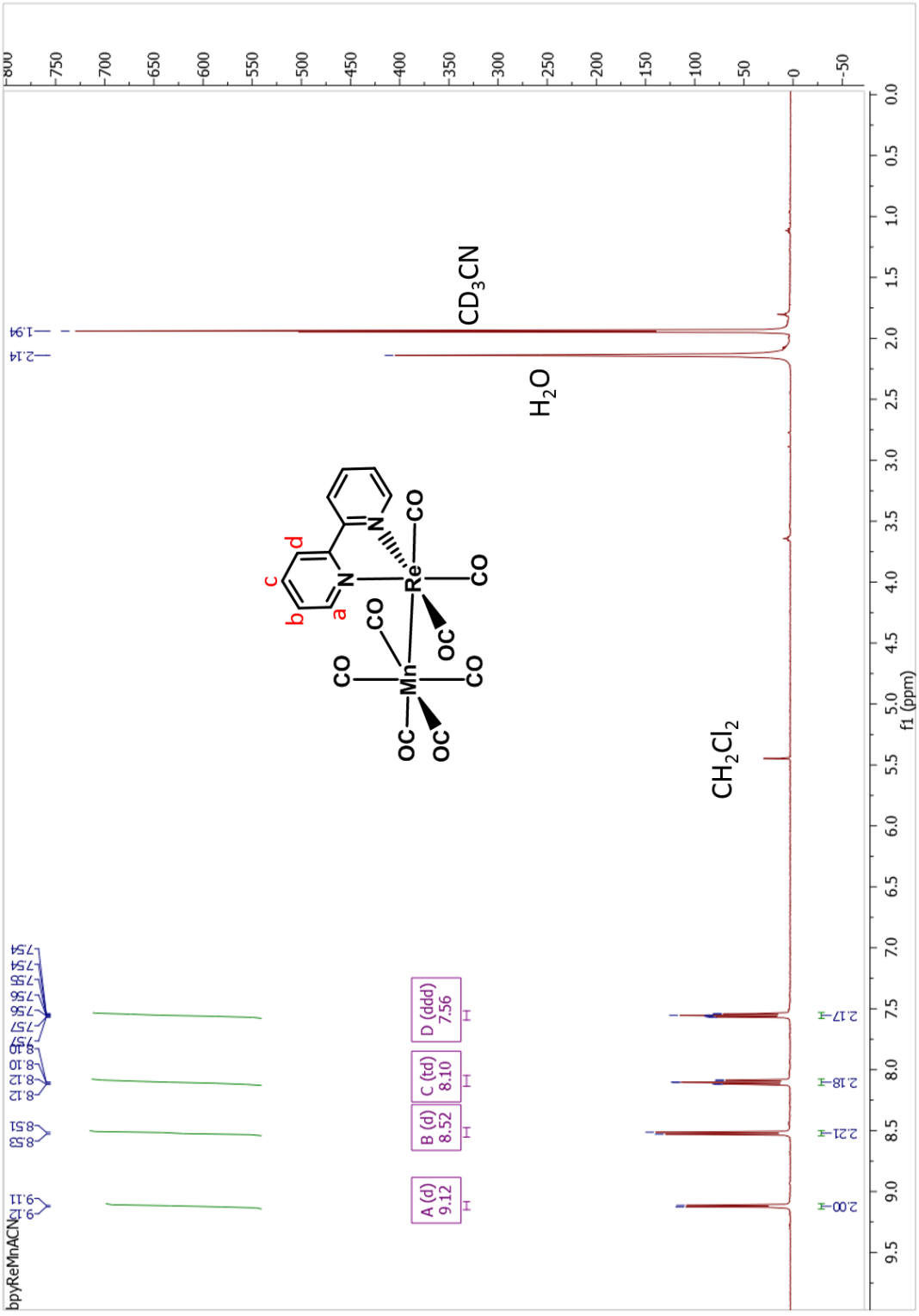

Figure 4.2 ^{1}H NMR of **7** (500 MHz, CD_3CN, ppm) δ = 9.12 (d, J(H,H) = 5.6 Hz, 2H), 8.52 (d, J(H,H) = 8.3 Hz, 2H), 8.10 (td, J(H,H) = 8.2, 1.5 Hz, 2H), 7.56 (ddd, J(H,H) = 7.1, 5.7, 1.2 Hz, 2H).

B. ATR-IR spectra

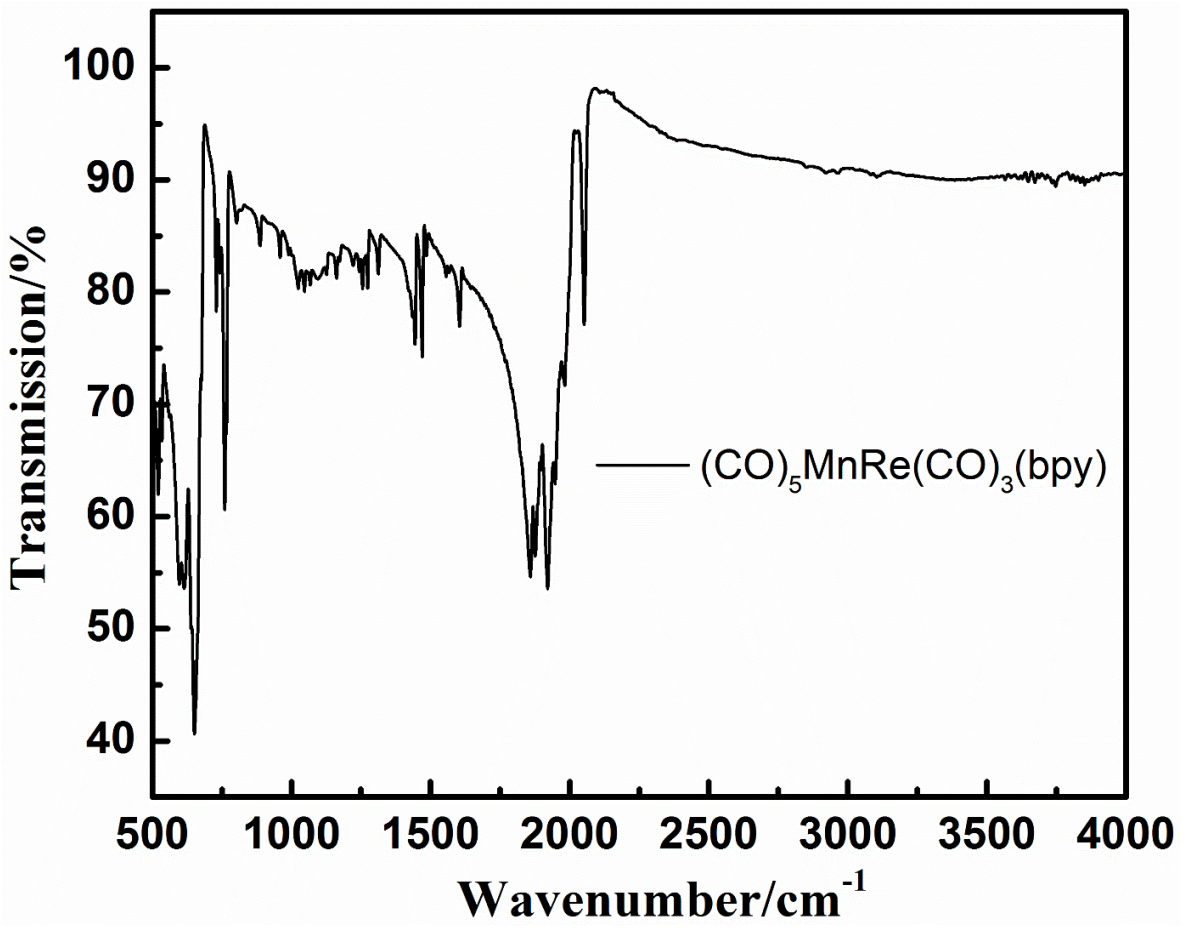

Figure 4.3 ATR-IR spectrum of compound **7** in solid state

Table 4.1 Solid state attenuated total reflectance (ATR)-IR absorption data for compounds **7**

Compound	IR absorption peak maxima in cm^{-1}
7	2053(s), 1984(s), 1949(s), 1922(s), 1875(s), 1860(s), 1604(m), 1471(m), 1445(m), 1313(w), 1274(w), 1256(w), 1162(w), 1068(w), 1047(w), 1024(w), 959(w), 888(w), 760(s), 651(s), 597(s)

C. Mass spectra

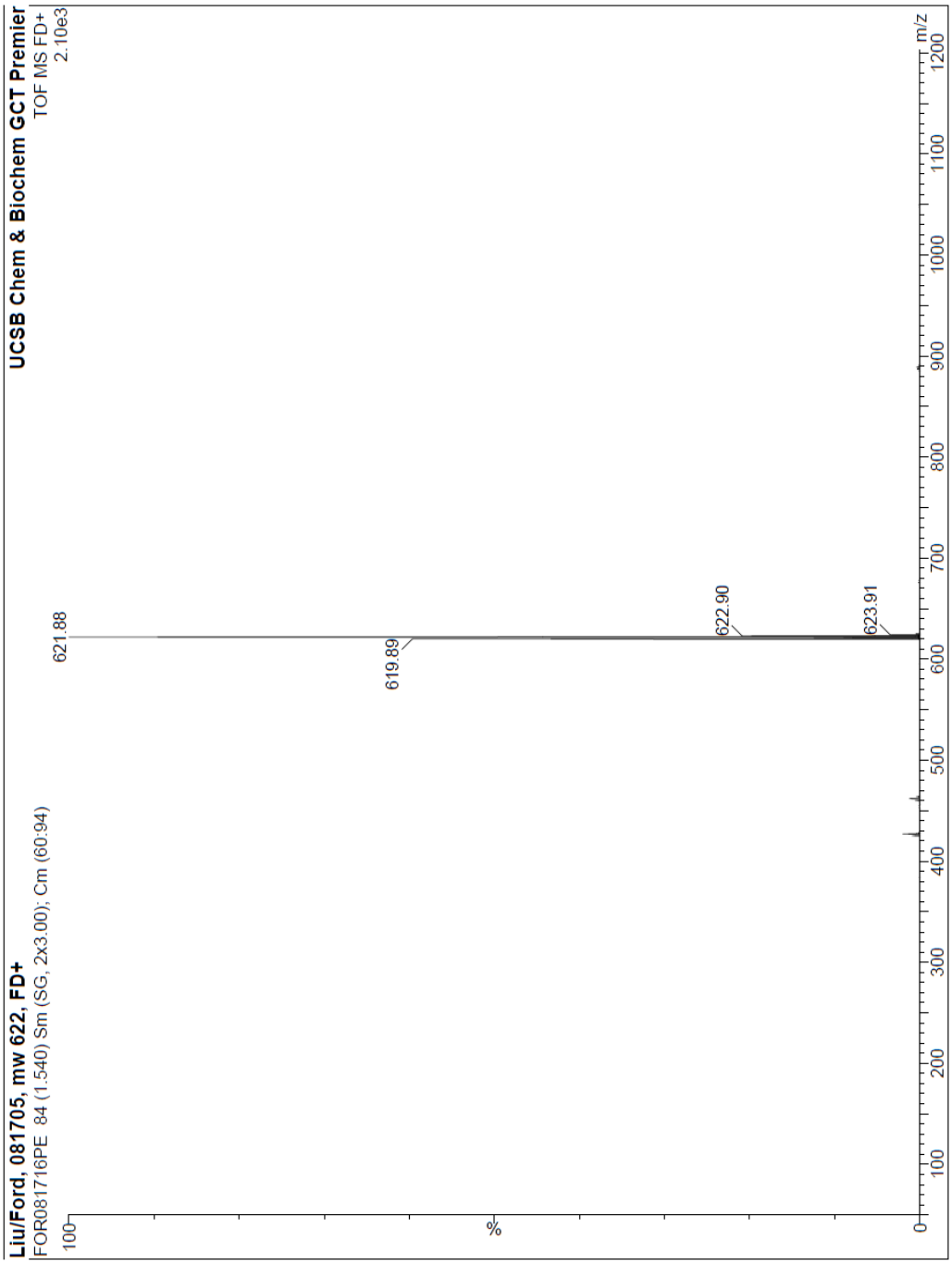

Figure 4.4 FD+ Mass spectrum of **7.** Molar mass: 621.87 m/z; Calculated: 621.92 m/z.

D. Electronic absorption spectra

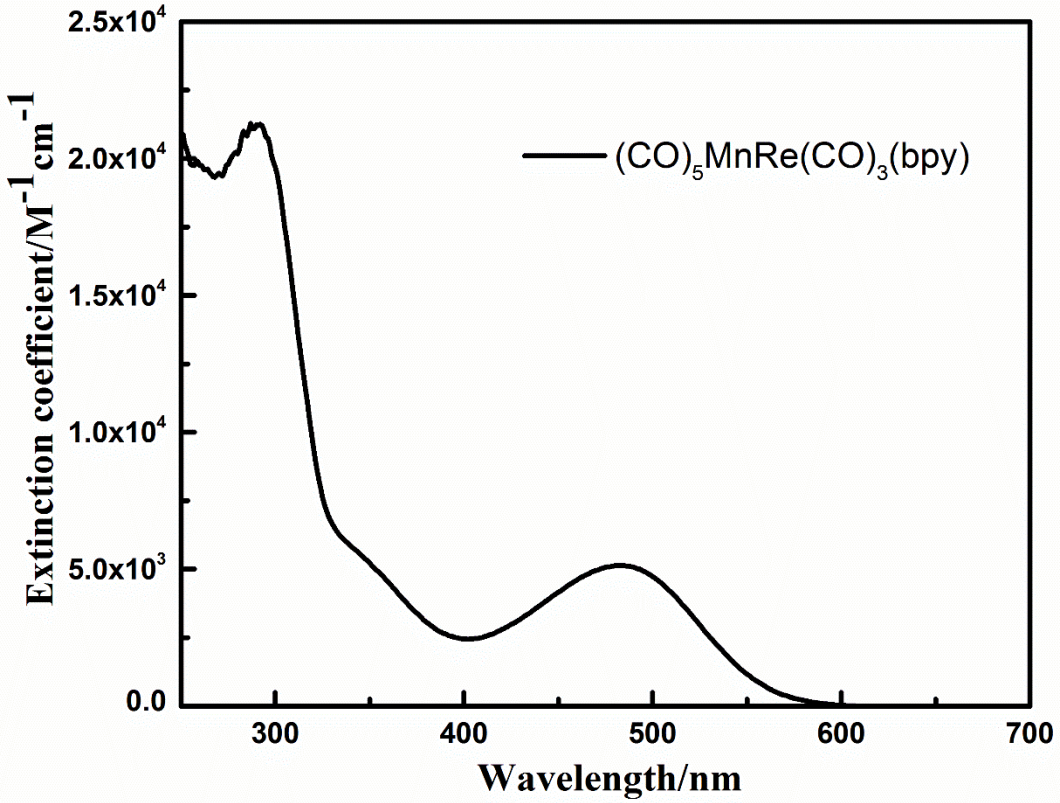

Figure 4.5. The visible absorption spectra **7** in aerobic MeCN solution, ambient temperature with a MMLCT λ_{max} at 483nm (extinction coefficients are 5.1×10^3 M^{-1} cm^{-1}).

Table 4.2 Uv-vis absorption data for 7

Compound	Uv-vis absorption λ_{max}/nm ($\varepsilon/M^{-1}cm^{-1}$)
7	287 (21232), 341 (5789), 483 (5133)

E. Crystal structures

The crystal structure of $(CO)_5MnRe(CO)_3(bpy)$ (**7**) was determined by X-ray diffraction on a Kappa Apex II single-crystal diffractometer. X-ray suitable crystals were grown by diffusing hexane vapor into an acetonitrile solution in which compound **7** was dissolved. The crystals are monoclinic, and the structure of **7** determined from X-ray is shown in Fig. 4.6. Complete parameters including bond lengths and angles are in the Appendix of this chapter. Similar to compound **2**, the three carbonyls on Re are in *facial* configuration and the Re-Mn bond length is 3.010 Å.

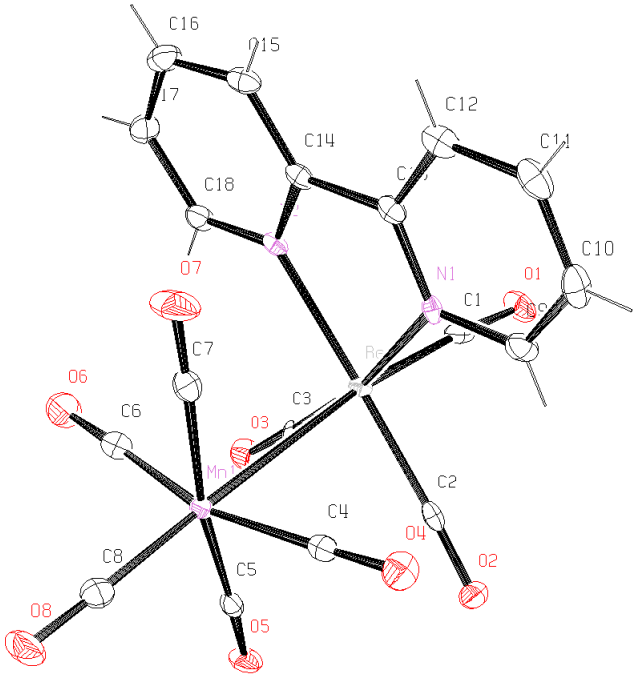

Figure 4.6 ORTEP drawing of the x-ray structures of $(CO)_5MnRe(CO)_3(bpy)$ (**7**) (Shown with 50% thermal ellipsoids).

IV. Photochemical study of $(CO)_5MnRe(CO)_3(bpy)$

A. Stability in dark

Aerobic MeCN solution of **7** shows good stability at 37 ºC when kept in the dark. Total intensity change of the MMLCT band at 483 nm was only 8% over a 16 h period (Fig. 4.7)

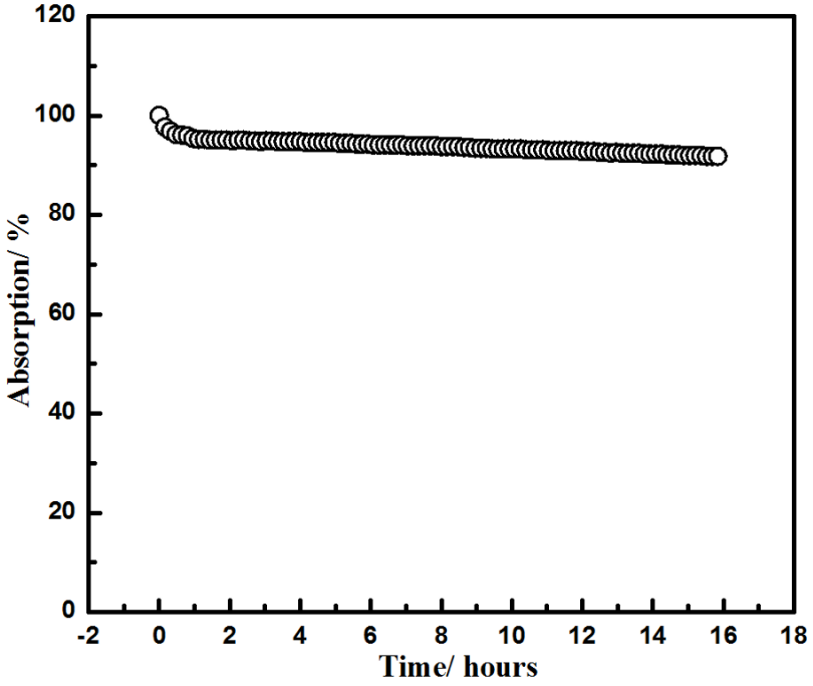

Figure 4.7 Normalized absorbance at the λ_{max} for the MMLCT band of aerobic **7** in MeCN at ~37 ºC over the course of 16 hours (92% remained after 16 hours).

B. Photochemical studies

In acetonitrile solution, $(CO)_5MnRe(CO)_3(bpy)$ shows an absorption peak at 483 nm and its MMLCT band extends to ~600 nm. For the photochemistry study, the "Green LED" (Chapter 2, Fig. 2.5 and table 2.2) with an emission peak centered at 532 nm was used. At the wavelength of 532 nm compound **7** has an extinction coefficient of 2397 $M^{-1}cm^{-1}$.

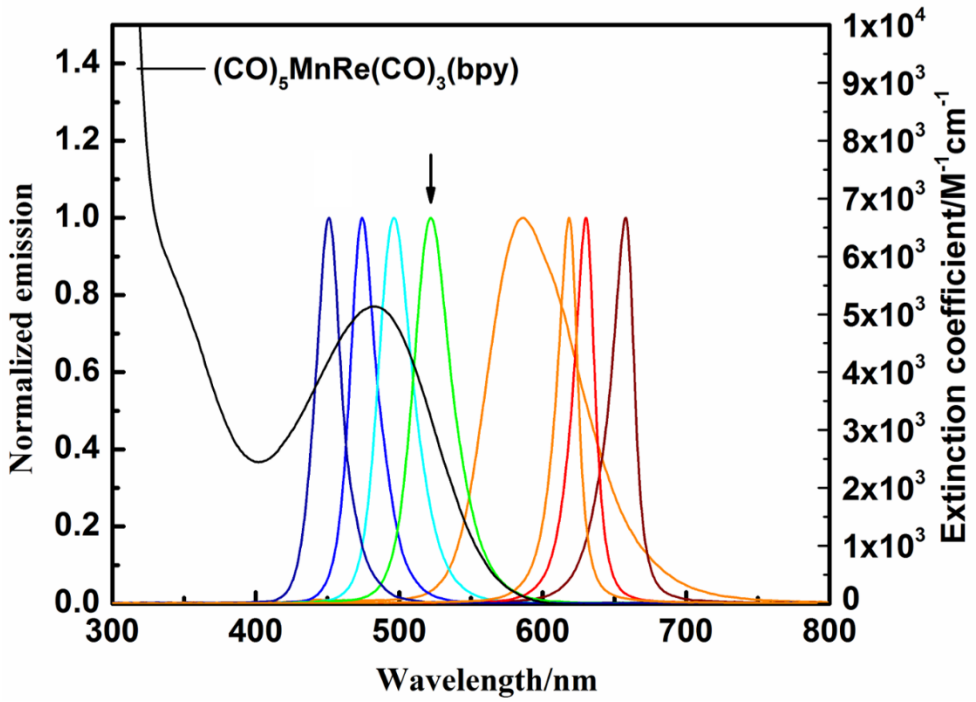

Figure 4.8 Absorption spectrum of $(CO)_5MnRe(CO)_3(bpy)$ in acetonitrile and emission spectra of the light emitting diode in the laboratory.

1. UV-vis absorption spectra change and quantum yield measurement

The photolysis of compound **7** in aerobic MeCN gives a result similar to those seen with dimers **1-4**. The photolysis of **7** in aerobic solution bleached the MMLCT band which indicates the cleavage of metal-metal bond (Fig. 4.9).

$$(CO)_5Mn\text{-}Re(CO)_3(bpy) \xrightarrow{h\nu} (CO)_5Mn\cdot + \cdot Re(CO)_3(bpy)$$

However, unlike compound **1**, after exhaustive photolysis the charge transfer band does not fully disappear, while the higher energy band at 341 nm does not change significantly. This may imply that one or more photoproducts have relative low energy absorptions perhaps a MLCT ($d\pi \rightarrow \pi_L^*$) transition of certain Re species.

The photochemical quantum yields (Φ_{MM}) of metal-metal bond cleavage were measured for compound **7** in aerobic acetonitrile using spectra changes from Fig. 4.9. Φ_{MM} was determined to be 0.313 ± 0.009 (Fig. 4.10), which is similar to the quantum yields measured for compounds **1** and **2**.

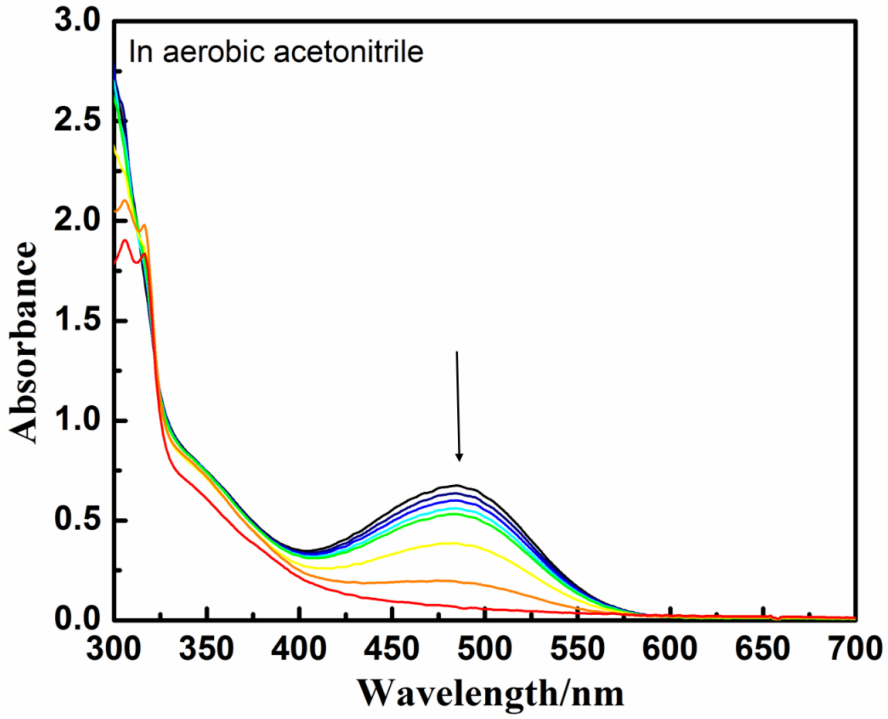

Figure 4.9 Absorption spectra changes upon 532 nm photolysis (21 mW) of **7** (1.42×10^{-4}) in aerobic MeCN.

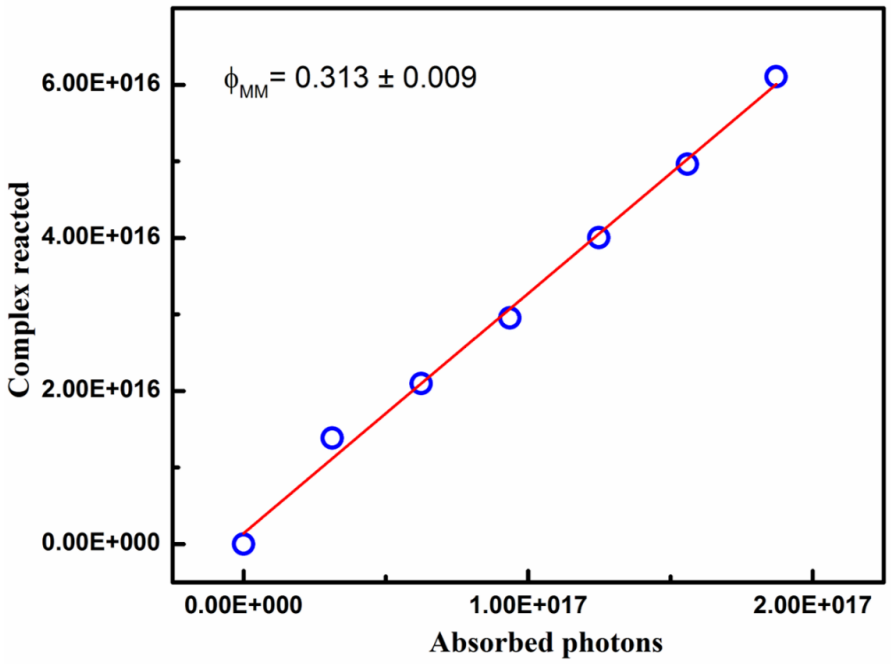

Figure 4.10 Quantum yield measurement for the disappearance of **7** (0.165 mM) in aerobic MeCN under 532 nm photolysis: $\Phi_{MM} = 0.313 \pm 0.009$.

2. CO release under photolysis

The quantitative gas release was measured by GC-TCD analysis of the gas phase after exhaustive photolysis of 4 mL aerobic acetonitrile solutions of **7** (3.18 mM, 0.0127 mmol) in a Schlenk cuvette. The quantity of CO released from total photolysis was measured to be 0.0117 mmol which corresponds to 0.92 CO/compound. The CO release quantum yield under such conditions was measured independently as 0.26 ± 0.018 by using GC-TCD analysis to measure the CO released at several time points during the photolysis (Fig. 4.11). The ratio between CO releasing quantum yield and metal-metal bond cleavage quantum yield is 0.84 which is consistent to the total CO releasing value: 0.92 CO/compound. Also, like compound **1**, photolysis of **7** led to 0.0107 mmol CO_2 which is 0.85 moles of CO_2 released per mole of compound. It is surprising that only one CO is released in this case given that 4 CO's should be available from Mn (The Re moiety is unlikely to release CO given that the strong ligand field would keep it as a low spin complex as noted in Chapter 3). From DFT calculations, $^2[OMn(CO)_5]$ to $^6[OMn(CO)_5]$ transition is endothermic with ΔE as 41 kcal/mol.

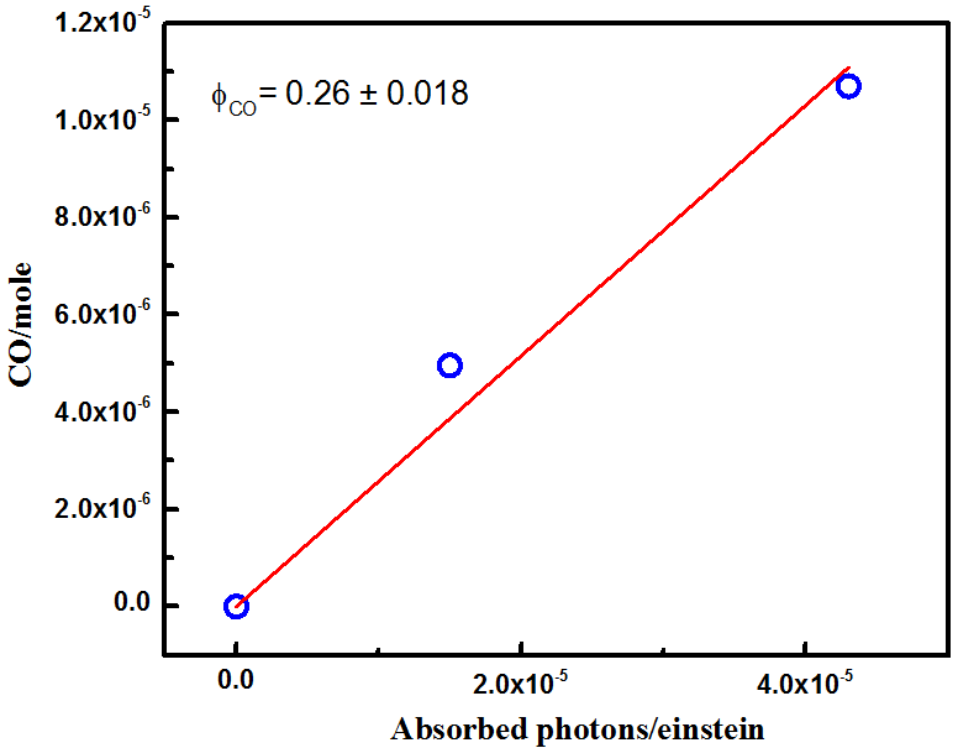

Figure 4.11 Φ_{CO} measurement for the 532 nm (24 mW) photolysis of **7** in aerobic MeCN (3.18mM).

3. Luminescence study of compound 7 and its photoproduct

Since compound **7** contains a rhenium tricarbonyl moiety (-$Re(CO)_3$(bpy)), it is possible that compound 7 or/and its photoproducts could be emissive at room temperature. Therefore, emission and excitation spectra were measured for **7** and its photoproducts (Fig. 4.12 and Fig. 4.14).

Fig. 4.12 shows that compound **7** in acetonitrile solution has a very low emission intensity with λ_{max} = 555 nm. However, it is worth noting that since compound **7** has a quite high photochemistry quantum yield of 31% it is possible that even this low emission detected is derived from photoreaction products. To evaluate this possibility, the temporal emission

intensity at single wavelength at 555 nm was recorded under continuous excitation at 380 nm (Fig. 4.13). Under continuous excitation, the emission increases linearly from approximately zero, showing that compound **7** is not emissive at all or at most very weakly emissive suggesting that the emission seen in the spectrum recorded for **7** is indeed from the photoproduct(s). Fig. 4.14 shows the emission and excitation spectra of an exhaustively photolyzed acetonitrile solution of **7**. Clearly these photoproducts show a strong emission with λ_{max} = 555 nm with an excitation spectrum having a λ_{max} = 346 nm. The observed Stokes' shift is large (209 nm).

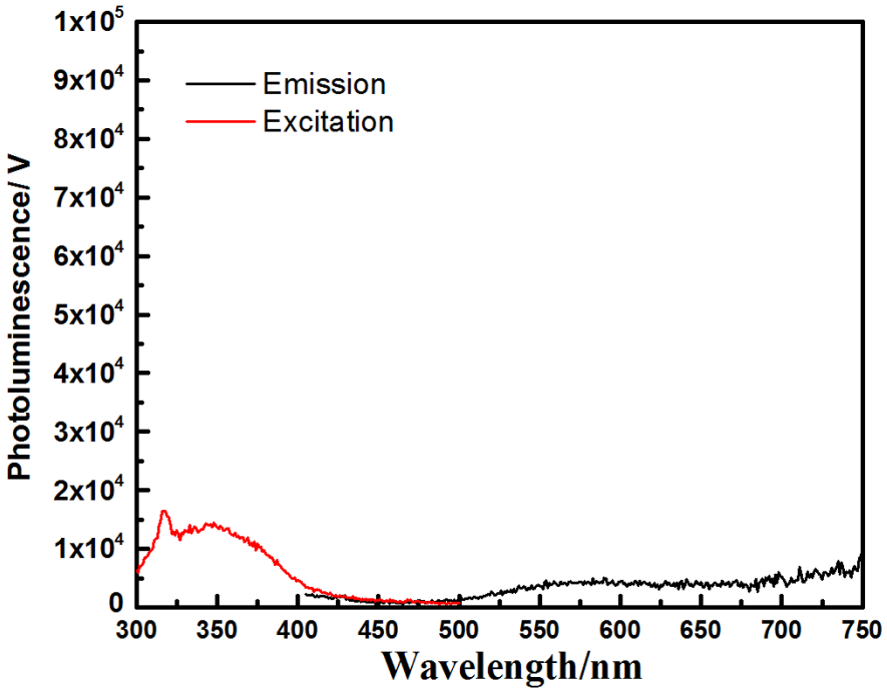

Figure 4.12 Black: Emission spectrum of **7** in aerobic MeCN (0.165 mM) with λ_{exc} = 380 nm. Red: The excitation spectrum of the same solution with the emission monitored at λ_{em} = 555 nm.

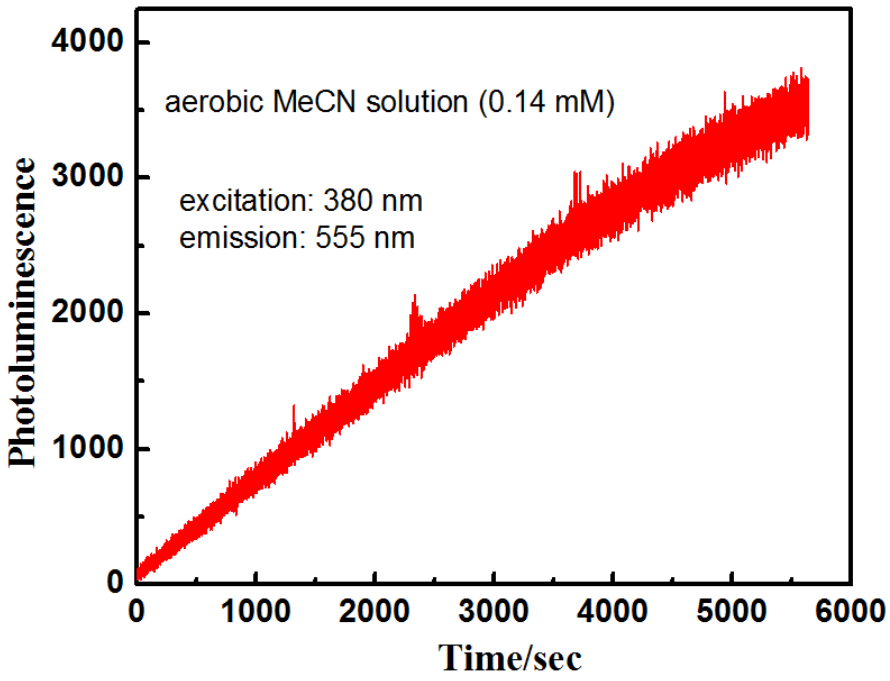

Figure 4.13 Temporal emission of a solution initially containing **7** in aerobic MeCN.under 380 nm excitation

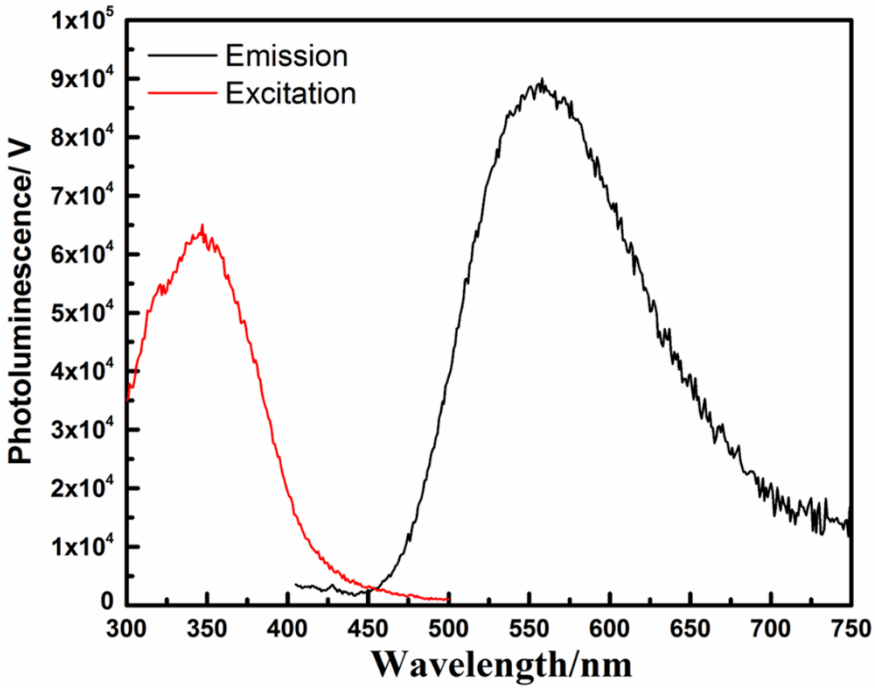

Figure 4.14 Emission spectra with λ_{exc} = 380 nm (black) and excitation spectra with λ_{em} = 555 nm (red) of a solution initially of **7** in aerobic MeCN after exhaustive photolysis at 532 nm.

Transient emission spectra of photoproducts of **7** were measured using a lab assembled time resolved optical spectroscopy instrument (Chapter 2, Fig. 2.7) at various emission wavelengths (450 nm - 600 nm). Emission lifetimes were obtained from exponential decay fitting on transient emission spectra (Fig. 4.15). Although signal intensity varies at different wavelength (due to emission intensity and PMT sensitivity), they all show single exponential decay with an indistinguishable life time of 135 ns, suggesting that photoproducts include only one emissive species. From its relatively long life-time and large Stokes' shift, it is likely that this emission is from a triplet excited state.

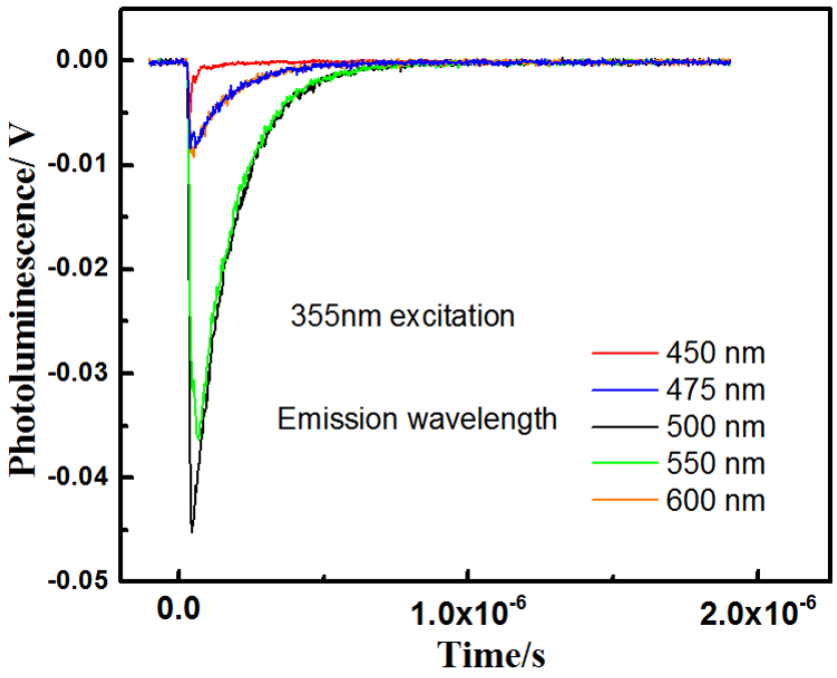

Figure 4.15 Transient emission of compound **7** photoproducts (532 nm irradiation) in aerobic MeCN.

Further spectroscopic characterizations of the photoproducts were done (Fig. 4.16-4.19). Compound **7** was photolyzed at 532 nm in deuterated acetonitrile, and the ^{1}HNMR spectrum of the photoproducts was recorded (Fig. 4.16). The photoproduct spectrum displays a series of broadened peaks at δ = 9.02, 8.48, 8.29, 7.72 ppm that significantly differs from the spectrum of compound **7.** The peak broadening could be attributed to the production of a paramagnetic species such as Mn^{2+}.

Scheme 4.6 Steps leading to photoproduct **8** and **9** from complexes **7**

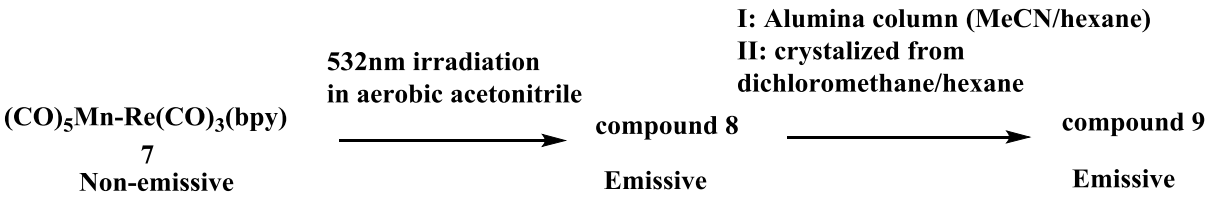

Recrystallization of the emissive photoproduct **8** was done by diffusing hexane into a DCM solution (shown in scheme 4.6) after column chromatography purification. However, recrystallization of compound **8** lead the conversion into another emissive species compound **9,** which has been proved to be the known complex $Re(CO)_3bpyCl$ by ^{1}H NMR and IR spectroscopy (Fig. 4.20 and 4.21).[9] The conversion suggests that **8** is a photo- or/and thermal-unstable compound which release a $Re(CO)_3bpy$ moiety that extracts Cl from DCM to form $Re(CO)_3bpyCl$. Mass spectroscopy data in Fig. 4.17 has shown the existence of $Re(CO)_3bpy$ moiety. By comparing the ^{1}H NMR spectrum and IR spectrum of compound **8** to the literature examples[10,11], compound **8** is close to neither $[Re(CO)_3bpy(CH_3CN)]^+$ nor $[Re(CO)_3bpy]_2$. From the IR spectra change recorded during irradiation, photoproducts of compound **7** in aerobic ACN do not contain $Mn_2(CO)_{10}$ so that the CO release may occur from the $Mn(CO)_5$ moiety. However, further study on **8** is needed to identify its structure.

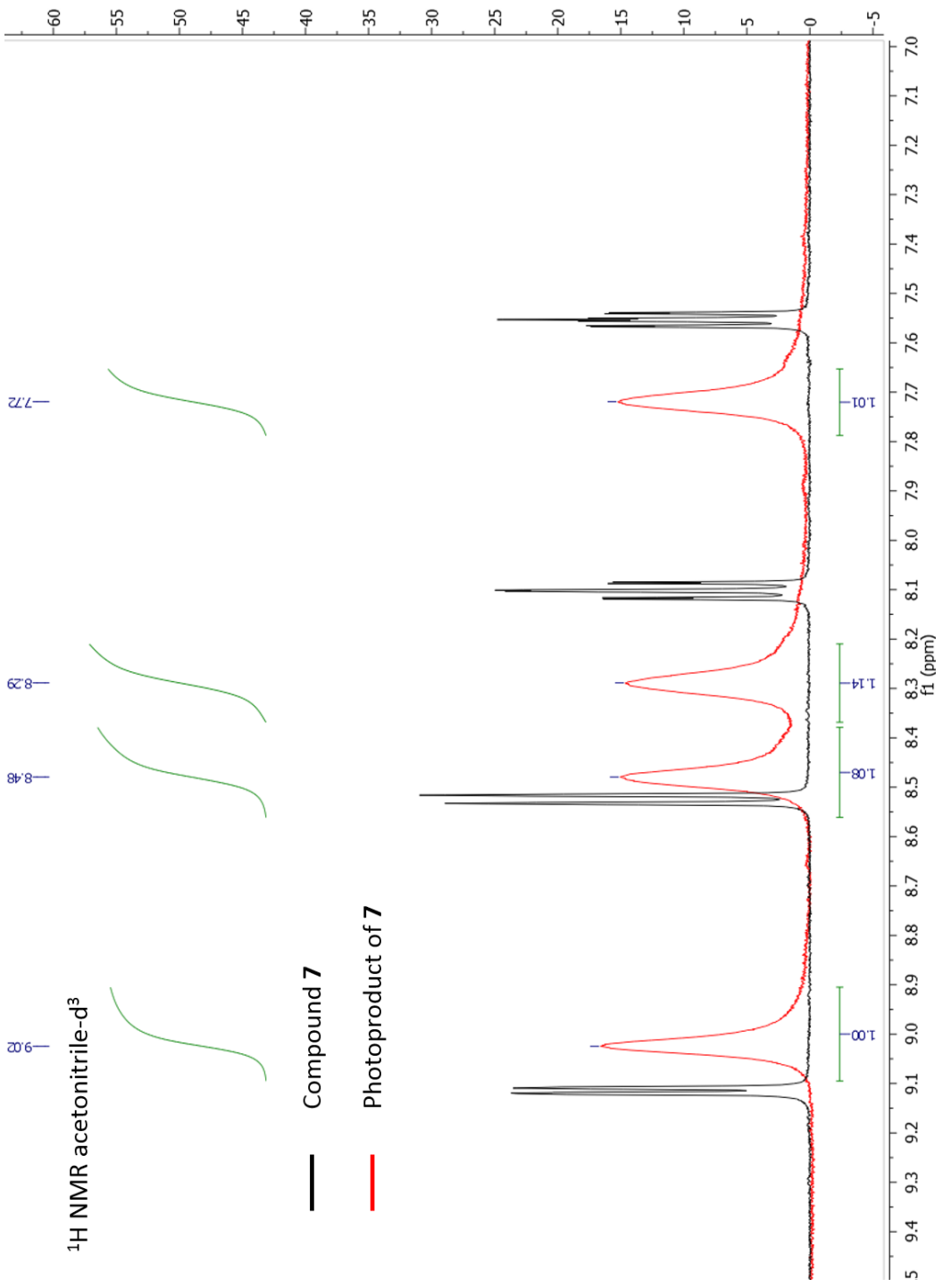

Figure 4.16 ^{1}H NMR (500 MHz, CD_3CN, ppm) spectra of compound **7** (black) and photoproducts of **7** (red) δ = 9.02, 8.48, 8.29, 7.72.

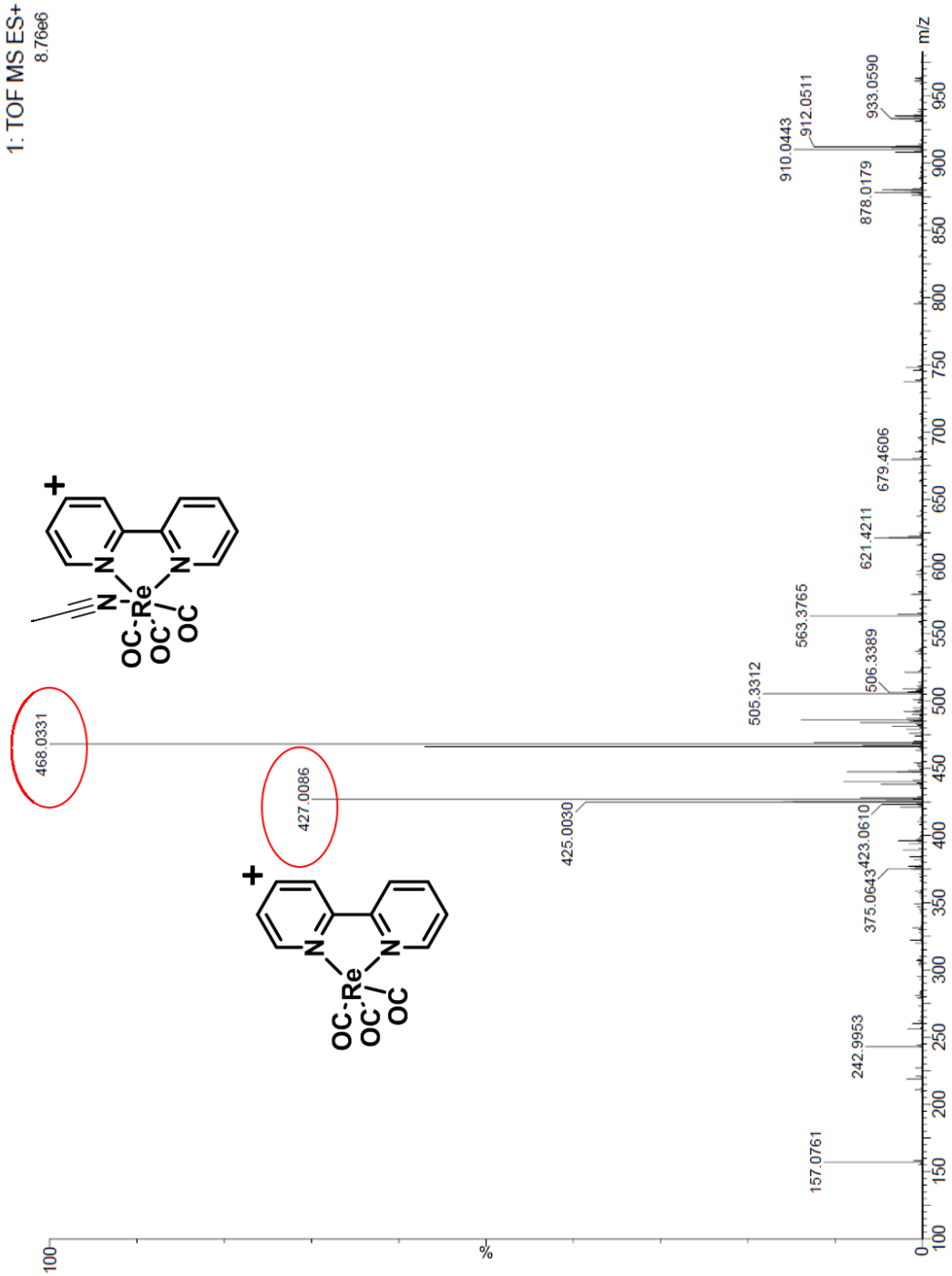

Figure 4.17 ESI+ Mass spectrum of photoproducts of **7** in acetonitrile.

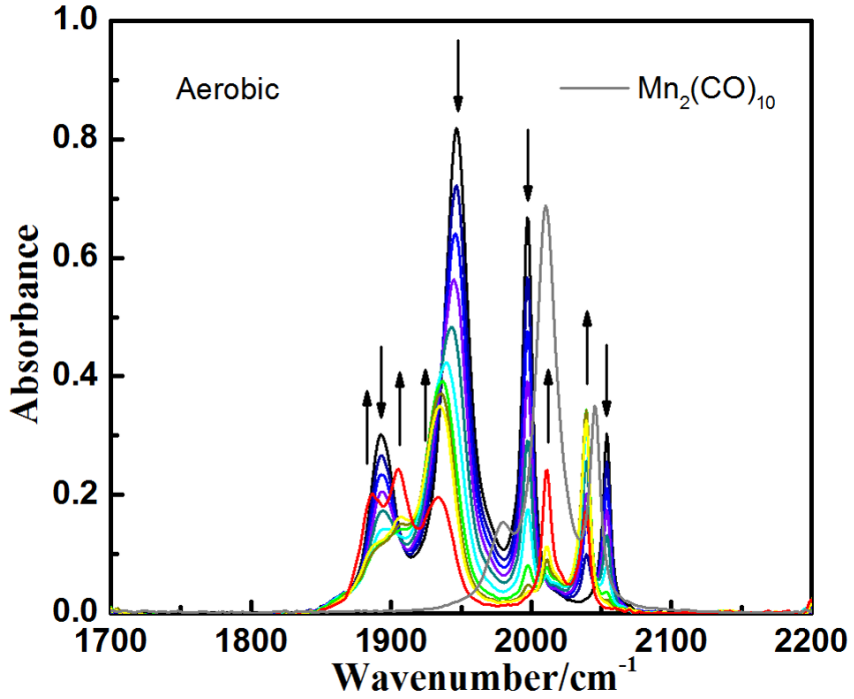

Figure 4.18 IR spectral changes upon 532 nm photolysis of **7** (4.2 mM) in aerobic MeCN in a 0.1 cm pathlength KBr cell.

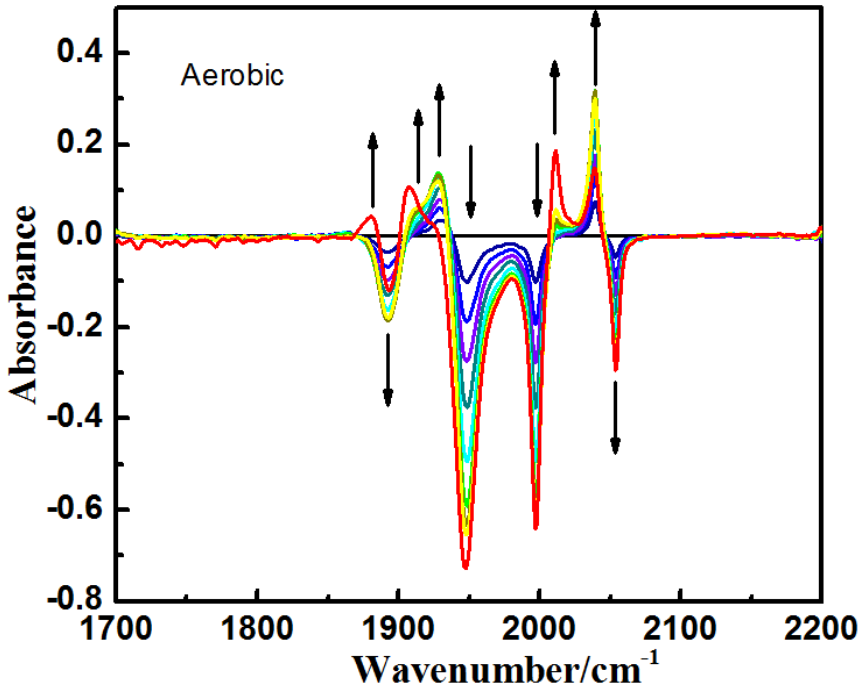

Figure 4.19 Difference spectra of data displayed in Figure **4.18**.

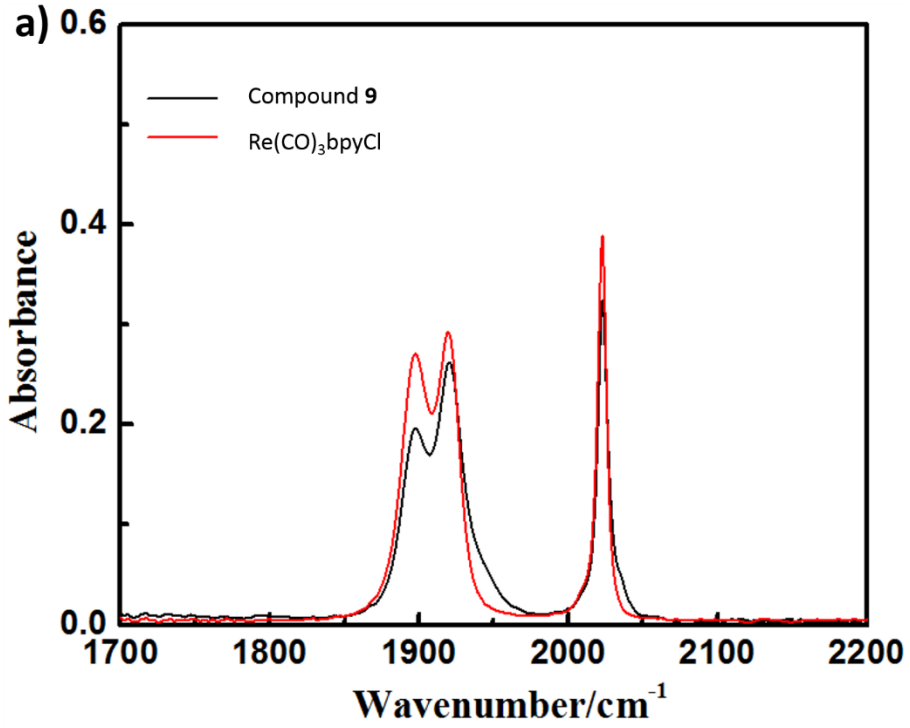

Figure 4.20 IR spectral of photoproduct of **9** in aerobic MeCN in a 0.1 cm pathlength KBr cell.

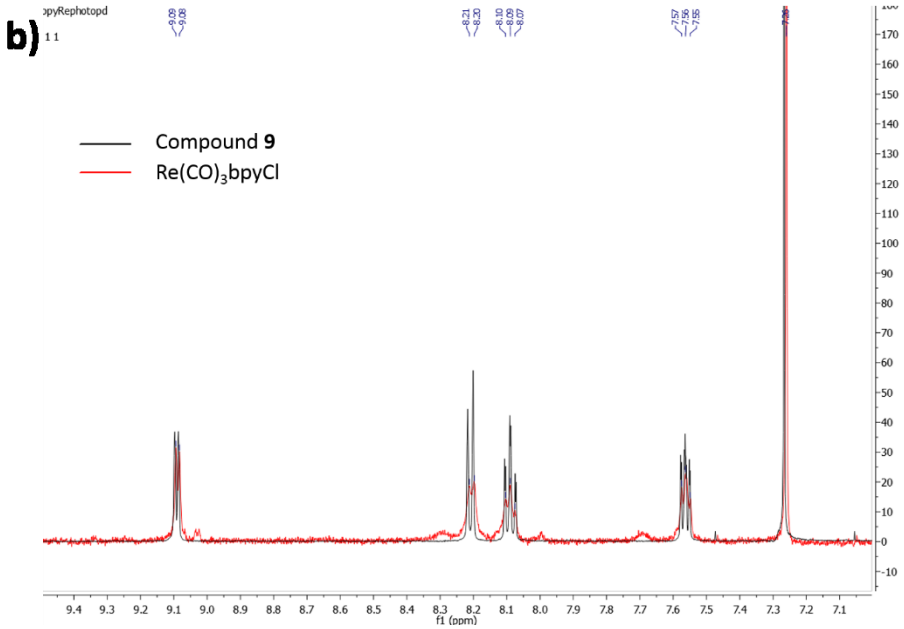

Figure 4.21 ^{1}HNMR (500 MHz, CD_3CN, ppm) spectra of photoproduct of **9** and synthesized $Re(CO)_3bpyCl$.

V. Summary and future work.

In this work, we synthesized a Re-Mn dinuclear photoCORM: $(CO)_5MnRe(CO)_3(bpy)$ (compound **7**). Like compound **1**-**5**, visible light excitation of the $\sigma_{MM} \rightarrow \pi_L^*$ transition leads to homolytic cleavage of the Re-Mn bond. Although compound **7** does not show any emission under irradiation, one of the photoproducts (**8**) displays a broad orange emission (λ_{max} = 555 nm). As a "turn-on" emissive photoCORM, photochemical reaction and location of photoproducts can be monitored and tracked in biological targets. Mascharak and co-workers synthesized a "turn-on" emissive photoCORM based on emission of the free ligand from rhenium carbonyls photolysis[4]. In their work, a fluorescence (λ_{max} = 390 nm) was seen from cells incubated with photoCORM after irradiation; however, this system would have limited applicability since such short wavelength emission has very shallow penetration in the tissue. In our work, broad and long wavelength ^{3}MLCT emission from rhenium photoproduct has more potential in biological study and emissive photoproduct (**8**) may also act as a photosensitizer to form singlet oxygen. In future, further characterization and study will be carried on photoproduct (**8**) to identify its structures and compound **7** will be studied in PLGA nano/micro carriers for biological purpose.

Reference

1. Li, Z.; Pierri, A. E.; Huang, P.-J.; Wu, G.; Iretskii, A. V.; Ford, P. C. Dinuclear PhotoCORMs: Dioxygen-Assisted Carbon Monoxide Uncaging from Long-Wavelength-Absorbing Metal–Metal-Bonded Carbonyl Complexes. *Inorg. Chem*. **2017**, 56, 6094-6104.

2. Wrighton, M. S.; Morse, D. L.; Gray, H. B.; Ottesen, D. K. Interpretation of the Electronic Spectra of Low-Spin d^6 $M(CO)_5X$ Complexes. Primary Excited State Decay Paths in $Re(CO)_5X$ Complexes. *J. Am. Chem. Soc*. **1976**, 98, 1111–1119.

3. Pierri, A. E.; Pallaoro, A.; Wu, G.; Ford, P. C. A Luminescent and Biocompatible PhotoCORM. *J. Am. Chem. Soc*. **2012**, 134, 18197–18200.

4. Carrington, S. J.; Chakraborty, I.; Bernard, J. M. L.; Mascharak, P. K. Synthesis and Characterization of a "Turn-On" photoCORM for Trackable CO Delivery to Biological Targets. ACS Med. *Chem. Lett*. **2014**, 5, 1324–1328.

5. Carrington, S. J.; Chakraborty, I.; Bernard, J. M. L.; Mascharak, P. K. A Theranostic Two-Tone Luminescent PhotoCORM Derived from Re(I) and (2-Pyridyl)-Benzothiazole: Trackable CO Delivery to Malignant Cells. *Inorg. Chem*. **2016**, 55, 7852-7858.

6. Chakraborty, I.; Jimenez, J.; Sameera, W. M. C.; Kato, M.; Mascharak, P. K. Luminescent Re(I) Carbonyl Complexes as Trackable PhotoCORMs for CO Delivery to Cellular Targets. *Inorg. Chem*. **2017**, 56, 2863–2873.

7. Van Outersterp, J. W. M.; Hartl, F.; Stufkens, D. J. Variable Temperature IR Spectroelectrochemical Investigation of the Stability of the Metal-Metal-Bonded Radical Anions [(CO)5MnRe(CO)3(L)].bul.- (L = 2,2'-Bipyridine (BPY), 2,2'-Bipyrimidine (BPYM), 2,3-Bis(2-Pyridyl)pyrazine (DPP)) and [(CO)5MnRe(CO)3(L)Re(Br)(CO)3].bul.- (L = BPYM, DPP) Controlled by the Lowest .pi. (alpha.-Diimine) Orbital Energy. *Organometallics* **1995**, 14, 3303–3310.

8. Morse, D. L.; Wrighton, M. S. Reaction of Pentacarbonyl-Manganese(-I) and -Rhenium(-I) with Metal Carbonyl Halide Derivatives. *Journal of Organometallic Chemistry* **1977**, 125, 71–77.

9. Yi, X.; Zhao, J.; Sun, J.; Guo, S.; Zhang, H. Visible Light-Absorbing Rhenium Tricarbonyl Complexes as Triplet Photosensitizers in Photooxidation and Triplet–triplet Annihilation Upconversion. *Dalton Trans*. **2013**, 42, 2062–2074.

10. Woźna, A.; Kapturkiewicz, A. The Luminescence Properties of the Heteroleptic [Re(CO)3(N∩N)Cl] and [Re(CO)3(N∩N)(CH3CN)]+ Complexes in View of the Combined Marcus–Jortner and Mulliken–Hush Formalism. *Phys. Chem. Chem. Phys*. **2015**, 17, 30468–30480.

11. Benson, E. E.; Kubiak, C. P. Structural Investigations into the Deactivation Pathway of the CO_2 Reduction Electrocatalyst Re(bpy)$(CO)_3$Cl. *Chem. Commun*. **2012**, 48, 7374–7376.

Appendix

Crystallographic parameters crystal data of $(CO)_5MnRe(CO)_3(phen)$ (**6**)

Table 1. Crystal data and structure refinement for Li07052015_0m.

Identification code	Li07052015_0m
Empirical formula	C18 H8 Mn N2 O8 Re
Formula weight	621.40
Temperature	100(2) K
Wavelength	0.71073 Å
Crystal system	Monoclinic
Space group	P21/c
Unit cell dimensions	a = 8.5977(3) Å □= 90°.
	b = 13.9292(6) Å□= 100.103(2)°.
	c = 15.9216(6) Å □ = 90°.
Volume	1877.19(13) $Å^3$
Z	4
Density (calculated)	2.199 Mg/m^3
Absorption coefficient	7.166 mm-1
F(000)	1176
Crystal size	0.2 x 0.1 x 0.03 mm^3
Theta range for data collection	1.956 to 27.149°.
Index ranges	-10<=h<=11, -17<=k<=10, -20<=l<=20
Reflections collected	10672
Independent reflections	4136 [R(int) = 0.0254]
Completeness to theta = 25.242°	100.0 %
Absorption correction	Semi-empirical from equivalents
Max. and min. transmission	0.7455 and 0.5338
Refinement method	Full-matrix least-squares on F2
Data / restraints / parameters	4136 / 0 / 271
Goodness-of-fit on F2	1.020
Final R indices [I>2sigma(I)]	R1 = 0.0216, wR2 = 0.0492
R indices (all data)	R1 = 0.0280, wR2 = 0.0513
Extinction coefficient	n/a
Largest diff. peak and hole	1.268 and -0.981 $e.Å^{-3}$

Table 2. Atomic coordinates (x 10^4) and equivalent isotropic displacement parameters ($Å^2$x 10^3)
for Li07052015_0m. U(eq) is defined as one third of the trace of the orthogonalized U^{ij} tensor.

	x	y	z	U(eq)
C(1)	8789(4)	1007(2)	-491(2)	13(1)
C(2)	9025(4)	2932(2)	-634(2)	12(1)
C(3)	10385(4)	2036(2)	816(2)	10(1)
C(4)	6761(4)	4268(2)	-9(2)	13(1)
C(5)	9738(4)	4172(2)	813(2)	12(1)
C(6)	8781(4)	3216(3)	1971(2)	18(1)
C(7)	5901(4)	3382(2)	1238(2)	17(1)
C(8)	7655(4)	5020(2)	1630(2)	16(1)
C(9)	5183(4)	2332(2)	-1196(2)	15(1)
C(10)	3621(4)	2187(2)	-1557(2)	18(1)
C(11)	2661(4)	1658(3)	-1119(3)	19(1)
C(12)	3286(4)	1281(2)	-335(2)	16(1)
C(13)	4870(4)	1449(2)	14(2)	12(1)
C(14)	5628(4)	1066(2)	847(2)	12(1)
C(15)	4818(4)	574(2)	1396(2)	15(1)
C(16)	5632(4)	229(2)	2159(2)	18(1)
C(17)	7250(4)	373(2)	2356(2)	17(1)
C(18)	7995(4)	871(2)	1788(2)	14(1)
Mn(1)	7779(1)	3904(1)	1065(1)	10(1)
N(1)	5810(3)	1975(2)	-419(2)	10(1)
N(2)	7206(3)	1230(2)	1044(2)	11(1)
O(1)	9142(3)	390(2)	-915(2)	19(1)
O(2)	9477(3)	3468(2)	-1085(2)	18(1)
O(3)	11631(3)	2000(2)	1226(2)	18(1)
O(4)	6089(3)	4480(2)	-661(2)	19(1)
O(5)	10996(3)	4329(2)	694(2)	17(1)
O(6)	9426(4)	2804(2)	2555(2)	29(1)

O(7)	4740(3)	3057(2)	1368(2)	29(1)
O(8)	7621(3)	5713(2)	2017(2)	25(1)
Re(1)	8295(1)	2067(1)	157(1)	8(1)

Table 3. Bond lengths [Å] and angles [°] for Li07052015_0m.

C(1)-O(1)	1.165(4)
C(1)-Re(1)	1.892(3)
C(2)-O(2)	1.151(4)
C(2)-Re(1)	1.925(3)
C(3)-O(3)	1.154(4)
C(3)-Re(1)	1.916(3)
C(4)-O(4)	1.134(4)
C(4)-Mn(1)	1.851(4)
C(5)-O(5)	1.151(4)
C(5)-Mn(1)	1.837(3)
C(6)-O(6)	1.150(5)
C(6)-Mn(1)	1.817(4)
C(7)-O(7)	1.147(4)
C(7)-Mn(1)	1.835(4)
C(8)-O(8)	1.148(4)
C(8)-Mn(1)	1.809(4)
C(9)-N(1)	1.354(5)
C(9)-C(10)	1.380(5)
C(10)-C(11)	1.383(5)
C(11)-C(12)	1.373(5)
C(12)-C(13)	1.398(5)
C(13)-N(1)	1.365(4)
C(13)-C(14)	1.471(5)
C(14)-N(2)	1.357(4)
C(14)-C(15)	1.391(5)
C(15)-C(16)	1.378(5)
C(16)-C(17)	1.386(5)
C(17)-C(18)	1.382(5)

C(18)-N(2)	1.353(4)
Mn(1)-Re(1)	3.0101(5)
N(1)-Re(1)	2.175(3)
N(2)-Re(1)	2.167(3)

O(1)-C(1)-Re(1)	176.1(3)
O(2)-C(2)-Re(1)	177.9(3)
O(3)-C(3)-Re(1)	178.3(3)
O(4)-C(4)-Mn(1)	177.6(3)
O(5)-C(5)-Mn(1)	176.8(3)
O(6)-C(6)-Mn(1)	178.2(3)
O(7)-C(7)-Mn(1)	178.3(4)
O(8)-C(8)-Mn(1)	177.1(3)
N(1)-C(9)-C(10)	122.0(3)
C(9)-C(10)-C(11)	119.4(3)
C(12)-C(11)-C(10)	119.3(3)
C(11)-C(12)-C(13)	119.8(3)
N(1)-C(13)-C(12)	120.7(3)
N(1)-C(13)-C(14)	116.2(3)
C(12)-C(13)-C(14)	123.0(3)
N(2)-C(14)-C(15)	121.8(3)
N(2)-C(14)-C(13)	114.5(3)
C(15)-C(14)-C(13)	123.6(3)
C(16)-C(15)-C(14)	119.6(3)
C(15)-C(16)-C(17)	118.9(3)
C(18)-C(17)-C(16)	119.1(3)
N(2)-C(18)-C(17)	122.6(3)
C(8)-Mn(1)-C(6)	96.87(16)
C(8)-Mn(1)-C(7)	97.81(15)
C(6)-Mn(1)-C(7)	88.81(16)
C(8)-Mn(1)-C(5)	94.01(15)
C(6)-Mn(1)-C(5)	87.47(15)
C(7)-Mn(1)-C(5)	167.95(15)
C(8)-Mn(1)-C(4)	99.45(16)
C(6)-Mn(1)-C(4)	163.63(16)
C(7)-Mn(1)-C(4)	87.80(15)

C(5)-Mn(1)-C(4)	92.56(15)
C(8)-Mn(1)-Re(1)	174.99(11)
C(6)-Mn(1)-Re(1)	81.03(12)
C(7)-Mn(1)-Re(1)	86.72(11)
C(5)-Mn(1)-Re(1)	81.38(10)
C(4)-Mn(1)-Re(1)	82.79(11)
C(9)-N(1)-C(13)	118.9(3)
C(9)-N(1)-Re(1)	124.6(2)
C(13)-N(1)-Re(1)	116.3(2)
C(18)-N(2)-C(14)	117.9(3)
C(18)-N(2)-Re(1)	124.2(2)
C(14)-N(2)-Re(1)	117.9(2)
C(1)-Re(1)-C(3)	90.15(14)
C(1)-Re(1)-C(2)	90.11(14)
C(3)-Re(1)-C(2)	89.44(14)
C(1)-Re(1)-N(2)	95.71(12)
C(3)-Re(1)-N(2)	95.81(12)
C(2)-Re(1)-N(2)	172.14(12)
C(1)-Re(1)-N(1)	91.25(12)
C(3)-Re(1)-N(1)	170.65(12)
C(2)-Re(1)-N(1)	99.80(12)
N(2)-Re(1)-N(1)	74.85(10)
C(1)-Re(1)-Mn(1)	172.59(10)
C(3)-Re(1)-Mn(1)	87.64(9)
C(2)-Re(1)-Mn(1)	82.80(9)
N(2)-Re(1)-Mn(1)	91.55(7)
N(1)-Re(1)-Mn(1)	92.07(7)

Symmetry transformations used to generate equivalent atoms:

Table 4. Anisotropic displacement parameters ($Å^2 x\ 10^3$) for Li07052015_0m. The anisotropic
displacement factor exponent takes the form: $-2\pi^2[\ h^2\ a^{*2} U^{11} + ... + 2\ h\ k\ a^*\ b^*\ U^{12}\ ]$

	U^{11}	U^{22}	U^{33}	U^{23}	U^{13}	U^{12}
C(1)	10(2)	11(2)	17(2)	3(1)	1(1)	-2(1)
C(2)	12(2)	12(2)	12(2)	-6(1)	0(1)	1(1)
C(3)	19(2)	9(2)	4(2)	-1(1)	7(1)	-1(1)
C(4)	12(2)	11(2)	16(2)	-2(1)	3(2)	-2(1)
C(5)	18(2)	8(2)	10(2)	-1(1)	-2(1)	0(1)
C(6)	22(2)	15(2)	18(2)	-2(2)	4(2)	-6(2)
C(7)	23(2)	12(2)	16(2)	-4(1)	7(2)	0(2)
C(8)	12(2)	18(2)	18(2)	-1(2)	4(1)	-3(1)
C(9)	16(2)	10(2)	18(2)	0(1)	0(1)	0(1)
C(10)	21(2)	17(2)	14(2)	-1(1)	-5(2)	8(2)
C(11)	12(2)	20(2)	23(2)	-8(2)	-1(2)	2(1)
C(12)	10(2)	14(2)	24(2)	-4(2)	4(1)	2(1)
C(13)	13(2)	8(2)	15(2)	-4(1)	3(1)	2(1)
C(14)	11(2)	7(1)	16(2)	-4(1)	2(1)	1(1)
C(15)	14(2)	10(2)	21(2)	-2(1)	4(1)	-1(1)
C(16)	23(2)	12(2)	21(2)	2(1)	9(2)	-1(1)
C(17)	24(2)	11(2)	15(2)	3(1)	4(2)	1(1)
C(18)	15(2)	10(2)	16(2)	0(1)	-1(1)	-1(1)
Mn(1)	11(1)	8(1)	11(1)	-1(1)	3(1)	-2(1)
N(1)	12(1)	10(1)	8(1)	-4(1)	2(1)	2(1)
N(2)	12(1)	7(1)	13(1)	-3(1)	2(1)	-1(1)
O(1)	22(1)	13(1)	24(2)	-8(1)	5(1)	0(1)
O(2)	27(1)	14(1)	14(1)	0(1)	8(1)	-3(1)
O(3)	11(1)	22(1)	20(1)	0(1)	-3(1)	-1(1)
O(4)	14(1)	24(1)	19(1)	2(1)	1(1)	1(1)
O(5)	13(1)	16(1)	22(1)	-2(1)	4(1)	-6(1)
O(6)	45(2)	19(1)	18(2)	5(1)	-5(1)	-5(1)
O(7)	23(1)	23(1)	45(2)	-8(1)	19(1)	-11(1)
O(8)	32(2)	15(1)	33(2)	-10(1)	14(1)	-4(1)
Re(1)	8(1)	7(1)	10(1)	0(1)	1(1)	0(1)

Table 5. Hydrogen coordinates (x 10^4) and isotropic displacement parameters ($Å^2$x 10^3) for Li07052015_0m.

	x	y	z	U(eq)
H(9)	5839	2693	-1501	18
H(10)	3209	2449	-2102	22
H(11)	1581	1556	-1358	23
H(12)	2644	908	-32	19
H(15)	3710	477	1246	18
H(16)	5092	-102	2543	21
H(17)	7839	133	2874	20
H(18)	9105	965	1926	17